REPORT DOCUMENTATION PAGE

AFRL-SR-AR-TR-07-0335

Public reporting burden for this collection of information is estimated to average 1 hour per response, including the time for reviewing instr
data needed, and completing and reviewing this collection of information. Send comments regarding this burden estimate or any other as
this burden to Department of Defense, Washington Headquarters Services, Directorate for Information Operations and Reports (0704-018
4302. Respondents should be aware that notwithstanding any other provision of law, no person shall be subject to any penalty for failing t
valid OMB control number. **PLEASE DO NOT RETURN YOUR FORM TO THE ABOVE ADDRESS.**

...not display a currently

1. REPORT DATE *(DD-MM-YYYY)*	2. REPORT TYPE	3. DATES COVERED *(From - To)*
16-08-2007	Technical	01-06-2005 - 31-05-2006

4. TITLE AND SUBTITLE

(U) Army Research Office and Air Force Office of Scientific Research 2006 Contractors Meeting in Chemical Propulsion

5a. CONTRACT NUMBER

5b. GRANT NUMBER

5c. PROGRAM ELEMENT NUMBER

61102A, 61102F

6. AUTHOR(S)

Ralph Anthenien and Julian M. Tishkoff

5d. PROJECT NUMBER

5e. TASK NUMBER

5f. WORK UNIT NUMBER

7. PERFORMING ORGANIZATION NAME(S) AND ADDRESS(ES)

Army Research Office
Research Triangle Park NC
27709-2211

Air Force Office of Scientific Research
Arlington VA 22203-1768

8. PERFORMING ORGANIZATION REPORT NUMBER

9. SPONSORING / MONITORING AGENCY NAME(S) AND ADDRESS(ES)

AFOSR/NA
875 North Randolph Street
Suite 325, Room 3112
Arlington VA 22203-1768

10. SPONSOR/MONITOR'S ACRONYM(S)

11. SPONSOR/MONITOR'S REPORT NUMBER(S)

12. DISTRIBUTION / AVAILABILITY STATEMENT

Approved for public release; distribution is unlimited

13. SUPPLEMENTARY NOTES

14. ABSTRACT

Abstracts are given for 6.1 basic research in chemical propulsion sponsored by the Army Research Office and the Air Force Office of Scientific Research.

20070910360

15. SUBJECT TERMS

Flames, Propulsion, Gas Turbines, Diesel Engines, Scramjets, Pulse Detonation Engines, Hydrocarbon Fuels, Diagnostics, Spray, Droplet, Supercritical Fluids, Turbulence, Combustion

16. SECURITY CLASSIFICATION OF:			17. LIMITATION OF ABSTRACT	18. NUMBER OF PAGES	19a. NAME OF RESPONSIBLE PERSON
a. REPORT	b. ABSTRACT	c. THIS PAGE			Julian M. Tishkoff
Unclassified	Unclassified	Unclassified	UL	148	19b. TELEPHONE NUMBER *(include area code)* (703) 696-8478

Standard Form 298 (Rev. 8-98)
Prescribed by ANSI Std. Z39.18

ARO/AFOSR CONTRACTORS MEETING

IN

CHEMICAL PROPULSION

Boulder CO
11-13 June 2007

MONDAY, 11 JUNE

1:00 - 1:15	Army Research Office Overview – Ralph Anthenien
1:15 - 1:30	AFOSR Combustion and Diagnostics Program – Julian Tishkoff

TOPIC: High-Speed and Diesel Propulsion

1:30 - 2:00	Ramjet Research Campbell Carter, AFRL/PR
2:00 - 2:45	Dispersion, Mixing, and Combustion in Turbulent and High-Speed Flows, Air-Breathing Propulsion, and Hypersonic Flight Paul Dimotakis, California Institute of Technology
2:45 - 3:15	Pulse Detonation Physicochemical and Exhaust Relaxation Processes Fred Schauer, AFRL/PR
3:15 - 3:30	BREAK

TOPIC: Sprays

3:30 - 4:00	Break-Up of Liquid Streams at High Pressure William Sirignano, University of California, Irvine
4:00 - 4:30	Shock Tube Measurements of Ignition Processes and Spray-Shock Wave Interactions Ron Hanson, Stanford University
4:30 - 5:00	Extinction, Entrainment, and Stabilization Studies in Spray Flames Kevin Lyons, North Carolina State University
5:00	DINNER

TUESDAY, 12 JUNE

8:15 - 8:30	Announcements

TOPIC: Combustion Fundamentals

8:30 - 9:00	Experimental and Computational Characterization of Combustion Phenomena James Gord, AFRL/PR
9:00 - 9:30	Two-Point Scalar Time-Series Measurements in Turbulent Partially Premixed Flames Galen King, Purdue University
9:30 - 10:00	Combustion Research Joseph Zelina, AFRL/PR
10:00 – 10:30	BREAK
10:30 – 11:00	Turbine Burners: Turbulent Combustion of Liquid Fuels William Sirignano, University of California, Irvine
11:00 – 11:30	Chemical Kinetics and Turbulence in Ignition C. K. Law, Princeton University
11:30 – 12:00	Physical and Chemical Processes in Flames C. K. Law, Princeton University
12:00 - 1:00	LUNCH

TOPIC: Fuels

1:00 - 1:30	Development of Detailed and Reduced Mechanisms for Surrogate Fuels Jackie Sung, Case Western Reserve University
1:30 - 2:00	Autoignition and Combustion of JP-8 Kal Seshadri, University of California, San Diego
2:00 - 2:30	Formation of Soot in High Pressure Diffusion Flames William Roberts, North Carolina State University
2:30 - 2:45	BREAK
2:45 - 4:30	DISCUSSION

TOPIC: Cyber Combustion

4:30 - 4:50	ARO BUSINESS SESSION ARO-Funded Researchers

4:50 - 5:10	AFOSR BUSINESS SESSION AFOSR-Funded Researchers
5:20	DINNER

WEDNESDAY, 13 JUNE

8:15 - 8:30	Announcements

TOPIC: Modeling and Simulation

8:30 - 9:00	PDF Modeling of Turbulent Combustion Steve Pope, Cornell University
9:00 - 9:30	Filtered Density Function for Subgrid Scale Modeling Of Turbulent Combustion Peyman Givi, University of Pittsburgh
9:30 - 10:00	Chemical modeling of Large-Eddy Simulation of Turbulent Combustion Heinz Pitsch, Stanford University
10:00 – 10:30	BREAK
10:30 - 11:00	Investigation of Subgrid-Scale Mixing and Turbulence- Chemistry Interaction in Turbulent Partially Premixed Flames Using Experimental Data Chenning Tong, Clemson University

TOPIC: Propulsion Concepts

11:00 – 11:30	Plasma Propellant Ignition Studies Stefan Thynell, Pennsylvania State University
11:30 – 12:00	Computer-Based Adaptation Tool for Advanced Diesel Engines Used in Military Applications Dinu Taraza, Wayne State University
12:00 – 1:15	LUNCH
1:15 - 3:30	Tour of NIST Laboratory Facilities
3:30	ADJOURN

AFOSR SPONSORED RESEARCH IN COMBUSTION AND DIAGNOSTICS

PROGRAM MANAGER: JULIAN M. TISHKOFF

AIR FORCE OFFICE OF SCIENTIFIC RESEARCH
875 North Randolph Street
Suite 325, Room 3112
Arlington VA 22203-1768

SUMMARY/OVERVIEW: The Air Force Office of Scientific Research (AFOSR) program in combustion and diagnostics currently is focused on five areas of study: high-speed propulsion, turbulent combustion, diagnostics, supercritical fuel behavior, and plasma-enhanced combustion. An assessment of major research needs in each of these areas is presented.

TECHNICAL DISCUSSION

AFOSR is the single manager for Air Force basic research, including efforts based on external proposals and in-house work at the Air Force Research Laboratory (AFRL). Combustion and Diagnostics is assigned to the AFOSR Directorate of Aerospace, Chemical, and Materials Sciences along with programs in rocket and space propulsion, fluid and solid mechanics, structural materials, and chemistry.

Interests of the AFOSR Combustion and Diagnostics subarea are given in the SUMMARY section above. Many achievements can be cited for these interests, yet imposing fundamental research challenges remain. The objective of the program is publications in the refereed research literature describing significant new understanding of multiphase turbulent reacting flow. Incremental improvements to existing scientific approaches, hardware development, and computer codes fall outside the scope of this objective.

The Combustion and Diagnostics subarea supports the Air Force commitment to aerospace propulsion. Accordingly, the research in this subarea will address research issues related to chemical propulsion for all Air Force aerospace missions, including combined cycle propulsion for access to space. This program will complement related research activities in space propulsion and energetic materials.

The primary focus of research in turbulent combustion is the creation of computational modeling tools for combustor designers that are both computationally tractable and quantitatively predictive. This research has been directed in two areas: the formulation of augmented reduced chemical kinetic mechanisms for the combustion of current and future alternative hydrocarbon fuels and the development of subgrid-scale models for large eddy simulation of turbulent combustion. Fiscal Year 2007 marked substantial growth in support for research on characterizing hydrocarbon fuels through the initiation of a Department of Defense Multidisciplinary University Research Initiative (MURI) topic on Science-Based Design of Fuel-Flexible Chemical Propulsion/Energy Conversion Systems. Further funding growth in this area is expected in Fiscal Year 2008.

Future airbreathing and chemical rocket propulsion systems will require propellants to absorb substantial thermal energy, raising their temperatures to supercritical thermodynamic conditions.

Understanding and controlling fluid properties at these conditions will be crucial for avoiding thermal degradation and for optimizing subsequent processes within the combustor. Research has focused on the role of supercritical transport in the thermal destabilization of hydrocarbon fuel prior to combustion and on primary and secondary fuel breakup under transcritical and supercritical conditions.

Plasma research is supported through the AFOSR Theme, Plasma Dynamics for Aerospace Applications and focuses primarily on the utilization of plasmas for ignition and flame stabilization in scramjets; however, the extension of this technology to other modes of chemical propulsion and energy conversion also is of interest. Research has been supplemented by research coordinated between universities and small businesses under the Department of Defense Small Business Technology Transfer (STTR) Program. The Air Force also supports related research activity in Russia under the Air Force Research Laboratory Russian Research Initiative. The Theme and Russian research activity was presented as part of a Weakly Ionized Gas Dynamics (WIG) Workshop at the 35th AIAA Aerospace Sciences Meeting and Exhibit in January 2007. The next workshop will take place in January 2008.

Decisions on support for research proposals are based on scientific opportunities and technology needs. Researchers interested in submitting proposals should contact Dr. Tishkoff for information on time constraints associated with proposal evaluations. Further information on research interests and proposal preparation can be found on the AFOSR web site, http://www.afosr.af.mil. These interests include special programs such as the Department of Defense University Research Instrumentation Program (DURIP), the Defense Experimental Program to Stimulate Competitive Research (DEPSCoR), the Small Business Technology Transfer Program (STTR), the Multidisciplinary University Research Initiative, and the new AFRL Discovery Challenge (DCT) Program. The availability of funds places a major constraint on program redirection and growth. Figure 1 shows the recent trend of funding for basic research in combustion and diagnostics from Air Force and DOD sources. Informal inquiries for new research are encouraged throughout the year. Formal proposals should be submitted by 1 April for peer review.

The purpose of this abstract has been to communicate AFOSR perceptions of research trends to the university and industrial research communities. However, communication from those communities back to AFOSR also is desirable and essential for creating new research opportunities. Therefore, all proposals and inquiries for fundamental research are encouraged even if the content does not fall within the areas of emphasis described herein. Comments and criticisms of current AFOSR programs also are welcome.

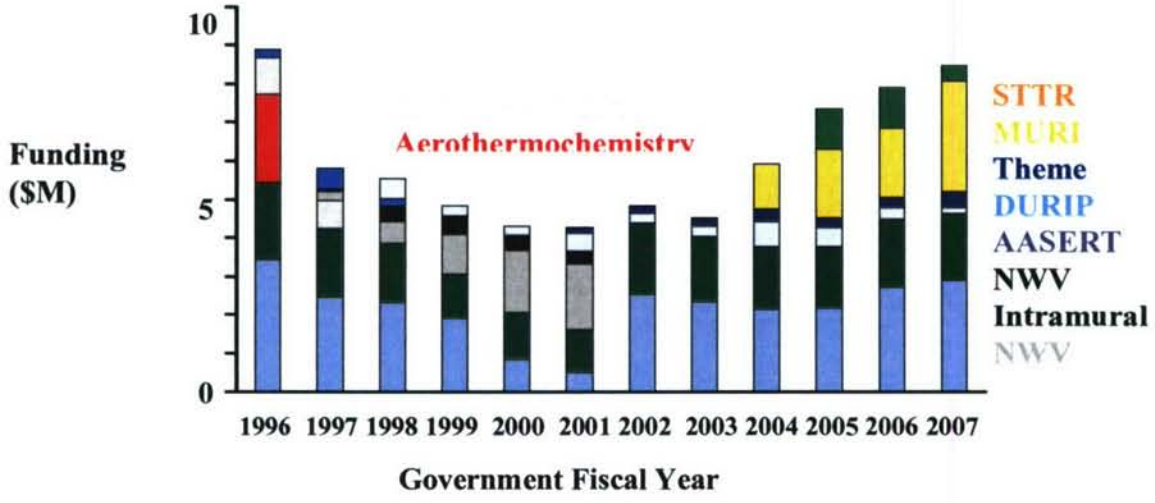

Figure 1. AFOSR Funding for Combustion and Diagnostics

TITLE: RAMJET RESEARCH

AFOSR TASK 2308BW

Principal Investigators: Campbell D. Carter
Mark R. Gruber
Skip Williams

Aerospace Propulsion Division, Propulsion Directorate (AFRL/PRA)
Air Force Research Laboratory
Wright-Patterson AFB OH 45433

SUMMARY/OVERVIEW

This research task includes work in three primary focus areas: (1) multiphase flows relevant to fuel injection into high-speed, oxidizing streams, (2) shock/boundary-layer interactions within the scramjet flowpath, and (3) multidisciplinary laser measurements for benchmarking modeling and simulation and for elucidating the physics of high-speed flows. Within each of these areas, there is a strong relevance to the scramjet propulsion system, and that relationship helps frame the context of our research. The motivation for this program is the need to develop the science basis to enable the design of high-speed, air-breathing propulsion systems at a variety of scales. Lack of a science basis—and, in general, technology basis—is a limiting factor in design of scramjet vehicles. The approach will be to couple numerical computations and experimentation, to yield a thorough understanding of each problem.

TECHNICAL DISCUSSION

Areas of focus in the past year included the following:

1) Study of fuel injection, gaseous and supercritical, and the development/testing of plasma-based ignition methods.
2) Development/Application of laser diagnostic techniques for use in scramjet testing; application of X-ray diagnostics for optically thick condensing jets.
3) Characterization of mixing of co-annular jets into a low-speed co-flow to build a validation database.

Three collaborations are ongoing with AFOSR extramurally funded personnel: Profs. R. Hanson (Stanford, tunable diode laser absorption for scramjets); C. Tong (Clemson, LES validation); Y. Ju (Princeton, non-equilibrium discharges). Other university collaborators include R. Pitz (Vanderbilt, validation measurements for high-speed flows), J. Driscoll

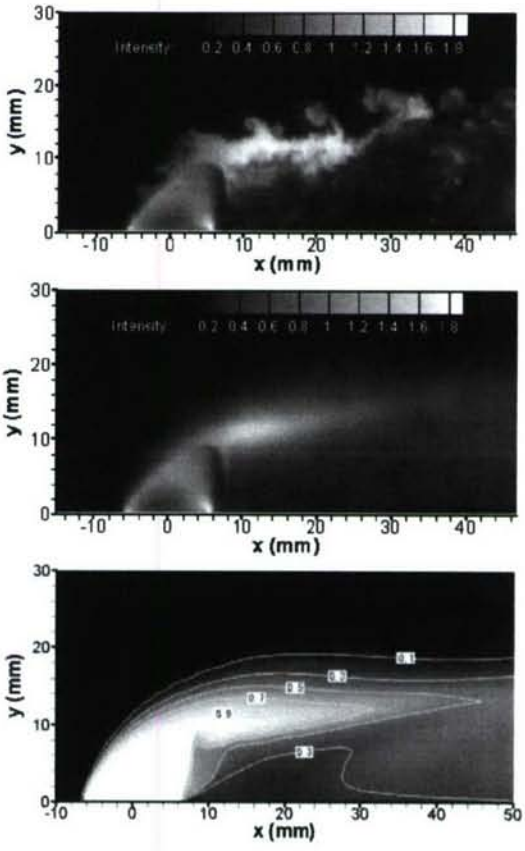

Fig. 1 Instantaneous and frame-averaged NO PLIF measurements (top and middle) and computations of the jet mole fraction from a diamond-shaped injector.

(Michigan, cavity flameholding), J. Edwards (N.C.S.U., two-phase and supercritical injection modeling), M. Gundersen (U.S.C., pulsed non-equilibrium discharges), and R. Bowersox (Texas A&M, fuel injection). AFRL collaborations worth noting are those with Drs. T. Edwards (PRTG, supercritical fluids/injection), F. Schauer (PRTC, PDE ignition), and J. Gord (PRTC, ballistic imaging for fuel sprays). Drs. S. Lin, Taitech, and K.-Y. Hsu, Innovative Scientific Solutions, lead our in-house contractor efforts

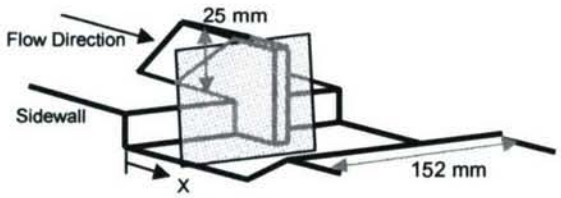

Fig. 2. Strut-cavity configuration. Image plane shown in grey

A study begun in FY06 focused on the potential for flush-wall diamond-shaped injectors to improve fuel mixing and to act as flameholders. This work is based on the observation that the diamond-shaped injector produces a lateral counter-rotating vortex pair (LCVP) wherein the residence time may be sufficient for flameholding. The goal for this study was to characterize the near-field flow structures and mixing of a diamond-shaped, normal injector, in comparison to that of a normal circular injector, in a Mach-2 crossflow. The diamond injector also included a "tandem" port used as an igniter or to simulate the flowfield of igniter; this port could be oriented upstream or downstream of the diamond injector. For mixing experiments NO-laden air was injected through the diamond injector or the tandem *igniter* port and the NO PLIF (planar laser-induced fluorescence) technique was used to characterize the injection. Sample instantaneous and frame-averaged NO PLIF images are shown in Fig. 1 along with a RANS calculation of the injectant mole-fraction. Although this effort demonstrates the presence of the LCVP and that the torch injector does not significantly interfere with its formation, this region is fuel rich and no significant burning takes place. Future efforts will focus on quantifying the flowfield (with particle image velocimetry) and determining under what conditions flameholding may occur.

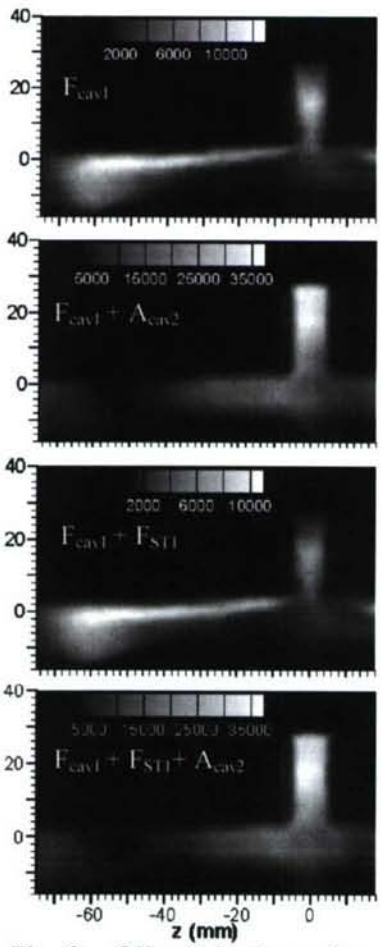

Fig. 3. OH within the cavity-integrated strut (x=32 mm, see Fig. 2). F_{cav} and A_{cav} indicate fuel and air fed directly into cavity (ramp face). F_{ST1} indicates strut side-face fueling

Understanding flameholding and fuel injection in a high-speed crossflow, so that one can scale up combustor duct sizes, is critical to the development of scramjets (beyond the current scale). Consequently, intrusive fuel injector designs are now being studied, as opposed to flush-wall designs. Clearly, a challenge is to enable fuel to reach the middle of the flowfield while maintaining "communication" with the flameholder.

One such fuel injector concept is shown in Fig. 2. Here a strut-injector is integrated into the flameholding cavity; the freestream Mach number was 2. Measurements of the burning downstream of the strut and within the cavity, accomplished using the OH PLIF technique, are shown in Fig. 3. Ideally, the strut should help distribute the fuel and spread the flame (from the cavity) to the center of the duct but not otherwise interfere with the flameholder. In this case both fuel and air are fed directly into the cavity from the cavity ramp, while the ramp fueling is from either side (of the ramp). Fueling from the end face of the ramp, however, is not effective in spreading the flame, because the mixture behind the ramp will then be too rich to burn. Indeed, the region in and

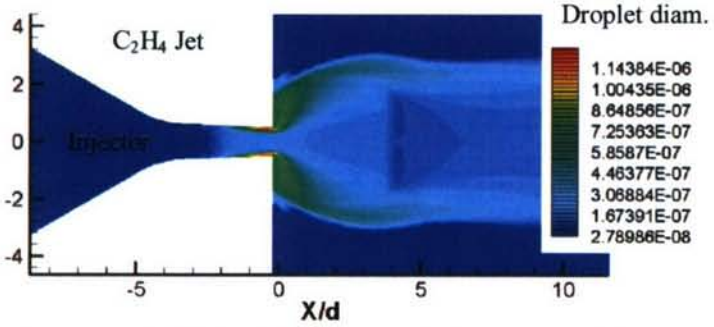

Fig. 4. Modeled droplet diameters with $T_{inj} = 288$ K $\approx T_{crit}$. Measurements were at $T_{inj} = 285$ K. Diam. units: meters.

around the cavity flameholder is typically fuel rich (especially when fuel is injected only from the walls), and thus air addition to the cavity improves the cavity burning.

Injection of a supercritical fluid into a superheated, low-pressure, high-speed crossflow is relevant to much of the flight envelope. Extensive studies conducted in our laboratory have shown that the plume structure of supercritical fuel jets can be dramatically different from those of liquid or gaseous jets, due to the thermodynamic properties of the supercritical fluid and the occurrence of condensation. Typically, supercritical jets behave like ideal-gas jets when $T_{inj} > T_{crit}$. A two-phase jet with a large number of nucleated droplets, however, can be generated when $T_{inj} \approx T_{crit}$ (see Fig. 4). Onset conditions for condensation and the content and properties of the liquid phase within the injector are being studied, in collaboration with Drs. T. Edwards (AFRL) and J. Edwards (N.C.S.U.). Modeling results (J. Edwards) are shown above (Fig. 4) for C_2H_4 (ethylene). Typical optical methods do not allow us to probe this jet; consequently, alternatives to conventional diagnostics are now being explored, including the use of small-angle X-ray scattering (SAXS), in collaboration with Drs. J. Wang and A. Sandy (Advanced Photon Source, Argonne National Laboratories). Here, a monochromatic, 0.1×0.1 mm^2 X-ray beam having a photon flux of $\sim 10^{11}$ s^{-1} was directed through a C_2H_4 plume from an injector with a 0.5-mm exit diameter; the C_2H_4 jet was injected into quiescent N_2. A large-area CCD detector, located 2-m from the jet, captured the forward scattered X-ray photons (while a "mask" blocked the direct beam). The resulting scattering profile (intensity vs. magnitude of scattered photon momentum transfer, $Q = 4\pi\sin\theta/\lambda$) from one such measurement—with a strongly condensing C_2H_4 jet and recorded 0.5 mm ($X/d = 1$) from the injector exit—is shown in Fig. 5. An estimate of mean droplet diameter, based on a model fit, is ~50 nm (whereas predictions are an order of magnitude greater). Furthermore, with a scattering calibration, droplet number density can be derived from the scattering intensity.

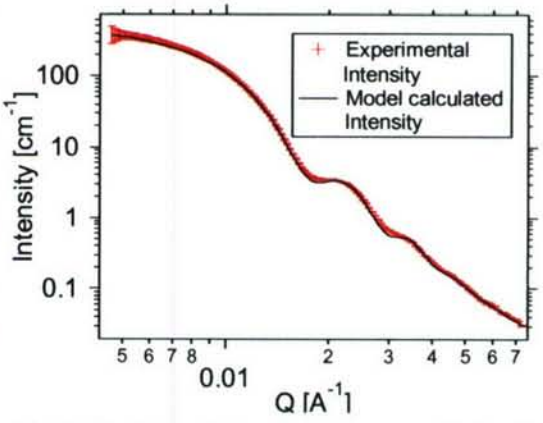

Fig.5. Scattering intensity versus magnitude of Q vector from a supercritical ethylene jet.

Advanced computational modeling approaches such as Large Eddy Simulation, LES, will play a role in the design of future combustors. However, much developmental work remains, particularly to understand multi-scalar sub-grid-scale, SGS, mixing, which is, of course, critically important to modeling turbulence-chemistry interactions. The focus of this effort (begun in FY05 with Prof. Tong) is to provide a validation database that will make a significant contribution to the understanding of multi-scalar SGS mixing. To this end a three-jet mixing experiment was conceived. To quantify concentrations of both inner and outer jets, planar Rayleigh scattering (of C_2H_4), using a 532-nm beam, and PLIF of acetone-seeded air, using a 266-nm beam, are used. Two cameras would normally be required, which significantly complicates any experiment (making registration of the two fields of view necessary) and degrades spatial resolution. To mitigate these problems, a single interline-transfer CCD camera (PCO 1600) is employed, and image pairs are recorded se-

quentially, 250-ns apart (= laser pulse separation). This is made possible by a charge transfer time of ~150 ns, the time to shift the first image to the *storage frame*.

Due to the desire for high spatial resolution, a special lens was configured consisting of Rodenstock *close-up* lens and a 58-mm f/1.2 Noct-Nikkor lens. The resulting resolution was evaluated by translating a razor blade across the field of view (with $\Delta x \approx 10$ μm), from which a contrast transfer function could be derived; resolution was judged to be ~2 binned pixels, corresponding to ~85 μm, a number slightly smaller than the laser sheet thicknesses. Even with this high resolution, signal-to-noise ratios are reasonably high, 60-70 for "pure" jet fluid for images shown here (~600 mJ/pulse at 532 nm and 80 mJ/pulse at 266 nm). It should be noted that high acetone concentrations lead to some undesirable effects, including 266-nm beam absorption, *enhanced* Rayleigh scattering from the *air* jet, and acetone mass loading that is significant and potentially varying during the measurement time; as a consequence, limiting the acetone concentration well below saturation is necessary.

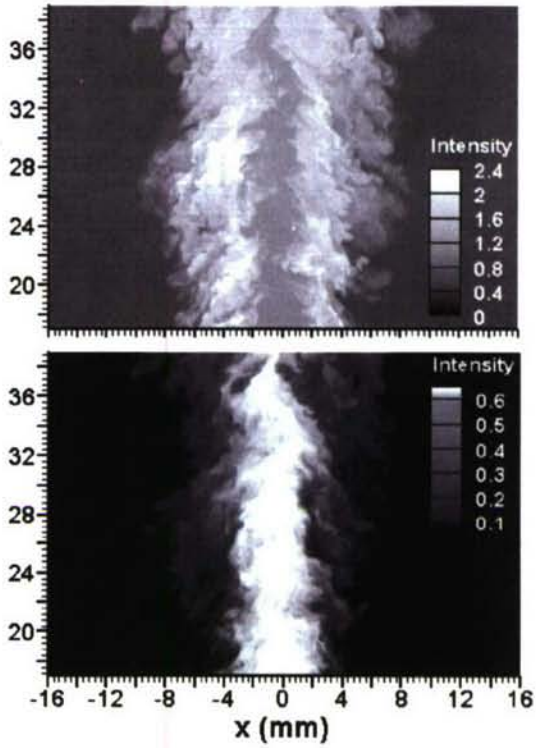

Fig. 6. Rayleigh scattering (top) and acetone LIF (bottom) from turbulent co-annular jets.

A sample image pair, each from an original frame composed of 512×800 pixels, is shown in Fig. 6; the inner jet is air, seeded with acetone, while the outer jet is C_2H_4. Jet-exit velocities are ~35 m/s; the resulting displacement from one frame to the next is ≤ 9 μm (with Δt = 250 ns), a value much less than the image blur. One can see that the core of the inner jet is intact at this downstream location (~17 to 39 mm above jet exit). Sample sets consist of up to 4000 images pairs.

Another focus area is plasma-assisted ignition/combustion, and for the past two reporting periods the efficacy for the PDE has been studied. Here, a variety of plasmas were tested for their effect on the ignition delay time within the AFRL research PDE fueled with aviation gasoline. The shortest times of 6 ms were achieved with a transient-pulse igniter (producing a 70-ns, 60-kV pulse) near stoichiometric conditions, while the standard igniter induced ignition at 11 ms. However, a relatively simple modification of the standard igniter was shown to lower ignition times to values as short as 7 ms.

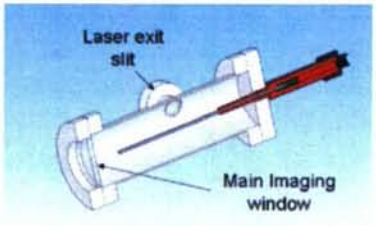

Fig. 7. Combustion chamber, 101 mm ID, 202 mm length.

Fig. 8. OH from initial streamer distribution 500 ns after initial high-voltage pulse

A parallel effort has recently begun to study radical formation and ignition induced by the transient-pulse igniter. Here a quiescent chamber (Fig. 7) is filled with a stoichiometric mixture of CH_4 and air; the high voltage ensures that the region for radical creation extends throughout the chamber. Shown on the left (Fig. 8) is the relative OH distribution (represented by the *streaks* produced from the initial streamer field), recorded 500 ns after the discharge; the field of view, looking from the end window, is from the chamber wall (left edge, just visible as an arc) to just beyond central electrode (bottom right-hand corner, out of the field of view). Note that many streamers are initially produced by this 0.8-J pulse, but only a few intersect the laser sheet. Temperature rise *within the streamers* is currently unknown but estimated to be < 20 K on average.

DISPERSION, MIXING, AND COMBUSTION IN TURBULENT AND HIGH-SPEED FLOWS, AIR-BREATHING PROPULSION, AND HYPERSONIC FLIGHT

Grant/Contract Number: FA-9550-07-1-0091

Principal Investigators: Paul E. Dimotakis & Dan I. Meiron

Graduate **A**eronautical **L**aboratories of the **C**alifornia **I**nstitute of **T**echnology
1200 E. California Blvd., Pasadena, Ca 91125

Summary/Overview

This research focuses on fundamental investigations of dispersion, mixing and combustion, in turbulent, subsonic and supersonic flows and is motivated by problems in high-speed air-breathing propulsion. The work is a closely coordinated effort between experiments and numerical simulation, and exploits recent developments in diagnostics and instrumentation. This is a brief report of work performed under this grant since 1 January 2007.

Technical discussion

Work to date on hydrocarbon combustion under this grant is focusing on laminar, premixed methane-air, ethane-air, and ethylene-air flames, at atmospheric pressure.

Bergthorson & Dimotakis (2006a) showed that the comparison of detailed axial velocity and CH radical profiles measurements using Particle Streak Velocimetry (PSV) and CH planar laser-induced fluorescence (PLIF) in strained premixed flames stabilized in a jet-wall stagnation flow with flame simulations can be used to validate and compare chemical-kinetic mechanisms. The simulations are performed with the CANTERA reacting-flow software package and rely on a one-dimensional hydrodynamic model, a multi-component transport formulation, and several detailed chemical-kinetic mechanisms. The kinetic models used in Bergthorson & Dimotakis (2006a) are GRI-MECH3.0 (GRI3.0); the C_3 mechanism by Davis, Law, and Wang (DLW1999); and two releases of the C_1-C_3 San-Diego mechanism (SD200308, SD200503). Predictions of CH_4-air, C_2H_6-air, and C_2H_4-air stagnation flames made using these kinetic models are at variance with experiments and with each other. An on-going simulation effort is adding predictions based on other kinetic models to assess their relative performances in flame propagation predictions for these fuel-air mixtures. The amount of information contained in the axial velocity and CH radical profiles can be reduced to one scalar: the CH profile location x_{CH}, in order to assess the adequacy of kinetic mechanisms. Comparison between experiments and predictions based on the models permits ranking the latter. Comparative sensitivity analysis is then used to identify the most-important reactions for each flame investigated. The rates of reactions identified in this manner can then be compared between the different mechanisms. Several reaction rate differences are identified in the process that are mostly responsible for the variance in flame predictions. This part of the work is part of the Ph.D. research of Laurent Benezech and performed in collaboration with Jeffrey Bergthorson, now at McGill University.

A code has been developed that performs Direct Numerical Simulations (DNS) of the laboratory setup employed in the cold stagnation-flow and flame experiments, in which axisymmetric flames of air mixtures with C1-C3 fuels were stabilized (Bergthorson 2005, Bergthorson *et al.* 2005, and Bergthorson & Dimotakis 2006a,b). It simulates both cold flow (Bergthorson *et al.* 2005) and unsteady flames in a 2D axisymmetric domain with a full hydrocarbon chemistry model and all relevant length scales resolved. The code was used to study methane-air flames in the laboratory. As shown in Fig. 1, the axial velocity profile compared to an earlier experiment by Bergthorson (2005) shows excellent agreement for a near stoichiometric flame (left), while the agreement is not as good for a lean flame (right). For the lean flame, the computed flame speed is over-predicting the observed value by nearly 10%, using GRI-Mech 3.0. This work is part of the Ph.D. research of K. Sone, is co-funded by Caltech's DOE ASC Center.

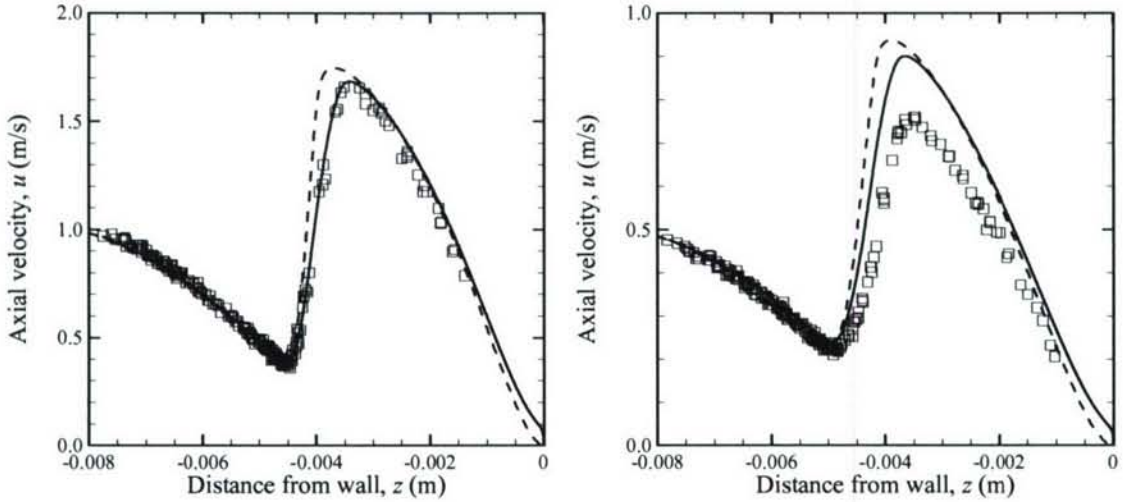

Fig. 1 Comparisons of the axial velocity profile between laboratory measurements and two-dimensional numerical simulations of stagnation-flow-stabilized flames. The square symbols are PSV data from Bergthorson (2005). The dashed line indicates the raw numerical velocity data. Solid line is the simulated PSV data based on numerical velocity profile. Left: $\Phi = 0.90$. Right: $\Phi = 0.70$.

A successful hydrocarbon-fueled scramjet engine will rely on a detailed understanding of the turbulent processes that mix fuel and air within the device, as well as the chemical kinetics and flame processes that result in conversion of the reactants to products. Work on compressible turbulent mixing in complex geometries under this grant is focused on studying (passive) flow control and mixing in an expansion-ramp flow geometry.

In this flow, a high-speed upper "air" stream is expanded over a perforated ramp inclined at 30° to the flow. A low-speed "fuel" stream is injected through perforations in the ramp and generates a mixing layer between the two streams. A key feature of this flow is the recirculation zone that transports hot products back toward the fuel injection location and provides a low-strain-rate flameholding region (Johnson 2005, Bergthorson *et al.* 2007). Presently, measurements of the molecular mixing achieved by this geometry have been completed at various speeds, up to a top stream Mach number of $M_1 = 2.5$. The observed trend of decreasing mixing with increasing velocity of the "air" stream is also followed in supersonic velocities. Interest now lies in improving the mixing characteristics of the geometry, by incorporating jet injectors to interact with the mixing layer. A new splitter plate is being designed to incorporate the jets, and also allows for variable boundary layer thickness through surface suction or injection and variable height of the expansion ramp. A schematic of the new splitter plate design is presented in Fig. 2. This part of the work is part of the post-doctoral research of Aris Bonanos.

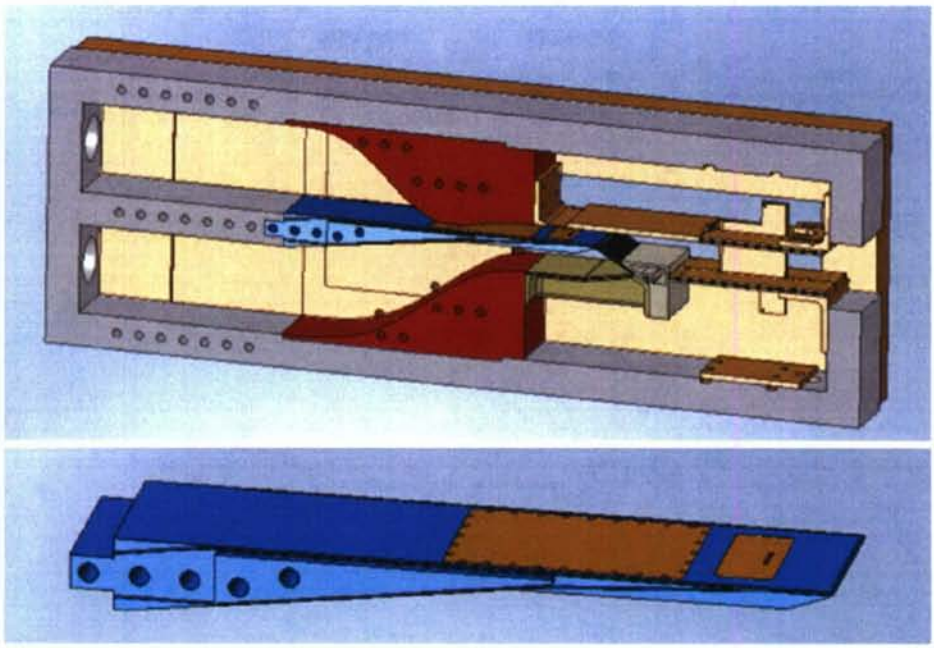

Fig. 2 Schematic of the supersonic shear layer facility (top) and detail of the new splitter plate (bottom) that incorporates a modular injector block, allowing for multiple jet arrangements to be investigated. This development is in its final design stages.

A parallel computational effort of these experiments is currently in progress. Flows corresponding to the subsonic experimental conditions are computed using Large Eddy Simulation (LES) with Sub-Grid Scale (SGS) modeling. Currently, our effort concentrates on simulations of the high-speed subsonic experimental conditions with top-stream velocities of 240 m/s. The high-resolution requirements of high-speed flows are being addressed using Adaptive Mesh Refinement (AMR) to control numerical errors in places were the numerical solution exhibits high gradients, such as in thin shear zones for example, resulting in significant computational savings compared to computations that would be performed on a uniform-spacing grid (unigrid). Fig. shows passive scalar contours in a vertical plane at mid-span and the grid density resulting from the AMR. This work is part of the Ph.D. research of George Matheou and performed in collaboration with Carlos Pantano, now at the U. Illinois at Urbana-Champagne.

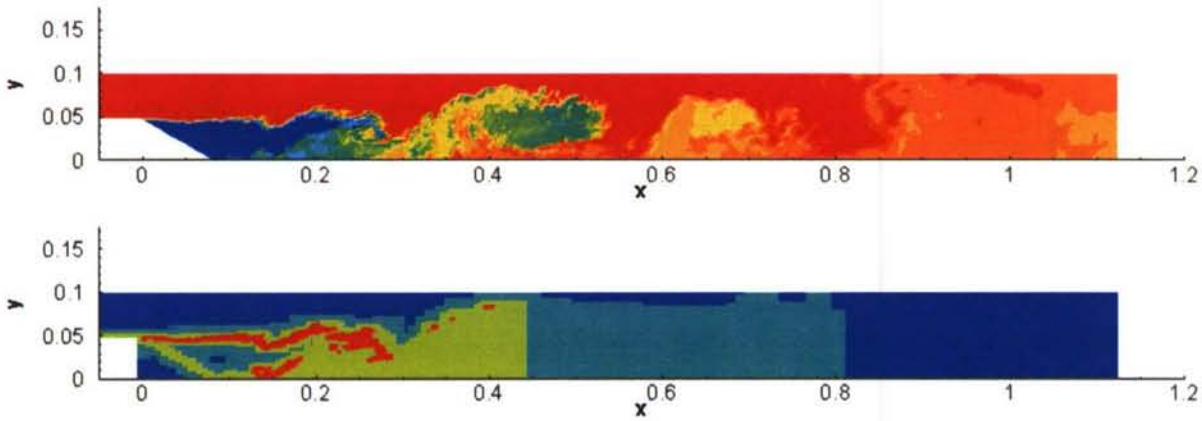

Fig. 3 Instantaneous passive scalar contours on a spanwise plane at mid-span (top) and grid density.

The scalar dispersion portion of this grant focuses on the 3-D dispersion of a scalar in a well-characterized turbulent flow (uniform grid turbulence produced by a grid with a wire size of ¼" and spacing between the wires of 1"). Current work in this project includes completion of the first experimental data acquired in the GALCIT Free Surface Water Tunnel (FSWT) for publication. The FSWT data were acquired at a mean flow velocity of 5.4 cm/s with a stationary camera. A distance of 55.3 cm from the grid to the beginning of the camera field of view and 75.3 cm to the end of the field of view means that we are looking at the scalar for 10-14 s after injection immediately downstream of the grid. The FSWT data were acquired with an image framing

rate of 100 fps and 32 frames/volume. This arrangement yielded three-dimensional scalar-field data as a function of time, across the full dispersion extent of the plume, at grid mesh Reynolds numbers of $Re_M \sim 1400$ to be investigated. A new facility is presently in its final phases of completion with an improved flow arrangement, improved optics, and a quad Yag laser. This will permit higher framing rates to be used and more than ten times higher Reynolds numbers to be investigated. In particular, this will permit the mixing transition (Dimotakis 2000, 2005) to be attained and exceeded crossed for this flow. This part of the work is part of research conducted by Dan Lang, in collaboration with Santiago Lombeyda and Jan Lindheim of Caltech's Canter for Advanced Computing Research (CACR).

In collaboration with L. Danaila and B. Renou and their co-workers at the CORIA Laboratory of the University of Rouen, work is continuing to explore the flow and mixing in a Partially Stirred Reactor (PaSR), in which scalar-bearing and pure fluids are introduced through an array of opposed jets. The measurements rely on simultaneous Particle Imaging Velocimetry (PIV) and acetone PLIF in flows at Taylor Reynolds number that span the mixing transition (Dimotakis 2000). An early report was presented by Krawczynski *et al.* (2006).

References

BERGTHORSON, J.M. 2005 *Experiments and Modeling of Impinging Jets and Premixed Hydrocarbon Stagnation Flames*. Ph.D. thesis, California Institute of Technology.

BERGTHORSON, J.M., M.B. JOHNSON, A.M. BONANOS, AND P.E. DIMOTAKIS 2007 Measurements of Molecular Mixing in an Expansion-Ramp Combustor. 21st ICDERS (23-27 July 2007, Poitiers, France).

BERGTHORSON, J.M., K. SONE, T.W. MATTNER, P.E. DIMOTAKIS, D. GOODWIN, AND D. MEIRON 2005 Impinging laminar jets at moderate Reynolds numbers and separation distances. *Phys. Rev.* E 72:066307.

BERGTHORSON, J.M., AND P.E. DIMOTAKIS 2006a Premixed laminar C1-C2 stagnation flames: experiments and simulations with detailed thermochemistry models. *Proceedings of the Combustion Institute* 31:1139-1147.

BERGTHORSON, J. M., AND P.E. DIMOTAKIS 2006b Particle velocimetry in high-gradient/high-curvature flows. *Exp. Fluids* DOI:10.1007/s00348-006-0137-6

DIMOTAKIS, P. E. 2000 The mixing transition in turbulence. *J. Fluid Mech.* 409:69-98.

DIMOTAKIS, P. E. 2005 Turbulent Mixing. *Ann. Rev. Fluid Mech.* 37:329-356.

JOHNSON, M.B. 2005 *Aerodynamic Control and Mixing with Ramp Injection*. Ae thesis, California Institute of Technology.

KRAWCZYNSKI J.F., B. RENOU, P.E. DIMOTAKIS, AND L. DANAILA 2006 Determination of the kinetic energy dissipation rate in a Partially Stirred Reactor", 13th International Symposium on applications of Laser Techniques to Fluid Mechanics (Lisbon, 26-29 June 2006).

Pulse Detonation Physiochemical and Exhaust Relaxation Processes

LRIR 01PR02COR

Principal Investigator: Dr. Fred Schauer (AFRL/PRTC)

AFRL/PRTC
1790 Loop Road North, Building 490
Wright-Patterson AFB OH 45433-7103

SUMMARY/OVERVIEW:

The objective of this program is to establish the scientific knowledge of detonation initiation, propagation, and blow-down needed to develop a pulse detonation engine (PDE) that will function on hydrocarbon fuels. The complex interaction of chemistry, gas dynamics, turbulent mixing, and geometry are responsible for the success or failure of the detonation phenomena required to operate a PDE. Detonation tube exhaust blow-down conditions, which are predicted to have a significant impact upon performance, will be explored in order to achieve basic understanding of the relationships between detonations, nozzles, and multiple detonation tube interactions.

TECHNICAL DISCUSSION

The technological motivation for this program is the need to develop low-cost high-performance PDE's that can operate on hydrocarbon fuels. PDE's rely upon detonation combustion to produce a pressure rise in the combustion chamber instead of the expensive rotating machinery used in gas turbine engines. Consequently, the most expensive and maintenance-intensive components of a conventional turbine engine, namely the compressor and turbine stages, will not be necessary in PDE's. PDE's operates on a near-constant-volume heat addition cycle as opposed to the constant-pressure cycle employed in nearly all conventional aero-propulsion systems. The constant volume cycle offers improvements to specific thrust, specific fuel consumption, and specific impulse at a greatly reduced cost. In theory, the PDE can efficiently operate at Mach numbers from zero to above four without using a combined cycle/rocket approach. However, there are some major technical problems that must be resolved before the full potential of PDE's can be realized.

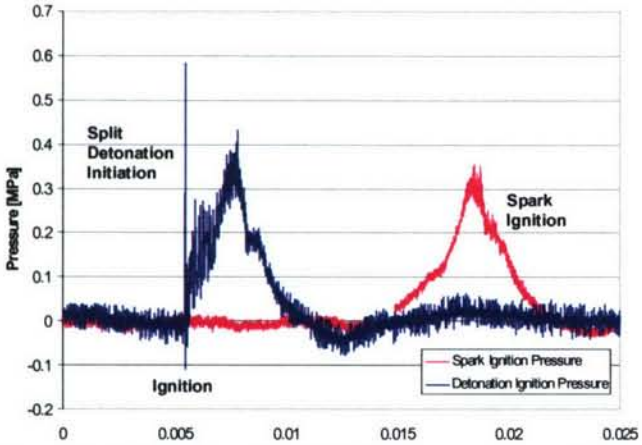

Figure 1. Split detonation initiation versus conventional spark ignition with JP8/air.

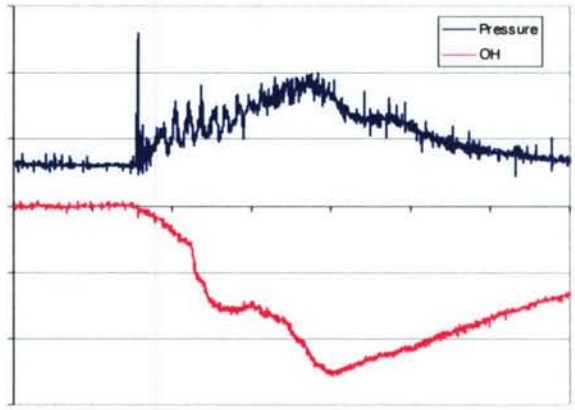

Figure 2. Split detonation initiated JP8/air; OH and pressure signals.

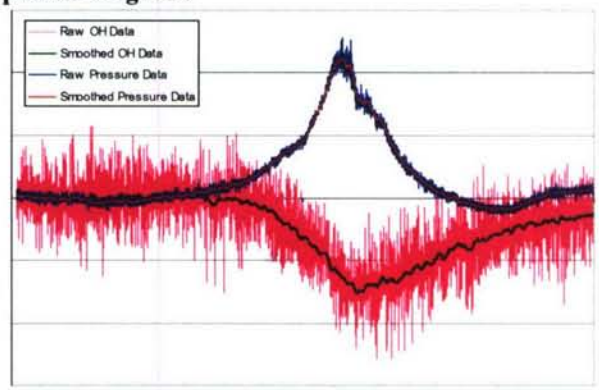

Figure 3. Spark Initiated JP8/air; OH and pressure rise begin 10msec after spark discharge.

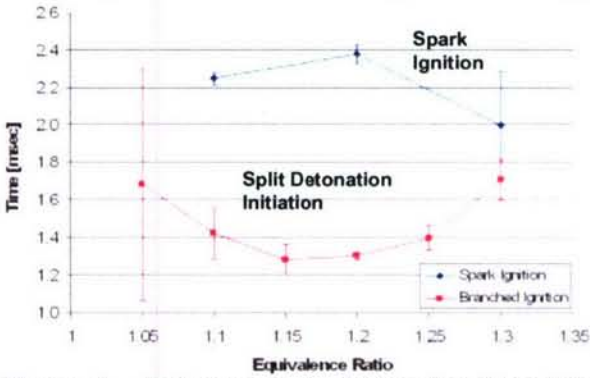

Figure 4. Deflagration to Detonation Transition time (from ignition) versus equivalence ratio.

Foremost among the hurdles for a practical PDE system are the requirements for initiation and successful propagation of a detonation with hydrocarbon fuels in air. Although this has not been achieved in 60 years of PDE research, modern computational fluid mechanics (CFD), laser diagnostics, and high-speed instrumentation have not been applied to this challenge until recently. CFD and experimental studies of deflagration-to-detonation transition (DDT) and propagation are being carried out in order to explore the parameters controlling detonation initiation including: geometry effects, plasma ignition, hybrid fueled pre-detonators, and endothermic fuels.

Recent improvements in understanding of detonation diffraction, shock reflections, and deflagration-to-detonation transition (DDT), have renewed efforts to obtain true direct initiation of hydrocarbon/air mixtures with split detonation initiation. As shown by the rapid pressure rise for split detonation initiation versus conventional spark ignition in Figure 1, recent efforts have very nearly successfully transmitted a detonation in JP8/air mixtures. Further details on the ignition dynamics are clarified in Figures 2 and 3, which show both pressure OH emission during split detonation initiation and conventional spark discharge respectively. The rise in pressure and OH signal (which is inverted in the figures above) does not occur until nearly 10 milliseconds after spark discharge. In contrast, the rise in pressure and OH is virtually instantaneous with the arrival of a split detonation into the detonation tube.

Although split detonation has not yet resulted in direct initiation of HC/air mixtures, it has set new benchmarks for DDT time as shown in Figure 4. These results are even more impressive when 6-16 milliseconds are added to conventional spark ignition DDT times for chemical induction time. This order of magnitude reduction in total DDT time is an enabling technology for high frequency, and thus high thrust density operation on practical fuels. These ignition times were obtained at static flight conditions, and yet are still shorter than the previous high frequency ignition records obtained previously at supersonic flight conditions which were greatly aided by the stagnation pressure and temperature recovery.

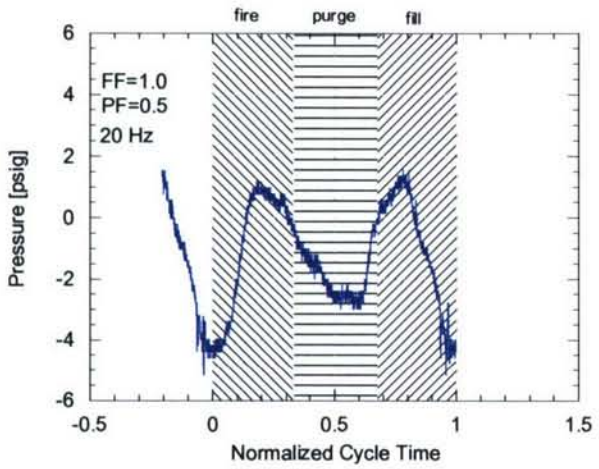

Figure 5. Pressure dynamics in cold flowing detonation tube as a function of normalized cycle time.

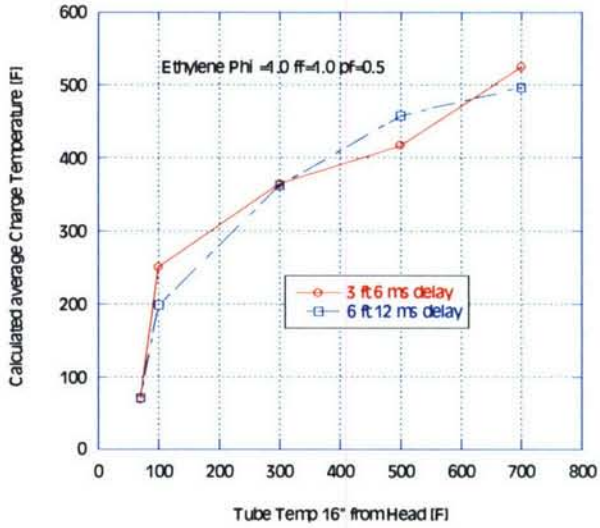

Figure 6. Charge temperature from time-of-flight of compresssion versus wall temperature.

Previously identified fill dynamics have been used advantageously for optimizing nozzle performance and ignition timing. These same flow dyamics, as shown in the pressure oscillations of Figure 5, were used to examine the effects of heat transfer on charge temperature. Convective heating of the incoming charge occurs due to heat transfer from high velocity products depositing heat in the detonator tubes. Even though this only occurs for milliseconds, the effects can be dramatic, as shown in the calculated charge temperatures reported in Figure 6. The charge temperature was obtained by deriving the speed of sound from the 'bounce' of the compression and expansion waves shown in Fig. 5. This temperature rise can result in significant decreases in charge density, and thus competes with faster combustion chemistry for detonability and ultimately detonation performance. For example, charge heating can attenuate thrust by as much as 40% due to loss of charge density and shortened blow-down times. They highly unsteady heat transfer is undergoing further study in order to control this loss mechanism and optimize performance.

Promising results from regenerative fuel cooling to provide supercritical fuel injection have been extended 1175F fuel injection temperatures. Previously, this system was developed for looking at the effects of supercritical fuel injection. A catalyst was applied to the next-generation, higher temperature heat exchanger in order to promote endothermic effects which will theoretically promote DDT. Preliminary results are extremely positive as shown in Figure 7. At the higher fuel injection temperatures, ignition times were reduced by a factor of two. This dramatic impact can only be explained by endothermic effects, which are currently being further quantified. In addition to the dramatic reduction in ignition and DDT time, endothermic fuel injection temperatures resulted in a new benchmark for lean hydrocarbon/air detonation initiation. At an equivalence ratio of 0.7, hydrocarbon/air mixture are not normally detonable in detonation tubes of this configuration.

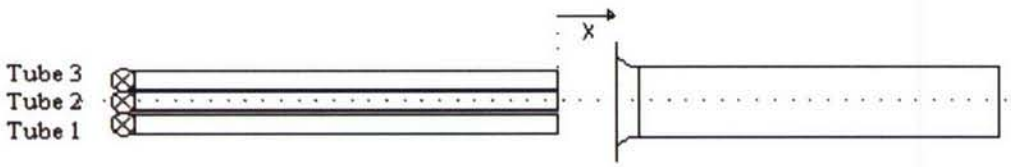

Figure 8. Multitube detonation driven ejector experimental setup.

Progress in exhaust relaxation processes includes nozzle studies, back pressurization at altitude, and unsteady detonation/ejector flow dynamics. The previously identified, unsteady detonation blow down process is conducive to exhaust vortex formation, which interacts with ejector inlets for dramatic performance improvements. results with single detonation tube driven ejectors were used in designing several multi-tube ejector configurations, such as that shown in Figure 8. In general scaling rules were found to be consistent for single and multi-tubes despite the interaction of tube blow down dynamics. The tube-to-tube variations observable in Figure 9 were found to be the result of the interaction of fill and blow-down fluid dynamics with the secondary flows.

There was little difference between the augmentation of the detonation tubes as they were fired individually even though, tubes one and three were a full diameter off of the center of the ejector, confirming results found with single tube off-axis detonation driven ejectors. The combination of two tubes firing had very similar results with an augmentation ratio of approximately 1.4. The augmentation of the out-board tube combination, tube 1 and 3, appeared to drop at high axial downstream locations. It was noted however, that the augmentation of the 2, 3 tube combination, which had a significantly longer delay between the detonations entering the ejector had a slightly higher augmentation, possibly indicating an interaction. With all three tubes firing, there was a definite interaction as the augmentation level dropped to between 1.25 and 1.3. The ejector studied was not optimized for diameter ratio and does not have a diffusion section but the augmentation results compare well with other investigators. Although a simpler geometry was used for this parametric study, utilizing diverging ejectors with multi-tube ejectors should result in significant increases in both augmentation ratio and thrust density. In addition, the linear engine employed for this study will be used to examine a linear multi-tube ejector. Now that simple ejector designs have been validated, a more optimum configuration will be fabricated and studied with more practical circular tube arrays.

Divergence in detonation driven ejectors has been found to result in significantly improved pressure recovery, as shown in Figure 10. Contrary to common faith that diverging nozzles improve thrust via providing a positive pressure thrust surface, static surface pressure measurements indicate that the enhanced pressure recovery obtained with a divergent nozzle actually improves suction on the ejector inlet.

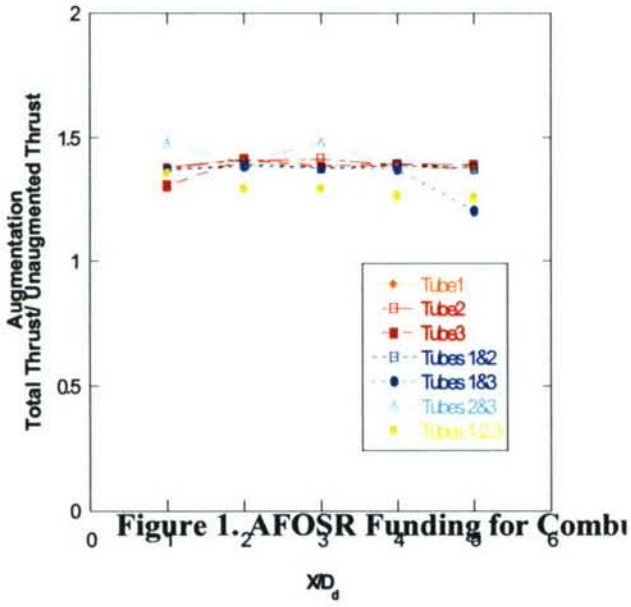

Figure 1. AFOSR Funding for Combi

Figure 9. Ejector thrust augmentation with varying driving detonation tubes versus ejector downstream location.

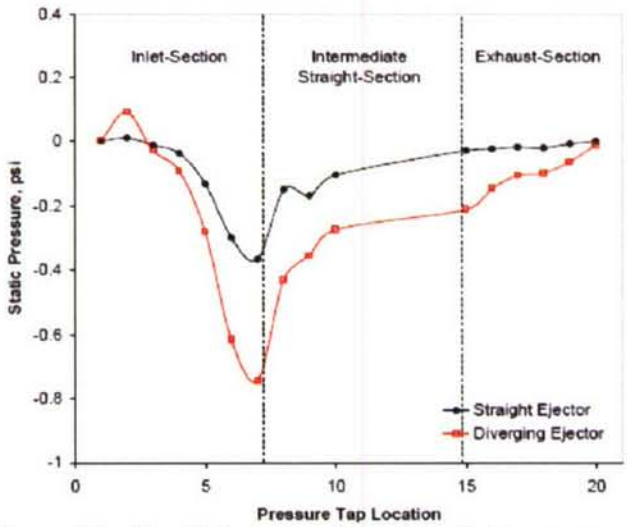

Figure 10. Straight versus diverging ejector pressure profiles.

TITLE: BREAKUP OF LIQUID STREAMS AT HIGH PRESSURE

Grant/Contract Number: W911NF-06-1-0225

Principal Investigators: William A. Sirignano and Daniel D. Joseph

Department of Mechanical and Aerospace Engineering

University of California, Irvine, CA 92697-3975

SUMMARY/OVERVIEW:

The purpose of this study is to identify the role of cavitation in high pressure atomization. The flow in a liquid injector and the resulting jet are analyzed by means of numerical simulation of two-phase flow. This study will lead to a better understanding and predictive capability of effects of cavitation inside the injector on the breakup process.

THECHNICAL DISSCISION

Background

Recent experimental studies [1-4] show that the occurrence of cavitation inside the nozzle makes a substantial contribution to the breakup of the exiting liquid jet. In the traditional criterion of cavitation, cavitation occurs when the pressure drops below the breaking strength of liquid (P_c) which in an ideal case is the vapor pressure at local temperature. Winer and Bair [5] and, independently, Joseph [6] proposed that the important parameter in cavitation is the total stress which includes both the pressure and viscous stress. Kottke, Bair and Winer [7] conducted an experiment on cavitation in creeping shear flow where the reduction of hydrodynamic pressure does not occur. However due to high shear stress they observed appearance of cavitation bubbles at pressures much higher than vapor pressure. Archer et al. [8] observed a drop in the shear stress in start-up of steady shearing flow of a low-molecular-weight polystyrene due to opening of bubbles within the flow at stress equal to 0.1MPa.

To study the mechanisms by which cavitation enhances the breakup process, a numerical model is developed via finite volume method and using of level-set formulation to track the interface and model the surface tension. The code is validated with several benchmark problems and compared with available literature.

Flow through an aperture

Flow of a liquid through an aperture is one of free jet problems that offers an analytic solution for the flow field. It has been proved [9] that for a viscous potential flow(VPF), the constant speed condition on the free surface leads to zero normal viscous stress on the free surface, hence satisfies the boundary condition of viscous flow as well. The full Navier-Stokes equations (N-S) for the aperture flow are solved numerically for Reynolds numbers, Re, between 1 and 1000 and Weber number, We, between 10 and 1000. Employing the theory of viscous

potential flow the viscous stresses could be found and using the total-stress criterion for cavitation, the regions that are vulnerable to cavitation are identified and the results are compared to the solution of viscous potential flow. For high Reynolds numbers solutions are similar except in boundary layers.

Flow through an axisymmetric orifice

A numerical simulation of two-phase incompressible flow is conducted in an axisymmetric geometry of the orifice [10]. The orifice has a rounded upstream corner with radius r and a sharp downstream corner with length-to-diameter ratio (L/D) between 0.1 and 5. Figure 1 shows an example of solution for velocity field and pressure field for Re=2000 and We=1000. The total stress including viscous stress and pressure has been calculated in the flow field and, from there, the maximum principal stress is found (T_{11}). The total-stress criterion for cavitation is applied to find the regions where cavitation is likely to occur and compared with those of the traditional pressure criterion. Results are shown in Figure 2. It is observed that the viscous stress has significant effects on cavitation especially for nozzles with larger length-to-diameter ratio. Figure 3a shows the threshold value of cavitation number above which cavitation occurs in the nozzle. Cavitation number is defined as $K = \frac{P_u - P_d}{P_d - P_c}$ where P_u, P_d are upstream and downstream pressures, and P_c is the critical pressure. The effect of geometry and occurrence of hydraulic flip in the orifice on the total stress is also studied. Here flow in nozzles with different radii of curvature at the inlet corner is considered. r/D is varied between 0.01 and 0.04 while keeping other parameters of the flow and domain constant. Figures 3b and 3c show the threshold value of K versus r/D. For both Reynolds numbers of 1000 and 2000, the K_{th} increases as the r/D increases. This is expected because the larger the radius of curvature, the smaller the increase in velocity and drop in pressure, so the less chance of cavitation.

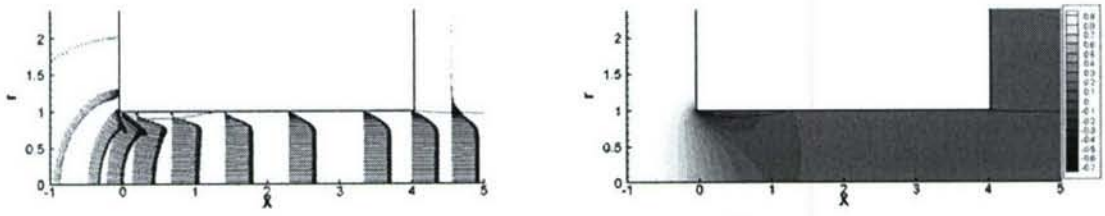

Figure 1. Velocity profiles and contours of $(p-p_d)/\frac{1}{2}\rho U^2$ for flow with Re=2000

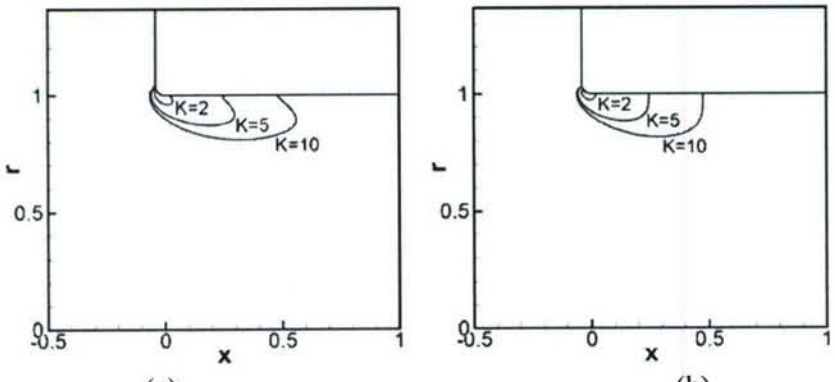

(a) (b)

Figure 2. The cavitation threshold curves on which $T_{11} + p_c = 0$ in different flows with K = 2; 5; 10; Re=1000, We=1000; L/D=1, (a) total stress criterion, (b) pressure criterion

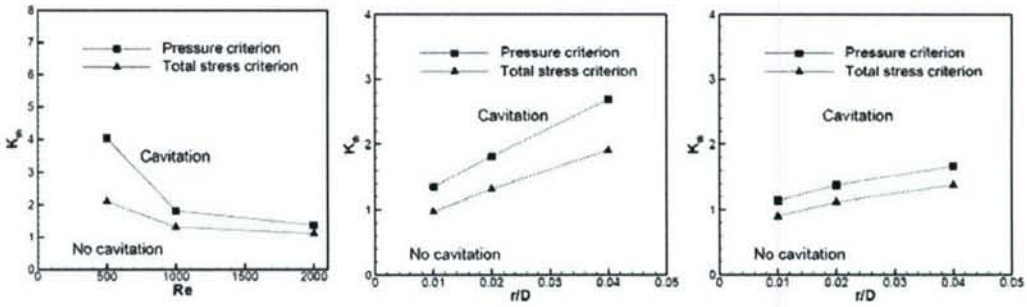

(a) r/D=0.02 (b) Re=1000 (c) Re=2000

Figure 3. Threshold values of K above which cavitation occurs in the orifice for L/D=2.

Laminar jet breakup

The flow of a liquid through a nozzle and resulting jet in a stagnant gas is investigated numerically [11]. The flow is considered to be laminar and axisymmetric. Creation and growth of surface waves due to Kelvin- Helmholtz and capillary instabilities leading to breakup of jet are captured. The disturbance in jet is caused by perturbing the mass flux of liquid through nozzle. Effects of the geometry such as length-to-diameter ratio and curvature of corners of the nozzle on the growth of interfacial waves and breakup distance are studied. It is observed that longer nozzles create a more stable jet with longer breakup distances. Further calculation will address higher values of Re and We.

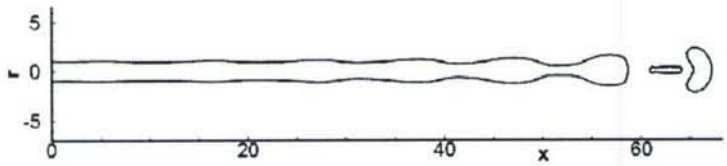

Figure 4. Liquid jet emerging from a nozzle with L/D=1 and r/D=0.04 at Re=500 and We = 50

Bubbles in the flow

The growth and collapse of cavitation bubbles in the nozzle flow is simulated by a one-way-interaction model. This analysis provides with the effects of different flow parameters such as Reynolds number, Weber numbers and size of nucleation sites on the cavitation characteristic. In the one-way interaction it is assumed that a nucleation cite which could be represented as a sub-micron size bubble is moving with the local velocity of flow and as it reaches the low pressure regions, near corners, it expands and creates a cavitation bubble and later by moving to higher pressure regions, it will collapse. Also, it is assumed the existence of the bubble will not significantly change the flow field around it. In the future, this model will be expanded to consider a two-way-interaction between bubbles and the flow, where the change in the flow field due to bubble growth and collapse will also be modeled.

Starting from a point in the flow, one can find the streamline and position of particle with time and pressure felt by particle. Then, this pressure is used to solve the equation governing size of the bubble. Figure 5 shows the pressure and bubble size in a flow with Re=1000. In the low pressure region near the corner, bubbles grow and then collapse.

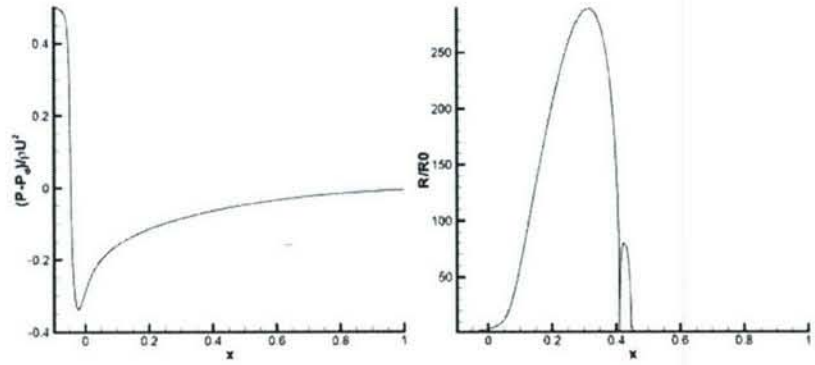

(a) (b)

Figure 5. (a) Pressure vs. x-component of bubbles position in the orifice, (b) bubble size relative to its original size

References

[1] N. Tamaki, M. Shimizu, K. Nishida, and H. Hiroyasu, "Effects of cavitation and internal flow on atomization of a liquid jet", Atomization and Sprays 8, 179 (1998).

[2] N. Tamaki, M. Shimizu, and H. Hiroyasu, "Enhancement of the atomization of a liquid jet by cavitation in a nozzle hole", Atomization and Sprays 11, 125 (2001).

[3] H. Hiroyasu, "Spray breakup mechanism from the hole-type nozzle and its applications", Atomization and Sprays 10, 511 (2000).

[4] F. Payri, V. Bermudez, R. Payri, and F. J. Salvador, "The influence of cavitation on the internal flow and the spray characteristics in diesel injection nozzles", Fuel 83, 419 (2004).

[5] W. O. Winer and S. Bair, "The influence of ambient pressure on the apparent shear thinning of liquid lubricants-an overlooked phenomenon" (1987), conference Publication Vol.1 London Inst. Mech. Eng. C190-87, 395-398

[6] D. D. Joseph, "Cavitation and the state of stress in a flowing liquid", Journal of Fluid Mechanics 284, 367 (1998)

[7] P. A. Kottke, S. S. Bair, and W. O. Winer, "Cavitation in creeping shear flows", AICHE Journal 51, 2150 (2005)

[8] L. A. Archer, D. Ternet, and R. G. Larson, "fracture phenomena in shearing flow of viscous liquids", Rheologica Acta 36, 579 (1997)

[9] S. Dabiri, W. A. Sirignano, D. D. Joseph, "Two-Dimensional Viscous Aperture Flow: Navier-Stokes and Viscous-Potential-Flow Solutions", In preparation for publication.

[10] S. Dabiri, W. A. Sirignano, D. D. Joseph, "Cavitation in an orifice flow", Accepted for publication in the Physics of Fluids.

[11] S. Dabiri, W. A. Sirignano, "Breakup of a laminar axisymmetric liquid jet", to be presented at 20th ILASS Conference, May 2007.

SHOCK TUBE MEASUREMENTS OF LIQUID FUELS COMBUSTION KINETICS

ARO Contract Number DAAD19-01-1-0597

Principal Investigator: Ronald K. Hanson

Mechanical Engineering Department
Stanford University, Stanford CA 94305-3032

SUMMARY/OVERVIEW:

We report results of high-temperature shock tube research aimed at improving knowledge of the combustion behavior of diesel, jet and related fuels. Research is being conducted in three Stanford shock tube facilities and current work focuses on the following topics: (1) ignition delay time measurements of gasesous jet fuels (JP-8 and Jet-A) at high pressures and low temperatures; (2) mid-IR laser absorption measurements of species time-histories and decomposition rates of n-heptane and n-dodecane; (3) ignition delay times of n-dodecane, jet fuel and diesel using the aerosol shock tube technique; and (4) ignition delay time measurements of gaseous methylcyclohexane (MCH) at high and low pressures.

TECHNICAL DISCUSSION:

Validation of the predictive power of large reaction mechanisms and development of reduced mechanisms describing the pyrolysis, oxidation and ignition of practical fuels require a reliable database of experimental combustion targets such as ignition delay times and species concentration time-histories. Only a limited amount of shock tube ignition time data presently exist for the heavier practical fuels and fuel components, and virtually no shock tube species time-history measurements exist for reactants (practical fuels and pure surrogate components), small transient radical species (such as OH, HCO, CH_3, and benzyl) and combustion products (H_2O, CO and CO_2). To help remedy this deficiency, we have launched an effort to build a unique database of ignition time and species concentration time-history measurements derived from in-house shock tube studies. This database will cover fuel components, such as n-alkanes, branched alkanes, cyclo-alkanes, alkenes and aromatics, as well as surrogate mixtures, and practical fuels including gasoline, jet fuel and diesel. We will use this database to validate and refine existing reaction mechanisms and to develop and test proposed surrogate fuel mixtures; and of course we will make this database available to others.

Jet Fuel Ignition Time Measurements: Ignition delay times were measured for gas-phase jet fuel mixtures (Jet-A and JP-8) in air behind reflected shock waves in a heated high-pressure shock tube. Initial reflected shock conditions spanned the following wide ranges: temperatures of 715-1220 K, pressures of 17-51 atm, equivalence ratios of 0.5 and 1, and oxygen concentrations of 10 and 21 % in synthetic air. Ignition delay times were measured using sidewall pressure and OH* emission at 306 nm. See Figs. 1 and 2. Longer ignition delay times at low temperatures (700-850 K) were accessed by utilizing driver-gas tailoring methods. The Jet-A/JP-8 results have very low scatter and are in excellent agreement with the very limited previous data, all from Dean et al. [2006]. A simple 1/P dependence was found for ignition delay times from 874 to 1220K for the pressure range studied for both fuels. A clear trend of longer ignition delay times for the lean (Φ=0.5) when compared to the stoichiometric case (Φ=1.0) was evident and also for the 10 % O_2

data when compared to the 20.7 % O_2 data. Test times in excess of 4 ms were achieved, using He/N_2 driver-gas tailoring methods to study the NTC region (near 700 K). At low temperatures (700-850 K), ignition delay times were longer (> 2 ms) and showed negative temperature coefficient (NTC) type behavior. Ignition delay times are relatively insensitive to small variations in the temperature in the NTC region, though at the lowest temperatures (~700K), ignition delay times increase with decreasing temperature. Using different jet fuel surrogate mixtures, the new experimental results were compared with predictions of several kinetic mechanisms including Ranzi et al. [2006], Zhang et al. [2006], Mawid et al. [2006], and Lindstedt and Maurice [2000]. Work is in progress to study jet fuel samples with different cetane numbers and selected jet fuel surrogate components and mixtures, over a range of pressures, temperatures and equivalence ratios.

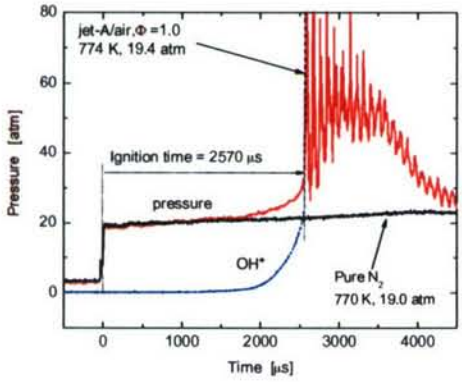

Fig. 1. Jet-A/Air ignition delay time measurement. Near-ideal behavior of the shock tube is represented by the pure-N_2 pressure trace.

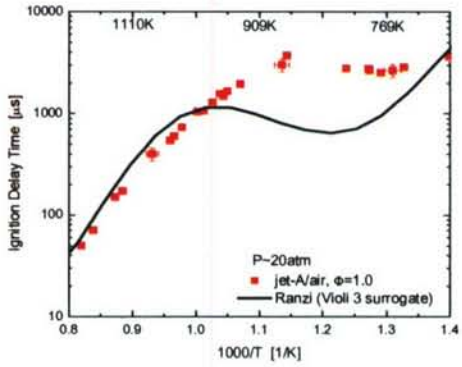

Fig. 2. Jet-A/Air ignition delay times as a function of temperature. Current models *do not* accurately capture the behavior in the lower temperature (NTC) regime.

n-Heptane Decomposition Measurements using Mid-IR Laser Absorption: We have recently developed (under AFOSR support) a novel multi-wavelength mid-IR laser absorption diagnostic for fuel concentration measurements. We utilize a unique difference-frequency-generation (DFG) laser system that rapidly alternates (~200 kHz) between two-mid-IR wavelengths. The mid-IR wavelengths are tailored to the quantities of interest including the concentration of specific hydrocarbons and temperature. Our two-color diagnostic has been used successfully to measure fuel concentration in the presence of interference from aerosol scattering or from another absorbing species.

The first application of this new diagnostic has been to study n-heptane pyrolysis; see Figs. 3 and 4. A simultaneous measurement of temperature and n-heptane were made in shock-heated heptane/argon mixtures. Preliminary measurements of the overall rate of decomposition for heptane show good agreement with previous high-temperature data using CH_3 absorption, also performed in our laboratory, and the reaction rates proposed by Davis and Law (1998). Future experiments will be directed at studying specific reaction pathways that lead to ethylene and methane, two additional hydrocarbons that can be measured by our new methods.

Aerosol Shock Tube Measurements of n-Dodecane Ignition Delay Times: We have developed a method to study low-vapor-pressure fuels in a shock tube using aerosol fuel loading. This method has several advantages over existing methods: reactants are not preheated in the mixing assembly or shock tube as occurs in conventional heated shock tube experiments; and the measurement does not have the spray loading non-uniformities or slow evaporation times found in shock tube experiments that use direct spray injection using high-pressure diesel injectors.

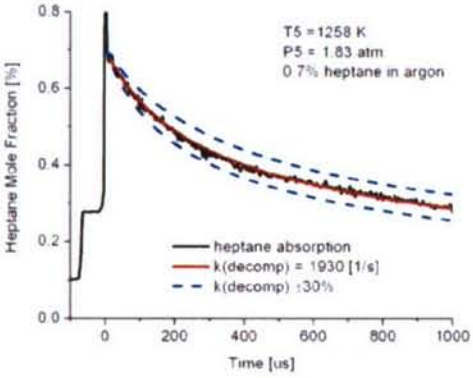

Fig. 3. Heptane pyrolysis concentration time-history measured using mid-IR laser absorption at 3410 and 3433 nm. Rate determination using the Davis and Law [1998] mechanism.

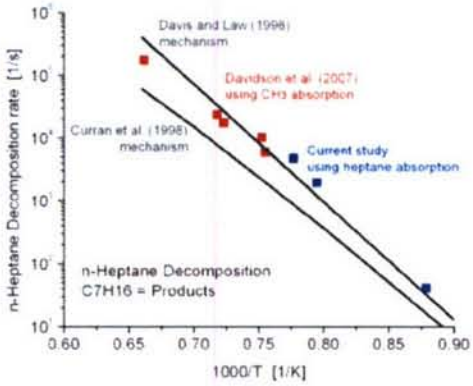

Fig. 4. Heptane overall decomposition rate: C_7H_{16} = products. Agreement with higher temperature measurement of Davidson et al. (2007) and the Davis and Law (1998) recommended rate.

The aerosol shock tube method develop in this program permits the direct measurement of ignition times for high concentrations of low vapor pressure fuels at such as JP-8 and diesel and surrogates such as decane, dodecane and hexadecane. To quantify the amount of fuel in our mixtures for these experiments we employ gas-phase mid-IR laser absorption. Ignition delay times were measured in n-dodecane/20% O_2/balance argon mixtures for equivalence ratios of 0.5 at pressures near 6 atm for temperatures from 1030 to 1350 K. These are the first high-concentration n-dodecane ignition measurements using the aerosol method; see Figs. 5 and 6. These measurements have been compared with ignition delay time measurements made in Stanford's heated shock tube at 20 atm [Vasu et al., 2006] and good agreement is found between the two methods. We have also measured ignition delay times in JP-7 and diesel (DF-2) using this method. Future work includes extension of this method to heavier fuel components such as hexadecane.

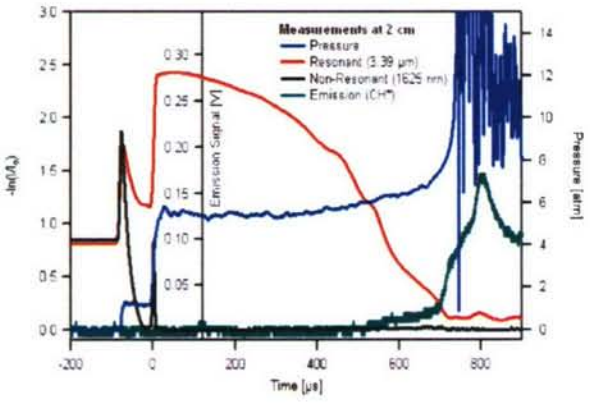

Fig. 5. Aerosol shock tube measurement of n-dodecane ignition. Pressure and CH* emission measurement indicate ignition. Resonant and non-resonant laser measurements indication consumption of fuel and aerosol respectively.

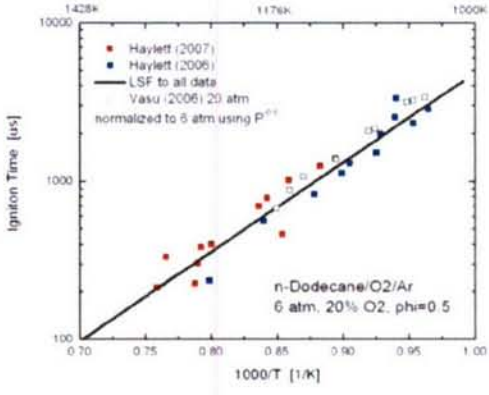

Fig. 6. n-Dodecane ignition delay times. Current aerosol shock tube measurements of Haylett (2006/7) are in excellent agreement with heated shock tube measurements of Vasu (2006).

High Pressure Ignition Delay Time Measurements of Methylcyclohexane: Naphthenes (cyclo-alkanes) are an important component of practical fuels, and methylcyclohexane (MCH), one of the simplest naphthenes, is widely used as a component of jet fuel surrogate mixtures. Hence,

there is a critical need for high-temperature MCH ignition data. Though limited shock tube studies of MCH ignition delay times have been performed previously at low-pressures, no high-pressure shock tube MCH ignition measurements have been reported. In the current study, we have measured ignition delay times of MCH mixtures over a wide range of conditions including pressures of 1-50 atm, temperatures of 795-1560 K and equivalence ratios of 0.5-2.0. Ignition delay times were measured behind reflected shock waves using pressure and emission diagnostics (CH*, OH*) at side wall locations; see Figs. 7 and 8. Our high-pressure measurements near 45 atm showed NTC type behavior and complement recent ignition time studies of MCH in a RCM by Pitz et al. [5]. Future work will study the apparent near-zero pressure dependence of the ignition times at very low temperatures.

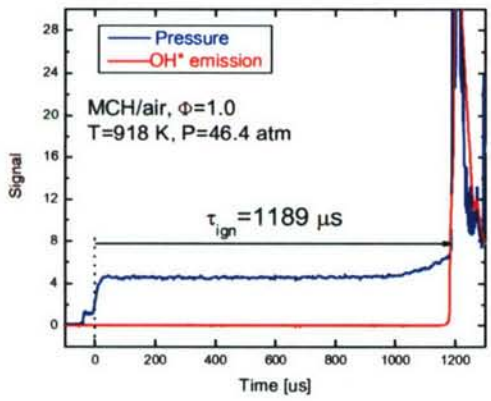

Fig. 7. Ignition delay time measurement for MCH/Air.

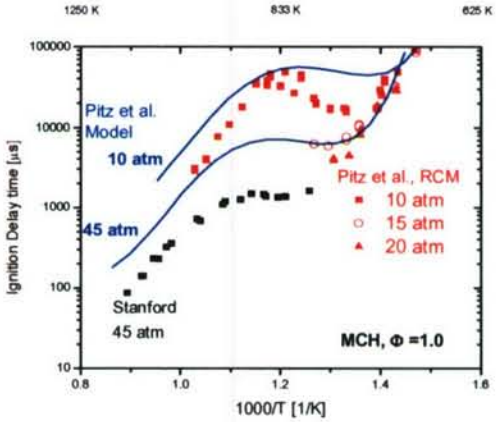

Fig. 8. Comparison of MCH ignition delay time measurements with RCM data of Pitz et al. (2006).

ARO-SPONSORED PUBLICATIONS (2006-2007)

S. S. Vasu, D. F. Davidson, R. K. Hanson, "Shock Tube Measurements of Jet Fuel Ignition Delay Times," submitted to *Combustion and Flame,* January 2007.

S. S. Vasu, D. F. Davidson, R. K. Hanson, "Jet Fuel Ignition Delay Times and Modeling: Studies at High Pressures and Low Temperatures in a Shock Tube," *43nd AIAA Joint Propulsion Conference*, Cincinnati OH, July 2007.

D. Haylett, D. F. Davidson, R. K. Hanson, "Ignition Times of Low Vapor-Pressure Fuels using the Aerosol Shock Tube Method," accepted for publication, *43nd AIAA Joint Propulsion Conference*, Cincinnati OH, July 2007.

S. S. Vasu, D. F. Davidson, R. K. Hanson, "Jet Fuel Ignition Delay Times: Shock Tube Investigations at High Pressures," *21st ICDERS Meeting*, Poitiers France, July 2007.

S. S. Vasu, N. N. Parikh, D. F. Davidson, R. K. Hanson, "Methylcyclohexane Oxidation: Shock Tube Experiments and Modeling," *5th U.S. Combustion Meeting*, Paper D17, San Diego CA, March 2007.

D. F. Davidson, M. A. Oehlschlaeger, R. K. Hanson, "Methyl Concentration Time Histories during iso-Octane and n-Heptane Oxidation," *Proceedings of the Combustion Institute* 31, 321-328, 2007.

T. C. Hanson, D. F. Davidson, R. K. Hanson, "Shock Induced Behavior in Micron-Sized Water Aerosols," accepted for publication, *Physics of Fluids* 2007.

D. F. Davidson and R. K. Hanson, "Fundamental Kinetics Database Utilizing Shock Tube Measurements, Vol. 2: Concentration Time-History Measurements" *Mech. Eng. Dept. Report*, Stanford University, December 2006.

E. L. Petersen, R. K. Hanson, "Measurement of Reflected-Shock Bifurcation over a Wide Range of Gas Composition and Pressure," *Shock Waves* 15, 333-340 (2006).

S. S. Vasu, D. F. Davidson, R. K. Hanson, "Shock Tube Ignition Delay Times and Modeling of Jet Fuel Mixtures," Paper AIAA-2006-4402, *42nd AIAA/ASME/SAE/ASEE Joint Propulsion Conference*, Cincinnati OH, July 2006.

EXPERIMENTAL AND COMPUTATIONAL CHARACTERIZATION OF COMBUSTION PHENOMENA

AFOSR Task No. 02PR01COR

Principal Investigator: James R. Gord

Air Force Research Laboratory
AFRL/PRTC Bldg 5
1950 Fifth St
Wright-Patterson AFB OH 45433-7251

SUMMARY/OVERVIEW

Propulsion systems represent a substantial fraction of the cost, weight, and complexity of Air Force aircraft, spacecraft, and other weapon-system platforms. The vast majority of these propulsion systems are powered through combustion of fuel; therefore, the detailed study of combustion has emerged as a highly relevant and important field of endeavor. Much of the work performed by today's combustion scientists and engineers is devoted to the tasks of improving propulsion-system performance while simultaneously reducing pollutant emissions. Increasing the affordability, maintainability, and reliability of these critical propulsion systems is a major driver of activity as well. This research effort is designed to forward the scientific investigation of combustion phenomena through an integrated program of fundamental combustion studies, both experimental and computational, supported by parallel efforts to develop, demonstrate, and apply advanced techniques in laser-based/optical diagnostics and modeling and simulation.

TECHNICAL DISCUSSION

Acetylene Measurements by ERE-CARS. Measurements of acetylene (C_2H_2) concentration are important for understanding many combustion processes. Acetylene plays an important role in the chemical kinetics of both soot initiation and growth, and also in the formation of polycyclic aromatic hydrocarbons. Measurements of acetylene, moreover, are useful for understanding surface chemistry related to chemical vapor deposition as well as to carbon nanotube synthesis via combustion. Electronic-resonance-enhanced coherent anti-Stokes Raman scattering (ERE-CARS) spectroscopy was used to obtain acetylene spectra at pressures ranging from 0.1 to 8 bars. Visible pump and Stokes beams are tuned into resonance with Q-branch transitions in the ν_2 Raman band of acetylene. An ultraviolet probe beam is tuned into resonance with the $\tilde{A}-\tilde{X}$ electronic transition of C_2H_2, resulting in significant electronic resonance enhancement of the CARS signal. Figure 1 shows a comparison between theoretical and measured spectra for pulse energies of 2 mJ/pulse, 2 mJ/pulse, and 0.5 mJ/pulse for the pump, Stokes, and probe beams, respectively. Reasonably good agreement is achieved between theory and experiment. The remaining differences between theory and experiment are probably due to slight saturation of the experimental spectrum. Figure 2 shows that the square root of the integrated ERE-CARS signal increases sharply with increasing pressure from 0.1 to 4 bars and then increases gradually beyond 5 bars at 300 K. The detection limit under the experimental conditions presented here is approximately 25 ppm at room temperature. Future research will

focus on investigating the pressure-scaling laws and the detection limit at elevated temperatures under realistic gas-turbine operating conditions.

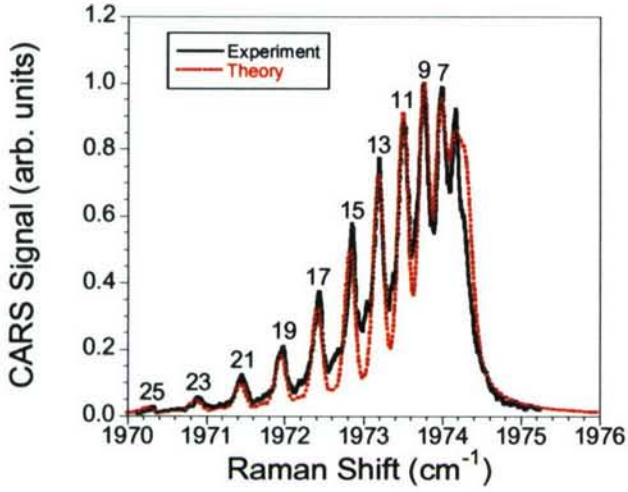

Fig. 1. Comparison between experimental and theoretical C_2H_2 ERE-CARS spectra for 1% C_2H_2 in N_2 buffer gas at 0.05 bars and 300 K.

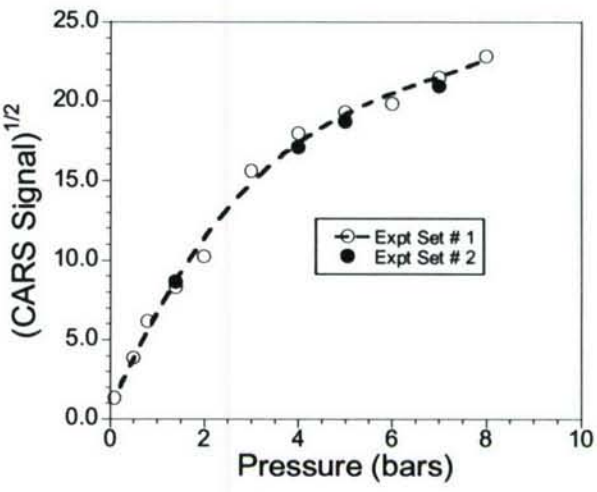

Fig. 2. Variation of the square root of the integrated C_2H_2 ERE-CARS signal with increasing pressure in the pressure range from 0.05 to 8 bars.

Femtosecond Coherent Anti-Stokes Raman Scattering Thermometry. Despite major advances in femtosecond (fs) lasers over the last decade, the use of these systems for gas-phase diagnostics and sensing has been minimal. The cost of these systems has been one barrier to their use, but a more serious barrier to the development of fs-laser-based diagnostic techniques has been a lack of understanding over how to couple spectrally broad fs laser pulses with much narrower resonance transitions in gases. For Raman resonances, there are numerous pump-Stokes frequency "pairs" under the laser spectral envelope that can contribute to resonance excitation. Fs CARS and other fs-laser-based techniques have the potential to revolutionize the field of gas-phase diagnostics because fs laser technology addresses many limitations that have plagued ns laser techniques for over two decades. For example, a 10-Hz repetition rate is typical for "standard" CARS experiments performed with ns Nd:YAG and dye lasers. Preliminary fs CARS experiments indicate signal levels are sufficiently high that single-laser-pulse measurements are possible, enabling the acquisition of CARS spectra at data rates of 1 kHz (or higher as fs laser technology advances). These high data rates are advantageous for diagnostics in turbulent flames and for measurements in advanced combustors in large-scale test facilities where test time is limited and very expensive.

Time-resolved fs CARS spectroscopy of nitrogen molecule was applied to the measurement of temperature in near-adiabatic hydrogen-air diffusion flames. The initial dephasing rate (generally up to 10 ps after the excitation) of the Raman coherence induced by the ultrafast (80 fs) pump and Stokes beams is used to measure temperature. This initial dephasing rate of the Raman coherence is completely independent of collisions and depends only on the extent of the transition bandwidth, which is a function of temperature. A simple theoretical model based on impulsive excitation of the Raman coherence followed by signal decay, arising due to the frequency mismatch of the various spectral components that contribute to the coherence, is used to extract temperature information from the experimental signal. The temperatures extracted from time-resolved fs-CARS signals show excellent agreement with the theoretical temperatures calculated using adiabatic reaction mechanisms, as depicted in Fig. 3.

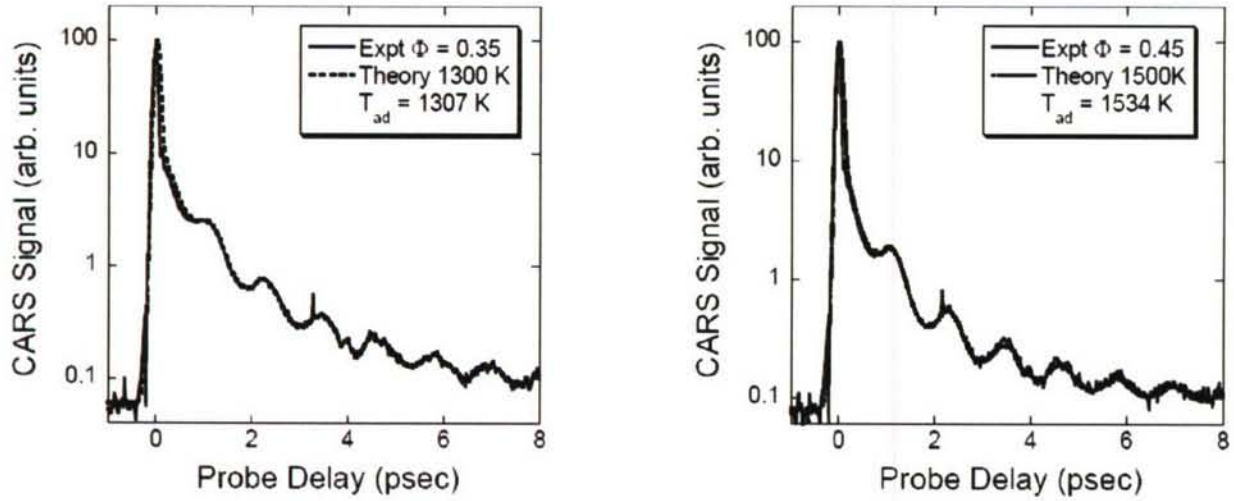

Fig. 3. Comparison of temperatures extracted from time-resolved fs-CARS signals with calculated adiabatic flame temperatures.

Direct Comparison of Ballistic Imaging and Shadowgraphy in Dense Sprays. Time-gated fs ballistic imaging was compared directly with traditional shadowgraphy techniques for visualizing core structures in dense sprays produced with various model rocket injectors. The optical components for the ballistic-imaging system are based on a previous design used for gas-turbine augmentor sprays. For the current work, a number of innovations were implemented, as shown in Fig. 4, to test feasibility for the rocket-spray environment. First, the new optical system uses an 80-fs laser system instead of the 40-fs system used in previous work. The new new laser is much more stable and fits neatly in a single, hardened 2 ft x 4 ft box as opposed to the four separate boxes associated with the original laser system. In the new system, a thin-film polarizer is used rather than a fixed beamsplitter to control the distribution of laser energy between the imaging and switching beams. When coupled with an upstream half-wave plate and additional polarizers downstream, this enables fine control of the laser energy in each beam with full utilization of the available laser energy. Another important change in the current system is the use of a 1:4 upcollimating system to provide four times the viewing area (16.25 mm x 16.25 mm) as compared with the previous system. To ensure the spray is relay imaged into the camera, a single focusing lens is used in the imaging beam between the spray and the camera. This provides a diffraction-limited beam at the CCD imager without complicated alignment. All lenses are removed from the optical-Kerr-effect (OKE) switching beam to minimize the introduction of stray birefringence in the switching beam and reduce undesired leakage through the second polarizer. Furthermore, the imaging screen is eliminated and the imaging beam sent

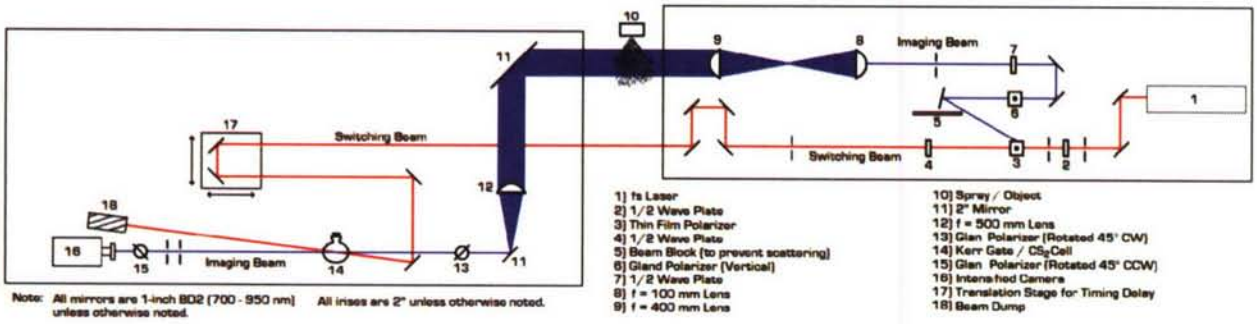

Fig. 4. Schematic diagram of the improved ballistic-imaging system.

directly into the CCD camera, significantly reducing background scattering introduced by the

imaging screen and increasing the light-collection efficiency of the system. Finally, a more robust alignment is achieved by implementing the delay stage in the switching-beam path, substantially reducing alignment difficulties associated with the imaging-beam path.

A comparison of ballistic imaging with the shadowgraphy technique for a dense spray is shown in Fig. 5. It is evident the ballistic images provide superior visualization of the liquid core regions of the spray and enhanced discrimination against the surrounding cloud of droplets as compared to traditional shadowgraphy achieved with either the ultrafast fs laser source or the cw source.

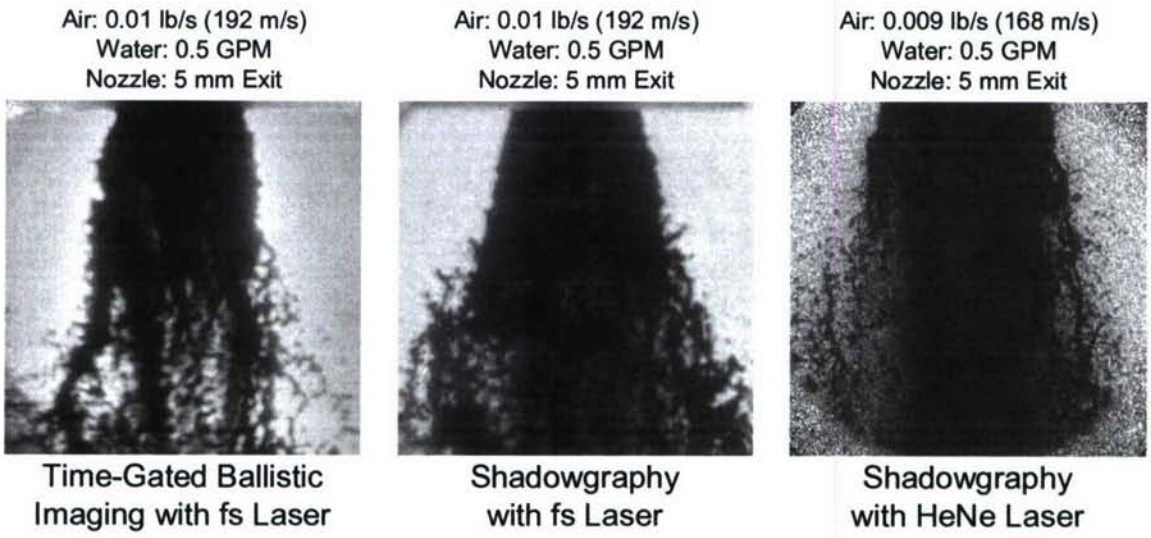

Fig. 5. Direct comparison of ballistic imaging and shadowgraphy in a dense spray.

SELECTED RECENT PUBLICATIONS

Lucht, R. P., Kinnius, P. J., Roy, S., and Gord, J. R., "Theory of Femtosecond Coherent Anti-Stokes Raman Scattering Spectroscopy of Gas-Phase Resonant Transitions," accepted for publication in the Journal of Chemical Physics, May 2007.

Chai, N., Kulatilaka, W. D., Naik, S. V., Laurendeau, N. M., Lucht, R. P., Kuehner, J. P., Roy, S., Katta, V. R., and Gord, J. R., "Nitric Oxide Concentration Measurements in Atmospheric-Pressure Flames using Electronic-Resonance-Enhanced Coherent anti-Stokes Raman Scattering," accepted for publication in Applied Physics B, February 2007.

Naik, S. V., Chai, N., Kulatilaka, W. D., Laurendeau, N. M., Lucht, R. P., Roy, S., and Gord, J. R., "ERE-CARS Measurements of Nitric Oxide and Kinetic Analysis in Diluted Hydrogen Counter-Flow Flames at Atmospheric Pressure," submitted to Combustion and Flame, December 2006.

Kulatilaka, W. D., Chai, N., Naik, S. V., Laurendeau, N. M., Lucht, R. P., Kuehner, J. P., Roy, S., and Gord, J. R., "Effects of Pressure Variations on the Electronic-Resonance-Enhanced Coherent Anti-Stokes Raman Scattering of Nitric Oxide," Opt. Comm. 274, 441-446, 2007.

Chai, N., Naik, S. V., Kulatilaka, W. D., Laurendeau, N. M., Lucht, R. P., Roy, S., and Gord, J. R., "Detection of Acetylene by Electronic-Resonance-Enhanced Coherent Anti-Stokes Raman Scattering," accepted for publication in Applied Physics B, February 2007.

Kulatilaka, W. D., Lucht, R. P., Roy, S., Gord, J. R., and Settersten, T. B., "Detection of Atomic Hydrogen in Flames Using Picosecnd Two-Color Two-Photon-Resonant Six-Wave-Mixing Spectroscopy," accepted for publication in Applied Optics, November 2006.

Lucht, R. P., Roy, S., Meyer, T. R., and Gord, J. R., "Femtosecond CARS Measurement of Gas-Phase Temperatures from Frequency-Spread Coherence Dephasing of Raman Coherence," Appl. Phys. Lett. 89, 251112, 2006.

Kulatilaka, W. D., Chai, N., Naik, S. V., Laurendeau, N. M., Lucht, R. P., Kuehner, J. P., Roy, S., and Gord, J. R., "Measurement of Nitric Oxide Concentration in Flames using Electronic-Resonance-Enhanced Coherent Anti-Stokes Raman Scattering," Opt. Lett. 31(22), 3357-3359, 2006.

Roy, S., Kulatilaka, W. D., Naik, S. V., Laurendeau, N. M., Lucht, R. P., and Gord, J. R., "Effects of Quenching on Electronic-Resonance-Enhanced CARS of Nitric Oxide," Appl. Phys. Lett. 89(10), 104106-104108, 2006.

TWO-POINT SCALAR TIME-SERIES MEASUREMENTS IN TURBULENT PARTIALLY PREMIXED FLAMES

AFOSR Grant Number FA9550-06-1-0064
Principal Investigators: Galen B. King, Normand M. Laurendeau, and Michael W. Renfro

School of Mechanical Engineering, Purdue University, West Lafayette, IN 47907-2088
Department of Mechanical Engineering, University of Connecticut, Storrs, CT 06269-3139

SUMMARY/OVERVIEW

Two-point time-series measurements of OH have been obtained in four turbulent partially premixed H_2/CH_4 - air flames by employing the recently developed two-point picosecond time-resolved laser-induced fluorescence (PITLIF) technique. Spatial and temporal autocorrelation functions, and corresponding integral length and time scales, were computed from the time series, permitting a detailed investigation of [OH] structures within the partially premixed flames. By varying the Reynolds number and fuel-stream equivalence ratio, the effects of these parameters on the integral length and time scales were examined. Interpretation of these results relies on knowledge of turbulent nonpremixed jet flames and premixed combustion, which highlights turbulence-chemistry interactions.

Taking advantage of the high-speed measurement capacity of PITLIF, thermoacoustic instabilities were also investigated in a Rijke combustor. Simultaneous pressure and [OH] time series were obtained in preliminary studies of a premixed CH_4 – air flame supported on a flat honeycomb ceramic flameholder in a closed-open tube configuration. These time series were analyzed using statistical and spectral techniques similar to those utilized for the turbulent partially premixed flames, as well as for singular spectrum analysis (SSA). Capable of analyzing both stationary and non-stationary phenomena, SSA provides an additional tool for studying thermoacoustic instabilities in combustors.

TECHNICAL DISCUSSION

1. Partially Premixed Flames

Turbulent partially premixed flames (PPFs) are an important mode of combustion owing to their pervasiveness in practical combustion systems, including most gas-fired furnaces, gas-turbine engines, direct-injection engines, and even nonpremixed combustion systems with local extinction and reignition. Unlike nonpremixed and premixed flames, which typically contain a single reaction zone and can conveniently be described by a single conserved scalar, PPFs display complex flame structures often involving double- or even triple-flames,[1-2] hence giving rise to great difficulties in modeling PPFs. Quantitative experiments are thus valuable to elucidate flame structures and to validate combustion models.

Multi-point high-speed measurements provide important perspectives to understand turbulent combustion. In particular, two-point time-series measurements of important scalars, such as temperature[3] and mixture fraction[4], which have been demonstrated with high repetition-

[1] Z. Shu, C. W. Choi, S. K. Aggarwal, V. R. Katta, and I. K. Puri, *Combustion and Flame* 118 (1999) 91–107.
[2] R. Azzoni, S. Ratti, S. K. Aggarwal, and I. K. Puri, *Combustion and Flame* 119 (1999) 23–40.
[3] C. Ghenai and I. Gokalp, *Experiments in Fluids* 24 (1998) 347-353.

rate, laser-based techniques, reveal temporal as well as spatial statistics and shed light on the structures and dynamics of scalars within flames. By implementing two-point PITLIF[5-6], two-point time series of minor species concentrations, such as [OH], can be obtained to study interactions between hydrodynamic mixing and combustion chemistry, as has been successfully demonstrated in a set of turbulent nonpremixed jet flames[6-7]. In the present study, a recently developed two-point PITLIF technique is applied to a series of turbulent partially premixed H_2/CH_4-air jet flames, with different fuel-stream equivalence ratio (Φ) and Reynolds number (Re).

As shown in Figure 1, distinct double [OH] peaks can be found for a partially premixed flame with Φ = 1.2, where the inner peak is the rich premixed flame front and the outer peak the nonpremixed front. With increasing Φ, the two flame fronts start to merge, and eventually disappear for Φ = 2.0. An increase in Reynolds number also causes the two flame fronts to merge. At the same z/D, the nonpremixed peak has a higher OH concentration than the premixed peak, as the OH radical is mainly produced through oxidation reactions within the nonpremixed front. Peak [OH] values decrease with increasing downstream distance, which can be attributed to the enhanced residence time for slow three-body recombination reactions. The FWHMs of the [OH] profiles also increase with height, indicating a thickened OH zone and greater flame corrugation.

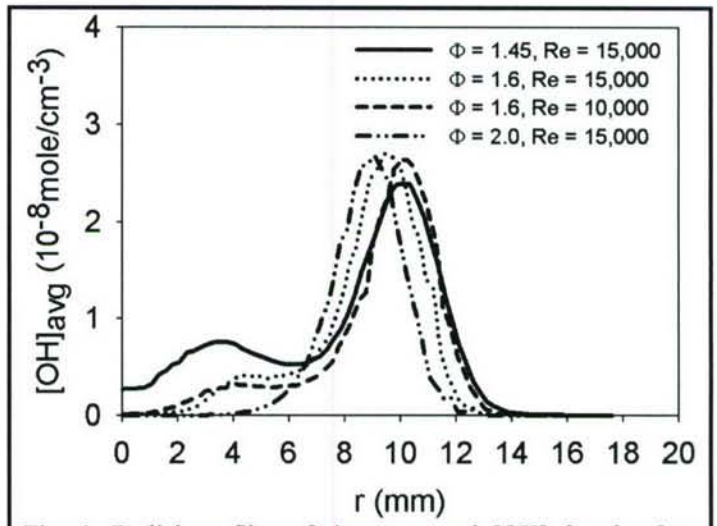

Fig. 1. Radial profiles of time-averaged [OH] for the four flames at z/D = 10.

Figure 2 shows typical time-series data measured at the mean nonpremixed and premixed peaks for the Φ = 1.45 case at Re = 15000. Compared with the nonpremixed peak, the rich premixed peak features rapid [OH] fluctuations with greater amplitude and intermittency. The corresponding temporal autocorrelation function, as shown in Fig. 3, displays a steeper decay at the mean premixed peak. This distinction between two flame locations can be explained by differences in flame structure. The rich premixed front is located within the mixing layer lower in the flame and is thus strongly affected by jet turbulence; in contrast, the nonpremixed front lies close to (or even outside) the edge of the turbulent mixing layer which, together with residual laminarization, leads to relatively slow fluctuations in [OH][7]. Moreover, the premixed front can propagate and is thus more susceptible to flow-field variations. Both factors contribute to rapid [OH] fluctuations at the mean premixed peak.

---

[4] M. E. Kounalakis, Y. R. Sivathanu, and G. M. Faeth, Journal of Heat Transfer 113 (1991) 437-445. (1991).

[5] J. Zhang, K. K. Venkatesan, G. B. King, N. M. Laurendeau, and M. W. Renfro, *Optical Letters* 30 (2005), 3144-3146.

[6] J. Zhang, G. B. King, N. M. Laurendeau, and M. W. Renfro, Two-point time-series measurements of hydroxyl concentration in a turbulent nonpremixed flame. *Applied Optics*, accepted for publication (Apr. 2007).

[7] J. Zhang, G. B. King, N. M. Laurendeau, and M. W. Renfro, Two-point OH time-series measurements in non-premixed turbulent jet flames, Proceedings of the 2006 Technical Meetings of the Central States Section, The Combustion Institute, Cleveland, OH, 2006.

Spatial autocorrelation functions for the flame with $\Phi = 1.45$ and Re = 15000 are shown at the nonpremixed peak in Fig. 4a. In general, the spatial autocorrelation functions broaden with downstream distance, indicating an increased coherence length, which is similar to that in nonpremixed jet flames[7] and can thus be similarly attributed to a growth in the mixing layer and to thickened OH structures. The spatial autocorrelation functions are typically not symmetric with respect to displacement Δr along the fuel and air sides, a behavior probably due to the proximity of the measurement location to the jet axis and the presence of an additional flame front. At z/D=10, the spatial autocorrelation function exhibits a negative value at large displacements, instead of an exponential approach towards zero, as found in most turbulent nonpremixed jet flames.

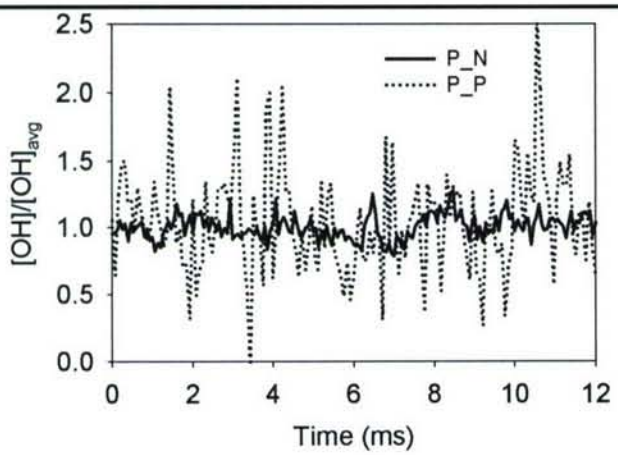

Fig. 2. Representative time series of [OH] at the mean nonpremixed peak (P_N) and the mean premixed peak (P_P) within the flame at $\Phi = 1.45$ and Re = 15000 for z/D=10.

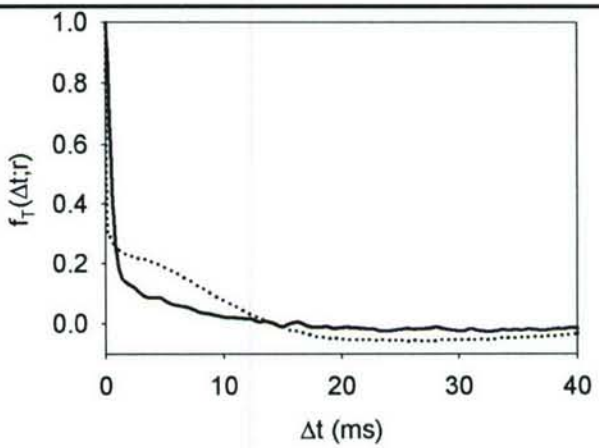

Fig. 3. Hydroxyl temporal autocorrelation functions at the mean nonpremixed peak (P_N) and mean premixed peak (P_P) for the flame at $\Phi = 1.45$ and Re = 15000 for z/D=10.

This behavior may suggest the presence of large-scale coherent structures, i.e., vortices. Figure 4b displays corresponding spatial autocorrelation functions at rich premixed peaks. Compared with those at the nonpremixed peak, the spatial autocorrelation functions at the premixed peak are typically broader. Moreover, in the near-nozzle region (z/D=10), the spatial autocorrelation function displays much greater asymmetry between the fuel-side and air-side displacements, which can be explained by the fact that this location is even closer to the jet axis.

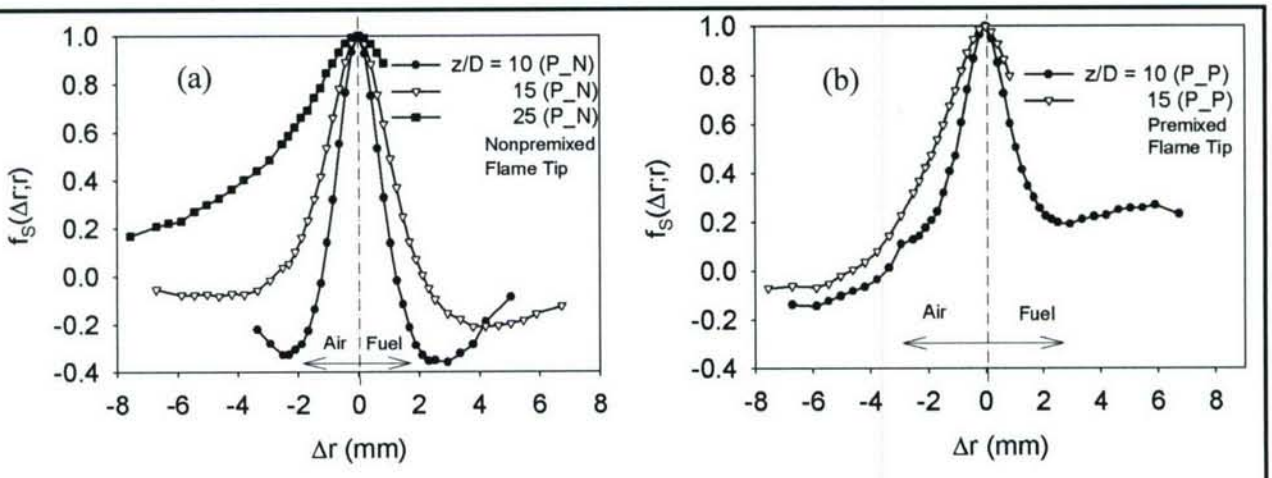

Fig. 4. Measured spatial autocorrelation functions for the flame with $\Phi = 1.45$ and Re = 15000 at the (a) mean nonpremixed peak (P_N) and (b) mean premixed peak (P_P).

2. Rijke Combustor

Thermoacoustic instabilities (TAIs) have always been an obstacle in the design and operation of solid and liquid rockets[8] as well as of gas turbines and thrust augmentors[9]. In the present section, the application of PITLIF to the study of thermoacoustic instabilities is discussed for an optically accessible Rijke tube combustor. A Rijke combustor is perhaps the simplest configuration capable of self-excited TAIs. Operating points for the combustor over a range of flowrates and equivalence ratios have been determined and preliminary time series have been obtained of both pressure and relative [OH]. Additionally, the use of an alternative analytical technique is explored applicable to non-stationary time series.

The Rijke combustor consists of a stainless steel tube of dimensions 9.0×9.0×91.4 cm, with the height extendable to 152 cm. Fused quartz windows permit optical access for laser-based measurements. The tube operates in an acoustically closed-open configuration, with premixed CH_4-air entering the bottom through a sintered metal plate. The flameholder is a 62 cell/cm^2 cordierite honeycomb with variable axial position. When the flameholder is at the tube midpoint the second standing wave mode is excited in fulfillment of the Rayleigh criterion[10]. The result is a transient increase in sound pressure followed by a steady-state limit cycle.

The limit cycle [OH] oscillations are shown in Fig. 5, along with an associated pressure time series. Corresponding power spectra show peaks at the second mode of the tube (189 Hz), as well as harmonics of this frequency. For Fig 5, z is the height above the flameholder, Φ is the equivalence ratio, and Q is the total flow rate. In addition to Fourier analyses; these data were examined using singular spectrum analysis (SSA)[11], a procedure designed to extract information from short, noisy and/or non-stationary time series. SSA is thus capable of providing new insight into the physics unresolved by Fourier analyses.

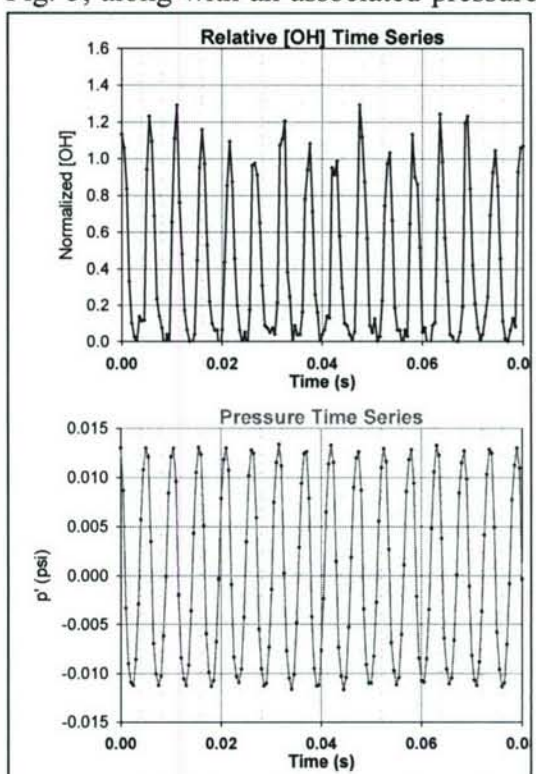

Figure 5, Relative [OH] and pressure time series for z = 0.5 mm, ϕ = 0.7, Q = 30 slpm

The starting point of SSA is to embed the time series ($P(t)$: $t = 1, \ldots, N$) in a vector space of dimension M, essentially representing the time series as a trajectory in phase space of the hypothetical system that generated the time series. In more general terms, this approach creates a succession of overlapping 'views' of the series through a sliding M-point window which is used to create a covariance matrix. Linear algebraic techniques can then be applied to this matrix to produce a noise-reduced reconstruction of the original time series. SSA has mainly been used for data adaptive signal-to-noise (S/N) enhancement and for recognizing patterns in noisy time series. Furthermore, unlike spectral methods, SSA does not require the signal to be statistically stationary and thus may be applied to non-limit cycle instabilities.

[8] A.A. Putnam, W. R. Dennis, Journal of the Acoustical Society of America 28 (1956) 246
[9] S. Sivasegaram, J.H. Whitelaw, AIAA/SAE/ASME/ASEE 23rd Joint Propulsion Conference (1987) AIAA-87-2107
[10] L. Nord, A Thermoacoustic Characterization of a Rijke-type Combustor (2000), PhD Thesis, Virginia Tech
[11] M. Ghil et al, Reviews of Geophyics 40 (2002) 3.1-3.41

HIGH GRAVITY (g) COMBUSTION

(LRIR: 99PR12COR)

Principal Investigator: Dr. Joseph Zelina

Air Force Research Laboratory
AFRL/PRTC
WPAFB, OH 45433

SUMMARY/OVERVIEW

A program is underway at AFRL on a gas turbine combustor concept that uses high g-loading in a circumferential cavity to provide the foundation for development of a low-emissions, ultra-compact, high performance combustion system for future military and commercial aircraft. This work comprises experimental testing as well as modeling and simulation of different high g-loaded combustion cavity configurations. Initial tests indicate that, by using highly swirling flows, the combustor performance can be enhanced in the form of improved combustor efficiencies at reduced combustor length. Understanding the impact of high g-loading on the pollutant emissions, operability limits, and fuel efficiency improvements are three major areas where the AFOSR program will progress the scientific understanding of the physical processes involved in this novel combustion system.

TECHNICAL DISCUSSION

Background: This work addresses fundamental combustion issues that will lead to the development of a revolutionary propulsion system that operates on a highly efficient, near constant temperature (NCT) cycle instead of the constant pressure cycle of today's engines. Such a propulsion system could provide increased power extraction, thrust augmentation, and specific thrust (ST) enhancements. A key technology essential for the development of a propulsion system that operates on a NCT cycle is an ultra-compact combustion (UCC) system that can be used as the main combustor and can efficiently add heat between the turbine stages. This combustor has been referred to in the literature as an inter-turbine burner (ITB).

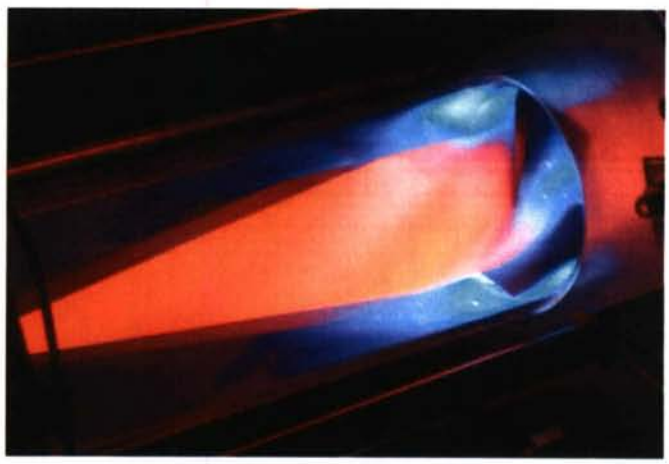

Figure 1: Experimental high-g ultra-compact combustor (UCC).

An ultra-compact combustor (UCC) concept, shown in Fig. 1, could be used in a CT cycle gas turbine engine. As seen in Fig. 1, the guide vanes comprise the combustor. The guide vanes contain trapped vortex pilots that are operated as part of a rich-burn, quick-quench, lean-burn mode. Cavity combustion and cooling air are provided at the inlet of the combustor. All of the fuel is injected in the cavity, thereby creating a rich-quench-lean configuration. The rich combustion products are transported along the front face of the cavity and entrained into the main air stream where rapid mixing and lean

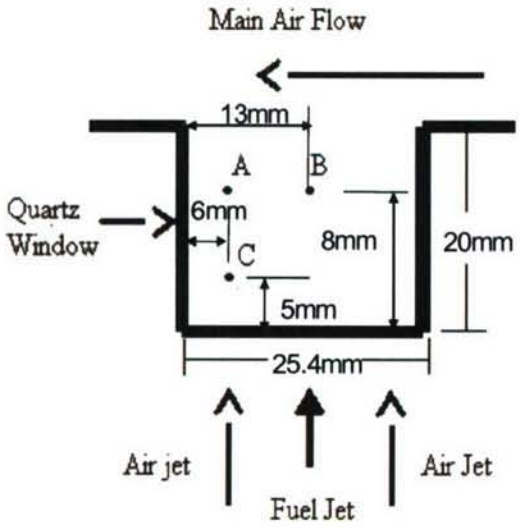

Figure 2: Schematic of LDV measurement Locations for positions A, B & C. Measurement locations are 16° downstream of fuel injector.

burning take place. Circumferential transport of reacting mixture between cavities is provided by the circumferential cavity that contributes to light-around on starting. The lean burn process is completed in the curved section of the vanes where high-g forces are created. Spatial non-uniformities of temperature and density created in the vortex cavity section and by the lateral transfer channels will promote the formation of Rayleigh-Taylor (associated with density gradients) and Taylor-Gortler (associated with centripetal and Coriolis accelerations in a curved flow) vortices in the curved section of the vanes. Adverse high strain generated by the high-g environment will be ameliorated by the chemical reactions in these vortices.

The AFRL team has been working on the premise that high g loading can provide benefits compared to conventional gas turbine combustion systems. A concept design for a high-g combustion system that can serve as a main combustor or as an ITB has been completed however, understanding of the combustion process at high g-loading conditions is necessary. The AFRL team is focused on what we believe are the key combustion issues.

1. What are the fundamental processes that control combustion in a highly accelerated (high-g) flows?
2. How does swirling flow from the main air supply impact the cavity combustion process?
3. How does vitiated flow impact the high g combustion process?
4. What are the losses associated with burning in highly accelerated (high Mach number) flow?

High g Experiments – Re-laminarization: The high-g combustor experiences tremendous acceleration on the order of 500 -5000 g's. Early work by Lewis[1] shows that the flame extinguishes at high levels of g-loads of the order of 7000 g's. Initially, it was believed that the flame extinguishes due to high velocities in the accelerating flow (flame stretch) or quenching effects. Recent work in the high g combustor by Anthenien and Zelina[2] suggests that the flow may transition to laminar flow under the high acceleration on the circumferential cavity. Other

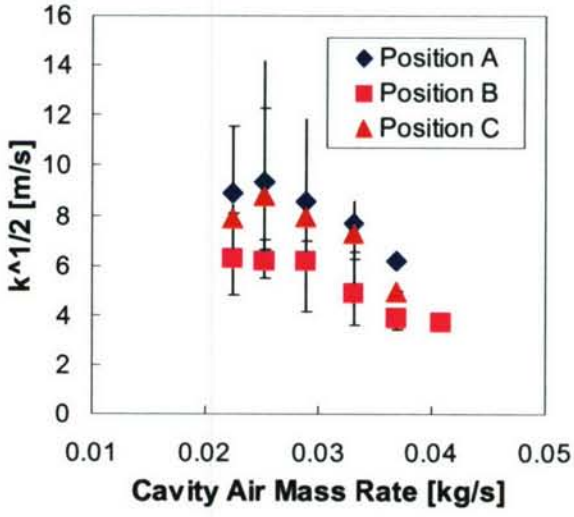

Figure 3: Characteristic turbulent velocity vs. cavity mass rate for 3 measurement positions and all operating conditions. Points indicate average measurements. Error bars indicate entire range of data scatter.

[1] Lewis, G.D., "Centrifugal-Force Effects on Combustion," proc. *14th. Symposium (International) on Combustion,* The Combustion Institute, 1973, pp. 413-419.

[2] Anthenien, R., and Zelina, J., "Experimental Results on the Turbulent Combustion Regimes within a Small-Scale Atmospheric Pressure High-g Combustor," Central States Section, Combustion Institute, 2006.

researchers have shown similar phenomena in non-reacting flows[3,4]. A two-component TSI Laser Doppler Velocimeter in back scatter was used to gather velocity data within the cavity of the UCC. Data was taken at three discrete points within the cavity over the entire operating range of air flows and cavity equivalence ratio ranging from $0.8 \leq \varphi \leq 1.5$. A schematic of the location of these points is shown in Fig. 2. All data points were taken 16° downstream of a fuel injector.

Plots of the characteristic turbulent velocity (square root of the turbulent kinetic energy) and the turbulent integral length scale for three measurement locations and all operating conditions are shown in Figs. 3 and 4. It is seen that as cavity mass injection is increased, both the turbulent velocity and turbulent length scale decrease. Further, the scatter among various operating conditions also decreases. This simultaneous decrease in both velocity fluctuation and length scale results in a significant decrease in the turbulent Reynolds number ($Re=k^{1/2}l/\nu$, ν is the kinematic viscosity) as seen in Fig. 5. Reynolds number is seen to fall as low as approximately Re=30. Combustion was unable to be sustained at cavity mass flows above 0.041kg/s. This corresponds to the lowest Re observed. Although initially attributed to an over-loading of the cavity (too little residence time) this limit on the combustor may in fact be due to a re-laminarization of the flow within the cavity. This would lead to a significant reduction in flame speed leading to extinction within the cavity.

There exist several ways to view the types of flames, premixed or non-premixed, that exist at various turbulence levels. Here we use the method developed by Borghi[5] where the ratio of characteristic turbulent velocity and flame velocity is compared to the ratio of characteristic turbulent length and flame length. The ratios of the turbulent flow characteristics to the flame characteristics are then plotted, resulting in Fig. 6. It is immediately noted that all the data falls in the distributed reaction regime, bounded below by the $\tau_c=\tau_k$ line and from above by the Damkohler number (Da) = 1 line. The data is bounded parallel to the Da=1 line. Not shown, a Da=2 line precisely demarcates the upper bounding line seen in the data of Fig. 6. It is also seen from Fig. 6 that the data is not grouped by position within the cavity (different color points). The bulk of the data falls both within a range $1<Da<10$; all the data falls below Da=100. Additionally, nearly all the data falls above the Klimov-Williams criterion ($l_k=\delta_L$). Above this line both Klimov[6] and Williams[7] assert that a laminar flame may not exist due to the high turbulent gradients (data not shown).

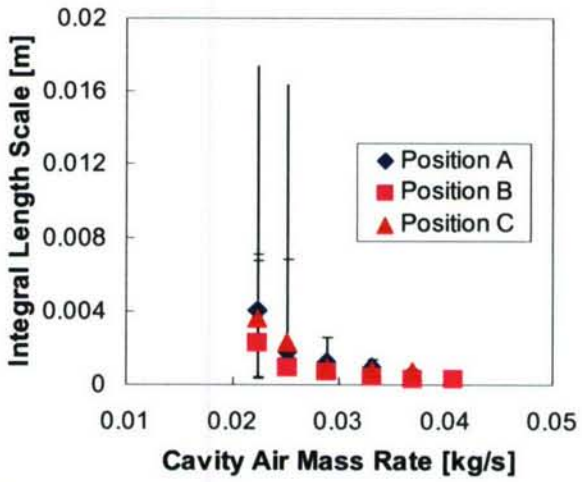

Figure 4: Integral length scale vs. cavity mass rate for 3 measurement positions and all operating conditions. Points indicate average measurements. Error bars indicate entire range of data scatter.

Rayleigh Losses – Ultra-Compact Combustor: Conventional gas turbine combustion systems must reduce combustion velocities to below Mach = 0.1 to prevent large pressure losses associated with heat addition in high velocity flow, commonly referred to as the Rayleigh loss. For example, pressure loss

[3] Launder, B. E., "Laminarization of the Turbulent Boundary Layer in Severe Acceleration," Journal of Applied Mechanics, ASME Vol. 31, December 1964.
[4] Narasimha, R., and Sreenivasan, K. R., "Relaminarization of Fluid Flows," Advances in Applied Mechanics, Vol. 19, Academic Press, 1979.
[5] R. Borghi, Prog. Energy Combust. Sci. 14 (1988) 245-292.
[6] A.M. Klimov, Zh. Prikl. Mekh. Tekh. 3 (1963) 49.
[7] F.A. Williams, Combust. Flame, 26 (1976) 269.

associated with Mach = 0.1 accounts for about 1% of the total pressure loss through a conventional swirl-stabilized combustion system. At Mach = 0.32, this pressure loss value is nearly 10%. Since most combustion systems in gas turbine engines must operate at 5-6% total pressure loss to maintain good fuel consumption performance, the high levels of Rayleigh losses associated with the high Mach flow would be prohibitive. The high g UCC concept lends itself to integration into the engine where the swirl and high velocity coming from the compressor can feed directly to the combustion device, minimizing combustor length and engine weight by removing compressor de-swirl and diffuser components. One major concern is the Rayleigh loss associated with the UCC, limiting the Mach number of the combustion system and thereby requiring some diffuser geometry to reduce inlet Mach numbers. It is hypothesized that since the heat release takes place within the sheltered cavities (both circumferential and radial vane cavities), upstream of the gauge point of the vanes, Rayleigh losses will be minimized and only mixing losses will be encountered. Experiments are underway to determine if the Rayleigh losses associated with the UCC will be significantly different than those losses associated with conventional swirl-stabilized devices.

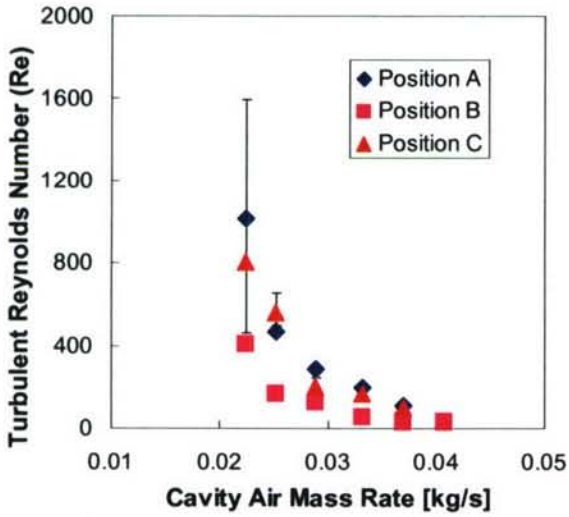

Figure 5: Turbulent Reynolds Number vs. cavity mass rate for 3 measurement positions and all operating conditions. Points indicate average measurements. Error bars indicate entire range of data scatter.

External Collaboration: AFRL continues to collaborate with universities, industry and other government laboratories on specific high g combustor problems. AFRL is actively involved with industry to transition compact, high-g combustor concepts. We continue to look for opportunities to start 6.2 programs utilizing our 6.1 results to demonstrate an UCC/ITB. This collaborative approach provides a clear transition path for the 6.1 research and would provide additional funds needed to demonstrate a turbine burner concept.

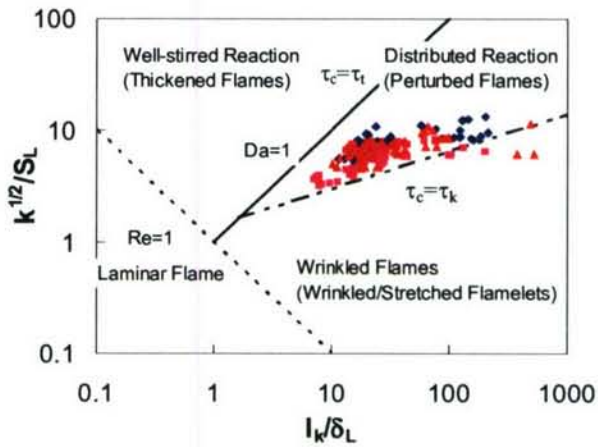

Figure 6: Combustion regimes for 3 measurement positions and all operating conditions.

Future Work: The AFRL team plans to investigate different turning vane geometries in the UCC configuration to understand to impact of swirl on combustion processes. Efforts will focus on the radial vane cavity geometry to understand the transport mechanisms from the circumferential high g cavity to the high Mach main flow. Four windows were placed around the circumferential cavity (see Fig. 1) to allow access for diagnostics in the highly turbulent high g cavity. The team plans to use the diagnostics to quantify the turbulent length scales and velocity field in the cavity. Future studies may include more rigorous diagnostics techniques to determine species concentration and velocity field in the circumferential cavity.

TURBINE BURNERS: TURBULENT COMBUSTION OF LIQUID FUELS

FA 9550-06-1-0194

Principal Investigators : William A. Sirignano and Derek Dunn-Rankin

Department of Mechanical and Aerospace Engineering
University of California, Irvine 92697-3975

SUMMARY/OVERVIEW:

This program addresses the two-way coupling between combustion processes and fluid dynamic phenomena associated with burning liquid fuels in high-speed, accelerating and turning turbulent flows. Experimental and computational studies will improve the scientific understanding of fundamental issues related to the ignition and flame-holding of a liquid fuel spray in the high-acceleration flow and will optimize the injection of liquid fuel into a protected recirculation zone. Non-reacting, accelerating and turning experimental results have improved our understanding of the associated fluid dynamic phenomena, while two-dimensional, non-accelerating, reacting computational results have provided insight into the combined combustion and fluid dynamic processes.

TECHNICAL DISCUSSION

In the current experimental design, the apparatus consists of a large (2 m long, 30 cm diameter) PVC flow straightener tube connected to a completely transparent channel made entirely in lexan (Fig.1). The apparatus is prepared exclusively to run cold flow experiments. The flow is provided by high-capacity house air-compressors, and passes through a series of pipes that convey the air through the PVC tube and into the channel. A vortex flow meter is installed to measure the airflow rate existing in the pipe. After the air leaves the flow meter, it follows a 2 inch (5 cm) diameter pipeline to the PVC tube where it is connected by a pressure-resistant rubber hose. The tube stands on two 0.5 inch-thick steel flanges, connected to mating tube flanges by means of several uniformly-distributed bolts. The channel section has curved contracting walls (25 cm radius of curvature) producing a rectangular cross section that contracts from 10 x 5 cm at the inlet to 10 x 1 cm at the outlet over a 70 degree arc. A removable small auxiliary cavity can be attached to the curved section to provide a recirculating low speed zone, in which liquid spray can be injected via small simplex-atomizers producing spray droplets of mean diameter less than 100 microns. The cavity is as wide as the channel (10 cm); its other dimensions are 5.5 cm in both directions and it is located at about one third of the channel length. There are three possible injection locations in the cavity, one on the top, and two on the sides perpendicular to the main stream direction. Two additional injection points are present in the channel itself, upstream of the cavity.

The experimental conditions consist of airflows ranging from 0.12 kg/s to 0.36 kg/s, and pressures ranging from 1 to 5 atmospheres. The velocity profile has been measured at the entrance and exit of the chamber with a pitot tube connected to a digital reader and supported by a position sensor to control the position of the tube at any survey. Air was run inside the channel

at 0.17 kg/s mass flow rate. The mean flow is very uniform at both the entrance and exit of the channel, as desired. At this mass flow rate, the average entrance velocity is 26.4 m/s, and the average exit velocity is 86.1 m/s. The results indicate that the flow is very close to 2D inside the channel. Another important result is that the thickness of the boundary layer at the exit section is small enough to prevent significant choking of the flow.

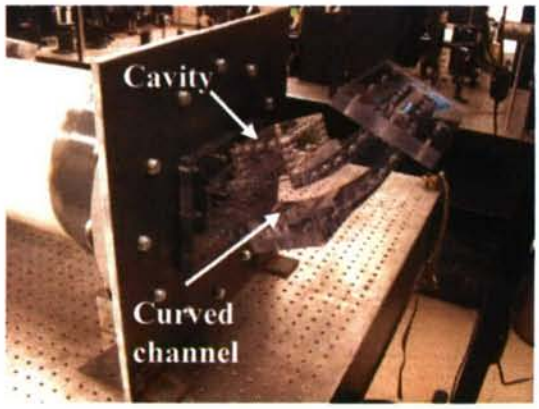

Figure 1. Lexan channel connected to the flange

Figure 2. Smoke inside the test chamber

To visualize the velocity profile of the air inside the cavity and the channel, we used smoke generated from dry ice (solid CO2) in contact with water. 4 small hoses of 1/8'' (3.2 mm) ID enter the test section in four different locations, two in the channel (top and bottom), and two in the cavity (one on the top and one on the right side). We used air at 0.04 kg/s mass flow rate, representing an entrance velocity of approximately 7 m/s. A frequency-doubled Nd-YAG laser sheet was created inside the test section to illuminate the smoke, and images were recorded by a CCD camera synchronized to the laser firing and connected to a computer. Figure 2 shows clearly that the velocity inside the cavity is much smaller than the velocity in the channel, since the smoke in the channel is carried away and dissipated much more easily than in the cavity. The figure also shows evidence of cavity smoke being drawn into the main flow along the boundary. Also, there is a distinct shear interface between the cavity flow and the channel flow, so we expect that liquid fuel sprayed into the cavity will be effectively trapped for sufficient time to allow vaporization and mixing in the confined space. There will likely be an issue, however, of drawing the reactive mixture into the main stream flow and allowing it to burn there while traveling at higher speed. The smoke indicates that the flow in the cavity is a single vortex whose dimensions are comparable to those of the cavity. Recirculation occurs and it is stable. An estimation of the residence time inside the cavity has been made. The air resides in the cavity is about 33 times longer than in the channel, and has a velocity about 33 times smaller than in the channel, at this particular flow rate. Streamer tests confirmed the presence of counterclockwise recirculation inside the cavity, and that a thin boundary layer exists at the exit.

Injection of water spray inside the cavity and the channel has been performed using simplex atomizers placed in different locations, to provide qualitative information regarding the mixing properties of fuel and air. The atomizers can work at a flow rate range of 2.2 to 5 gallons per hour, corresponding to pressures of 200 to 1000 psi, respectively. The experiments have been run at a water flow rate of 3.5 G/h, corresponding to 500 psi pressure inside the atomizer. Air has been run inside the channel at a flow rate of 0.12 kg/s, which, if the liquid were heptane fuel, would provide an overall equivalence ratio of 0.15. This value was chosen to provide a 300 K temperature increase of the inlet gas, Two selected results are shown in Figures 3 and 4. The arrows show that the droplets, when they come out of the cavity, tend to be carried by the air into the upper portion of the channel, where the top wall is. It is clear that the spray doesn't follow

the recirculation pattern of the air inside the cavity. This occurs because the momentum of the spray is much greater than that of the air. The spray therefore can partially reach the main channel stream. This may help improve ignition, flame holding, and stability, but combusting experiments will be needed to confirm this expectation. It also appears from these non-reacting spray studies that additional air will be needed in the cavity to avoid excessively rich local equivalence ratios.

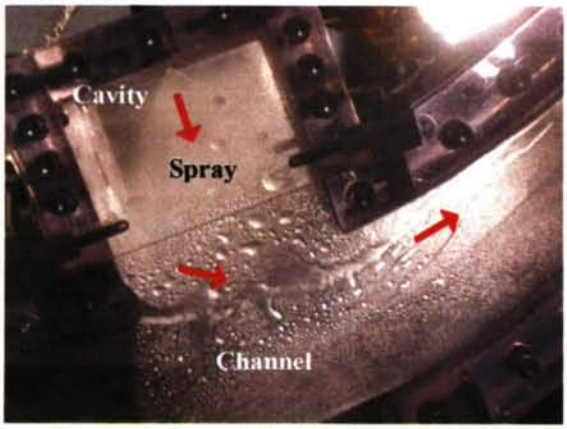

Figure 3. Spray injection from cavity top

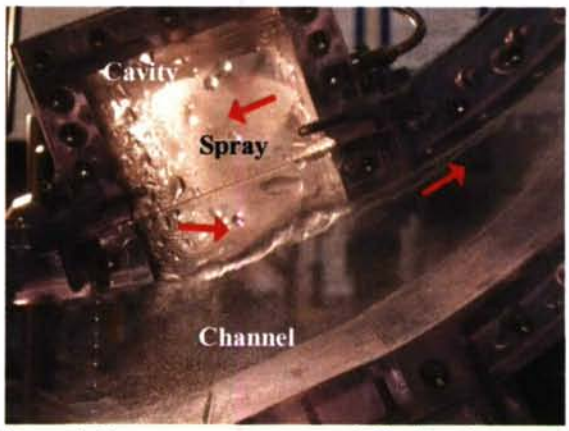

Figure 4. Countercurrent spray injection from cavity

According to the measurements collected, the Reynolds number (*Re*) at the exit of the channel is of the order of 10^5. The Reynolds number everywhere in the channel is of the same order of magnitude because for any constant-width contracting channel the height varies inversely with velocity. The design of the metal chamber meant for the reacting flow experiments will be similar to that of the lexan chamber. Some more tests are planned for the transparent channel, however. Liquid PLIF diagnostics will be used to assess liquid mixing from the auxiliary chamber, and shadowgraph visualization will be performed to verify the current results.

Numerically, the turbine passage is modeled as a two-dimensional straight channel flow over an open cavity, as shown in Figures 5 – 8. Hot air enters the channel at a constant velocity. Gaseous fuel is injected from any of the three cavity walls. The fuel used in these calculations is gaseous n-heptane, and the combustion is described as a one-step overall chemical reaction. The governing equations are solved numerically using a finite-volume method with a pressure-correction equation. The scheme is second-order accurate in both space and time.

Non-reacting simulations show that without injection into the cavity, transition to unsteady flow occurs at $Re \approx 2500$. With steady gaseous injection into the cavity, instability occurs as low as $Re \approx 950$. Simulations of the same injection Reynolds number into a quiescent field show that the jet alone is steady, indicating that there is a coupling between the two flows that causes transition to occur at a lower Reynolds number. This can have significant impact on mixing and flameholding.

Figure 5 shows the streamlines and vorticity contours for a non-reacting case at $Re = 10{,}000$ without fluid injection. There is a single main vortex in the cavity, and vorticity is periodically shed from the cavity into the channel, which compares well with the experimental results shown in Figure 2.

Figure 6 shows the temperature contours for a reacting case at $Re = 1000$ with gaseous fuel injected from the upstream wall of the flow cavity. The air inlet temperature is 1000 K and the wall temperature is 600 K. The fuel is injected at 300 K at stoichiometric proportions. In a straight channel without a cavity, 28% of the fuel is burned before exiting the channel. With the addition of the cavity, 32% of the fuel is burned before exiting. The flame is anchored in the

relatively low-velocity and high-vorticity shear layer spanning the cavity. It is interesting to note that injecting fuel into the cavity at Re = 1000 produces a steady flame, despite the cavity region being unsteady.

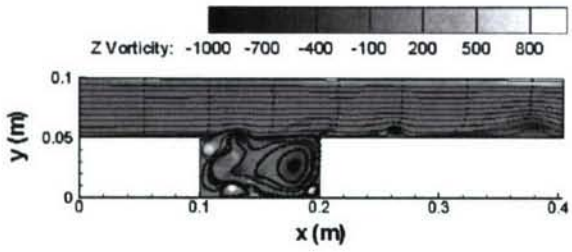

Figure 5 Streamlines and vorticity contours for Re = 10,000

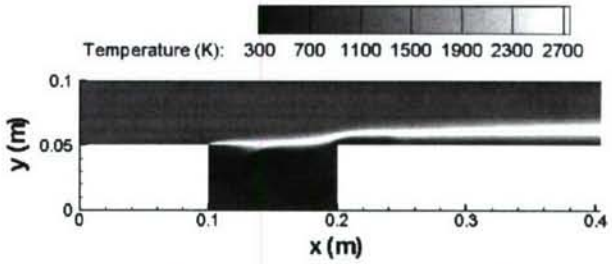

Figure 6 Temperatures contours for Re = 1000 with fuel injection from the upstream wall

Results at Re = 500 show that the flame is anchored further upstream than in the Re = 1000 case, and that the percentage of injected fuel burned increases further to 34% because of the longer residence time in the channel. Injecting fuel from the downstream wall of the cavity at Re = 1000 reduces the amount of fuel burned to 22%.

At Re = 2000 the flame is no longer steady, as shown in Figure 7. The amount of fuel burned increases significantly to 61%, despite the flame being anchored a significant distance downstream and the residence time being shorter. This increase in the amount of fuel burned is explained by the increased mixing rate that accompanies the transition from laminar to turbulent flow.

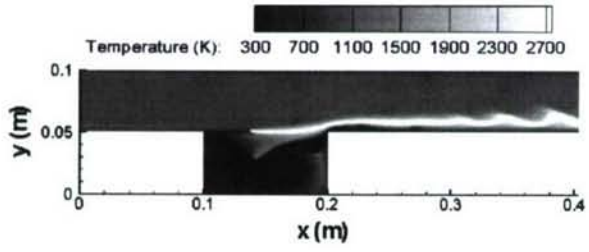

Figure 7 Temperatures contours for Re = 2000 with fuel injection from the upstream wall

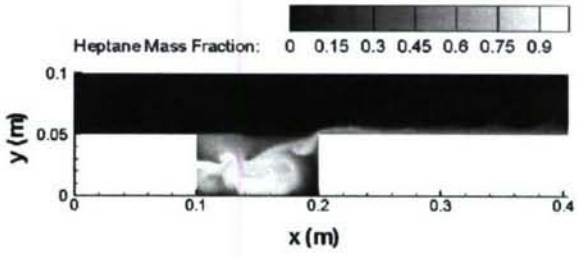

Figure 8 Fuel mass fraction contours for Re = 2000 with fuel injection from the upstream wall

Figure 8 shows that the unburned fuel remains very close to the wall of the channel, similar to the smoke shown in Figure 2. This is because the two-dimensional approximation in the model constrains the injected fluid to behave as a sheet rather than as a jet. Three-dimensional results may be qualitatively different.

Injection of additional air from the bottom and downstream walls can force the flame further into the channel. At Re = 1000 the amount of fuel burned increases from 32% to 35% with additional air injected while maintaining a stoichiometric air-fuel ratio.

IGNITION KINETICS IN FUELS OXIDATION

(ARO Grant No. W911NF-04-1-0151)

Principal Investigator: Chung K. Law, Princeton University

SUMMARY/OVERVIEW

This program studies fundamental chemical kinetics as well as its individual and coupled effects with aerodynamics on laminar nonpremixed ignition of hydrocarbons and nitrogen-containing compounds, using experimental, computational, and theoretical approaches. During the reporting period, four projects were undertaken, namely: (1) development of an elementary reaction mechanism for the thermal decomposition of monomethylhydrazine; (2) kinetic analysis of the reactions of O_2 with products from OH addition to isobutene; (3) computational study on the multiple ignition states of methane by heated counterflowing air; and (4) experimental and computational determination of counterflow ignition temperatures of mixtures of methane and ethylene.

TECHNICAL DISCUSSION

1. An Elementary Reaction Mechanism of the Thermal Decomposition of Monomethylhydrazine

Hydrazine and its methyl derivatives are of interest as bipropellant fuels as well as monopropellants for thrusters used in long-term satellite and space activities because of their high energy content, versatility, and reactivity. The objective of the present study is to develop an elementary reaction mechanism of the thermal decomposition of monomethylhydrazine (MMH) by using quantum chemistry, thermochemistry, and kinetic theories. The stationary points of the potential energy surface for MMH decomposition were calculated at the CBS-QB3 and CCSD(T)/6-311++G(3df,2p)//MPWB1K/6-31+ G(d,p) level, as shown in Fig. 1. The major reaction paths for MMH decomposition were found to be the N—N and C—N bond scission to the products CH_3NH+NH_2 and CH_3+NHNH_2. Thermochemical properties of the species on the potential energy surface of MMH decomposition were calculated using statistical mechanics and molecular parameters from various DFT and *ab initio* methods. The bond dissociation energies of MMH were determined, and different bond strengths of MMH were discussed based on the stability of the forming radicals. The reaction barriers of the thermal decomposition, abstraction, and substitution reactions of MMH were determined. Furthermore, elementary reaction rate constants were calculated by transition state theory with correction of tunneling factors, and the kinetic parameters of MMH dissociation to intermediate and product channels were calculated by QRRK and master equation analyses as functions of temperature and pressure (Fig.2). An elementary reaction mechanism was constructed to model the overall MMH thermal decomposition rate, and was compared with available experimental data (Fig.3).

This work is reported in Publication No. 1.

2. Kinetic Analysis of the Reactions of O_2 with Products from OH Addition to Isobutene

Unimolecular dissociation of neopentyl radical to isobutene and methyl radical is competitive with the neopentyl association with O_2 in thermal oxidative systems. Furthermore, both isobutene and OH radical are important primary products from the reactions of neopentyl with O_2. Consequently, reactions of O_2 with the 2-hydroxy-1,1-dimethylethyl ($C_2C•COH$) and 2-hydroxy-2-methylpropyl ($C_2C(OH)C•$) radicals resulting from the OH addition to isobutene are important to understanding the oxidation of neopentane and other branched hydrocarbons. The stationary points on the potential energy surfaces of 2-hydroxy-1,1-dimethylethyl and 2-hydroxy-2-methylpropyl radicals with O_2 (Fig.4 and Fig.6) and the thermochemical properties of the species involved in these reaction systems were characterized based on *ab initio* and density functional theories. Internal rotation potential barriers for the reactants and intermediate peroxy adducts were also determined to accurately predict the thermochemical properties of these oxy-generated species. The kinetic parameters for intermediate and product formation channels of the above systems were calculated as functions of temperature and pressure. High-pressure limit rate expressions for reaction channels on the potential energy surfaces are provided, and chemical activation

and dissociation rate constants versus pressure and temperature are presented (Fig. 5 and Fig.7). These kinetic parameters can serve as models for branched alcohol oxidation mechanisms, where the radical site is adjacent to the alcohol carbon such as that in primary radical of ethanol and for other OH + olefin addition adducts.

This work is reported in Publication No. 2.

3. Computational Study of Multiple Ignition in Nonpremixed Methane Ignition

In the present study, the counterflow system is employed to investigate methane ignition chemistry in the presence of diffusive transport and strained flows, focusing on the possible existence of the double-turning behavior of the S-curve. Kinetic mechanisms, GRI 2.11 and GRI 3.0, were used to compute the ignition temperatures of nitrogen-diluted methane by heated air, over a wide range of system pressure, fuel concentration, and flow strain rate. It was found that, depending on the system parameters, both mechanisms under-predict the ignition temperature (T_g), while the T_g's predicted by GRI 3.0 are 30 - 60 K lower than those predicted by GRI 2.11, as shown in Fig.8. To further identify the underlying reasons for such discrepancies, detailed ignition response curves were computationally analyzed. A double-turning behavior was observed on the S-curve with GRI 3.0, as shown in Fig. 9. It was further found that the first turning is a radical induced runaway, while the second turning is driven by both chemical branching and thermal feedback, as demonstrated in Fig.10. Sensitivity analysis and computational singular perturbation (CSP) were applied to investigate the species and reactions which lead to radical explosion around the first turning point. Furthermore, both sensitivity and CSP analysis showed the dominate role of $CH_3+HO_2 \rightarrow CH_3O+OH$ in leading to the radical runaway. Experimental investigation of the possible existence of the double turnings is underway.

This work is reported in Publication No. 3.

4. Experimental and Computational Determination of Counterflow Ignition Temperature of Mixtures of Methane and Ethylene

Ethylene is a component in natural gas, and it is more reactive than any alkanes because of the existence of the double bond. Several studies have explored the effectiveness of ethylene as a catalyst for the conversion of methane to higher hydrocarbons. The present study is undertaken to understand the ignition chemistry of CH_4/C_2H_4 mixtures, especially the role of ethylene in facilitating methane ignition. Ignition temperatures were measured with ethylene added to nitrogen-diluted methane, with the mole fraction of methane fixed, as show in Fig.11. It was found that the ignition temperature decreases by about 150 K with 20% ethylene addition, thereby demonstrating that a small amount of ethylene addition to methane indeed promotes methane ignition. Ignition temperatures were computed by using two different mechanisms by Wang, consisting of 70 and 75 species respectively, and were compared with the experimental data (Fig.11). Our further study on this work will focus on: 1) identify the key species and reactions which promote ignition when ethylene is added; 2) analyze the preferential diffusion within the ignition kernel and its role in affecting the ignition temperatures; 3) investigate the pressure and strain rates effects on the ignition temperature.

JOURNAL PUBLICATIONS

[1] "Thermochemical and Kinetic Analysis on the Thermal Decomposition of Monomethylhydrazine: An Elementary Reaction Mechanism", Hongyan Sun and Chung K. Law, *J. Phys. Chem. A.* 2007, ASAP.

[2] "Thermochemical and Kinetic Analysis on the Reactions of O_2 With Products from OH Addition to Isobutene, 2-Hydroxy-1,1-Dimethylethyl and 2-Hydroxy-2-Methylpropyl Radicals: HO_2 Formation From Oxidation of Neopentane, Part II." Hongyan Sun, Joseph W. Bozzelli, and Chung K. Law, *J. Phys. Chem. A.*, 2007, in press.

[3] "On Multiple Criticality in Hydrocarbon Ignition" by Wei Liu and Chung K. Law, Paper No. 2007-1405, 45th AIAA Aerospace Sciences Meeting and Exhibit Online Proceedings, Reno, Nevada, 2007.

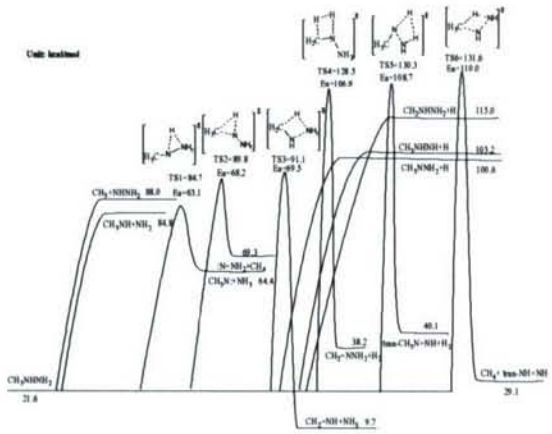

Fig. 1. Potential energy diagram of MMH decomposition calculated at the CBS-QB3 and CCSD(T)/6-311++G(3df,2p)//MPWB1K/6-31+G(d,p) levels.

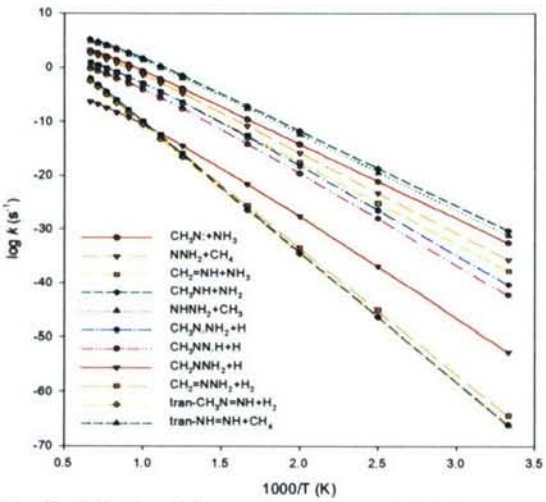

Fig. 2. Calculated thermally activated MMH dissociation rate constants at P = 1 atm.

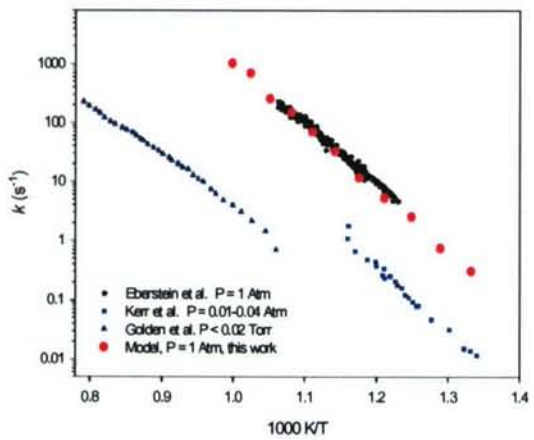

Fig.3. Comparison of the predicted rate constant for overall thermal decomposition of MMH with available experimental data.

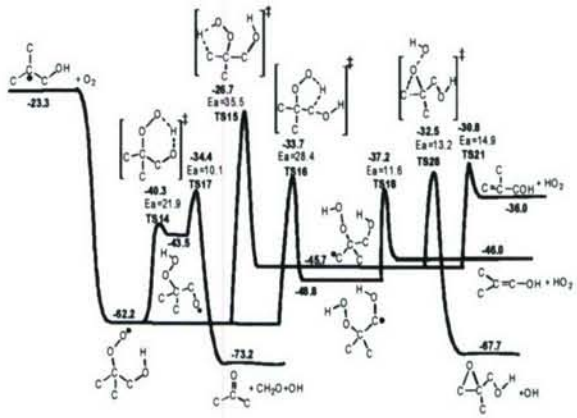

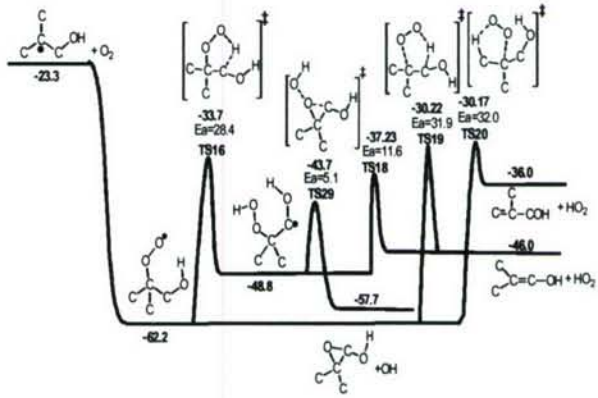

Fig.4. Potential energy diagram for $C_2C{\bullet}COH + O_2$ reaction system calculated at the CBS-Q\\B3LYP level. (Unit in kcal mol^{-1}).

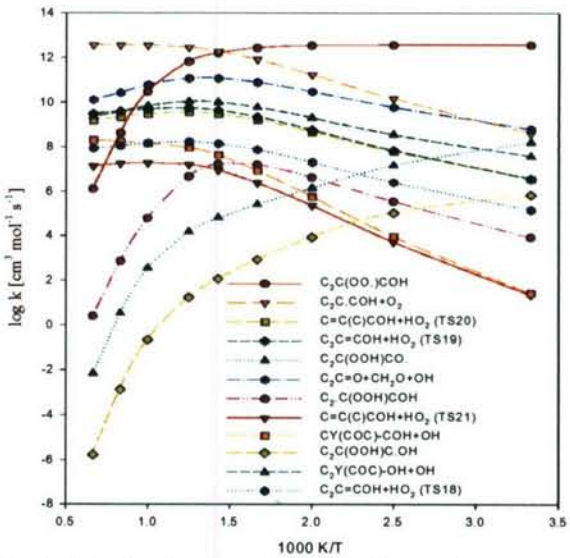

Fig.5. Calculated temperature dependence of rate constants for chemically activated $C_2C{\bullet}COH + O_2$ system at 1 atm.

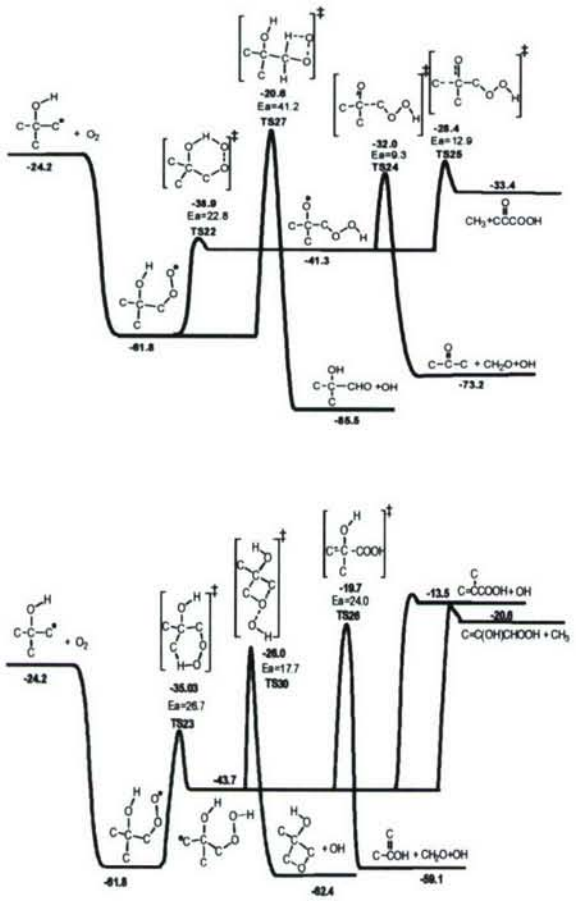

Fig.6. Potential energy diagram for $C_2C(OH)C\bullet + O_2$ reaction system calculated at the CBS-Q\\B3LYP level. (Unit in kcal mol^{-1})

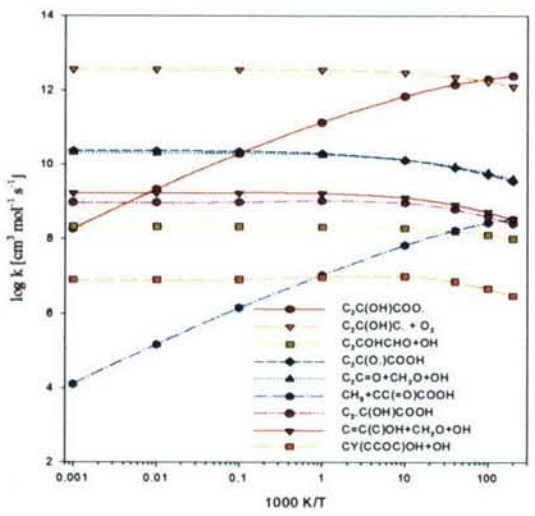

Fig.7. Calculated pressure dependence of rate constants for chemically activated $C_2C(OH)C\bullet + O_2$ system at 1000 K.

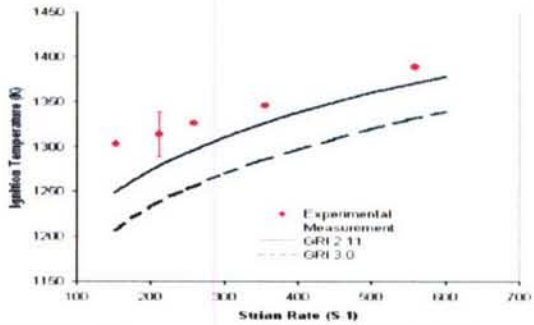

Fig.8. Ignition temperatures of 20% CH_4 in N_2 versus strain rate, at p = 1atm.

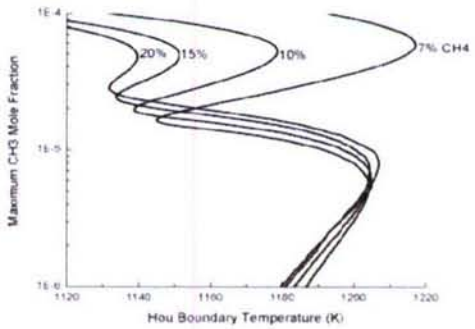

Fig.9. Maximum CH_3 mole fractions as functions of air temperature for various CH_4 concentrations in nitrogen.

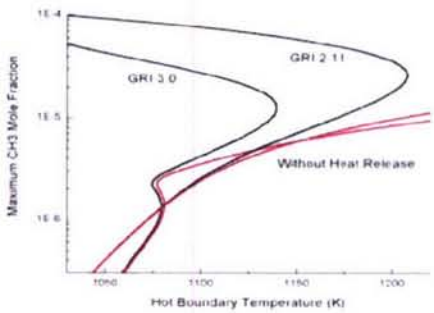

Fig.10. Maximum CH_3 mole fractions as functions of hot air temperatures for 7% CH_4 in N_2, p=3atm, a=150 S^{-1}.

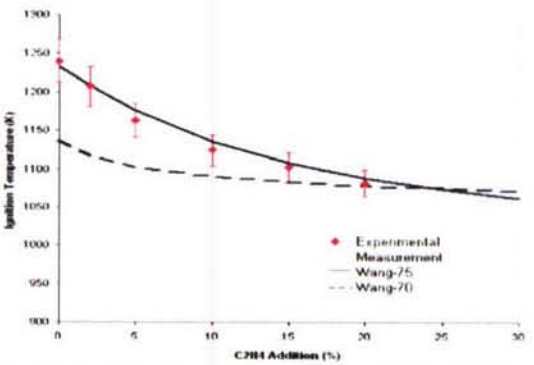

Fig.11. Ignition temperature versus C_2H_4 addition to 20% CH_4 in N_2, p = 3atm, strain rate =300 S^{-1}.

PHYSICAL AND CHEMICAL PROCESS IN FLAMES

(AFOSR Grant No. FA9550-07-1-0052)

Principle Investigator: Chung K. Law

Department of Mechanical and Aerospace Engineering
Princeton University, Princeton, NJ 08544

SUMMARY/OVERVIEW

The objective of the present program is to develop detailed and simplified chemical kinetics models for hydrocarbon combustion, and to understand and quantify the dynamics of flames. During the reporting period progress was made in the following projects: (1) Derived a sufficient and necessary condition for quasi steady state approximation; (2) developed a method of isomer lumping for reduction of large hydrocarbon mechanisms; (3) developed diffusion coefficient reduction through species bundling; (4) developed a 55-species reduced mechanism for n-heptane oxidation; and (5) analyzed the response of stretch-affected premixed flames to flow oscillations.

TECHNICAL DISCUSSION

1. Sufficient and necessary condition for quasi steady state approximation (QSSA)

QSSA is one of the major classical approaches to removing short time scales induced by fast self-depleting intermediate species in detailed mechanisms. Reduced mechanisms based on QSSA facilitated with analytic solution with the method of QSS graph [1] that we developed last year was found to be superior in efficiency and robustness than those obtained through systematic approaches such as computational singular perturbation (CSP) and intrinsic low-dimensional manifold (ILDM), and the classical QSSA with algebraic iterations.

In the reporting year, we further investigated the algorithm for the rigorous identification of QSS species, which is probably the last major problem remained in the QSSA method, and identified the sufficient and necessary condition that a species can be assumed to be in steady state with specified accuracy requirement. The condition was expressed as: $\mathbf{Q}_{i,i} < \varepsilon$, $\mathbf{Q} = \mathbf{A}_{slow}\mathbf{B}_{slow}$, where $\mathbf{Q}$ is the projection matrix to the slow space spanned by vectors $\mathbf{A}_{\text{slow}}$ and $\mathbf{B}_{\text{slow}}$ obtained through eigenvalue decomposition or CSP refinement. This condition was applied to reduce GRI3.0, and a highly accurate 15-step mechanism was derived with less than 10% worst case error, as shown in Figs 1 and 2.

Compared with the previous methods for QSS species identification, such as those based on lifetime analysis, small normalized species net production rates, and small concentrations, the current algorithm rigorously distinguishes the two different types of fast species, that is, the self-depleting species which are good QSS candidates, and the fast species associated with partial equilibrium reactions. The species satisfying the above condition projects only to the fast subspace, such that the species is guaranteed to be self-depleting, and the fast species associated with partial equilibrium reactions is project to both the fast and the slow subspaces because each partial equilibrium reaction involves both a fast and a slow mode.

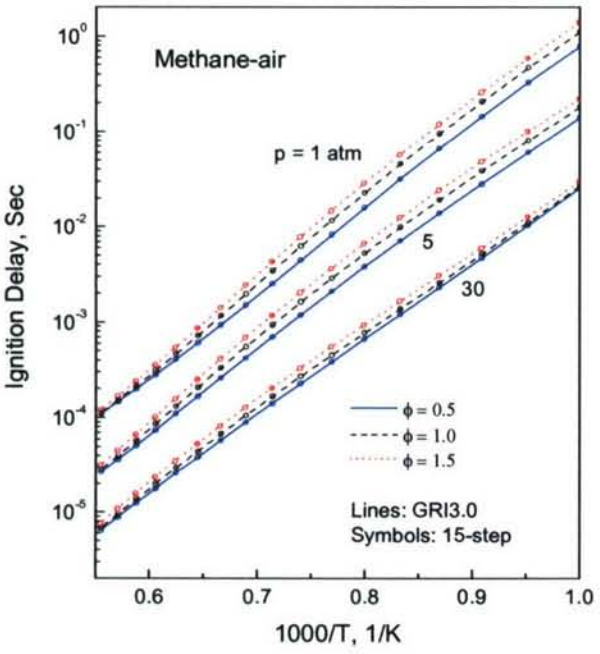

Figure 1

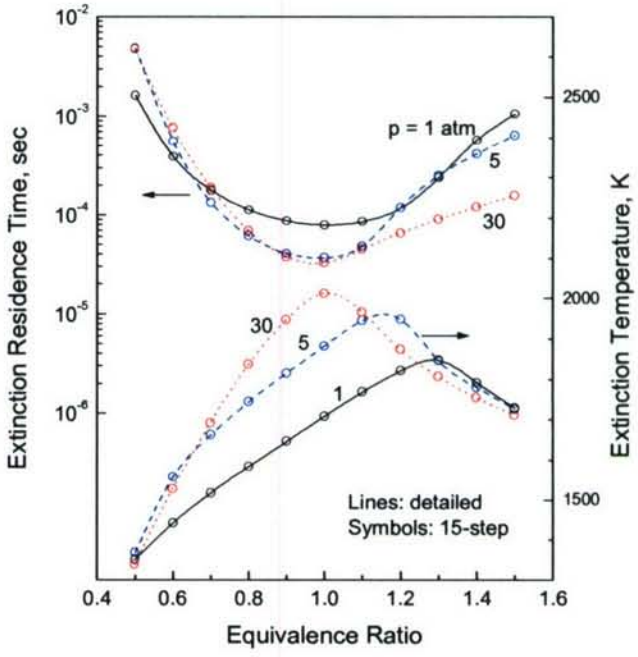

Figure 2

2. Isomer lumping in the reduction of large hydrocarbon mechanisms

The existence of large amount of isomers is a major reason for the large size of detailed or skeletal mechanisms for large hydrocarbon fuels. Such isomers typically have near-identical thermal and transport properties such that they can be lumped in the governing equations with minor accuracy loss, leading to the effective reduction of the number of variables. We have formulated the general approach for isomer lumping, which bundles all the isomers in the same group to a composite species. The intra-group mass fraction for each isomer is retrieved through a regressed function taking as input the temperature, isomer group concentrations and other relevant parameters. The individual isomer concentrations are then employed to evaluate of the chemical source terms.

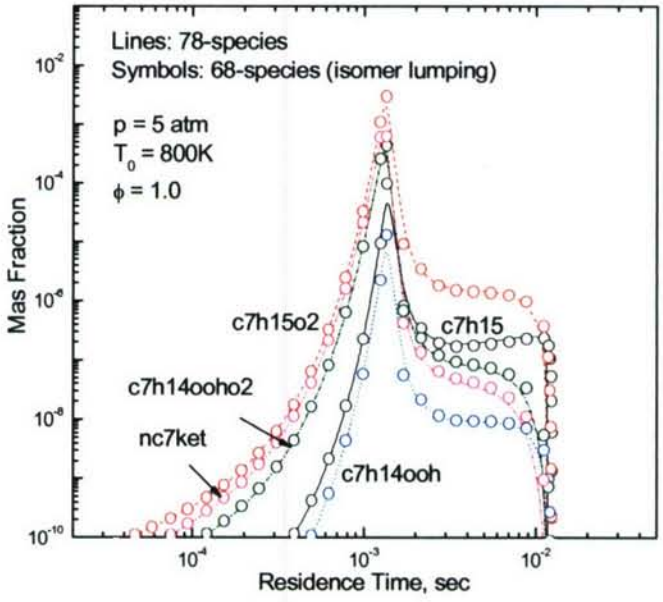

Figure 3

The isomer lumping method was applied to a 78-species skeletal mechanism for n-heptane derived by directed relation graph (DRG) and DRG aided sensitivity analysis (DRGASA) developed previously. The 15 isomers were bundled to 5 groups, resulting in a 68-species reduced mechanism. The intra-group mass fraction of the isomers was accurately approximated by constants, such that the reactions in

the resulting reduced mechanism remain in elementary form. The accuracy of the isomer-bundling approach is demonstrated in Fig. 3.

3. Diffusion coefficient reduction through species bundling

The evaluation of chemical reaction and diffusion terms are two of the most time-consuming components in most combustion simulations. For mechanisms with large number of species, the CPU time for the diffusion evaluation dominates that for chemistry, as shown in Fig. 4. The reduction of diffusion term is therefore crucial for large mechanisms. A systematic approach was developed to bundle species with similar diffusivities to groups, such that the size of the diffusion coefficient matrix can be effectively reduced. Quadratic speedup was achieved for the evaluation of mixture-averaged diffusivity through species bundling. The reduction error was controlled by a user-specified threshold value. The method was successfully applied to various mechanisms for methane, ethylene and n-heptane. It was found that it only needs less than 20 groups to describe the diffusion of a 188-species n-heptane mechanism with about 10% accuracy loss. This result indicates that, with species bundling, the evaluation of the diffusion terms is no longer more time consuming than that of chemistry, as shown by the crossing point in Fig. 4. It is further shown in Fig. 5 that the reduction error dramatically increases when the number of diffusion groups is too small, say less than 3. This result indicates that the conventional unity Lewis number approach is unnecessarily inaccurate in many combustion simulations. The overall time savings by diffusion reduction was found to be significant for simulations with explicit integration solvers or implicit solvers with analytic Jacobian, such as those frequently employed in direct numerical simulations of turbulent flames.

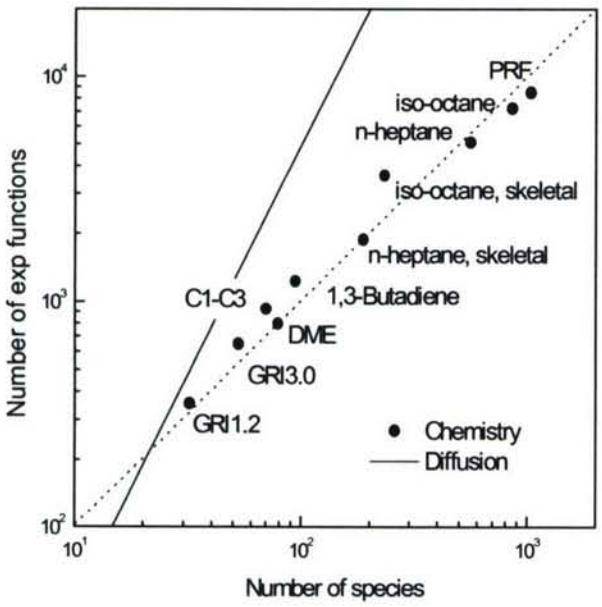

Figure 4

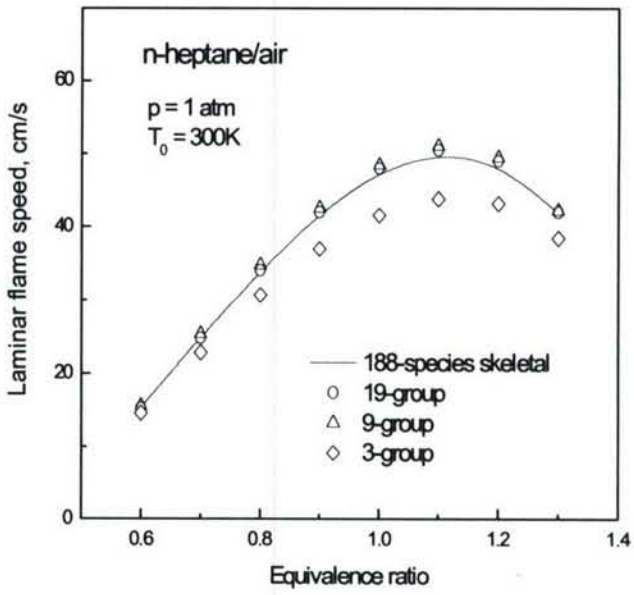

Figure 5

4. A 55-species reduced mechanism for n-heptane oxidation

While mechanisms with about 20 species were found to be adequate to describe small hydrocarbon fuels of C1 and C2, it typically requires much larger mechanisms for the larger

molecules. For example, detailed mechanisms for n-heptane contain up to hundreds of species and thousands of reactions. Such mechanisms for large fuels are crucial for engine and propulsion studies, and the lack of small and accurate reduced mechanisms have severely limited the research in these fields. In the present work, the large n-heptane mechanism from LLNL was reduced by a systematic approach that integrates a suite of methodologies developed previously as well as those presented in the above three sections. Specifically, a 188-species skeletal mechanism was derived with DRG. Since DRG is reliable and highly efficient, it is an ideal choice to quickly bring down the large mechanisms to a size which can be handled by other reduction methods. A 78-species skeletal mechanism was next derived by DRGASA, a 68-species through isomer-lumping, and a 55-species reduced mechanism through QSSA. Finally, the 55 species were then bundled to 14 diffusive groups. Mechanisms of such sizes are already feasible for many 2-D or even 3-D simulations in parallel computing environment. The reduced mechanisms were extensively validated for both ignition and extinction applications, as shown in Figs. 6 and 7. Further validation in premixed flames shows that the flame speeds are over-predicted for all the reduced mechanisms as compared to the counterflow experiment results, as shown in Fig. 8. This discrepancy is likely to be inherited from the detailed mechanism, which has not been validated in premixed flames due to its large size. The reduced mechanisms therefore are efficient starting points for identification and modification of the reaction pathways that induced inaccuracies in diffusive systems.

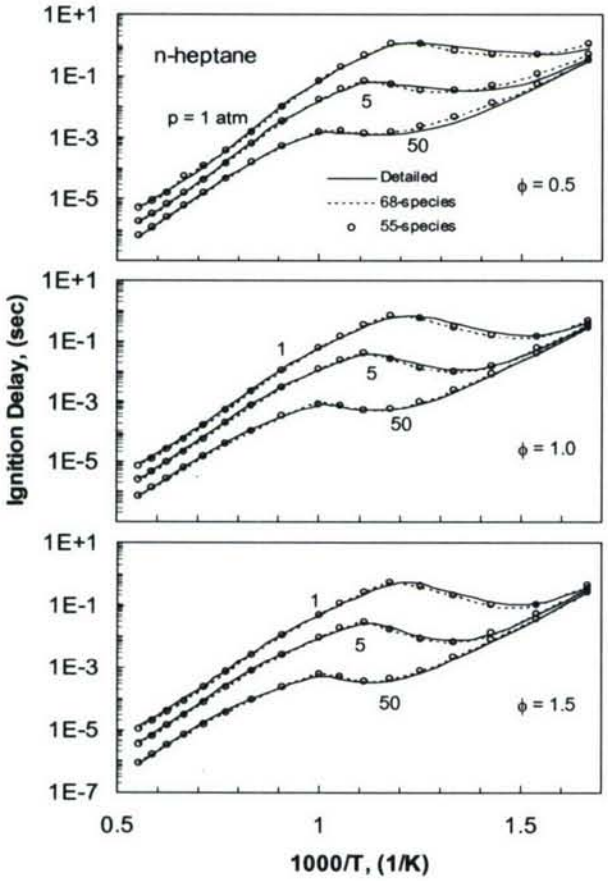

Figure 6

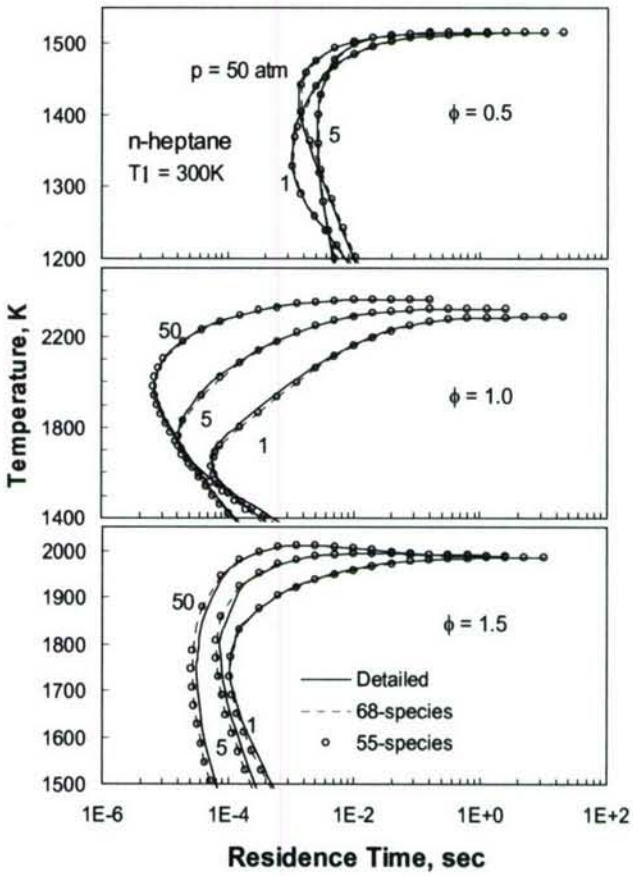

Figure 7

5. Response of stretch-affected premixed flames to flow oscillations.

Self-induced oscillations that are combustion driven are frequently encountered in combustion systems that operated at lean premixed conditions to reduce NO_x emissions. These oscillations result from the resonant coupling between the unsteady combustion heat release and natural acoustic modes of the combustor, and could be harmful to the system hardware and performance. Consequently, it is important to determine the response of heat release to acoustic modulations.

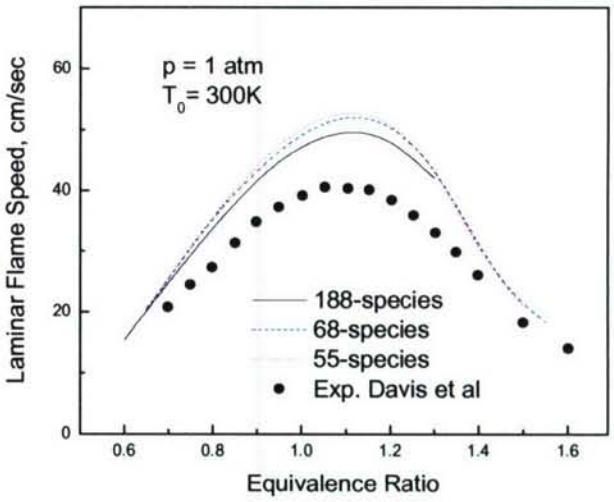

Figure 8

Different from previous investigations, the present study considers the effects of flame stretch manifested as variations in the local flame speed along the wrinkled flame front. Such variations are believed to be responsible for the experimentally observed damping of the flow oscillation-induced flame surface wrinkling which cannot be explained by the constant flame speed assumption. Since combustion heat release is determined by the integration of the local flame speed over the entire flame surface area, the direct effect of flame stretch on the flame speed and its indirect effect through the modulation of the flame shape, and thereby flame surface area, are expected to affect substantially the overall heat release rate.

The flame stretch effects on the unsteady heat release are studied through the transfer function, defined as the ratio of the normalized fluctuation of heat release rate to that of velocity. Results obtained from analyzing the G-equation show that the effects of flame stretch are mainly characterized by a Markstein number, $\hat{\sigma}_C$, and a Strouhal number, St_f, which measure the effects of flame stretch and the oscillation frequency, respectively. Flame stretch is found to become important when the oscillation frequency satisfies $\hat{\sigma}_C St_f^2 \sim O(1)$, i.e. $St_f \sim O(\hat{\sigma}_C^{-1/2})$, while the constant flame speed approximation adopted in previous studies is only valid for frequencies below this order. When the oscillation frequencies are of this order, the unsteady heat release is contributed mostly from fluctuations of the flame surface area, which is now affected by stretch. Finally, as the oscillation frequency increases to $St_f \sim O(\hat{\sigma}_C^{-1})$, i.e. $\hat{\sigma}_C St_f \sim O(1)$, the direct contribution from the stretch-affected flame speed fluctuation to the unsteady heat release becomes comparable to that of the flame surface area. This trend is clearly demonstrated in Fig. 9, where G_A and G_S are the transfer

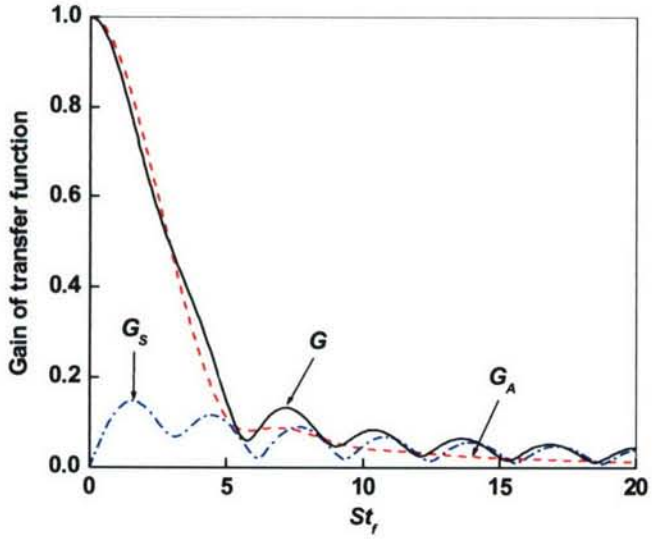

Figure 9

functions contributed from the fluctuations of flame surface area and flame speed, respectively, $G=G_S+G_A$ is the total transfer function, and we have adopted $\hat{\sigma}_C = 0.05$. It is seen that at small frequencies ($St_f < 5 \sim O(\hat{\sigma}_C^{-1})$) the overall transfer function G can be approximately represented by G_A, whereas at large St_f, G follows closely the trend of G_S, indicating that contributions from fluctuations of the flame surface area and flame speed dominate at small and large frequencies, respectively.

The present study phenomenologically explains the experimentally observed damping phenomenon of flame wrinkling in which the flame wrinkles developed at the flame base decay along the flame surface. This work gives us further understanding about the entire coupling processes in the development of combustion-driven oscillations, and hence will help us to propose schemes to prevent the oscillation-induced hardware failures from happening.

JOURNAL PUBLICATIONS

1. Lu T. F., and Law C. K., "A Systematic approach to obtain analytic solution of quasi steady state species in reduced mechanisms", *J. Phys. Chem. A*, 110(49) 13202-13208, 2006.
2. Law, C.K., Makino, A., and Lu, T.F., "On the off-stoichiometric peaking of adiabatic flame temperature with equivalence ratio", *Combustion and Flame*, 145(4) 808-819, 2006.
3. Lu T. F., and Law C. K., "On the applicability of directed relation graph to the reduction of reaction mechanisms," *Combustion and Flame*, 146(3) 472-483, 2006.
4. Zheng X. L., Lu T. F., and Law C. K., "Experimental counterflow ignition temperatures and reaction mechanisms of 1,3-butadiene," *Proceedings of the Combustion Institute,* 31(1) 367-375, 2007.
5. Sankaran R., Hawkes E. R., Chen J. H., Lu T. F. and Law C. K., "Structure of a spatially-developing turbulent lean methane-air Bunsen flame," *Proceedings of the Combustion Institute,* 31(1) 1291–1298, 2007.
6. Lu, T. F., and Law, C. K., "Diffusion coefficient reduction through species bundling," *Combust. Flame*, 148(3) 117-126, 2007.
7. Egolfopoulos, F.N., Holley, A.T., and Law, C.K., "An assessment of the lean flammability limits of CH4/air and C3H8/air mixtures at engine-like conditions," *Proceedings of the Combustion Institute*, 31(2) 3015-3022, 2007.

GLOBAL COMBUSTION PROPERTIES OF SURROGATE AERO-FUEL COMPONENTS

Grant Number: W911NF-06-1-0155

Principal Investigator: Chih-Jen Sung*

Department of Mechanical and Aerospace Engineering
Case Western Reserve University
Cleveland, Ohio 44106

SUMMARY/OVERVIEW:

This study involves the development of a detailed database of global combustion properties for some key components of surrogate jet fuels through experimentation using a counterflow burner system and a rapid compression machine facility. The experimental data will be subsequently utilized to develop detailed and reduced kinetic mechanisms capable of predicting the combustion characteristics of jet fuels and their surrogates, which can be integrated into computational fluid dynamic codes for combustor simulations.

TECHNICAL DISCUSSION:

This research program aims at developing extensive experimental database and kinetic models for jet fuels and the associated surrogates. Experiments are performed for measuring the global combustion properties of premixed flames, such as laminar flame speeds and extinction stretch rates, in a counterflow burner system, and ignition delays at elevated pressures in a rapid compression machine (RCM). In order to obtain reliable experimental data, both experimental setups have been extensively characterized to ensure that the challenges associated with the handling of liquid hydrocarbon fuels are properly addressed. In contrast to gaseous fuels, experimentation using high-boiling-point liquid hydrocarbons, which are relevant to jet surrogates, poses significant challenges due to their low vapor pressure. While careful preheating is needed for preparing a homogeneous premixture of fuel/oxidizer and avoiding condensation within the mixture delivery system, fuel cracking/pyrolysis may become significant at higher preheat temperatures. Furthermore, due to large density differences between heavy hydrocarbon fuel and oxidizer, stratification may occur in the prepared mixture if proper mixing is not ensured. In the case of apparatus involving a continuous flow system, such as in the counterflow burner system, a transient period is noted before the resulting mixture composition reaches the desired set value. In order to provide experimental data of high fidelity, we systematically developed and characterized our mixture preparation and delivery system that avoids all such sources of error when dealing with liquid fuels. This has led to significant improvements in our experimental facilities. Thereafter, investigations [1-3] using these facilities have focused on the combustion characterization of *n*-decane, *n*-dodecane, and toluene, which are recognized as

* TEL: (216) 368-2942; FAX: (216) 368-6445; E-MAIL: cjs15@case.edu.

relevant components for formulating jet fuel surrogates. Further kinetic simulations have highlighted the deficiencies of literature mechanisms in predicting the combustion characteristics of all three neat fuel components.

During the reporting period, progress has been made in the following projects: (1) laminar flame speeds and extinction limits of preheated *n*-decane/O_2/N_2 and *n*-dodecane/O_2/N_2 mixtures; (2) autoignition of toluene and benzene at elevated pressures in a rapid compression machine; and (3) autoignition of *n*-decane under high pressure conditions.

1. Laminar Flame Speeds and Extinction Limits of Preheated n-Decane/O_2/N_2 and n-Dodecane/O_2/N_2 Mixtures

Laminar flame speeds of *n*-decane/air and *n*-dodecane/air mixtures were measured using the counterflow twin-flame configuration at preheat temperatures ranging from 360 to 470 K and equivalence ratios ranging from 0.7 to 1.4. Here, 'air' was synthesized by mixing oxygen and nitrogen in the molar ratio of 1:3.76. Extinction stretch rate measurements as a function of equivalence ratio were also carried out for fuel/O_2/N_2 mixtures with $[N_2/(O_2+N_2)]$=0.84 by mole and preheat temperature of 400 K. All experiments were conducted under atmospheric pressure conditions. The experimental data for laminar flame speeds and extinction stretch rates were also simulated using chemical kinetic mechanisms available in the literature.

The measured laminar flame speeds of *n*-decane/air mixtures as a function of equivalence ratio for three different mixture preheat temperatures, T_u=360, 400, and 470 K, are shown in Fig. 1. Figure 1 also compares the present flame speed data with the computed values using two published reaction mechanisms. The experimental data for *n*-dodecane/air mixtures along with the computed values are shown and compared in Fig. 2. Two different unburned mixture temperatures, T_u=400 and 470 K, were studied. Figures 3 and 4 show comparisons of experimental and simulated extinction stretch rates for *n*-decane/O_2/N_2 and *n*-dodecane/O_2/N_2 mixtures, respectively.

While the kinetic mechanisms for *n*-decane [4,5] are seen to predict the laminar flame speeds satisfactorily at some equivalence ratios, noticeable discrepancies are identified. Comparison of the experimental and computed laminar flame speeds of *n*-dodecane/air mixtures at varying preheat temperatures shows significant over-prediction by the mechanism of [6]. Furthermore, the measured extinction stretch rate data for both fuels are lower than the predicted values for all the kinetic mechanisms used, as shown in Figs. 3 and 4, although the trend is well predicted, with the extinction stretch rate peaking at ϕ~1.4. This rich-shift is cause by the combined effects of positive stretch and sub-unity Lewis number for fuel rich mixtures.

This work is reported in Ref. [1].

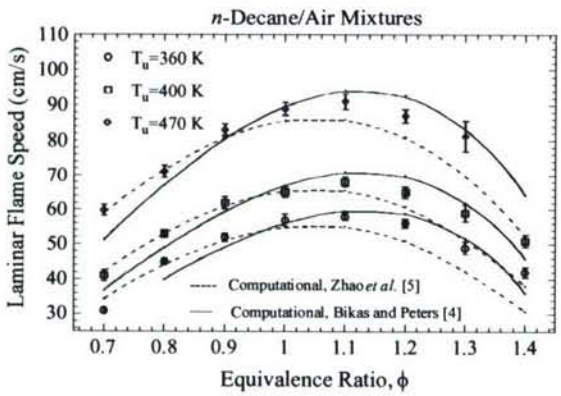

Figure 1: Experimental (symbols) and computed (lines) laminar flame speeds of *n*-decane/air mixtures with unburned mixture temperatures of 360, 400, and 470 K.

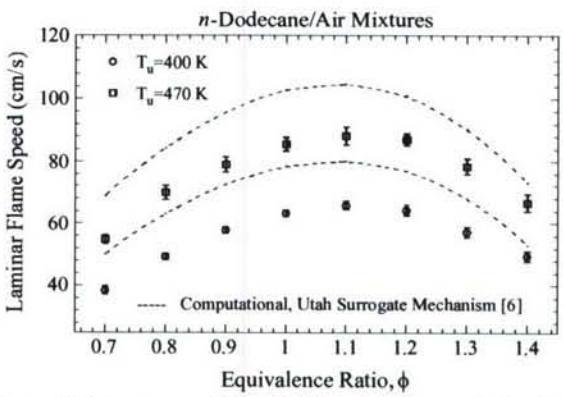

Figure 2: Experimental (symbols) and computed (dashed lines) laminar flame speed of *n*-dodecane/air mixtures with unburned mixture temperatures of 400 and 470 K.

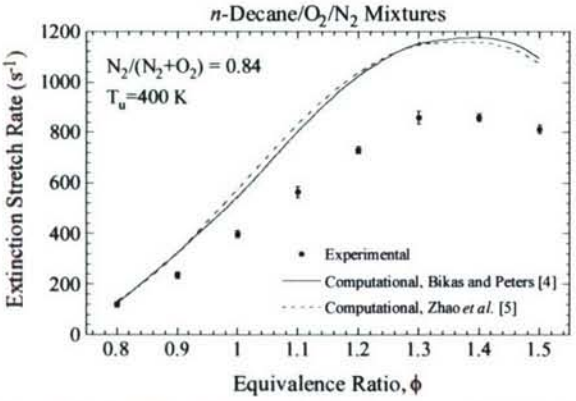

Figure 3: Experimental (symbols) and computed (lines) extinction stretch rates of *n*-decane/O_2/N_2 mixtures.

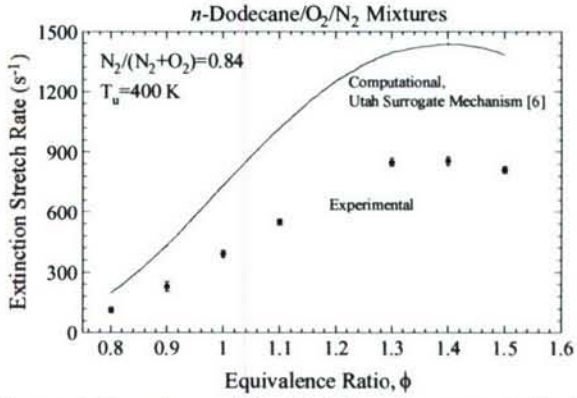

Figure 4: Experimental (symbols) and computed (line) extinction stretch rates of *n*-dodecane/O_2/N_2 mixtures.

2. *Autoignition of Toluene and Benzene at Elevated Pressures in a Rapid Compression Machine*

Autoignition of toluene and benzene was investigated in a rapid compression machine at conditions relevant to engine combustion [2]. Experiments were conducted for homogeneous mixtures over a range of equivalence ratios at compressed pressures, P_C, from 25 to 45 bar and compressed temperatures, T_C, from 920 to 1100 K. Figures 5 and 6 present the measured ignition delay times for toluene/O_2/inert and benzene/O_2/inert mixtures in the molar ratios of 1/9/94 and 1/7.5/95.5, respectively, at P_C near 45 bar as a function of the inverse of T_C, along with simulations using various available mechanisms. The inert portion of the mixture comprised of nitrogen and argon. Significant discrepancies between the experimental and computed results were noted. Experimental results by varying oxygen concentration, while keeping the mole fraction of fuel constant, revealed a strong influence of oxygen in promoting ignition. Reaction flux analysis was also conducted to identify the dominant reaction pathways and the reactions responsible for the mismatch of experimental and simulated data.

This work is reported in Ref. [2].

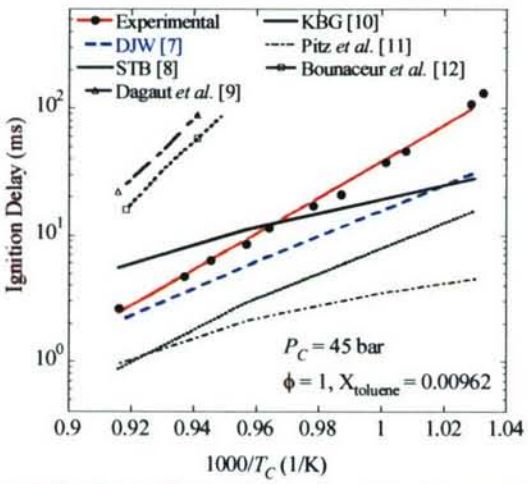

Figure 5: Comparison of experimental and computed ignition delays for stoichiometric toluene/O_2/inert mixtures. Toluene mole fraction, $X_{toluene}$, is 0.00962.

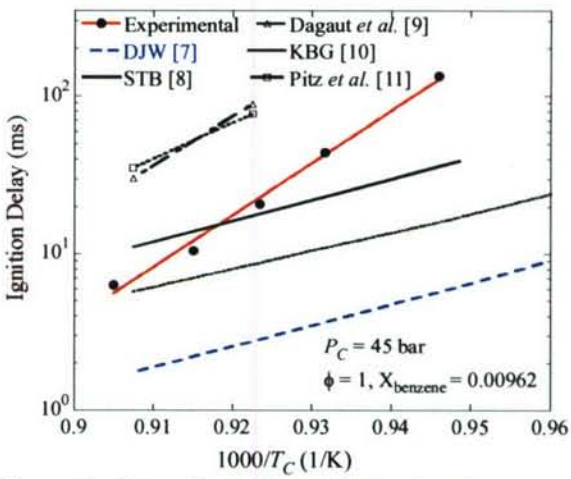

Figure 6: Comparison of experimental and computed ignition delays for stoichiometric benzene/O_2/inert mixtures. Benzene mole fraction, $X_{benzene}$, is 0.00962.

3. *Autoignition of n-Decane under High Pressure Conditions*

An experimental investigation of the autoignition delay times for *n*-decane/air mixtures was conducted using a heated rapid compression machine [3]. In the present investigation, while the

equivalence ratio was fixed at ϕ=0.8, the compressed pressures and temperatures were in the range of P_C=7–30 bar and T_C=630–706 K, respectively. The current experiments span a temperature range not fully investigated in previous autoignition studies on *n*-decane. Two-stage ignition was observed over the entire range of conditions investigated. Figure 7 shows representative pressure traces illustrating the effect of variation in T_C at P_C=14.3 bar. Figure 8 presents a comparison of the present experimental data with those of Pfahl *et al.* [13] and Zhukov *et al.* [14] under similar pressure conditions, albeit for slightly different equivalence ratios. This plot serves to demonstrate the fact that the current experiments have been conducted in a temperature range not investigated earlier, and that the current data are consistent with the few known sources for *n*-decane autoignition. Therefore, the experimental data obtained from the present investigation constitute valuable targets for validation and development of kinetic mechanisms for jet fuel surrogates.

This work is reported in Ref. [3].

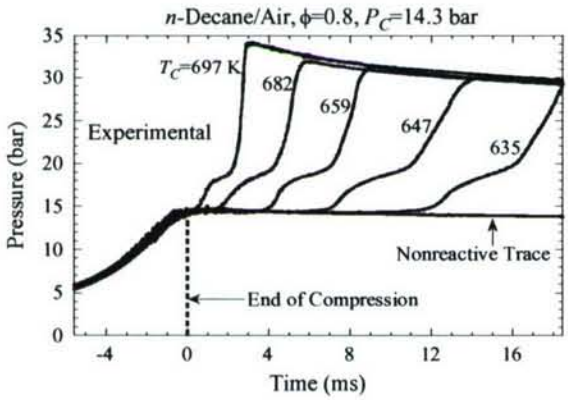

Figure 7: Experimentally obtained pressure traces for varying values of T_C, P_C=14.3 bar

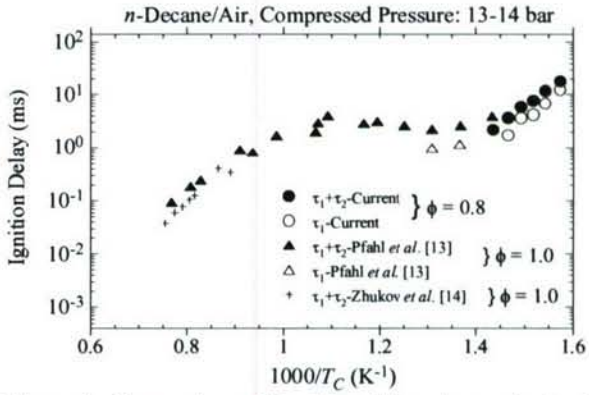

Figure 8: Comparison of ignition delay times obtained from the present RCM with literature data.

REFERENCES:

1. K. Kumar, C.J. Sung, "Laminar Flame Speeds and Extinction Limits of Preheated *n*-Decane/O_2/N_2 and *n*-Dodecane/O_2/N_2 Mixtures," Combust. Flame, in press.
2. G. Mittal, C.J. Sung, "Autoignition of Toluene and Benzene at Elevated Pressures in a Rapid Compression Machine," Combust. Flame, in press.
3. K. Kumar, G. Mittal, C.J. Sung, "Autoignition of *n*-Decane under High Pressure Conditions," 5th US Combustion Meeting, San Diego, CA, 2007.
4. G. Bikas, N. Peters, Combust. Flame 126 (1-2) (2001) 1456–1475.
5. Z. Zhao, J. Li, A. Kazakov, F.L. Dryer, Combust. Sci. Tech. 177 (1) (2005) 89–106.
6. H. Zhang, Personal Communication, University of Utah, January 18, 2005.
7. Z.M. Djurisic, A.V. Joshi, H. Wang, 2nd Joint Meeting of the U.S. Sections of the Combustion Institute, Oakland, CA, Paper 238, 2001.
8. R. Sivaramakrishnan, R.S. Tranter, K. Brezinsky, Proc. Combust. Inst. 30 (2005) 1165–1173.
9. P. Dagaut, G. Pengloan, A. Ristori, Phys. Chem. Chem. Phys. 4 (2002) 1846–1854.
10. S. Klotz, K. Brezinsky, I. Glassman, Proc. Combust. Inst. 27 (1998) 337–344.
11. W.J. Pitz, R. Seiser, J.W. Bozzelli, K. Seshadri, C.-J. Chen, I. Da Costa, R. Fournet, F. Billaud, F. Battin-Leclerc, C.K. Westbrook, Report No. UCRL-CONF-201575, Lawrence Livermore National Laboratory, 2004.
12. R. Bounaceur, I. Da Costa, R. Fournet, F. Billaud, F. Battin-Leclerc, Int. J. Chem. Kinet. 37 (2005) 25–49.
13. U. Pfahl, K. Fieweger, G. Adomeit, Proc. Combust. Inst. 26 (1996) 781–789.
14. V.P. Zhukov, V.A. Sechenov, A. Yu. Starikovskii, Thirty-First International Symposium on Combustion, Work in Progress Poster Session.

AUTOIGNITION AND COMBUSTION OF DIESEL AND JP-8

(Grant/Contract Number 45241-EG)

Principal Investigator: Dr. Kalyanasundaram Seshadri

Department of Mechanical and Aerospace Engineering
University of California at San Diego, La Jolla, California 92093

SUMMARY/OVERVIEW:

Experimental studies are carried out to characterize non premixed combustion of jet fuels and a number of its surrogates in laminar flows. The counterflow configuration is employed. Critical conditions of extinction and autoignition are measured for JP-8, Jet-A, and Fisher Tropsch (FT) JP-8. Fifteen surrogates of JP-8 and one surrogate of FT JP-8 are tested. It is found that critical conditions of extinction and autoignition of JP-8 and Jet-A are similar, while FT JP-8 is more reactive than JP-8 and Jet-A. Among the surrogates tested, the Aachen surrogate made up of *n*-decane (80 %) and trimethylbenzene (20 %) by liquid volume, and the UCSD surrogate made up of *n*-dodecane (60 %), methylcyclohexane (20 %), and *o*-xylene (20 %) by liquid volume best reproduce extinction and autoignition characteristics of JP-8. A surrogate made up of *n*-decane (60 %) and iso-octane (40 %) by liquid volume best reproduces the combustion characteristics of FT JP-8.

TECHNICAL DISCUSSION:

An experimental investigation is carried out with the aim of developing appropriate surrogates for JP-8 and Fisher Tropsch (FT) JP-8. The counterflow configuration is employed. Critical conditions of extinction and autoignition are measured. The burner used in the experiments has two ducts: the fuel-duct and the oxidizer-duct. Prevaporized fuel and nitrogen is injected from the fuel-duct, and air is injected from the oxidizer-duct. The mass fraction of fuel, the temperature, and the component of the flow velocity normal to the stagnation plane at the exit of the fuel-duct are represented by $Y_{F,1}$, T_1, and V_1, respectively. The mass fraction of oxygen, the temperature, and the component of the flow velocity normal to the stagnation plane at the exit of the oxidizer-duct are represented by $Y_{O_2,2}$, T_2, and V_2, respectively. The strain rate, is calculated using the densities and velocities of the reactant streams at the exit of the ducts. Critical conditions of extinction and autoignition depend on the strain rate, and temperatures and composition of the reactants. The extinction experiments are carried out with $T_1 = 473\ (\pm 10)\,\mathrm{K}$, $T_2 = 298\,\mathrm{K}$, and $Y_{O_2,2} = 0.233$ (air). The strain rate at extinction, $a_{2,e}$, is measured as a function of $Y_{F,1}$. Critical conditions of autoignition are measured with $T_1 = 473\,\mathrm{K}$, $Y_{O_2,2} = 0.233$ (air). Two sets of measurements are obtained. In one set $Y_{F,1}$ is maintained at a constant value of 0.4. The value of T_2 is recorded for various values of the strain rate at autoignition, $a_{2,I}$. In the other set the strain rate, a_2 is maintained at a constant value of $550\,\mathrm{s}^{-1}$. Here

the value of T_2 is measured for various values of $Y_{F,1}$. The experimental accuracy of the measured value of T_2 is $\pm 30\,K$ and that of the strain rate is $\pm 7\,\%$ of recorded value.

The fuels tested are:

- Multicomponent fuels:
  1. JP-8 (obtained from China Lake), JP-8 POSF 4177 (obtained from Wright Patterson Air Force Base (WPAFB)), JP-8 POSF 3773 (obtained from WPAFB).
  2. Jet-A (obtained from San Diego Airport), Jet-A POSF 3602 (obtained from WPAFB) , Jet-A POSF 3638 (obtained from WPAFB), Blend POSF 4658.
  3. Fisher Tropsch JP-8 (obtained from WPAFB).
- Fuel mixtures (liquid volume): Possible surrogates of JP-8:
  1. Surrogate A: 60 % *n*-decane, 20 % methylcyclohexane, 20 % toluene. $H/C = 1.93$.
  2. Surrogate B: 60 % *n*-decane, 20 % methylcyclohexane, 20 % *o*-xylene. $H/C = 1.93$.
  3. Surrogate B1: 60 % *n*-decane, 20 % methylcyclohexane, 15 % *o*-xylene, 5 %1-methylnaphthalene.
  4. Surrogate C (UCSD surrogate): 60 % *n*-dodecane, 20 % methylcyclohexane, 20 % *o*-xylene. $H/C = 1.92$.
  5. Surrogate C1 : 60 % *n*-dodecane, 20 % methylcyclohexane, 15 % *o*-xylene, 5 %1-methylnaphthalene.
  6. Surrogate D: *n*-decane 50 %, butylcyclohexane 25 %, butylbenzene 25 %. $H/C = 1.92$.
  7. Surrogate E: *n*-decane 34 %, butylcyclohexane 33 %, butylbenzene 33 %. $H/C = 1.84$.
  8. Surrogate F: *n*-decane 60 %, butylcyclohexane 20 %, butylbenzene 20 %. $H/C = 1.97$.
  9. Aachen Surrogate: *n*-decane 80 %, trimethylbenzene 20 %. $H/C = 1.99$.
  10. Modified Aachen Surrogate: *n*-dodecane 80 %, trimethylbenzene 20 %. $H/C = 1.97$.
  11. Surrogate N1: *n*-decane 80 %, propylbenzene 20 %.
  12. Surrogate N2: *n*-decane 70 %, propylbenzene 30 %.
  13. Drexel Surrogate 1: *n*-dodecane 26 %, iso-cetane 36 %, methylcyclohexane 14 %, decaline 6 %, and 1-methylnaphthalene 18 %. $H/C = 1.82$.
  14. Drexel Surrogate 2: *n*-dodecane 43 %, iso-cetane 27 %, methylcyclohexane 15 %, and 1-methylnaphthalene 15 %. $H/C = 1.87$.

15. Utah Surrogate: n-dodecane 30 %, n-tetradecane 20 %, iso-octane 10 %, methylcyclohexane 20 %, o-xylene 15 %, and tetraline 5 %. $H/C = 1.93$.

- Fuel Mixtures (liquid volume). Possible surrogate of F-T JP-8.

1. Surrogate G: n-decane 60 %, iso-octane 40 %. $H/C = 2.22$.

The surrogates of JP-8 are ranked employing the following criteria listed in the order of importance: (1) how well they reproduce critical conditions of autoignition, (2) how close is the hydrogen to carbon ratio to that of JP-8, (3) simplicity (availability of chemical kinetic mechanisms), and (4) how well they reproduce critical conditions of extinction. Using this criteria the surrogates are listed in the following order:

1. Aachen Surrogate,
2. Surrogate C, Surrogate C1, Surrogate B1.
3. Drexel Surrogate 2, and Modified Aachen Surrogate.

Overall the Aachen surrogate and Surrogate C (UCSD surrogate) appear to best reproduce the combustion characteristics of JP-8. Surrogate G reproduces the combustion characteristics of F-T JP-8.

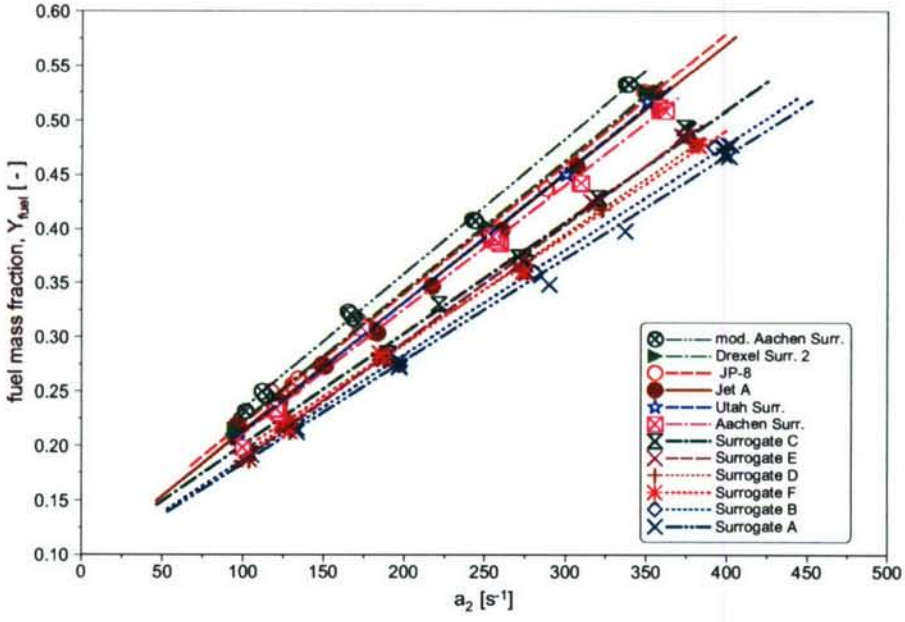

Figure 1: The mass fraction of fuel, $Y_{F,1}$, as a function of the strain rate at extinction. The symbols represent experimental data, and the lines are best fits to experimental data. The figure compares extinction characteristics of various surrogates of JP-8.

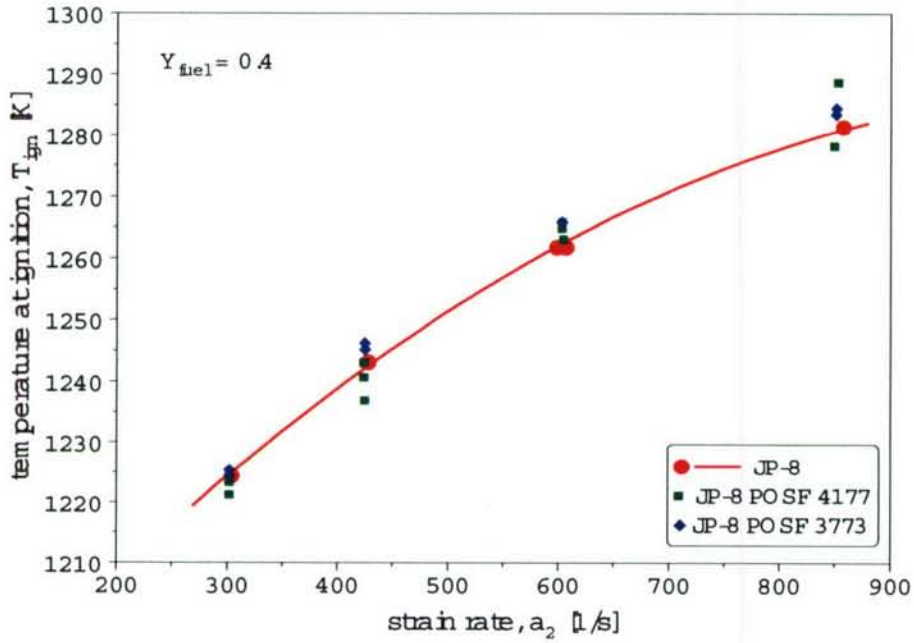

Figure 2: The temperature of the oxidizer stream at autoignition, as a function of the strain rate at fixed values of $Y_{F,1} = 0.4$. The symbols are experimental data. The lines are best fit. The figure compares of autoignition characteristics of various batches of JP-8.

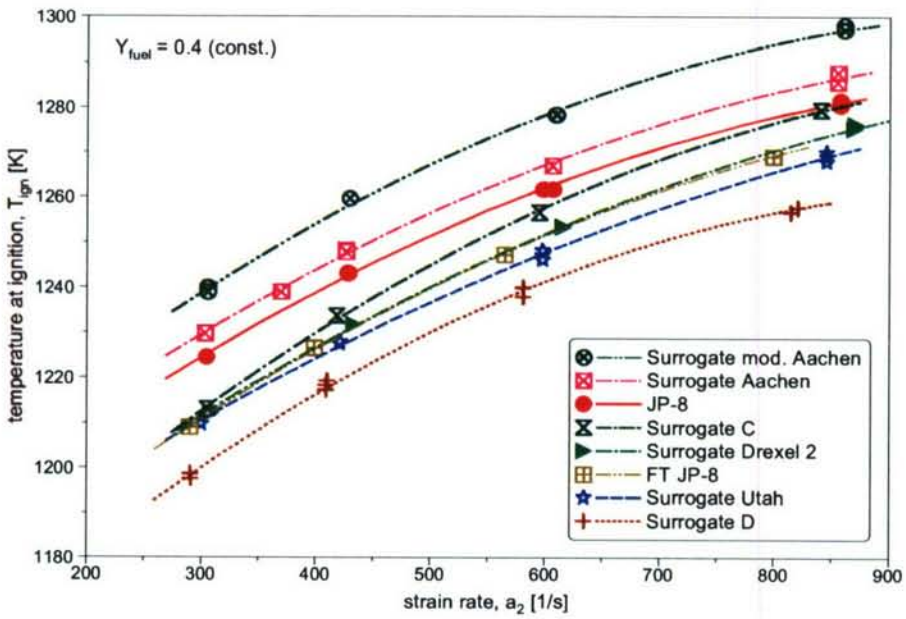

Figure 3: The temperature of the oxidizer stream at autoignition, as a function of the strain rate at fixed values of $Y_{F,1} = 0.4$. The symbols are measurements. The lines are best fit. The figures compares autoignition characteristics of various surrogates of JP-8.

SOOT SURFACE TEMPERATURE AND SPECIES CONCENTRATION MEASUREMENTS IN HIGH-PRESSURE DIFFUSION FLAMES

(Grant/Contract Number: W911NF-05-1-0060)

Principal Investigator: William L. Roberts

Department of Mechanical and Aerospace Engineering
North Carolina State University
Campus Box 7910, Raleigh, North Carolina 27695

SUMMARY/OVERVIEW:

Diesels are the most efficient internal combustion engine available, and thus continue to be the US Army's primary engine for both propulsion and power generation. Through several studies it has been determined that pressure has a direct effect on the peak temperature and species concentrations which both effect the kinetics of soot formation. Previous research by others has focused on atmospheric and sub-atmospheric studies, while this work has focused on high-pressure flames, pressures approaching those observed in Diesel engines. Smoke points and temperature profiles have been measured, at atmospheric and elevated pressures, in a laminar, steady co-flow diffusion flame. Measurement of species concentrations, via sampling and GC-MS, is currently underway in these high-pressure flames, with particular attention being paid to concentrations of acetylene and benzene. With these three measurements, the chemical kinetics and the role of transport with regard to soot formation and oxidation at high pressures can be better understood. With this increased understanding, the overall goal of reducing soot emissions may be accomplished, leading to enhanced survivability through smaller thermal signatures.

TECHNICAL DISCUSSION

Specific Third Year Objectives

The objectives for the third twelve months of this effort were: (1) complete soot surface temperature measurements, in both undiluted and diluted flames, at and above atmospheric pressure; (2) design, build, and test a microprobe for extracting samples from the flame front for species concentrations analyses and make needed burner and vessel modifications in order to use the microprobe; (3) develop methodology for measuring acetylene and benzene concentrations with the GC-MS, and calibrate appropriately; (4) make species concentration measurements; and (5) begin measuring radical species concentrations using Li/LiOH reversal technique.

Experimental Apparatus

The apparatus used for this experiment is a classic over-ventilated Burke-Schumann flame inside a water-cooled pressure vessel that is rated at pressures up to 30 atmospheres. Surrounding the 4.4 mm fuel tube is a 65 mm co flow, and this is all housed in a quartz chimney

that is 400 mm tall. A ceramic honeycomb insert is used to straighten the air co-flow surrounding the fuel tube. The fuel tube is filled with super fine grit steel wool to make the fuel flow rate less sensitive to pressure fluctuations upstream. The addition of this steel wool flow straightener in the fuel tube turns out to be critical in the behavior of the smoke point with dilution and pressure. To ignite the flame within the pressure vessel, an electrode is installed and used to produce a spark against the lip of the fuel tube. The vessel has three non-intrusive glass windows to allow for optical viewing and diagnostics. Due to the high sooting tendencies of the fuels used, and the effect pressure has on these tendencies, the vessel has air ports at the windows to purge the area and prevent soot accumulation on the window surface.

The above mentioned set-up of the burner and quartz chimney (which was used for the soot surface temperature measurements) needed changes in order to accommodate the use of the stainless steel microprobe for species concentration measurements. Although the fuel tube and the air co-flow portions of the burner stayed identical, a new quartz chimney was designed. The quartz chimney had an outside diameter of 71 mm and a wall thickness of 3 mm, and was 400 mm tall. The chimney had a laser-cut elliptical opening cut into one wall that is 6.4 mm wide and 200 mm long in order to allow the microprobe access to the flame over a range of heights. To avoid potential flow-induced oscillations from vessel air entering the chimney, two shields were made. These quartz pieces fit up against the chimney and had a 6.4 mm diameter hole drilled into them (at two different heights).

The microprobe was constructed out of stainless steel based on research by [1], which showed very little difference between using stainless steel as opposed to quartz for species concentration sampling. The microprobe consisted of two pieces of stainless steel tubing: a long section (6.4 mm outside diameter) that starts outside of the pressure vessel and enters the vessel through a small port (sealed with a pipe plug), and a short section (1.6 mm outside diameter) that enters the quartz chimney and reaches the flame front (Fig. 1). A Tedlar bag is attached to the probe outside of the pressure vessel with a ball valve that allows the bag to be filled. Samples are then extracted from the bags for GC-MS analysis.

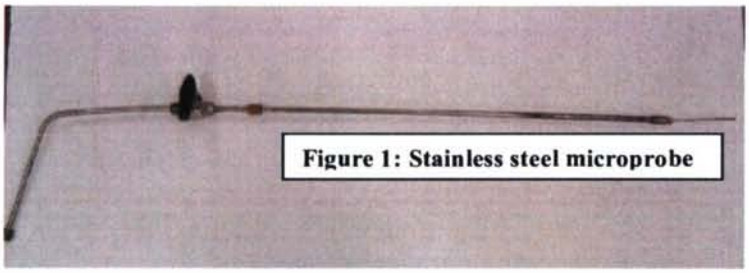

Figure 1: Stainless steel microprobe

Results and Discussion

Soot Surface Temperature Measurements

In Fig. 2 below, soot surface temperatures of undiluted ethylene flames, at their velocity matched air-to-fuel ratio smoke point, are plotted as functions of pressure. The peak soot temperatures were measured as an overall peak temperature as well as a peak temperature at 65% of the flame height as a function of pressure. Soot surface temperature measurements at 65% of their height were compared with previous soot volume fraction measurements by McCrain and Roberts [2]. This 65% of the flame height corresponds to the location of peak soot volume fraction in undiluted, atmospheric pressure flames [3].

In each of the cases shown, the soot temperature at 65% of the flame height is cooler than the measured overall peak soot temperature. This is expected at atmospheric pressure due to radiation losses from the high soot loading. As the pressure increases the location of maximum soot temperature moves towards the tip of the flame. It is interesting to note that the relative ratio of overall peak temperature to peak at 65% does not vary significantly. It should also be noted that as pressure increases, overall flame temperature decreases due to heat losses from

radiation and conduction to the fuel tube. Similar results were found (discussed in [4]) with diluted ethylene flame cases.

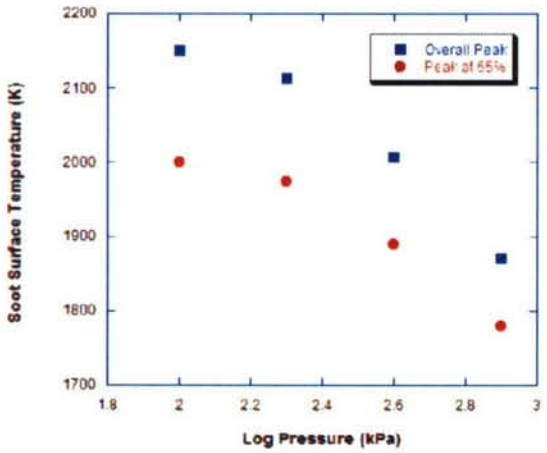

Figure 2: Maximum soot surface temperatures for undiluted ethylene as a function of pressure

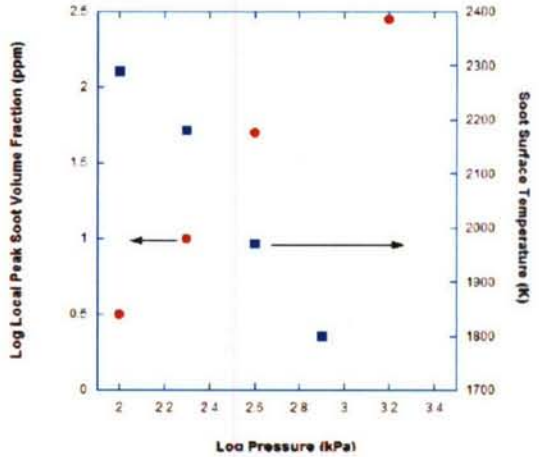

Figure 3: Local peak soot volume fraction and soot surface temperature as a function of pressure for undiluted ethylene flames

In order to compare with the previous soot volume fraction measurements [2], soot surface temperature measurements were made in undiluted ethylene flames with a constant fuel mass flux. As the pressure increases the fuel mass flux at the smoke point increases. Therefore, with constant fuel mass flux the flames were above their smoke points at low pressures and were below their smoke points at high pressures. The comparison between soot volume fraction and soot surface temperature is discussed in more detail in Fig. 3.

Soot volume fraction, f_v measurements were made using LII in a similar burner as used for the current investigation [2]. From Fig. 3 it is clear that as pressure increases the local peak f_v, measured at 65% of the flame's height, increases while the soot surface temperature in each case decreases. As expected, the increase in f_v with pressure leads directly to a decrease in soot surface temperature. As the pressure increases, the blue (soot-free) region of the flame is eliminated and more soot is produced (since flames are at or below the smoke point, the soot is completely oxidized) which eventually leads to an overall cooling of the flame.

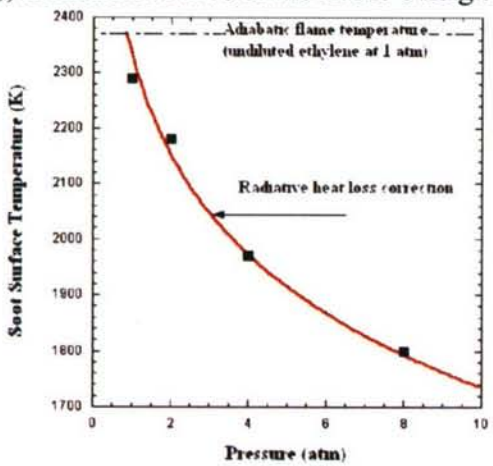

Figure 4: Measured soot surface temperature (square symbols) averaged radially at 65% of the flame height as a function of pressure in pure ethylene flames accounting for radiative losses from soot (line) shows reduction in temperature due to increased soot loading with pressure

The soot surface temperature at constant fuel mass flux decreased with pressure. f_v increases (non-linearly) with pressure and therefore, so do the losses from soot radiation. To determine if the reduction in soot surface temperature could be attributed completely to the increased radiation losses, a simple calculation was preformed. By knowing the f_v and the flame cross-sectional area at 65% of the flame height from [2], and assuming a constant soot spherule diameter and emissivity, a radiation loss can be calculated. The resulting calculated temperature is plotted in Fig. 4 along with the actual measurements at 65% flame height at constant fuel mass flux. As seen in this figure, the measured

reduction in soot surface temperature can be completely attributed to the increased radiation losses due to increased soot loading.

Species Concentration Measurements

Upon completion of the microprobe and necessary burner/pressure vessel modifications, a number of samples have been collected from pure ethylene flames over a range of pressures. An initial concern, which had been somewhat addressed by previous researchers [1], was that the heated stainless steel probe would catalytically react with the sample and reduce the acetylene and benzene concentrations. Two tests were conducted to determine if this concern was legitimate: a sample was taken half the distance from the chimney wall to the flame in front of the flame, and a sample was taken half the distance from the flame to the chimney wall through the flame. The two samples were analyzed with the GC-MS and it was clear that the concentrations of acetylene and benzene were almost identical in each case. With this settled, calibration has now begun and species concentration measurements are currently underway.

Observations

Soot surface temperature measurements have been completed and species concentration measurements are currently in progress. The findings from these most recent investigations are as follows:

1. With increasing pressure, the flame height decreases, increasing the rate of heat transfer to the fuel tube and causing a cooling at the base of the flame.
2. As expected, the addition of a diluent cools the soot surface. With dilution, the soot at the tip of the flame remains hotter than soot lower in the flame. This becomes more pronounced with continued addition of diluent to 40% dilution by volume. Overall, the helium diluted flames are the warmest and the CO_2 diluted flames are the coolest. This is both a heat capacity effect as well as a small contribution from radiative heat loss with CO_2.
3. The changes in measured temperature with both pressure and dilution were larger than calculated based on chemical equilibrium. The measured temperatures decrease more dramatically with dilution then predicted from equilibrium calculations, at all pressures, despite the similar soot loading between flames (due to each flame being at its smoke point).
4. There is a chemical effect on overall soot production in flames diluted with carbon dioxide, in agreement with previous findings by Glassman [5], such that higher fuel flow rates are required to reach the smoke point. Flame height scales directly with the molecular weight of the diluent, as expected. The helium diluted flame looks very similar to the undiluted ethylene flame in both height and temperature uniformity.
5. The overall peak temperature of the undiluted flames decreases with pressure from approximately 2300 K at one atmosphere to approximately 1800 K at eight atmospheres. This reduction in soot surface temperature can be fully explained by increased soot radiation, due to higher soot loading with pressure.

References

1. M.C. Drake, S.M. Correa, R.W. Pitz, W. Shyy, and C.P. Fenimore, Combust. Flame 69 (1987) 347-365.
2. L.L. McCrain and W.L. Roberts, Combust. Flame 140 (2005) 60-69.
3. R.J. Santoro, H.G. Semerjian, and R.A. Dobbins, Combust. Flame 51(2) (1983) 203-218.
4. T.L. Berry Yelverton and W.L. Roberts, (submitted to Exp. Therm. Fluid Sci. 2007).
5. Glassman, Proc. Combust. Inst. 27 (1981) 1589-1596.

PDF MODELING OF TURBULENT COMBUSTION

AFOSR Grant FA-9550-06-1-0048
Principal Investigator: Stephen B. Pope

Mechanical & Aerospace Engineering
Cornell University
Ithaca, NY 14853

SUMMARY

In both space and aircraft applications, the design of combustors in propulsion systems remains a significant technical challenge. Given the cost, difficulty and time consumed in experimental testing, it is well recognized that computer modeling is essential to exploring different design concepts, and to reducing the cost and time of the design cycle. While many phenomena may be involved – sprays, radiation, combustion dynamics, etc. – a central problem is that of modeling turbulent-chemistry interactions in turbulent combustion. The PDF approach to turbulent combustion has the advantages of fully representing the turbulent fluctuations of species and temperature, and of allowing realistic combustion chemistry to be implemented (e.g., of order 50 species). This methodology is also being applied in conjunction with large-eddy simulations, in which case it is referred to as LES/FDF. The overall objective of the proposed work is to advance and extend the PDF and LES/FDF approaches to modeling turbulent combustion in flows of relevance to aerospace propulsion systems. Recent work includes: (1) a study of different chemical kinetics mechanisms applied to piloted methane flames; (2) continued development of the LES/FDF methodology, both at Cornell and in collaboration with the University of Pittsburgh; (3) Lagrangian studies of the interaction between mixing and chemical reaction in PDF calculations of jet flames; (4) PDF investigations of the stabilization mechanism of lifted flames in vitiated co-flows; and (5) an examination of the effects of time averaging on the numerical accuracy of PDF calculations.

COMPARISON OF REACTION MECHANISMS IN PILOTED METHANE FLAMES

This investigation (Wang & Pope 2007a) is motivated by apparent discrepancies in previous PDF model calculations of the Sandia piloted non-premixed turbulent jet flames (the Barlow & Frank 1998 flames D, E and F). In 2000, both the Cornell and Imperial College groups reported accurate calculations of these flames, but with different sub-models. The former calculations (Xu & Pope, 2000) use an augmented reduced mechanism based on the GRI mechanism, and the EMST mixing model with model constant $C_\phi = 1.5$. The latter calculations (Lindstedt et al. 2000) use Lindstedt's reduced mechanism and the modified Curl mixing model with model constant $C_\phi = 2.3$. Since that time a number of studies, in particular Cao et al. (2005, 2007), have examined the effects of some different mechanisms and mixing models, and yet the differences between the two sets of calculations in 2000 remain unexplained.

In the study reported here (Wang & Pope 2007), a comparison is made between non-premixed flame calculations using the GRI 3.0 and Lindstedt detailed mechanisms and with different mixing models. Additional insights are provided by autoignition and non-premixed strained laminar flame calculations.

Figure 1 shows the ignition delay times given by different mechanisms for a stoichiometric methane/air mixture as a function of the initial temperature. As may be seen, for temperatures above 1,400K, the Lindstedt mechanism exhibits a shorter ignition delay time.

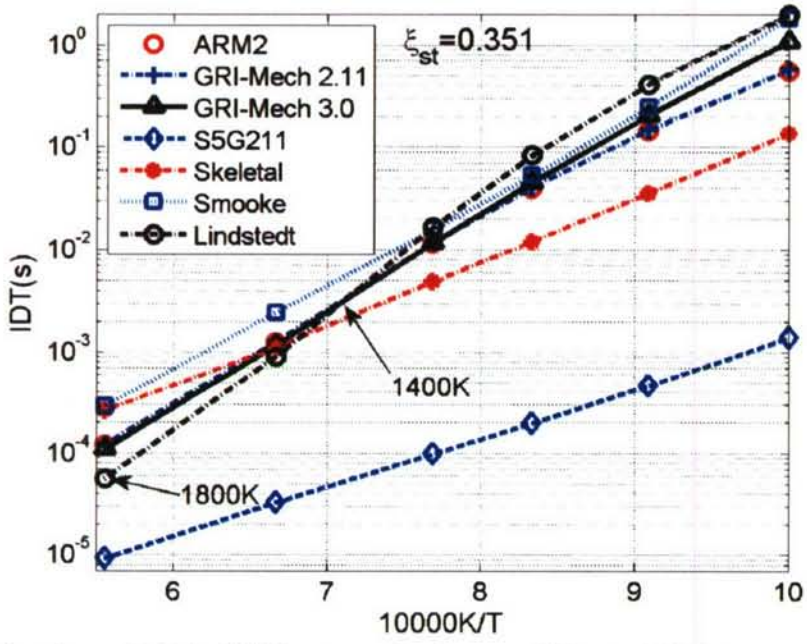

Fig. 1 Ignition delay times (IDTs) of different mechanisms at different initial temperatures *T*.

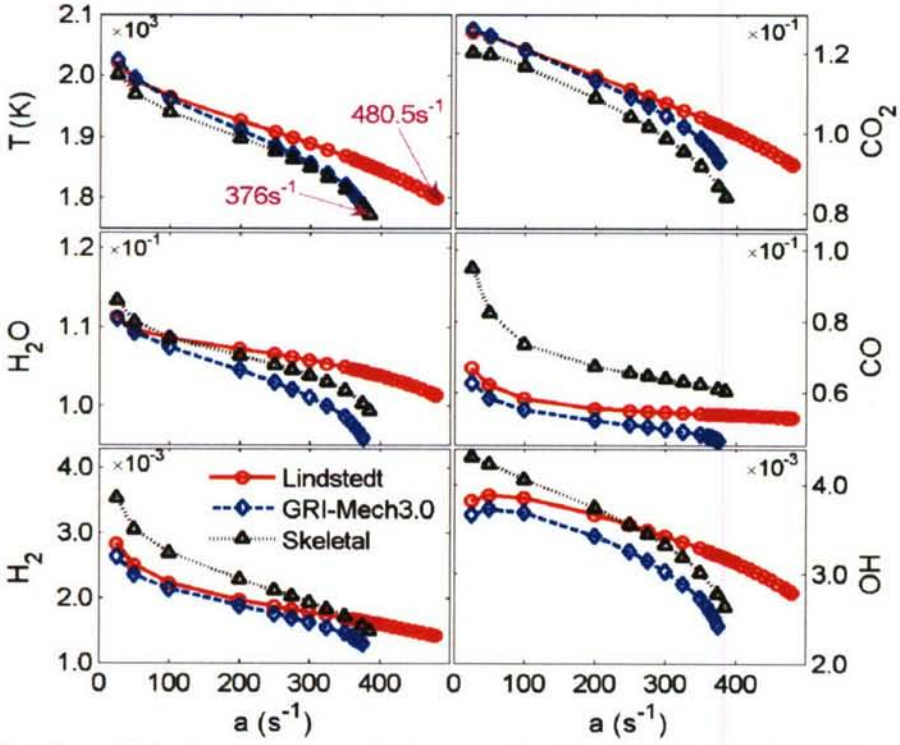

Fig. 2 The peak values of the temperature, and the mass fractions of CO_2, H_2O, CO, H_2, and OH against the nominal strain rate *a* in the opposed laminar jet non-premixed flames computed with different reaction mechanisms.

A series of calculations was performed of strained non-premixed laminar flames with the same fuel and oxidant used in the Barlow & Frank flames (i.e., the fuel is 1:3 methane/air, and the oxidant is air). Figure 2 shows the peaks of various quantities in these flames as functions of the imposed strain rate. While the Lindstedt and GRI mechanisms yield comparable properties at low strain rates, the Lindstedt mechanism exhibits a greater resilience to extinction.

A set of 28 PDF calculations of the Barlow & Frank flames have been performed, with both chemical mechanisms, three mixing models, and a range of values of the mixing model constant C_ϕ. Figure 3 shows some of the results on "burning indexes" (BIs) at an axial location of 7.5 fuel jet diameters. (The burning index is zero for complete extinction and one for complete combustion.) There are two fundamental observations from these results. First, for a given mixing model and value of C_ϕ, the Lindstedt mechanism uniformly yields higher values of BI than does the GRI mechanism. This is consistent with the previously observed shorter ignition delay time and higher extinction strain rate of the Lindstedt mechanism. Second, the two calculations closest to those of Xu & Pope (2000) and Lindstedt et al. (2000) (i.e., GRI, EMST, C_ϕ = 1.5 and Lindstedt, modified Curl, C_ϕ = 2.3) yield very similar values of BI which are generally in agreement with the experimental data (though less so for H_2O and OH). This, then, provides a full explanation for the similar calculations in 2000 using different submodels.

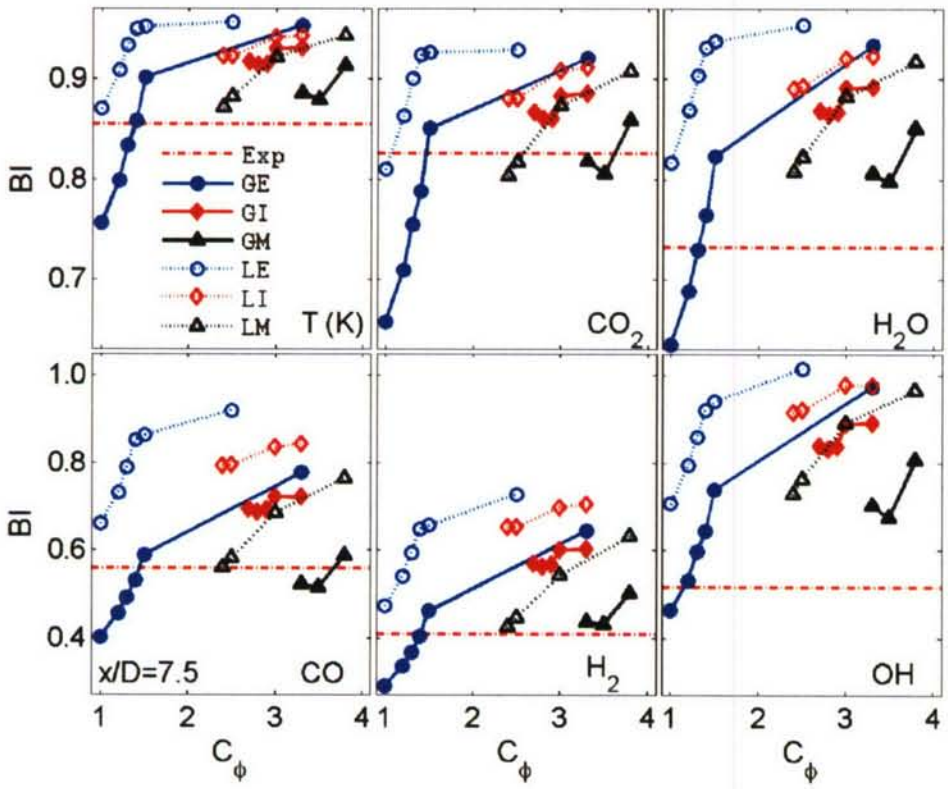

Fig. 3 The burning indexes of the temperature and the mass fractions of CO_2, H_2O, CO, H_2, and OH against C_ϕ at the location of x/D = 7.5 in the Sandia flame. The two letters in the legend identify the combination of the mixing models (E: ESMT, I: IEM, and M: modified Curl) and the reaction mechanisms (G: GRI-Mech 3.0, L: Lindstedt mechanism).

The present work reveals significant differences in the predictions of the two mechanisms, but does not determine which (if either) is accurate under the conditions investigated. There are experimental data for non-premixed laminar flame with the flame E fuel (methane/air mixture Barlow et al. 2001), but these are at very low strain rates. It would be extremely valuable to investigate experimentally the properties of strained laminar flames of this fuel close to the extinction strain rate.

PUBLICATIONS

The following papers based on AFOSR sponsored research have been published or written in 2006-2007.

[1] R.L. Gordon, A.R. Masri, S.B. Pope and G.M. Goldin (2006) "Transport budgets in turbulent lifted flames of methane auto-igniting in a vitiated co-flow," Combustion and Flame (submitted).

[2] R.L. Gordon, A.R. Masri, S.B. Pope and G.M. Goldin (2007) "A Numerical Study of Auto-ignition in Turbulent Lifted Flames Issuing into a Vitiated Co-flow," Combustion Theory and Modelling **11**, 351-376.

[3] B. Merci, D. Roekaerts, B. Naud and S.B. Pope (2006) "Comparative study of micro-mixing models in transported scalar PDF simulations of turbulent non-premixed bluff body flames," Combustion and Flame, **146**, 109-130.

[4] M.R.H. Sheikhi, P. Givi and S.B. Pope (2006) "Velocity-scalar filtered mass density function for large eddy simulation of turbulent reacting flows," Physics of Fluids (submitted).

[5] H. Wang and S.B. Pope (2007a) "Comparison of detailed reaction mechanisms in non-premixed combustion," Combustion & Flame (to be submitted).

[6] H. Wang and S.B. Pope (2007b) "Lagrangian investigation of local extinction, re-ignition and auto-ignition in turbulent flames," Combustion Theory and Modelling (submitted).

[7] H. Wang and S.B. Pope (2007c) "Time averaging strategies in the finite-volume/particle algorithm for the joint PDF equation of turbulent reactive flows," Combustion Theory and Modelling (to be submitted).

OTHER REFERENCES

[1] R.S. Barlow and J.H. Frank (1998). Proc. Combust. Inst. **27**, 1087-1095.

[2] R.S. Barlow, A.N. Karpetis, J.H. Frank, J.Y. Chen, (2001). Combust. Flame **127**, 2102-2118.

[3] R. Cao and S.B. Pope (2005) Combustion and Flame, **143**, 450-470.

[4] R.R. Cao, H. Wang and S.B. Pope (2007). Proceedings of the Combustion Institute, **31**, 1543-1550.

[5] R.P. Lindstedt, S.A. Louloudi, and E.M. Vaos (2000). Proc. Combust. Inst. **28**, 149-156.

[6] J. Xu, and S.B. Pope (2000). Combust. Flame **123**, 281-307.

FILTERED DENSITY FUNCTION FOR SUBGRID SCALE MODELING OF TURBULENT COMBUSTION

Grant Number FA9550-06-1-0015

Principal Investigator: Peyman Givi

Department of Mechanical Engineering and Materials Science
University of Pittsburgh
Pittsburgh, PA 15261

SUMMARY/OVERVIEW:

The specific objectives of this work are to further develop and improve the "filtered density function" (FDF) methodology for closure of the subgrid scales (SGS) in turbulent reacting flows, and to implement the resulting SGS closure for large eddy simulation (LES) of non-premixed turbulent flames.

TECHNICAL DISCUSSION

The filtered density function (FDF) methodology [1] has proven effective for large eddy simulation (LES) of turbulent reacting flows. The fundamental property of the FDF is exhibited by the closed form nature of the chemical source term appearing in the transport equation governing the FDF. This property is very important as evidenced in several applications of FDF for LES of a variety of turbulent reacting flows. Reference [2] provides a review of the latest progress in FDF modeling and its continuing widespread usage by many researchers within the combustion community. In our previous AFOSR sponsored work, we have successfully completed the developments and applications of the FDF and the density weighted filtered mass density function (FMDF) to account for the scalars (SFMDF) and the joint velocity-scalar (VSFMDF) fields.

There are four basic elements in our research conducted within the past year: (i) development and improvements of physical SGS models, (ii) improvement of the computational efficiency of the simulations, (iii) application of the resulting computational tool for actual simulations of turbulent reacting flows, and (iv) analysis of the simulations' results for assessing the physics of turbulent combustion. Reference [3] provides some of our recent results in our continuing progress in all of the basic elements of this research. A summary of our progress in each of these endeavors is provided below.

In regard to issue (i), our latest efforts have been focused on inclusion of the SGS "frequency" into the FDF formulation. For that, we have developed the joint frequency-velocity-scalar filtered mass density function (FVS-FMDF). This is the most comprehensive form of the FDF to date as it accounts for SGS closure of the velocity field, all of the scalars and the frequency in variable density flows. We have developed a modeled transport equation for the FVS-FMDF in which the effects of convection and chemical reaction appear in closed forms. The unclosed terms are modeled in a fashion similar to PDF methods [4]. The modeled FVS-FMDF transport equation is solved and the methodology is employed to simulate several turbulent shear flow configurations.

While issue (ii) is not of direct relevance to combustion physics, it an important issue in LES. In order to apply the FDF for prediction of realistic and complex flames, our hybrid finite-difference (FD) / Monte Carlo (MC) numerical solver has to be continuously improved. With today's computer architectures, this improvement is highly correlated with the extent of the computational parallelization. The parallelization is implemented by dividing the computational domain into equal-sized sub-domains. Each processor performs the FD procedure separately on each of these domains. The message-passing interface (MPI) library is used to pass the variables between processors. This implementation ensures load balancing. The message-passing is implemented in a non-blocking manner, to enable overlapping of communications with computations. This results in reduction of communication overhead. The parallelization of MC procedure is done by dividing the MC particles among the processors according to their spatial location. This way the particles have direct access to the FD variables they need for their evolution. Each MC particle evolves independently, thus there is no inter-particle interactions. As the particles move, they may translate to the neighboring sub-domain. This is done by communicating the particle values between the adjacent processors. Due to stochastic nature of particle motion, there is a substantial increase in communication overhead due to particle oscillation near the sub-domain's boundaries. To alleviate this, a buffer zone is devised in which the particles are accumulated. With this treatment, the particle communications are not needed at each time step and the communication overhead is decreased significantly. The procedure as developed here is examined extensively on up to 128 processors. The results show good load balancing and close to linear speed-ups. This is a major improvement as compared to balancing on 64 processors achieved last year. This efficiency has been particularly important as we are primarily using the computational resources at the Pittsburgh Supercomputing Center (PSC).

In efforts pertaining to issue (iii), we have used the VSFMDF for prediction of the Sandia's piloted jet flames. These flames have been the subject of broad investigations by other computational/modeling methodologies [5] and in fact have been successfully simulated in our previous SFMDF simulations [6]. In the experiments, three basic flames are considered, identified by Flames D, E, and F. The geometrical configuration in these flames is the same, but the jet inlet velocity is varied. In Flame D, the fuel jet velocity is the lowest and the flame is close to equilibrium. The jet velocity increases from flames D to E to F, with noticeable non-equilibrium effects in the latter two [5]. Various fuel jet and air co-flow speeds are studied to create an experimental database for different levels of flame blow-off. Previously, the SFMDF has been successfully implemented for prediction of all of these flames. In our current VSFMDF applications, only flame D is considered. For this flame, combustion is modeled via the near-equilibrium oxidation model and is enacted via "flamelet" simulations which consider a laminar counterflow (opposed jet) flame configuration [7]. The full methane oxidation mechanism of the Gas Research Institute (GRI) [8] accounting for 53 species and 325 elementary reactions is used. At low strain rates, the flame is close to equilibrium. Thus, the thermo-chemical variables are determined completely by the "mixture fraction." This flamelet library is coupled with our VSMFDF solver in which transport of the velocity field and the mixture fraction is considered.

In regard to (iv), we have had some very interesting observations in analyzing the results of our various simulations. Some of our key findings are summarized here. First, we have observed that the FVS-FMDF provides a much better prediction of the SGS kinetic energy and the overall flow structure as compared with the VSFMDF in which the frequency was modeled in

an *ad hoc* manner [9-11]. Secondly, we have observed that in both the FVS-FMDF and VSFMDF, the magnitudes of all of the second order moments are not sensitive to the values of the (empirical) model constants. While these values influence the allocations of the resolved and the SGS energies, the magnitudes of the "total" energies are independent of the model constants. Of course, the range of the constants as considered is such that the magnitude of the resolved energy remains in an accepted proportion (compared to that of SGS). Finally, we have observed that the VSFMDF is capable of simulating Sandia Flame D very effectively, without any need for adjustment of the model constants, as suggested in our previous work [5]. The methodology is capable of predicting the first two moments of the velocity field, the temperature, and all of the major and minor species concentrations. The PDFs of the mixture fraction and the temperature field as obtained by post processing of the *resolved* field also show good comparison with data.

Table 1. Current state of FDF progress

Methodology / Status	SFMDF 1998-2000	VFMDF 2000-2003	VSFMDF 2003-2006	FVS-FMDF 2006-2007
Fundamental Development	■	■	■	▒
Efficient Computation	■	▒	▒	
Basic Flow Simulations	■	■	■	■
Complex Flow Applications	■	■	■	
Implementations by Others	■			
Industry/Commercial Utilization	■			
CPU Requirements (Relative to conventional LES)	4	12	13.6	14.4

■ Completed ▒ In progress

At this point, it is useful to summarize the current state of progress in development and applications of the FDF. Table 1 is constructed for this purpose. It is now clearly established that the FDF provides an excellent means of SGS modeling as compared to most of the other conventional methods in LES of turbulent reacting flows. The issue of primary concern in FDF is associated with its computational costs. Currently, the SFMDF (simplest of the FDF methods) requires about 4 times of the computational requirement of conventional methods (for transport of a single conserved scalar variable). This comparison cannot be conducted for complex reacting flows due to inability of non-FDF methods to account for SGS effects in such flows. This overhead is surely expected to be reduced further with our better/enhanced capability of utilizing MPI (a never ending process!). Nevertheless it has been tolerated and is rated acceptable as the methodology is now being widely utilized by a large number of investigators worldwide; it has been used in commercial software and also being utilized for

industrial applications. See Reference [2] for a recent bibliography. Presently, the computational cost associated with simulations of the velocity field is prohibitive (despite the excellent results of complex flows obtained via the VSFMDF). This cost must be substantially reduced before the full-scale FVS-FMDF can be recommended for practical applications.

WORK IN PROGRESS

Our current work is concentrated on fine-tuning and further implementation of both of the VSFMDF and FVS-FMDF to simulate complex flames. Several alternatives (stochastic and deterministic closure) for SGS frequency are being investigated. Work is also continuing in reducing the computational overhead as required in communications between the processors in FDF simulations.

ACKNOWLEDGMENT

We are indebted to Professor Stephen B. Pope (Cornell University) for his valuable collaboration on various aspects of this work.

REFERENCES

[1] Givi, P., *AIAA J.*, Vol. **44**(1), p. 16, 2006.

[2] Givi, P., Sheikhi, M. R. H., Drozda, T. G. and Madnia, C. K., *AIAA paper* 2007-0190, 2007.

[3] Drozda, T. G., Sheikhi, M. R. H., Madnia, C. K. and Givi, P., *Flow Turbul. Combust.*, **78**, p. 35, 2007.

[4] Pope, S. B., *Turbulent Flows*, Cambridge University Press, Cambridge, UK, 2000.

[5] Sandia National Laboratories, TNF Workshop website, http://www.ca.sandia.gov/tdf/Workshop.html, 2007.

[6] Sheikhi, M. R. H., Drozda, T. G., Givi, P., Jaberi, F. A. and Pope, S. B., *Proc. Combust Inst.*, **30**, p. 549, 2005.

[7] Peters, N., *Turbulent Combustion*, Cambridge University Press, Cambridge, UK, 2000.

[8] Smith, G. P., Golden, D. M., Frenklach, M., Moriarty, N. W., Eiteneer, B., Goldenberg, M., Bowman, C. T., Hanson, R., Song, S., Gardiner, W. C., Lissianski, V., and Qin, Z., http://www.me.berkeley.edu/gri-mech.

[9] Gicquel, L. Y. M., Givi, P., Jaberi, F. A. and Pope, S. B., *Phys. Fluids*, Vol. **14**(3), p. 1196, 2002.

[10] Sheikhi, M. R. H., Drozda, T. G., Givi, P. and Pope, S. B., *Phys. Fluids*, Vol. **15** (8), p. 2321, 2003.

[11] Sheikhi, M. R. H, Givi, P. and Pope, S. B., *Phys. Fluids*, in press, 2007.

CHEMICAL MODELING FOR LARGE EDDY SIMULATION OF TURBULENT COMBUSTION

Grant number: FA9550-06-1-0060

Principal Investigator: Heinz Pitsch

Department of Mechanical Engineering
Stanford University
Stanford, CA 94305-3030

SUMMARY/OVERVIEW

The efforts of this research program are directed towards two goals. The first of these goals is the development of models that can describe more accurately the interaction of turbulence and chemistry in large-eddy simulations (LES). The second is the development of reduced chemical kinetic mechanisms for JP-8 surrogate fuels using a component library approach. In the most recent reporting period, significant steps towards meeting each of these goals have been taken. Specifically, a new and consistent dynamic LES model for the turbulent burning velocity has been formulated. Additionally, the efficiency of the reduction procedure has been improved and a tool for the automatic combination of chemical mechanisms from different sources has been developed.

TECHNICAL DISCUSSION

Combustion Models for LES

Most modern methods of dealing with premixed combustion in LES require information about how subfilter physics affect flame propagation. These physics, which tend to increase the speed of flame propagation, must therefore be incorporated into simulations using turbulent burning velocity models. Until recently, these models were being developed independently of the LES framework in which they were applied. This created consistency problems and prevented the advantages of modeling specifically for LES from being realized.

The present research program has produced a dynamic turbulent burning velocity model that deals with these issues. This model was developed within the framework of LES and was designed to produce flame speeds that predict filter-independent mean flame positions. Additionally, the new model allows the constant coefficients that appear in most functional descriptions of the burning velocity to be calculated locally and instantaneously within a simulation. This both limits the ability of the model developer to artificially affect flame behavior, and allows a wider variety of physics to be described by the model. A derivation of the model begins with the formulation of an equation describing the evolution of a flame front. When a flame front is defined to be the isocontour $c = c_0$ of a progress variable c, this evolution equation can be produced by multiplying the progress variable transport equation with a delta function,

$$\delta(c - c_0)\left[\frac{\partial c}{\partial t} + u_j \frac{\partial c}{\partial x_j}\right] = \delta(c - c_0)\left[\frac{1}{\rho}\frac{\partial}{\partial x_j}\left(\rho D \frac{\partial c}{\partial x_j}\right) + \frac{1}{\rho}\dot{\omega}_R\right]. \quad (1)$$

This delta function can equivalently be written as the derivative of the heaviside function

$H(c-c_0)$. It can then be combined with the other terms. This results in an equation describing the evolution of a sharp step function located at the flame front,

$$\frac{\partial [H(c-c_0)]}{\partial t} + u_j \frac{\partial [H(c-c_0)]}{\partial x_j} = D\kappa |\nabla [H(c-c_0)]| + s_{L,c_0} |\nabla [H(c-c_0)]|, \quad (2)$$

where the propagation speed of the c_0 surface, s_{L,c_0}, has been introduced to describe the source terms. Unlike level set formulations, this equation is valid everywhere in space, and not just at the 2-D flame front. This is an important property because it means that a standard LES volumetric filter can be applied to the equation. Making the notationally convenient substitution $\mathcal{G} = H(c-c_0)$ and filtering gives,

$$\frac{\partial \overline{\mathcal{G}}}{\partial t} + \overline{u_j \frac{\partial \mathcal{G}}{\partial x_j}} = \left(\overline{D\kappa}\right)_T \left|\nabla \overline{\mathcal{G}}\right| + \overline{s}_{T,c_0} \left|\nabla \overline{\mathcal{G}}\right|, \quad (3)$$

where $\overline{s}_{T,c_0} \left|\nabla \overline{\mathcal{G}}\right| = \overline{s_{L,c_0} |\nabla \mathcal{G}|}$ and $\left(\overline{D\kappa}\right)_T \left|\nabla \overline{\mathcal{G}}\right| = \overline{D\kappa |\nabla \mathcal{G}|}$ represent the introduction of models describing the filtered burning velocity, $\overline{s}_{T,c_0}$, and filtered curvature propagation, $\left(\overline{D\kappa}\right)_T$.

Equation (3) is significant because it explicitly describes the existence and form of the terms that need to be modeled by the subfilter turbulent burning velocity. Additionally, when both filtering and test filtering are used, it provides the framework for producing a dynamic equation that can be solved to determine the value of model constants. For example, since filters commute with temporal derivatives, the application of a broad test filter to Eq. (3) produces a transport equation for $\widehat{\overline{\mathcal{G}}}$ (the hat operator denotes the test filter). If primary and test filters are instead applied to Eq. (2) concurrently, a slightly different equation for $\widehat{\overline{\mathcal{G}}}$ is produced. These two equations are relatable at all times since they describe the same variable. However, since they also correspond to different sequences of filter application, the modeled terms appear in somewhat different forms. After manipulation, the relation between the modeled terms can be written as,

$$\overbrace{\left(\left(\overline{D\kappa}\right)_T + \frac{\rho_u}{\overline{\rho}} \overline{s}_{T,u}\right) \left|\nabla \overline{\mathcal{G}}\right|} = \left(\left(\widehat{\overline{D\kappa}}\right)_T + \frac{\rho_u}{\widehat{\overline{\rho}}} \widehat{\overline{s}}_{T,u}\right) \left|\nabla \widehat{\overline{\mathcal{G}}}\right|, \quad (4)$$

where the u subscript denotes conditioning on the unburned side of the flame front. Although $\left|\nabla \overline{\mathcal{G}}\right|$ is underresolved in an actual LES and cannot be computed, an accurate method of approximating this term using information about the area of the filtered flame front has also been developed. The introduction of this method makes it possible to solve Eq. (4) for either burning velocity or curvature propagation model constants.

A direct numerical simulation (DNS) of a front propagating in forced homogeneous isotropic turbulence was performed to validate this model. This DNS was run on a 256 x 128 x 128 mesh at a Reynolds number of $Re_\lambda = 40$. The simulation was run at a constant density and gas expansion effects were not considered. A level set was used to describe the flame front, and a laminar burning velocity of approximately one-third of the maximum velocity fluctuation magnitude was prescribed. An instantaneous snapshot from this simulation is shown in Figure. 1.

Figure 1 also shows mean front displacement as a function of time, computed both directly from the DNS and from a variety of models. If no turbulent burning velocity model is used to describe mean propagation, mean front displacement is severely under-predicted, as expected. The static turbulent burning velocity model, however, somewhat over-predicts mean front displacement. In contrast, the dynamic model accurately predicts this transition. This improvement can be attributed to the model's access to surface area information. For example, the solid line in Fig. 1 shows computed mean front displacement when the propagation speed is described by multiplying the laminar burning velocity by the ratio of the exact flame area and the

mean, or flat, flame area. Equation (4) reduces to this description in simple cases, and the results are in excellent agreement with the DNS data. The other two lines in Fig. 1 show front displacements computed by applying the dynamic model at different filter widths. These realizations are both considerably more accurate than the static model, and demonstrate that the effectiveness of the dynamic procedure holds under a variety of filters.

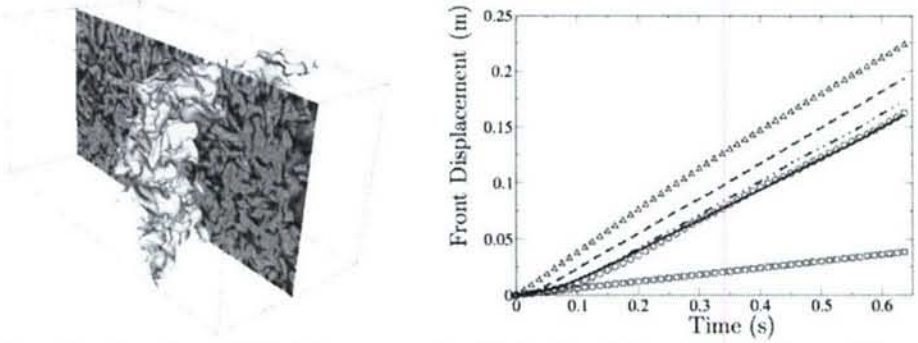

Figure 1: Left Pane: Snapshots from a DNS of front propagation. The level set is the wrinkled surface, and the cut plane shows voriticity magnitude. Right Pane: Front displacement from initial location as a function of time. O : Mean front position from DNS; □ : Laminar burning velocity model, $s_{L,u}$; △ : Static turbulent burning velocity model, $s_{T,u}$; Solid line: $s_{L,u}$ scaled by the ratio of the exact front area (from DNS) and the averaged front (planar) area; Dashed line: Dynamic model with overline filter width<<Δx and hat filter width=Δx; dash-dotted line: Dynamic model with overline filter width=4Δx and hat filter width=128 Δx.

Automatic Multi-stage Reduction of Large Chemical Kinetic Mechanisms

Several techniques, specifically tailored to hydrocarbon chemistry, have been developed for the reduction of large kinetic schemes. These techniques include the Directed Relation Graph with Error Propagation (DRGEP) method that eliminates negligible species and reactions, chemical lumping and quasi-steady state assumptions. Two major issues linked to the species elimination step have been identified and addressed, and tools for the combination of reduced mechanisms from different sources have been developed.

Group-based coefficients and integrity check

The effect of removing some group of species on a target is estimated more accurately by the introduction of a new, group-based direct interaction coefficient that better balances the contribution to the production and consumption of a given species and that takes into account the effect of the species already discarded. The coupling between two species A and B given a set $\{S\}$ of species already removed is defined as:

$$r_{AB,\{S\}} \equiv \frac{\left|\sum_{i=1,n_R} \nu_{i,A}\omega_i\delta^i_{B,\{S\}}\right|}{\max\left(P_A, C_A\right)}, \tag{5}$$

where the Kronecker symbol δ is unity, if the i^{th} reaction involves species B or any species in subset $\{S\}$, and 0 otherwise. P_A and C_A are the total production and consumption rates of species A. The DRGEP coefficients are recomputed regularly during the reduction procedure. A major advantage of this approach is the equal consideration of all species, whether they are being produced or consumed through many parallel chemical paths or not. Moreover, any intermediate species in a skeletal mechanism must have at least one production and one consumption path. Some species might fail this requirement, especially in very short skeletal mechanisms. If a species is not produced anymore, it should be removed. If a species is not consumed anymore, it creates a sink of mass that can impact greatly the kinetic equilibrium concentrations of the

products. An algorithm has been designed, that identifies truncated chemical paths and eliminates them by adequately reordering the list of species provided by the DRGEP method.

The use of the group-based coefficients along with the species reordering algorithm shows a significant improvement in the accuracy of the skeletal mechanisms, as displayed in Fig. 2. Errors in ignition delay times have been reduced considerably, resulting in smaller mechanisms for a given accuracy. The corresponding negligible error in the final mass fraction of CO proves the absence of any truncated chemical paths.

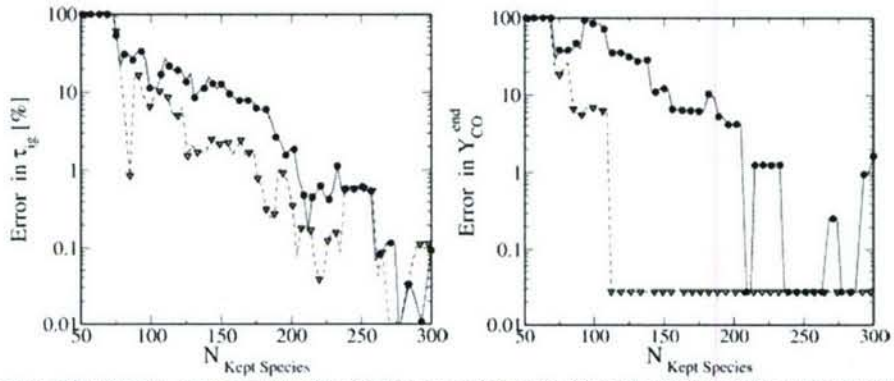

Figure 2: Reduction of LLNL iso-octane mechanism for low temperature ignition. Evolution of the error on targets when using the original method (solid line, filled circles) and the group-based coefficients and integrity check (dashed line, open triangles)

Combination of mechanisms

The reduction tools developed within this work are used to derive single component skeletal mechanisms for different sets of initial conditions. These short mechanisms can then be combined to obtain chemical models of surrogate fuels. The main assumption of this approach is that most of the interactions between two different fuels happen at the level of small species. Cross-reactions between fuel-specific molecules are assumed to be negligible or limited to a few easily identifiable species and reactions. Including several components in the surrogate definition implies that mechanisms from potentially very different sources will have to be combined. An interactive setup has been designed to assist in the merging of species, thermodynamic and transport data, and elementary reactions from different sources.

The construction of a reduced scheme for *n*-heptane and iso-octane mixtures is presented as an example of this modular approach. The detailed mechanisms from LLNL are reduced for a wide range of homogeneous initial conditions. Four modules are obtained: two high temperature mechanisms and two low temperature modules for *n*-heptane and iso-octane respectively. Reduced mechanisms for Primary Reference Fuel (PRF) mixtures are obtained by combining those modules together. The LLNL detailed mechanism for PRF is used for comparison purposes. The low temperature modules for the individual fuels are comparable in size to their high temperature counterparts, and therefore should be used only when required by the application. The combination of the various techniques allows reducing the number of species and reactions by nearly an order of magnitude. Comparison of ignition delay times obtained using the LLNL detailed mechanism for PRF and the reduced surrogate mechanism, shown in Fig. 3, are satisfactory.

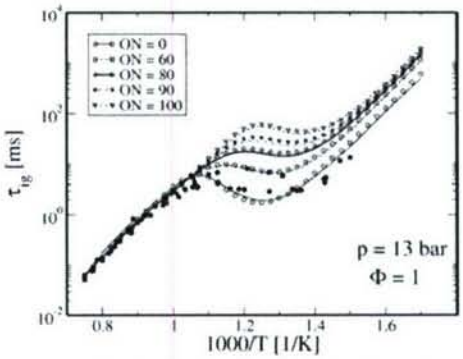

Figure 3: Comparison of ignition delay times between experiments (filled symbols), detailed (lines) and reduced (open symbols) mechanisms for PRF at various octane numbers.

INVESTIGATION OF SUBGRID-SCALE SCALAR MIXING AND TURBULENCE-CHEMISTRY INTERACTION IN TURBULENT PARTIALLY PREMIXED FLAMES

(AFOSR Grant FA9550-06-1-0036)

Principal Investigator: Chenning Tong

Department of Mechanical Engineering
Clemson University
Clemson, SC 29634-0921

SUMMARY

Our recent studies have shown that the subgrid-scale (SGS) mixture fraction has different structures and distributions for different SGS scalar variances. We study the effects of the structures on the scalar dissipation and temperature dissipation in the context of large-eddy simulation of turbulent combustion. Line images obtained in turbulent partially premixed (Sandia) flames are used to analyze the scalar and temperature dissipation rates conditional on the scalar and temperature, which must be correctly modeled in LES. The results show that for fully burning SGS fields with small and large SGS variance the scalar and temperature dissipation structures are consistent with those in quasi-equilibrium distributed reaction zones and strained laminar flamelets, respectively. For extinguished SGS fields, the scalar dissipation increases with SGS variance. The temperature dissipation is similar for small and large SGS variance but have different spatial structures. The results in the present study show that it is important for combustion models to predict both distributed reaction zones and flamelets as well as their extinction. Specifically, mixing models for FDF methods need to be able to account for the different SGS temperature structures and the SGS mixing time scales resulted from the different SGS mixture fraction structures.

TECHNICAL DISCUSSION

Turbulent mixing and turbulence-chemistry interaction are key processes in turbulent combustion. Accurate predictions of turbulent flames depend critically on correct modeling of these processes. In large-eddy simulation (LES) of turbulent combustion mixing by the large, resolved scales is computed. At the same time, the subgrid-scale (SGS) scalar mixing and the resulting instantaneous distribution of scalar values in each grid volume, the species filtered joint mass density function (FMDF) must be faithfully represented in order to accurately predict the chemical reaction rate[1, 2], which requires knowledge of SGS mixing and its interaction with chemistry.

Our recent studies ([3, 4, 5, 6, 7, 8]) have shown that the SGS scalar at a fixed location has qualitatively different filtered density function (FDF) shapes and structures depending on the *instantaneous* SGS scalar variance. When the SGS variance is small compared to its mean value, the SGS scalar has close to Gaussian distributions, indicating well mixed SGS scalar fields. When the SGS variance is large compared to its mean value, the SGS scalar has bimodal distributions, indicating highly nonpremixed SGS scalar fields. In a nonpremixed flame this would indicate that the fuel lean and rich regions of the SGS fields are highly segregated. There is a sharp interface separating the two regions, across which there is a large scalar value jump (can be as large as the integral-scale fluctuations). The conditional SGS structure on average resembles that of a counter-flow diffusion flame, which is a model for laminar flamelets.

The well-mixed and the highly nonpremixed SGS mixture fraction fields can potentially have strong influences on the flame structure. In this study we investigate the effects of the SGS mixture fraction structure on the conditional scalar dissipation rate and the temperature dissipation rate in turbulent partially premixed flames, which evolve the filtered joint mass density function of mixture fraction and temperature dissipation:

$$F_{\xi TL}(\hat{\xi};\mathbf{x},t) = \langle \rho(\mathbf{x},t)\delta(\xi-\hat{\xi})\delta(T-\hat{T})\rangle_\ell = \int \rho(\mathbf{x}',t)\delta(\xi-\hat{\xi})\delta(T-\hat{T})G(\mathbf{x}-\mathbf{x}')d\mathbf{x}', \quad (1)$$

where ξ, T, $\hat{\xi}$, and $\hat{T}$ are the mixture fraction, temperature, and their sample-space variables, respectively. ρ is the fluid density. The subscripts ℓ and L denote conventional and Favre filtered variables, respectively. The knowledge of these dissipation terms is a first step in understanding the SGS turbulence-chemistry interaction and an important step toward understanding the SGS mixing of multiple reactive scalars.

Experimental data and processing procedures

We use experimental data obtained in piloted turbulent partially premixed methane flames with a 1:3 ratio of CH_4 to air by volume (Sandia flame D and E, see [11, 12]). Their measurements employed combined line-imaging of Raman scattering, Rayleigh scattering, and laser-induced CO fluorescence. Simultaneous measurements of major species (CO_2, O_2, CO, N_2, CH_4, H_2O, and H_2), mixture fraction (obtained from all major species), temperature, and the radial component of scalar dissipation rate were made. The mixture fraction is calculated using a variation of Bilger's definition, which has been modified by excluding the oxygen terms. The length of the imaging line is 6.0 mm with a pixel spacing of of 0.2 mm.

Measurements of the filtered density functions require spatial filtering of scalar fields. In this research, both one-dimensional filtering will be employed. The filter sizes Δ employed in this work are 3.0 and 6.0 mm.

Results

The scalar dissipation and temperature dissipation are analyzed using their conditional samples. We use the Favre filtered mixture fraction, $\langle\xi\rangle_L = \langle\rho\xi\rangle_\ell/\langle\rho\rangle_\ell$, and the Favre SGS scalar variance,

$$\langle\xi''^2\rangle_L \equiv \frac{1}{\langle\rho\rangle_\ell}\int F_{\xi L}(\hat{\xi};\mathbf{x},t)(\xi-\langle\xi\rangle_L)^2 d\xi = \langle\rho\xi^2\rangle_\ell/\langle\rho\rangle_\ell - \langle\xi\rangle_L^2, \quad (2)$$

as conditioning variables.

The conditional samples of the scalar dissipation conditional on both the mixture fraction and temperature, $\{\chi|\xi,T\}_\ell$, at $x/D = 7.5$ for small SGS variance is shown in Fig. 1(a). The SGS flame is essentially fully burning with very few extinguished samples. Fluid parcels having temperatures close to the equilibrium values have low scalar dissipation rates. Higher scalar dissipation rate values generally correspond to reductions of temperature from the equilibrium values. The amount of reduction, however, does not depend strongly on the mixture fraction values. This is consistent with the weak dependence of the conditionally filtered scalar dissipation $\langle\chi|\xi\rangle_\ell$ on ξ under the same condition. Because the conditional SGS flame is likely in the form of quasi-equilibrium distributed reaction zones, the temperature-scalar-dissipation correlation for a fixed mixture fraction is consistent with the expectation that in a quasi-equilibrium distributed reaction zones the temperature decreases as the scalar dissipation increases[9].

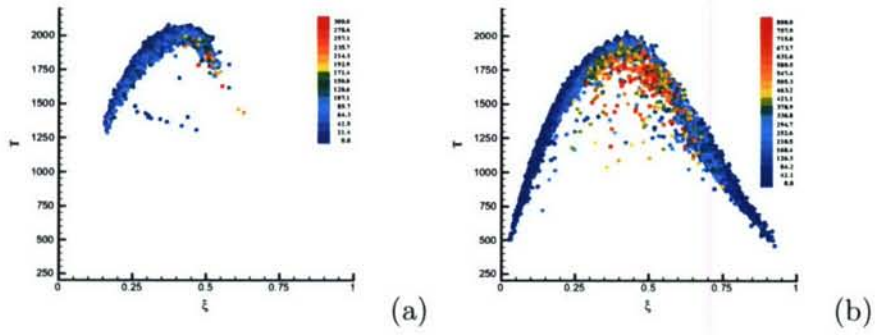

Figure 1: The mean conditionally filtered scalar dissipation conditional on both the mixture fraction and temperature, $\langle \chi | \xi, T \rangle_\ell$, for $\Delta = 3.0mm$ and $\langle \xi \rangle_L = \xi_s$ at $x/D = 7.5$ in flame D. The χ values are given in the legend. (a) $\langle \xi''^2 \rangle_L = 0.001$ and (b) $\langle \xi''^2 \rangle_L = 0.024$

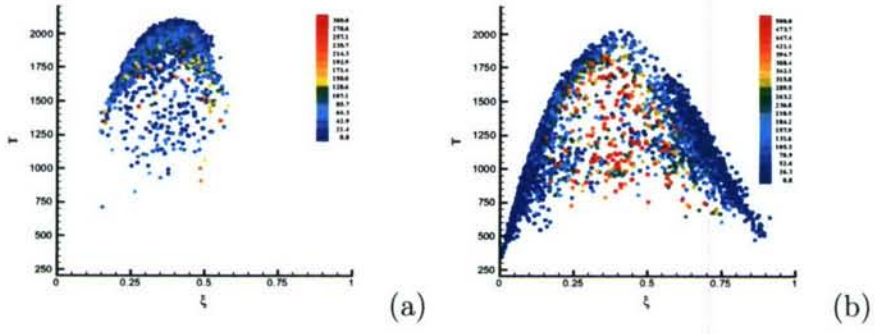

Figure 2: The mean conditionally filtered scalar dissipation conditional on both the mixture fraction and temperature, $\langle \chi | \xi, T \rangle_\ell$, for $\Delta = 3.0mm$ and $\langle \xi \rangle_L = \xi_s$ at $x/D = 15$ in flame D. The χ values are given in the legend. (a) $\langle \xi''^2 \rangle_L = 0.001$ and (b) $\langle \xi''^2 \rangle_L = 0.024$

The results for large SGS variance (Fig. 1b) is qualitatively different from that for small SGS variances. The scalar dissipation is generally small for very lean and rich mixtures and is large for slightly rich SGS mixtures near $\xi = 0.45$ (the stoichiometric mixture fraction $\xi_s = 0.35$) . This is consistent with the bell-shaped conditional dissipation under the condition of large SGS variance and the existence of the diffusion layer in the flame. The temperature near ξ_s is lower than the equilibrium values. At this downstream location there is little extinction; therefore, the temperature reductions in the diffusion layer are largely due to the straining of laminar flamelets.

The results for $x/D = 15$ (Fig. 2) show a large number of extinguished samples with very low temperatures ($< 1300K$). When the SGS variance is small, the dissipation rate increases with decreasing temperature for the burning samples. The dependence is insensitive to the ξ values, similar to the results shown in Fig. 1(a). For the extinguished samples the dissipation rate is generally well below the extinction rate for steady laminar flamelets.

The conditional scalar dissipation samples at $x/D = 15$ for large SGS variance is shown in Fig. 2(b). Similar to the results at $x/D = 7.5$, the dissipation is insensitive to the mixture fraction value and increases with decreasing temperature for the fully burning samples. However, this figure shows a large number of extinguished samples with large scalar dissipation values, in contrast to the low dissipation for extinguished samples for small SGS variance. The scalar dissipation appears even to increases for lower temperature. Because diffusion layer exists under the condition of large SGS variance in which scalar dissipation is large, these extinction events are most likely flamelet extinction.

The conditional samples of the temperature dissipation conditional on both the mixture

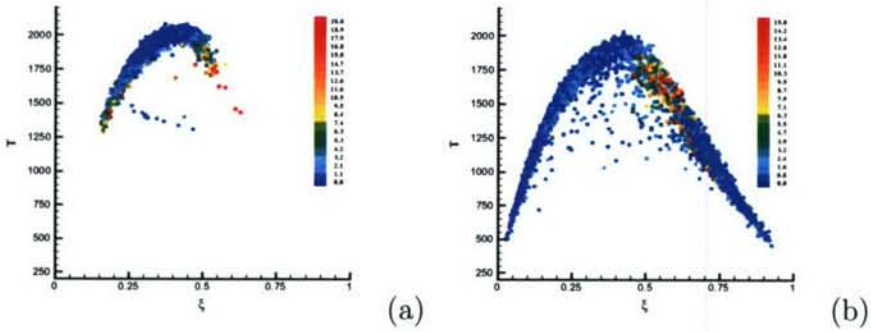

Figure 3: The mean conditionally filtered temperature dissipation conditional on both the mixture fraction and temperature, $\langle \chi_T | \xi, T \rangle_\ell$, for $\Delta = 3.0mm$ and $\langle \xi \rangle_L = \xi_s$ at $x/D = 7.5$ in flame D. The χ_T values are given in the legend. (a) $\langle \xi''^2 \rangle_L = 0.001$ and (b) $\langle \xi''^2 \rangle_L = 0.024$

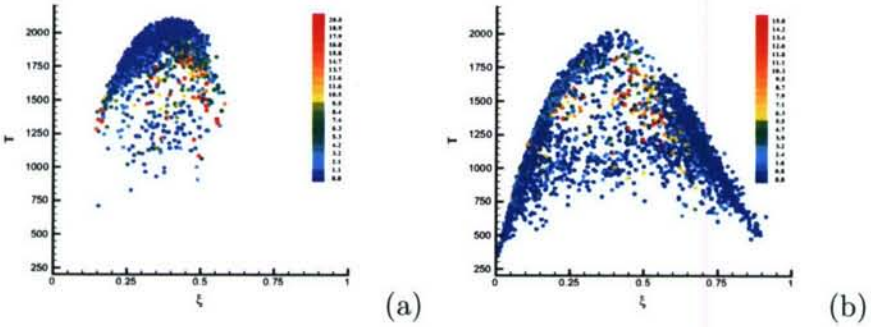

Figure 4: The mean conditionally filtered temperature dissipation conditional on both the mixture fraction and temperature, $\langle \chi_T | \xi, T \rangle_\ell$, for $\Delta = 3.0mm$ and $\langle \xi \rangle_L = \xi_s$ at $x/D = 15$ in flame D. The χ_T values are given in the legend. (a) $\langle \xi''^2 \rangle_L = 0.001$ and (b) $\langle \xi''^2 \rangle_L = 0.024$

fraction and temperature, $\{\chi_T | \xi, T\}_\ell$, at $x/D = 7.5$ for small SGS variance is shown in Fig. 3(a). Near ξ_s the flame reaches the local maximum temperature, leading to the lowest temperature dissipation. Away from ξ_s the temperature dissipation is small near the equilibrium curve and increases when the temperature decreases. The similarity between the conditional temperature dissipation and the conditional scalar dissipation samples for the rich and lean mixtures is because for mixture fraction values away from ξ_s, there exists correlation between ξ and T near the equilibrium curve (positive for $\xi < \xi_s$ and negative for $\xi > \xi_s$). Therefore, the temperature dissipation increases with the scalar dissipation for these mixture fraction values.

The conditional temperature dissipation samples for large SGS variance at $x/D = 7.5$ is shown in Fig. 3(b). The very rich and lean mixtures separated by the diffusion layer have low temperature dissipation because the temperature in laminar flamelets are closely related to the scalar dissipation, which is low for these SGS mixtures. The few extinguished samples generally have small temperature dissipation values because mixing tends to reduce temperature gradient. Large temperature dissipation values occur in rich mixtures with ξ values ranging from 0.5 to 0.65 near the equilibrium curve, but not in the lean mixtures. This is in contrast to the result for small SGS variance in Fig. 3(a).

At $x/D = 15$ the scalar dissipation and temperature dissipation for the fully burning samples (Fig. 4) are similar to those at $x/D = 7.5$, i.e., similar to distributed reaction zones and laminar flamelets, respectively. The extinguished samples with very low temperatures ($< 1300K$) generally have small temperature dissipation values because the temperature gra-

dient is reduced due to mixing. The samples with intermediate temperatures (1300-1600K) have the highest temperature dissipation and the dependence on the mixture fraction is weak for both small and large SGS scalar variance values. The seemingly similar temperature dissipation structures for these samples, however, result from different SGS mixture fraction structures.

For small SGS variance the SGS mixture fraction is well mixed. Away from the equilibrium the temperature does not follow the equilibrium relationship ($T_e = T_e(\xi)$), therefore, we expect little dependence of temperature dissipation on the mixture fraction. For intermediate temperatures there is intense SGS mixing as indicated by the relatively high values of χ (Fig. 4a), resulting in high temperature dissipation. Consequently, the scalar dissipation and the temperature dissipation have similar dependence on ξ and T for these temperature. For low temperatures, the SGS mixing has progressed much further, resulting in more uniform temperature and low dissipation. In addition, lower diffusivities resulted from the reduced temperature can also contribute to the lower dissipation rates.

For large SGS variance, the large temperature dissipation and its lack of dependence on the mixture fraction for intermediate temperatures are likely to be the results of both large scalar dissipation in the cliffs and the temperature gradient along the iso-ξ surface developed due to extinction (e.g, near flame holes). For very low temperatures, the extinguished regions are expected to be large and the temperature gradient in the cliff has been smoothed out, as indicated by the low temperature profiles in Fig. 2(d), which show mixing of cold fuel and oxidizer without reaction, resulting in reduced temperature dissipation. Contrary to the case of small SGS variance, the dependence of the temperature dissipation on ξ and T differs from that of the scalar dissipation (Fig. 4b), a result of different SGS mixture fraction structures.

References

[1] S. B. Pope. Computations of turbulent combustion: Progress and challenges. In *Proceedings of the 23rd Symposium (International) on Combustion*, pages 591–612. 1990.

[2] P. J. Colucci, F. A. Jaberi, P. Givi, and S. B. Pope. *Phys. Fluids*, 10 (1998) 499–515.

[3] C. Tong. *Phys. Fluids*, 13 (2001) 2923–2937.

[4] A. G. Rajagopalan and C. Tong. *Phys. Fluids*, 15 (2003) 227–244.

[5] D. Wang and C. Tong. *Phys. Fluids*, 14 (2002) 2170–2185.

[6] D. Wang, C. Tong, and S. B. Pope. *Phys. Fluids*, 16 (2004) 3599–3613.

[7] D. Wang and C. Tong. *Proc. Combust. Inst.*, 30 (2005) 567–574.

[8] D. Wang, C. Tong, R. S. Barlow, and A. N. Karpetis. *Proc. Combust. Inst.*, 31 (2007) 1533–1541.

[9] R. W. Bilger. The structure of turbulent nonpremixed flames. In *Proceedings of the Twenty-Second Symposium (International) on Combustion*, pages 475–488. 1988.

[10] N. Peters. *Turbulent Combustion.* Cambridge University press, Cambridge, England, 2000.

[11] A. N. Karpetis and R. S. Barlow. *Proc. Combust. Inst.*, 29 (2002) 1929–1936.

[12] A. N. Karpetis and R. S. Barlow. *Proc. Combust. Inst.*, 30 (2005) 665–672.

PLASMA-PROPELLANT INTERACTION STUDIES

Grant Number DAAD19-03-1-0340

Principal Investigators: Stefan T. Thynell and Thomas A. Litzinger

Department of Mechanical and Nuclear Engineering
The Pennsylvania State University
University Park, PA 16802

SUMMARY

The overall objective is to gain insights about of the various chemical and physical processes that occur during ignition of a solid propellant by a high-pressure and high-temperature plasma. The plasma is formed within a hydrocarbon capillary by an electrical discharge process. The plasma emerges into stagnant air as an underexpanded supersonic jet. Two experimental approaches are applied. A triple-quadrupole mass spectrometer is employed to examine species from the plasma and the pyrolysis products from the propellant generated by interactions with the plasma. A fast-response heat flux gauge has been designed and utilized to determine the transient variation of the radiant heat flux, with specific emphasis on the UV to near-visible components. The results show that the use of different trigger-wire and capillary materials yields significant differences in ignition and combustion of JA2 and transparent JA2, as well as in the radiative heat flux levels.

TECHNICAL DISCUSSION

Plasma-driven Ignition and Combustion of JA2 and Transparent JA2

We have continued our work to establish the effects of capillary material on plasma-propellant type interactions, including ignition and ablation studies. Progress over the past year was hampered by the departure of Dr. Li, who had a great deal of experience with the plasma-propellant project. Still we were able to obtain some interesting results.

The ignition and combustion studies were conducted in a small chamber with a volume of 8.2cm^3. The charging voltage was set at 4kV, corresponding to a peak power output about 19-20 kW, and a total energy of approximately 1.6 kJ. The distance from the exit to the sample was 3mm for all combustion tests to ensure ignition. Figure 1 illustrates the flow structure typical of such small distances between the nozzle exit and the sample. It shows the intimate contact of the plasma on the surface, which is expected to lead to the dominance of convective energy transfer over radiative transfer.

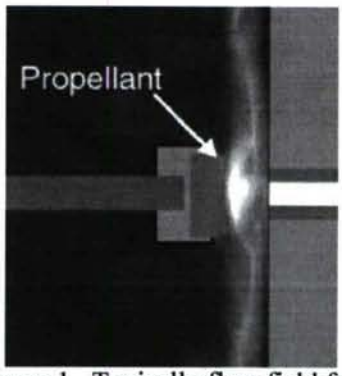

Figure 1. Typically flow field for small sample-to-nozzle distances

Figure 2 shows the combustion pressure traces for both JA2 and transparent JA2 solid propellants. The pressure traces show more rapid pressure rise for JA2 than for transparent JA2, contrary to trends reported by other research groups. The configurations of our tests in which convective heat transfer is expected to dominate may be

reason for this trend. The faster rate of pressure rise for the JA2 indicates that more mass is initially ablated from its surface compared to transparent JA2. To confirm this trend, ablation tests were conducted with the two materials.

The ablation experiments were conducted in open air so that the sample did not ignite. Also the sample to nozzle exit condition was extended slightly to 5mm. An 8mm×8mm test sample, weighing nominally 260mg, was cut from a thin (2.5mm) sheet of propellant and placed on the sample holder near the plasma exit. The charging voltage was set at 4kV. In these tests two different capillary materials, polyethylene and Teflon were used; they were selected based on previous heat transfer tests.

Figure 3 presents the results of the ablation tests for the two propellants and the two materials. Consistent with expectations, the JA2 has greater ablated mass than transparent JA2 regardless of the capillary material used. Previous measurements of radiative heat flux by Das and Thynell found that it was approximately 10% larger for the Teflon capillary than for polyethylene, yet the Teflon tests showed substantially smaller erosion. The mass loss of the capillary was also measured in these tests and the results showed larger mass losses for the polyethylene capillary, indicating greater mass flow from the nozzle. Thus the trends in the ablated mass are consistent with expectations that convective heat transfer dominants over radiation transfer in our test configuration.

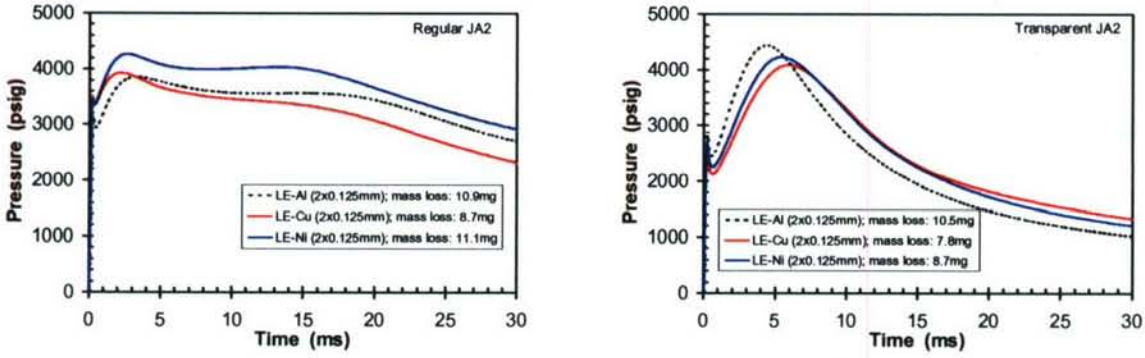

JA2 Transparent JA2

Figure 2: Comparison of combustion pressure traces for JA2 and transparent JA2

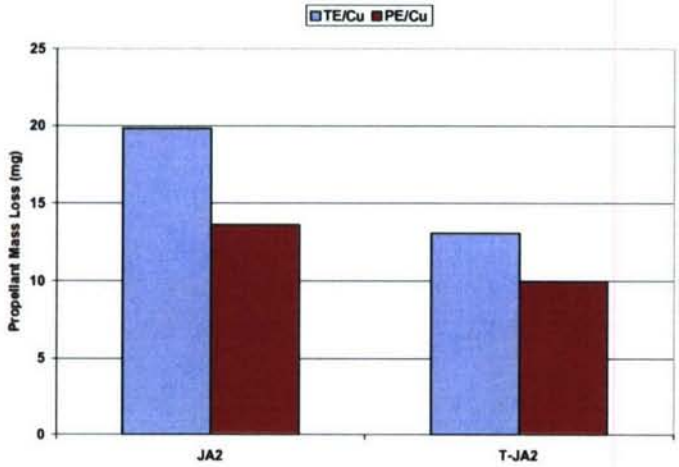

Figure 3. Ablated mass loss for 4kV tests

Testing is underway at a higher energy level of approximately 2.4kJ corresponding to a charging voltage of 5kV. Initial results indicate that the JA2 has larger ablated mass than transparent JA2 for the polyethylene capillary: 42 mg for JA2 and 16 mg for transparent JA2. Ablated masses for the Teflon capillary are inconsistent, apparently because the sample is igniting in some cases, causing nearly complete consumption of the sample. However, those tests also indicated that ablated masses are higher for JA2.

Radiant Heat Flux Measurements

Recent investigations have convincingly proved the effectiveness of electrothermal-chemical (ETC) ignition system in providing fast, and repeatable ignition and combustion of solid propellant. Overall objective of the present research is to gain useful insight about the various physical and chemical processes involved in the ETC ignition of solid propellant. ETC ignition system uses high-temperature, high-pressure, capillary-sustained plasma jet that impinges directly over the propellant. Part of the present research focuses on understanding the role of radiative heat transfer during ETC ignition. Particular interests comprise measurement of radiative flux, and electrical parameters during capillary discharge as well as the measurement of stagnation pressure during ETC plasma impingement.

The phenomena of ETC ignition involves high-temperature, high-pressure, and highly transient environment with substantial electromagnetic noise. Any measurement in this environment can be prohibitively difficult. Our early effort, however, resulted in the development of a thin film heat flux gage, and an inverse data reduction scheme that successfully captured the transient variation of the radiant flux. Initial success of this thin film heat flux gage prompted further development of a newly designed heat flux gage, and a two-dimensional inverse data reduction scheme that can be used in radiant flux estimation for a wide range of plasma energy level. While the previous reports described the heat flux measurement details, material dependence studies, and the performance of the higher order data reduction scheme, present report will provide results from the parametric studies on radiative heat transfer from a capillary discharge.

The transient trends of current, voltage, radiant flux, and pressure have been reported earlier. While these trends are quite repeatable, and do not vary much with material or energy level, the peak and average values of these quantities changes substantially with capillary or trigger wire materials, and energy level. Experiments are conducted for plasma charging voltage ranging from 2.5kV (0.6kJ) to 7.5kV (5.4kJ). ETC plasma, generated by exploding a thin metallic trigger wire and sustained by ablation of a hydrocarbon capillary, emerged from a Cu nozzle to impinge on a stagnation plate equipped with an array of heat flux gages. Gages were manufactured by sputtering 80nm Pt over 500μm sapphire substrate. Nozzle exit to stagnation plate distances were varied between 5 mm to 50 mm. Three different capillary materials, Polyethylene (PE), Lexan (LE), and Teflon (TE) were combined with three different wire materials Cu, Al, and Ni.

Figures 1 and 2 show the variation peak radiant heat flux with charging voltage, and nozzle outlet to stagnation plate distance. Similarly, Figs. 3 and 4 show the variation of peak stagnation pressure. To ensure the repeatability of the experiments, error bars are placed at $\pm 2\sigma$, where σ indicates the standard deviation from three repeated measurements. The results consistently follow the previous observations and indicate that high ablation provides high stagnation pressure but low radiant flux for a wide range of plasma energy levels. These phenomena can be explained by the possibility of developing optically thicker plasma as the ablation increases. It is also observed that LE+Al combination provides maximum radiant flux, while TE+Ni combination provides maximum stagnation pressure.

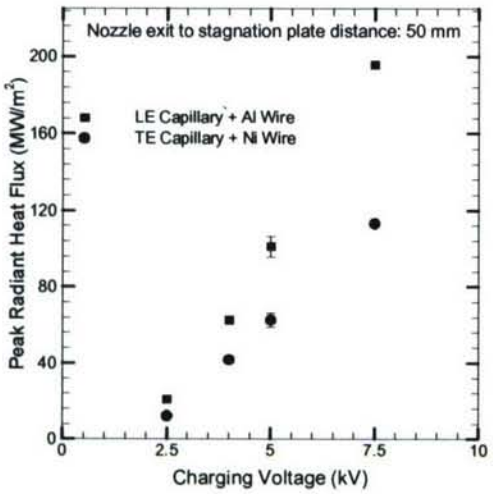

Figure 1. Variation of peak radiant heat flux with charging voltage for a nozzle exit to stagnation plate distance of 50mm.

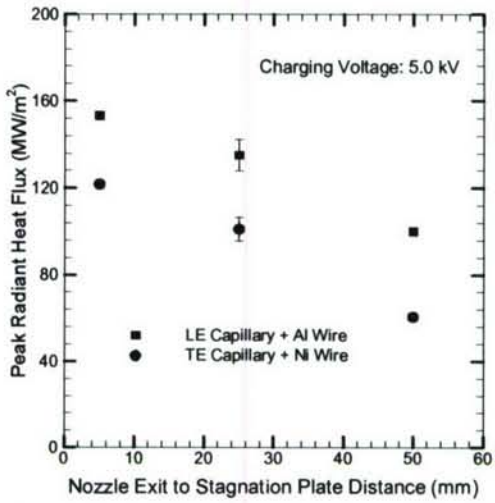

Figure 2. Variation of peak radiant heat flux with nozzle exit to stagnation plate distance at a fixed charging voltage of 5.0kV.

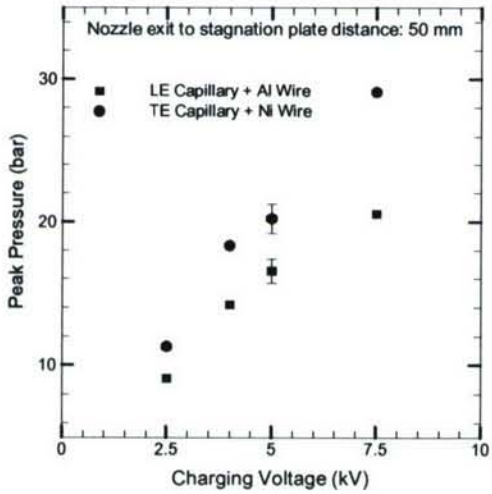

Figure 3. Variation in stagnation pressure with charging voltage at a nozzle exit to stagnation plate distance of 50mm.

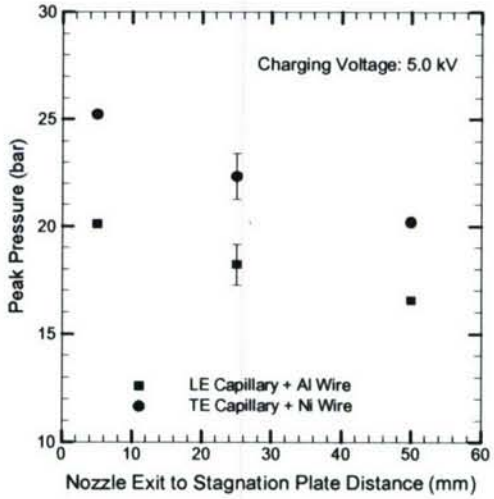

Figure 4. Variation in stagnation pressure with nozzle exit to stagnation plate distance at a charging voltage of 5.0kV.

Further computational and experimental investigations are in progress to investigate the effect of radiant flux, and the possibility of radiative ignition of solid propellant. A new experimental setup has been developed that can discharge higher energy level plasma with a longer pulse length. Initial tests on this new setup have been accomplished. Final results are awaited.

Technical Interactions

Over the last year we have several communications with the Boyd/Keidar group at Michigan, which has begun modeling of the results of our experiments. They published a paper in January of 2007 based on our earlier work and have additional modeling efforts underway.

TWO STAGE AUTOIGNITION IN DIESEL ENGINES RUNNING ON COMMERCIAL LOW-SULFUR DIESEL FUEL

Grant/Contract Number DAAD19-03-1-0338

Principal Investigators: Naeim A. Henein, Dinu Taraza, Nabil Chalhoub, Marcis Jansons

Address/Institution: Wayne State University, Detroit, Michigan

SUMMARY/OVERVIEW:

The adaptation of military engines for the use of different fuels requires further insight into the development of autoignition and combustion processes. In this study, the ignition and combustion of low-sulfur fuel were experimentally investigated using an optically-accessible engine. The study is focused on the operating condition for which autoignition occurs in two distinct stages. The influence of injection pressure, swirl number and speed are investigated, showing that at low compression temperature the injection pressure plays the dominant role in the autoignition process.

TECHNICAL DISCUSSION:

Exhaust gas recirculation (EGR) is a well-established method for the reduction of nitrogen oxide formation due to charge dilution and decreased combustion temperatures. Experiments undertaken in a high-speed, small-bore (diameter 79.5mm, stroke 85mm), single-cylinder diesel engine showed that at high EGR rates, the autoignition mechanism changes from the typical single stage to a two-stage process separated by the negative temperature coefficient (NTC) regime.

The phenomena responsible for the transition from a single to a two-stage process were investigated by analyzing chemiluminescent images and ultraviolet (UV) spectra in an optically-accessible engine. The experimental setup is shown in Fig. 1. The engine has a bore and stroke of 85mm x 90mm, with geometric compression ratio of 15:1. The images were taken through a 45^0 mirror and fused-silica window into the 40mm diameter cylindrical bowl of the piston.

Narrow-band filters together with an intensified CCD camera were used to capture filtered and broadband UV signals. A spectrometer was coupled to the ICCD camera to observe the emission spectrum.

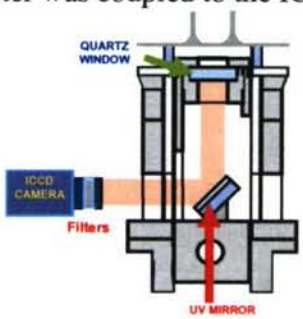

Fig. 1 Experimental setup

Figure 2 presents the cylinder pressure, apparent rate of heat release (ARHR), and injector needle lift together with broadband UV images at 2000RPM, 800bar injection pressure and swirl ratio of 4.5. It is observed that the intensity of chemiluminescence closely correlates with the ARHR during the first-stage ignition process, both clearly showing a decrease in the NTC regime.

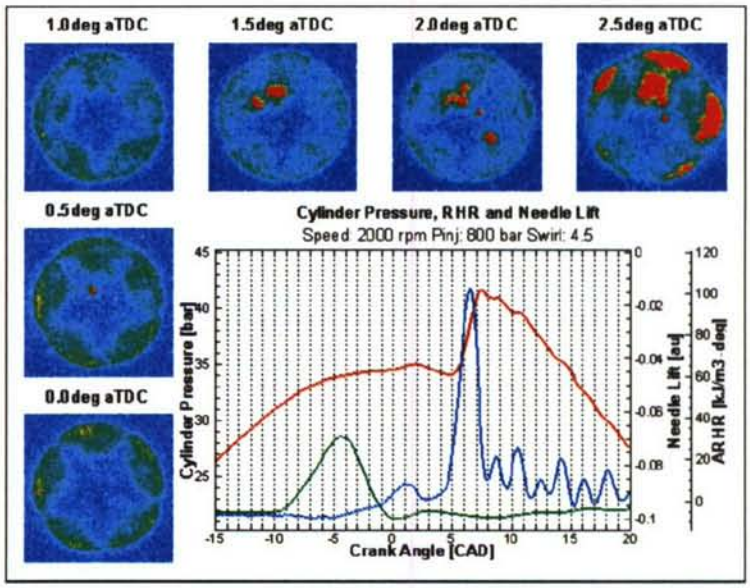

Fig. 2 Broadband UV chemiluminescence correlation with ARHR

For this running condition, the earliest spectrum was obtained at 3.5deg. after top-dead center (aTDC). This corresponds to the end of the NTC regime and beginning of premixed combustion, showing a strong signal for OH at 309nm, with distinct peaks of HCHO at 354, 395, 422 and 443nm, confirming the presence of aldehydes during the first-stage ignition process (Fig. 3).

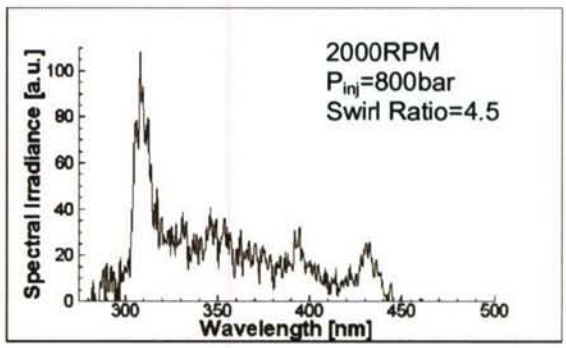

Fig. 3 Spectrum at 3.5deg. aTDC

This two-stage autoignition process was also observed at reduced engine speed. In the next series of experiments, narrow-band filters were used with the ICCD cameras to select signals from specific components in the cylinder gas mixture. Figure 4 presents chemiluminescent signal filtered at 431, +/- 5nm at 1000RPM and the same injection pressure of 800bar and swirl ratio of 4.5. This filter covers both HCHO and CH lines in this range, and the images show the peak intensity at the maximum ARHR of the first stage. It is assumed that this is mostly due to HCHO emission.

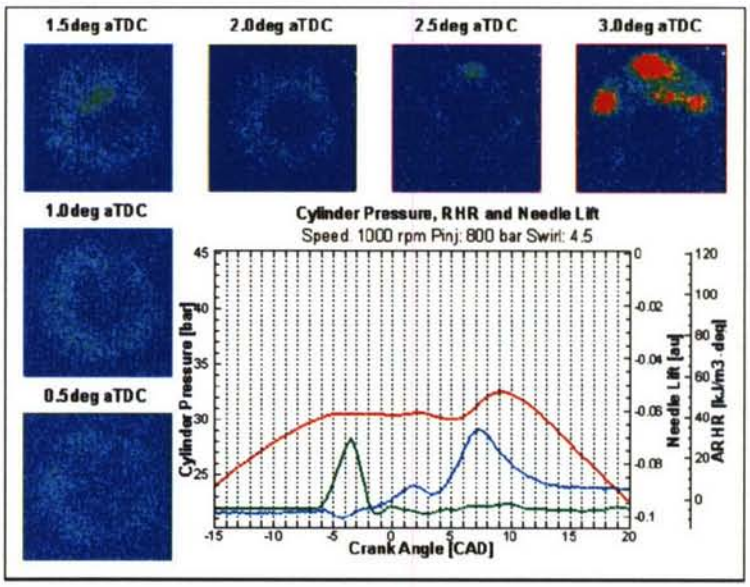

Fig. 4 Chemiluminescence filtered at 431 +/- 5nm

Fig. 5 Correlation of ARHR with chemiluminescence at 431 +/- 5nm

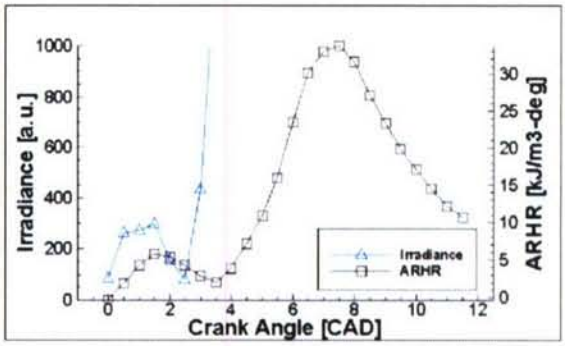

The chemiluminescence observed at 431 +/- 5nm is further analyzed by the spatial integration of recorded signal over the frame. Figure 5 shows a correlation of the intensity of the filtered spatially-integrated images with the ARHR, with both decreasing in the NTC regime. Figure 6 shows chemi-luminescent images filtered at 309 +/-5 nm, at 1000RPM, injection pressure of 800bar and swirl ratio of 4.5 The first detectable signal at this OH band occurs at 3.5deg. aTDC, just at the start of the heat release due to premixed combustion and increases with the ARHR as combustion progresses.

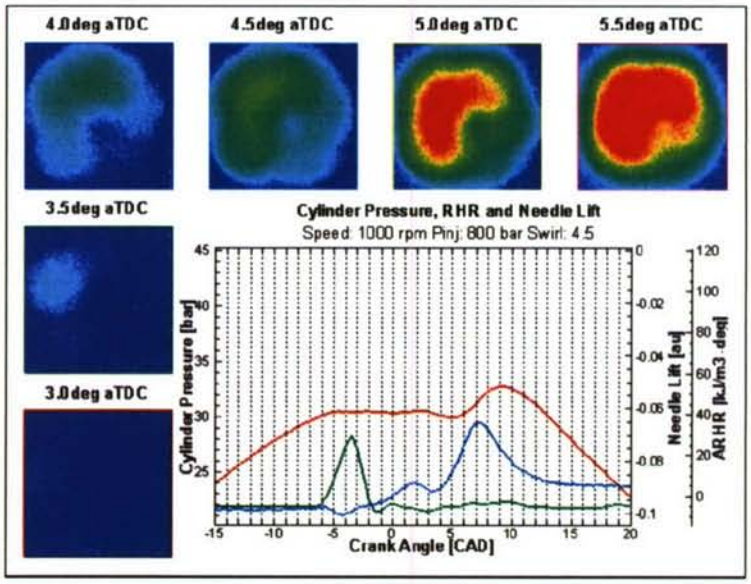

Fig. 6 Chemiluminescent images filtered at 309 +/- 5nm

The injection pressure was reduced to 400bar, maintaining the engine speed of 1000RPM and the swirl ratio of 4.5. Chemiluminescence filtered at 431 +/-5nm shows a continuous increase as the ARHR progresses (Fig. 7), in contrast to the results obtained at 800bar injection pressure, where a net decrease of the chemiluminescence intensity was observed in the NTC regime (Fig. 4-5).

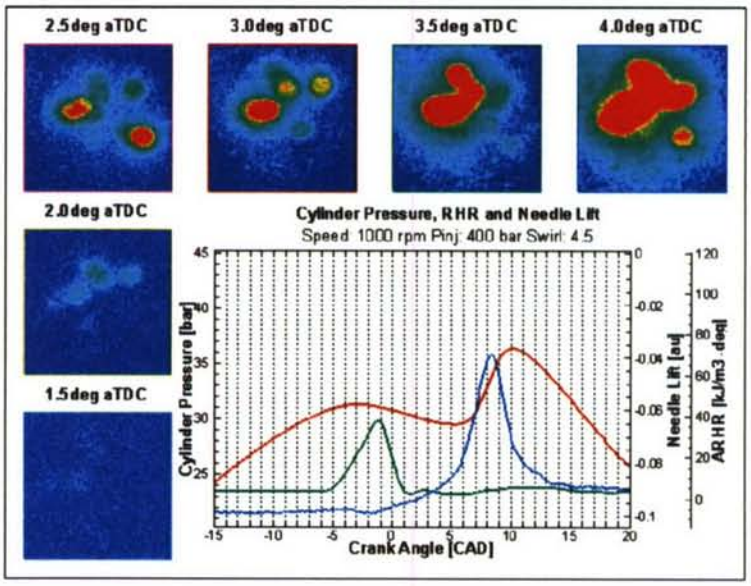

Fig. 7 Chemiluminescent images filtered at 431 +/- 5nm

Analysis of the spectra for this engine operating condition reveals that at an early stage of combustion (4deg. aTDC) a large amount of luminous radiation is present at longer wavelengths, presumably due to thermal emission of soot particles (Fig. 8). In contrast, at the same speed and swirl number but at 800bar injection pressure, there is almost no luminous radiation at wavelengths greater than 460nm (Fig. 9).

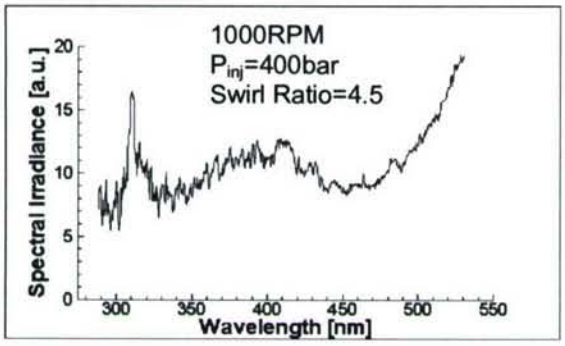

Fig. 8 Spectrum at 4.0 deg. aTDC

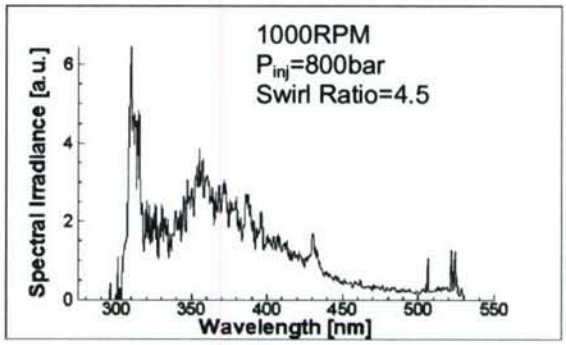

Fig. 9 Spectrum at 4.0 deg. aTDC

At low compression temperature and high injection pressure (800bar), the autoignition process occurs in two stages. Chemiluminescent HCHO emission follows the ARHR, showing a decrease in the NTC region. Chemiluminescent HCHO emission peaks at the maximum ARHR of the first stage of ignition. OH emission starts at the beginning of the premixed combustion and increases with the ARHR. Ignition occurs near the wall in the vicinity of fuel jet impingement, with the visible flame concentrated at the periphery of the combustion chamber. The combustion is dominated by a premixed phase with minimal subsequent mixing and diffusion-controlled combustion.

Decreasing the injection pressure to 400bar results in a single-stage autoignition process that occurs towards the center of the combustion chamber with no apparent correlation with the fuel spray. Combustion spreads throughout the combustion chamber volume with many luminous regions showing diffusion burning.

ABSTRACTS OF RESEARCH NOT PRESENTED

LARGE EDDY SIMULATIONS OF SUPERCRITICAL MIXING LAYERS BASED ON SUBGRID SCALE MODELS EXTRACTED FROM DIRECT NUMERICAL SIMULATIONS

(Contract Number (with NASA): AFOSR- NMO715852)
Principal Investigator: Dr. Josette Bellan

Jet Propulsion Laboratory
California Institute of Technology
4800 Oak Grove Drive
MS 125-109
Pasadena, Ca 91109-8099

SUMMARY/OVERVIEW:

The objective of this study is the fundamental understanding of fuel disintegration and mixing in a supercritical environment (relative to the fuel) in order to determine parameter regimes advantageous to mixing. The approach is based on the future goal of developing a model for a supercritical, turbulent jet mixing with surrounding fluid. The method is one that combines the modeling of supercritical fluids with a systematic development based on the Large Eddy Simulation (LES) approach. This systematic development includes a consistent protocol based upon Direct Numerical Simulations (DNS) for developing a Subgrid Scale (SGS) Model appropriate to supercritical fluids, rather than choosing in an ad hoc manner an existing SGS model developed under assumptions inconsistent with supercritical fluid behavior. This SGS model should be used in future studies of supercritical turbulent jets utilizing the LES methodology.

TECHNICAL DISCUSSION

The analysis performed in the initial year showed that the Large Eddy Simulation (LES) conservation equations derived through filtering the Direct Numerical Simulation (DNS) equations contain several types of terms: (1) terms which are akin to those of the DNS equations except that they are now functions of the filtered dependent variables, and thus are called "resolved" because the equations are solved at the scale of the filtered variables variation, (2) subgrid scale fluxes of momentum, enthalpy and species, and (3) terms that are gradients of the difference between a LES (i.e. filtered) quantity and the DNS mathematical form of the same quantity calculated as a function of the filtered variables, and other terms such as the difference between triple correlation terms also appearing in the energy equation. Type (1) terms are the basic terms in the LES equations. Type (2) terms are the classical subgrid scale (SGS) fluxes that are usually modeled in the LES equations to reproduce the behavior of the scales that have been filtered; the modeling of these terms was discussed in our first year report. Type (3) terms are usually neglected without justification other than to state that they are believed negligible – these are called "the LES assumptions".

However, using our DNS temporal binary-species mixing layer transitional-state database (see Fig. 1 and Table 1; details of the DNS and flow behavior are in [1–3]), we identified **two types of non-negligible LES assumptions**. Both of these additional terms are directly associated with the high density-gradient magnitude (HDGM) regions that are a distinctive feature of

supercritical mixing flows. Because supercritical fully turbulent flows [4-6] exhibit the same HDGM features, with density gradients of the same order of magnitude or even higher than our DNS transitional database, this shows that this database is relevant to turbulence modeling.

The **first type** of terms appears in the momentum equation and is the difference between the filtered pressure and the pressure calculated as a function of the filtered field; this term is prominent only under the strong real-gas and mixture non-ideality conditions of heptane/nitrogen (HN) DNS; the modeling of these terms was discussed in our first year report.

The **second type** of terms is dominant in the energy equation and is the difference between the filtered heat flux and the heat flux calculated as a function of the filtered flow field. The term is significant only for the near-perfect-gas near-ideal-mixture conditions of oxygen/hydrogen (OH) DNS, meaning that it could be significant for species not studied here when only slight departures from perfect-gas ideal-mixture conditions exist. For the oxygen/helium (OHe) DNS – moderate departures from perfect gas and near-ideal mixture – the situation was intermediary between HN and OH. This strong departure from subcritical flows, even for small departures from perfect gas, is due to the strongly nonlinear real-gas equation of state (EOS); the essence of nonlinearity is that small changes in one variable may induce very large changes in another variable. The strongly nonlinear real-gas EOS should be contrasted with the weakly nonlinear perfect-gas EOS. Although when deriving the LES equations one should also filter the EOS, the relatively weakly nonlinear perfect-gas EOS leads to valid assumptions which become invalid for the strongly nonlinear EOS. The modeling of the second type of terms is discussed below.

When examining the heat flux term

$$\mathbf{q}_{IK}(\psi) = C_Y(\psi)\nabla Y_2 + C_T(\psi)\nabla T + C_P(\psi)\nabla p \tag{1}$$

the difference in complexity between modeling the pressure term difference (first type) and modeling eq. (1) becomes quickly apparent. That is, whereas the pressure p is a function of the thermodynamic primitive variables (vector ψ), $q_{IK}(\psi)$ is a function of both the thermodynamic primitive variables, p, temperature T and mass fraction Y_2 (subscript 2 denotes the heavier species) **and** thermodynamic primitive variable gradients. Under the thermodynamic conditions of this study, the thermal diffusion transport coefficients appearing in C_Y, C_T and C_P cannot generally be expressed as accepted and/or comprehensive functions of thermodynamic variables in ψ [7]. In the present DNS, these coefficients were specified as constants and for computational efficiency, the transport coefficients λ and D were computed from accurate Schmidt and Prandtl number correlations, meaning that the complex dependence of all transport coefficients on thermodynamic variables in ψ has been simplified by a curve fit which makes some explicit dependencies unavailable. Faced with this modeling challenge, **three approaches** were assessed.

In a first approach, the approximation

$$\overline{\mathbf{q}_{IK}(\psi)} \simeq \overline{C_T(\psi)}\nabla T(\overline{\phi}) + \overline{C_P(\psi)}\nabla p(\overline{\phi}) + \overline{C_Y(\psi)}\nabla Y_2(\overline{\phi}) \tag{2}$$

was considered, where ϕ is the vector of conservative variables and the coefficients of eq. (2) were modeled following a Taylor series leading to δ_T, δ_P and δ_Y; for example

$$\delta_T \equiv \frac{1}{2}\frac{\partial^2 C_T}{\partial\phi_m\partial\phi_n}\bigg|_{\psi=\overline{\psi}}\left(\overline{\phi_m\phi_n} - \overline{\phi_m}\;\overline{\phi_n}\right) \tag{3}$$

Since owing to the aforementioned lack of knowledge regarding the transport coefficients dependency on ψ, the analytical functions $C_T(\phi)$, $C_P(\phi)$ and $C_Y(\phi)$ are typically not available, a numerical multivariate differentiation technique was used to obtain the encouraging results plotted in Fig. 2. The upper free-stream discrepancy between the modeled δ_Y and its exact value is not of great concern since ∇Y is null in those regions. However, when these results were used *a priori* in conjunction with a Taylor expansion of the entire heat flux according to eq. (2), the

DNS-extracted difference between filtered heat flux and heat flux calculated from the filtered field did not compare well with δ_i, indicating that this approach may not be appropriate.

The second approach involved the Taylor expansion differentiation applied to the entire heat flux, for each component, but the model again did not duplicate the DNS-extracted result.

A third approach was based on re-thinking the entire modeling methodology when both primitive variables and their gradients are involved. Thus, a Taylor series approach was devised where ϕ and $\nabla\phi$ are treated as independent variables:

$$q_{IKi}(\phi) = \sum_q C_q(\phi)\frac{\partial F_q(\phi)}{\partial x_i} \tag{4}$$

$$F_1(\phi) = T(\phi),\ F_2(\phi) = p(\phi) \text{ and } F_3(\phi) = Y_2, \quad \delta F_q = F_q(\phi) - F_q\left(\overline{\phi}\right) \tag{5}$$

$$\overline{q_{IKi}(\phi)} = \underbrace{\sum_q \overline{C_q(\phi)}\frac{\partial F_q\left(\overline{\phi}\right)}{\partial x_i}}_{\text{Part 1}} + \underbrace{\frac{\partial}{\partial x_i}\sum_q \overline{C_q(\phi)\delta F_q}}_{\text{Part 2}} - \underbrace{\sum_q \overline{\delta F_q \frac{\partial C_q(\phi)}{\partial x_i}}}_{\text{Part 3}} \tag{6}$$

Examination of the DNS database shows that Part 1 contains the bulk of the heat flux and could thus be modeled using the Taylor expansion of $C_q(\phi)$ (Fig. 2). Rigorous computation of Parts 2 and 3 of eq. (6) through a Taylor expansion is not possible because each Part is a sum of numerous terms only one of which is calculable; the other terms involve higher order correlations of ϕ and $F(\phi)$, which are unknown. One pragmatic way of modeling the heat flux would be to include only those terms for which a closed form is available and neglect the other terms. Further *a posteriori* studies will be conducted for a more definitive answer.

1. Okong'o, N. and Bellan, J., *J. Fluid Mech.*, 464, 1-34, 2002.
2. Okong'o, N., Harstad, K. and Bellan, J., *AIAA J.*, 40(5), 914-926, 2002.
3. Okong'o, N. and Bellan J., *Phys. Fluids*, 16(5), 1467-1492, 2004.
4. Chehroudi, B., Talley, D. and Coy, E., paper AIAA 99-0206.
5. Oschwald, M. and Schik, A., *Experiments in Fluids*, 27, 497-506, 1999
6. Polikhov, S. and Segal, C., Subcritical to supercritical jet mixing, paper AIAA-2007-0569.
7. Gonzales-Bagnoli, M. G., Shapiro, A. A. and Stenby, E. H., *Phil. Mag.*, 83(17-18), 2171-2183, 2003.

Name	HN400	HN500	HN600	HN800	OH750	OH550	OH500	OHe600
Species 2	C_7H_{16}	C_7H_{16}	C_7H_{16}	C_7H_{16}	O_2	O_2	O_2	O_2
Species 1	N_2	N_2	N_2	N_2	H_2	H_2	H_2	He
T_2 (K)	600	600	600	600	400	400	235	235
T_1 (K)	1000	1000	1000	1000	600	600	287	287
ρ_1/ρ_2	12.88	12.88	12.88	12.88	24.4	24.4	24.51	12.17
p_0 (atm)	60	60	60	60	100	100	100	100
Re_0	400	500	600	800	750	550	500	600

Table 1. Initial conditions of the Direct Numerical Simulations (DNS) database. In all simulations $M_{c,0} = 0.4$, $\delta_{\omega,0} = 6.859\text{x}10^{-3}$ m (see Fig. 1). For the C_7H_{16}/N_2 layers, $p_r = 2.22$ and $((\rho_2U_2)/(\rho_1U_1)) = 5.276$; for the O_2/H_2 layers, $p_r = 2.01$ and $((\rho_2U_2)/(\rho_1U_1)) = 5.001$ for OH550 and OH750, and $((\rho_2U_2)/(\rho_1U_1)) = 4.951$ for OH500 and for the O_2/He layer $p_r = 2.01$ and $((\rho_2U_2)/(\rho_1U_1)) = 3.500$.

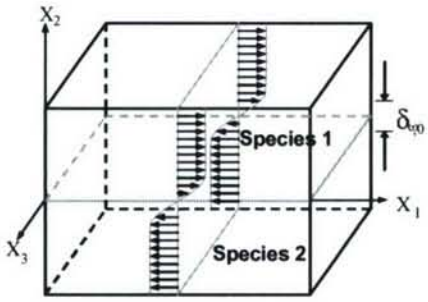

Figure 1. Mixing layer configuration for the DNS listed in Table 1.

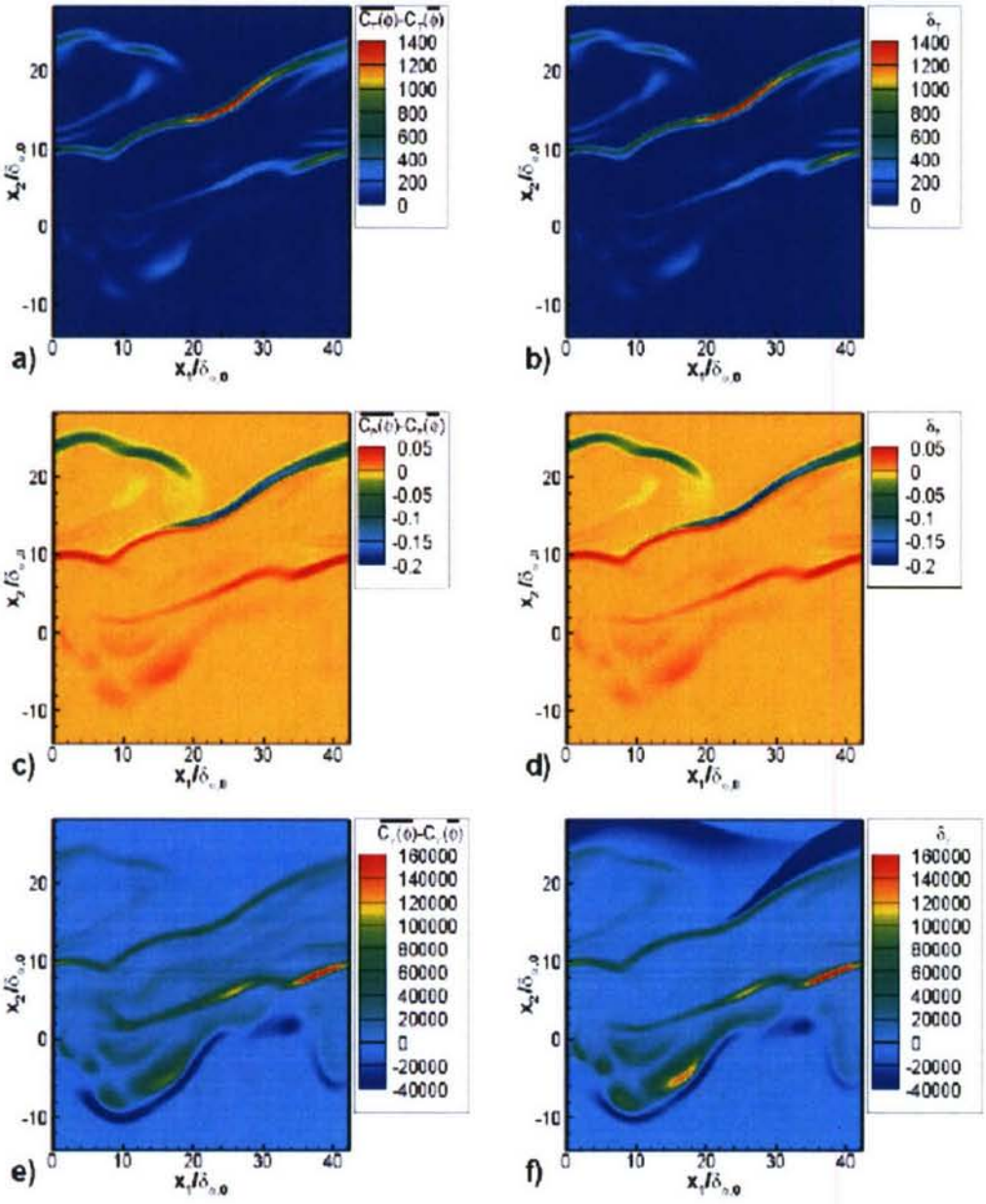

Figure 2. Taylor expansion of the heat flux coefficients C_T, C_P and C_Y of eq. (1) calculated for OH500 using numerical differentiation. a), c) and e) are the DNS-extracted values; and b), d) and f) are calculated using the model of eq. (3) for δ_T, and similar equations for δ_P and δ_Y.

THERMODYNAMIC, TRANSPORT AND CHEMICAL PROPERTIES OF "REFERENCE" JP-8

(Contract Number F1ATA06004G004)

Principal Investigator:
Thomas J. Bruno

Physical and Chemical Properties Division
National Institute of Standards and Technology
Boulder, CO 80305

SUMMARY/OVERVIEW:

The NIST research focuses on measurement of major thermophysical and chemical properties of JP-8, to develop it as a reference fluid. The properties include fluid volatility, density, speed of sound, viscosity and thermal conductivity. In addition, we are assessing the global thermal decomposition of the fluid, primarily to guide our property measurements. The measured properties will be used to develop a predictive surrogate fluid model for real JP-8. Three different samples of JP-8 have been obtained, and measurements are in progress on all three.

TECHNICAL DISCUSSION

Chemical Analysis:

A chemical analysis was done on each of the fluid samples by gas chromatography mass spectrometry ((30 m capillary column of 5% phenyl polydimethyl siloxane having a thickness of 1 μm, temperature program from 90 to 250 °C, 10 °C per minute). Mass spectra were collected for each peak from 15 to 550 RMM (relative molecular mass) units. Chromatographic peaks made up of individual mass spectra were examined for peak purity, then the mass spectra were used for qualitative identification. Components in excess of 0.5 mole percent were selected for identification and tabulated for each fluid. In addition to this detailed analysis, the hydrocarbon type classification based on ASTM D-2789 was performed. These results figure in the overall mixture characterization, and are also used for comparisons with the chemical analyses of individual distillate fractions (discussed in the section on distillation curves).

Thermal Decomposition:

The thermal decomposition of the JP-8 fluids has been assessed with an ampoule testing instrument and approach that has been developed at NIST[1-4]. It must be understood that this work was meant strictly to support the physical property measurement work, and not to delineate reaction mechanisms. The instrument we developed consists of a 304L stainless steel thermal block that is heated to the desired experimental temperature to within 0.1 °C (for this work, from 250 – 425 °C). The ampoule cells consist of 6.4 cm lengths of ultrahigh pressure 316L stainless steel tubing (0.64 cm external diameter, 0.18 cm internal diameter) that are sealed on one end with a stainless steel plug welded by a clean tungsten-inert-gas (TIG) process. Each cell is connected to a high-pressure high-temperature valve at the other end with a short length of 0.16

the cell. Each cell and valve is capable of withstanding a pressure in excess of 105 MPa at the desired temperature. The internal volume of each cell is known and remains constant at a given temperature. Fluid is added to the individual cell by mass (as determined by an approximate equation of state calculation) to give a total pressure of 34 MPa at the final fluid temperature. Thus far, we have completed measurements at 250, 275, 300, 350, 375, 400, 425, 450 °C.

Distillation Curves:
In previous work, several significant improvements in the measurement of distillation curves for complex fluids were introduced. The modifications to the classical measurement provide for (1) a composition explicit data channel for each distillate fraction (for both qualitative and quantitative analysis), (2) temperature measurements that are true thermodynamic state points, (3) temperature, volume and pressure measurements of low uncertainty suitable for equation of state development, (4) consistency with a century of historical data, (5) an assessment of the energy content of each distillate fraction, (6) trace chemical analysis of each distillate fraction, and (7) corrosivity assessment of each distillate fraction.[5-13] We also use a modification of the Sidney Young equation (to correct the temperatures to standard atmospheric pressure) in which explicit account is taken of the average length of the carbon chains of the fluid. As applied to this work, we have measured the distillation curve of three separate lots of Jet-A and one each of JP-8 and S-8, with the new approach. The curves, examples of which are provided in Figure 1, show clearly the variability in the fluids. For each fluid, we have collected sample aliquots of each distillate volume fraction for analysis by GC-MS. These individual fractions have been analyzed, and energy content calculations have been done. In addition, for each fraction, the ASTM D-2789 analysis has been done.

Thermophysical Properties:
The density, viscosity, and speed of sound of three Jet-A samples have been measured in two commercial rapid characterization instruments. A Stabinger viscodensimeter was used to determine the density and the absolute and kinematic viscosity in the temperature range from −40 °C to 100 °C (233.15 K to 373.15 K) at atmospheric pressure. A sound-speed analyzer was used to measure the speed of sound and the density of the samples at atmospheric pressure in the temperature range from 5 °C to 70 °C (278.15 K to 343.15 K). Combining a densimeter with a speed of sound measurement makes it possible to obtain the adiabatic compressibility $\kappa_s = -(\partial V/\partial p)_s/V = 1 / (\rho\, w^2)$ where V denotes volume, p is pressure, and w the speed of sound. The viscometer part of the instrument uses a rotational coaxial cylinder measuring system. The rotational speed of the inner cylinder establishes itself as the result of the equilibrium between the driving torque of the viscous forces and the retarding eddy current torque. This rotational speed is measured by an electronic system (Hall effect sensor) that counts the frequency of the rotating magnetic field of a magnet and a soft iron ring. The digital density analyzer in the viscodensimeter uses a U-shaped vibrating sample tube and a system for electronic excitation and frequency counting. The density of the sample liquid in the vibrating tube is obtained from the resonant frequency of the vibrating system relative to the resonant frequency with a calibration liquid of known density.

The combination of a viscometer and a densimeter makes it possible to obtain absolute viscosity η as well as kinematic viscosity ν of a sample. This apparatus is depicted in Figure 2. We completed measurements of the three Jet-A fluids (at atmospheric pressure) between -40 and 100 °C.

In addition to these atmospheric pressure instruments, compressed liquid measurements over the temperature range of 0 to 200 °C and pressures to 45 MPa were completed. The heart of the high pressure apparatus is a commercial vibrating tube densimeter, modified at NIST. The uncertainty in the temperature is 0.03 °C with short-term stability of 0.005 °C. Pressures are measured with an oscillating quartz crystal pressure transducer with an uncertainty of 5 kPa. The densimeter was calibrated with measurements of vacuum, propane and toluene, over the temperature and pressure range of the apparatus to achieve an uncertainty in density of 1 kg/m^3. Thus far, the three samples of Jet-A have been measured from 0-200 °C, and from 1 – 30 MPa.

Transient hot-wire measurements of the thermal conductivity were made on each of the three liquid samples of Jet-A; designated as 3602, 3638 and 4658. For each sample, measurements were made along 11 isotherms at temperatures from 300 to 500 K with pressures up to 70 MPa. The thermal conductivity without correction for thermal radiation less than 0.5 % at the highest temperature of 500 K. Corrections to the measured temperature rise require estimates for density and specific heat of the samples that were computed with REFPROP for dodecane

Model Development:
Upon completion of the experimental measurements of the physical and chemical properties described above, a model for the fluid will be developed. This model will be explicit in Helmholtz energy as a function of density and temperature. All single-phase thermodynamic properties can be calculated as derivatives of the Helmholtz energy. A preliminary equation of state for propane will be used as the starting point for the equation of state. The properties of individual mixture components, identified and evaluated in the experimental steps above, will be incorporated into the mixture model.

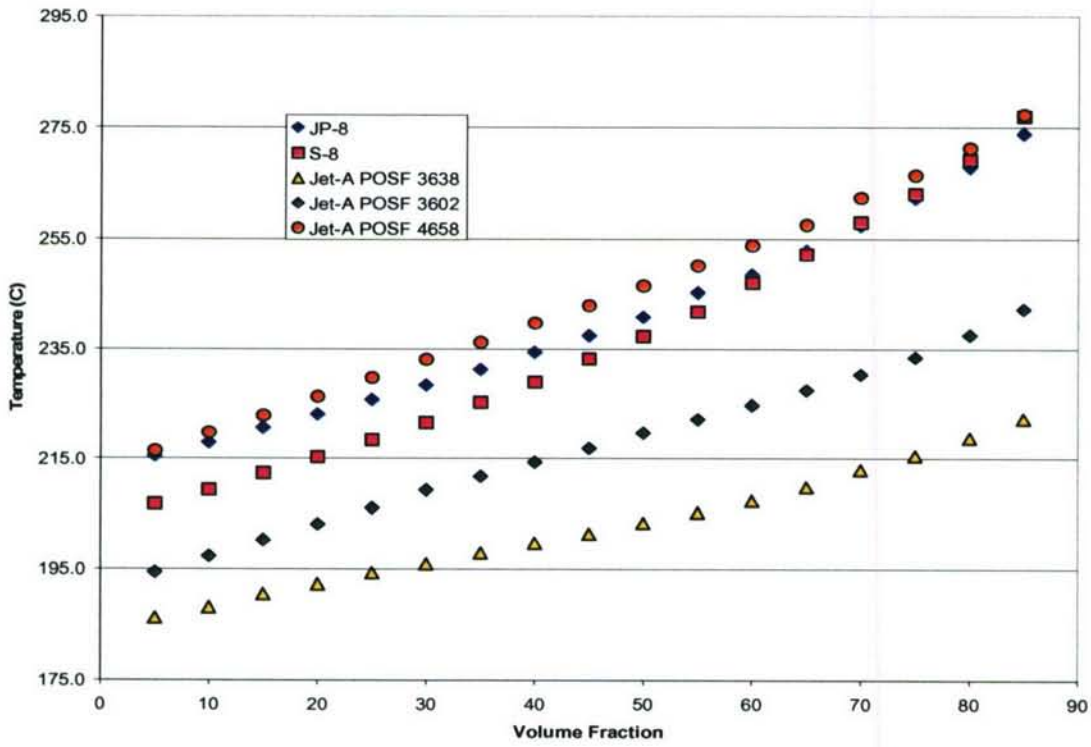

Figure 1: The distillation curves of three different lots of Jet-A, JP-8 and S-8, showing the variability that can be encountered.

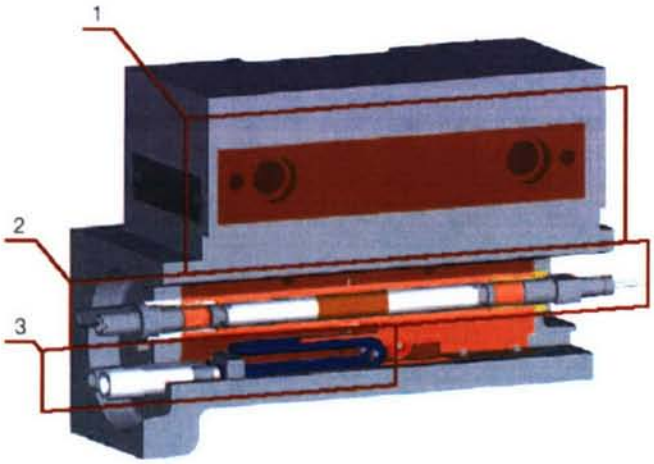

Figure 2: Main components of the Stabinger viscodensimeter SVM 3000. 1 – Thermostatting Peltier block, 2 – Concentric cylinder viscometer, 3 – Vibrating tube densimeter

References:

1. Andersen, P.C., Bruno, T.J., *Thermal decomposition kinetics of RP-1 rocket propellant.* Ind. Eng. Chem. Res., 2005. **44**(6): p. 1670-1676.
2. Andersen, W.A., Bruno, T.J., *Rapid screening of fluids for chemical stability in organic rankine cycle applications.* Ind. Eng. Chem. Res., 2005. **44**: p. 5560-5566.
3. Magee, J.W., Bruno, T.J., Friend, D. G., Huber, M.L., Laesecke, A., Lemmon, E.W., McLinden, M.O., Perkins, R.A., Baranski, J., Widegren, J.A., *Thermophysical Properties Measurements and Models for Rocket Propellant RP-1: Phase I, NIST- IR 6644, National Institute of Standards and Technology (U.S.),*. 2006.
4. Bruno, T.J., Huber, M.L., Laesecke, A, Lemmon, E.W., Perkins, R.A., *Thermochemical and thermophysical properties of JP-10, NIST-IR 6640, National Institute of Standards and Technology (U.S.),*. 2006.
5. Bruno, T.J., *Method and apparatus for precision in-line sampling of distillate.* Sep. Sci. Technol., 2006. **41**(2): p. 309-314.
6. Bruno, T.J., *Improvements in the measurement of distillation curves - part 1: a composition-explicit approach.* Ind. Eng. Chem. Res., 2006. **45**: p. 4371-4380.
7. Bruno, T.J., Smith, B.L., *Improvements in the measurement of distillation curves - part 2: application to aerospace/aviation fuels RP-1 and S-8.* Ind. Eng. Chem. Res., 2006. **45**: p. 4381-4388.
8. Bruno, T.J., Smith, B.L., *Enthalpy of combustion of fuels as a function of distillate cut: application of an advanced distillation curve method.* Energy and Fuels, 2006. **20**: p. 2109-2116.
9. Bruno, T.J., *The properties of S-8.* 2006, Final Report for MIPR F4FBEY6237G001, Air Force Research Laboratory.
10. Bruno, T.J., *Thermodynamic, transport and chemical properties of "reference" JP-8.* Book of Abstracts, Army Research Office and Air Force Office of Scientific Research, 2006 Contractor's meeting in Chemical Propulsion, 2006: p. 15-18.
11. Smith, B.L., Bruno, T.J., *Improvements in the measurement of distillation curves: part 3 - application to gasoline and gasoline + methanol mixtures.* Ind. Eng. Chem. Res., 2006. **46**: p. 297-309.
12. Smith, B.L., Bruno, T.J., *Improvements in the measurement of distillation curves: part 4- application to the aviation turbine fuel Jet-A.* Ind. Eng. Chem. Res., 2006. **46**: p. 310-320.
13. Smith, B.L., Bruno, T.J., *Advanced distillation curve measurement with a model predictive temperature controller.* Int. J. Thermophys., 2006. **27**: p. 1419-1434.

ADVANCED SUPERCRITICAL FUELS

LRIR 93PR02COR

Principal Investigators: Tim Edwards, Chris Bunker, Tom Jackson

Air Force Research Laboratory
AFRL/PRTG Bldg 490
1790 Loop Rd N
Wright Patterson AFB, OH 45433-7103

SUMMARY/OVERVIEW:

Increases in aircraft and engine performance are increasing the heat load being transferred into an aircraft's primary coolant--the fuel. This research is aimed at understanding the limitations of operation of fuel heated to 480 C (900 F) and beyond. Important issues are expected to be thermal stability, injection/combustion properties, and fuel characterization.

TECHNICAL DISCUSSION

Work has continued on improving the thermal-oxidative deposition modeling for jet fuels, as described in the 2006 abstract [1]. As described last year, the focus has been on building actual (measurable) fuel species into the model, rather than fitted constants. Work has also continued in a collaboration with Judy Wornat at LSU on PAH formation during pyrolysis of fuels at high temperatures. These PAH are generally accepted as precursors to carbon deposit ("coke") formation [2]. It is interesting that an initially-aromatic-free jet fuel (such as a Fischer-Tropsch-derived synthetic jet fuel) can form substantially more carbon deposits than conventional jet fuel containing ~17 vol% aromatics (Figure 1, 2) [2]. The F-T fuel also forms more PAH - quantitation is underway. This facile PAH formation is interesting and is undergoing further study. This coke formation is the key barrier to reusable hydrocarbon-fueled hypersonic propulsion.

Improvements in fuel characterization [3] are being made in support of the development of alternative (non-petroleum) fuels, including improved combustion modeling [4]. A improved version of ASTM D2425 GC-MS analysis of various jet fuels demonstrates the vast differences between conventional jet fuels and those derived from the Fischer-Tropsch process and a variant of direct coal liquefaction (Tables 1-3). Separate analysis of the F-T fuels reveals that the n-paraffin content is roughly 15%, with the remainder being iso-paraffins. Interestingly, U.S.-produced F-T jet (Syntroleum, "S-8") consists primarily of slightly-branched iso-paraffins (1-2 branches/molecule), while the Sasol iso-paraffinic kerosene which is blended into conventional jet fuel and delivered to aircraft in South Africa is apparently more highly branched. This difference in branching is evident in the cetane numbers for the Syntroleum fuel (~68) and the Sasol fuel (reported variously as ~64 and "low 40s"). Note that the average cetane index for JP-8 in 2005 was 44. It is AFRL's intention to make supplies of both F-T fuels available to AFOSR/ARO researchers to determine the experimental and modeling impact of these differences (efforts to obtain the Sasol IPK are underway). The University of Utah is using an

NMR technique to assess the branching in these fuels. The need to correctly model the iso-paraffins for jet fuel combustion models is being assessed [4].

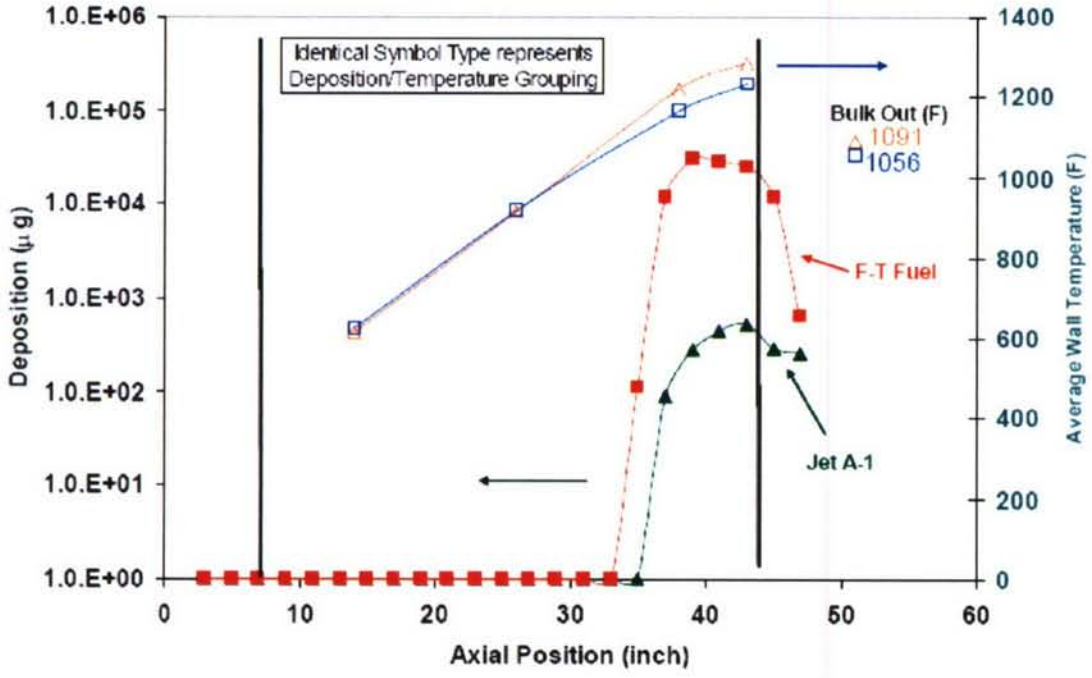

Figure 1. Deposition from Jet A-1 and F-T jet fuels under similar conversion (to gas) levels.

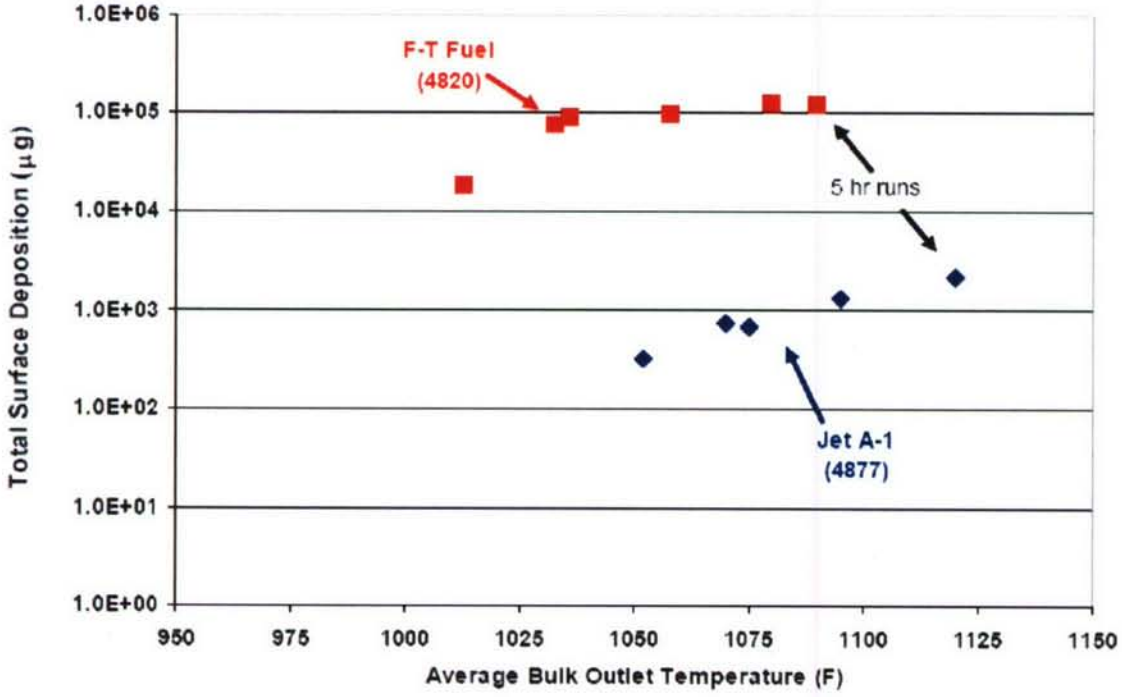

Figure 2. Total deposition as a function of fuel temperature for the two fuels.

Table 1. Compositional results for conventional jet fuels.

	World survey average, vol %	Composite Jet A blend (POSF-4658)	POSF 3602 ("high aromatic")	POSF 3638 ("low aromatic")
Paraffins (normal + iso)	58.8	55.2	49.4	64.5
monocycloparaffins	10.9	17.2	15.8	13.2
dicycloparaffins	9.3	7.8	10.8	7.1
tricycloparaffins	1.1	0.6	0.9	0.6
alkyl benzenes	13.4	12.7	14.0	10.8
indans+tetralins	4.9	4.9	7.9	2.1
naphthalene	0.1	<0.2	<0.2	0.4
substituted naphthalenes	1.6	1.3	1.2	1.3

* The technique also measures acenaphthenes, acenaphthylenes, tricyclic aromatics, and indenes, but these were below detection limits in all cases.

Table 2. Composition results for several specialty fuels.

	RP-1	JP-7	F-T Jet A-1	Coal-based fuel
		POSF 3327	POSF 4734	POSF 4765
paraffins	57.6	67.9	>99	0.6
monocycloparaffins	24.8	21.2	<1	46.0
dicycloparaffins	12.4	9.4	<1	46.7
tricycloparaffins	1.9	<1	<1	4.6
alkyl benzenes	2.1	0.7	<0.2	0.5
indans+tetralins	0.3	0.2	<0.2	1.6
naphthalene	<0.2	<0.2	<0.2	<0.2
substituted naphthalenes	<0.2	<0.2	<0.2	<0.2

Table 3. D2425 analyses of diesel fuels.

	4867 Diesel	4880 F-T Diesel
Summarized D2425 (vol%)		
Paraffins	44.3	>99
Cycloparaffins	15.9	<1
Dicycloparaffins	5.4	<1
Tricycloparaffins	<1	<1
Alkylbenzenes	10.3	<0.2
Indan and Tetralins	12.4	<0.2
Indenes CnH2n-10	1.9	<0.2
Naphthalene	0.3	<0.2
Naphthalenes	4.5	<0.2
Acenaphthenes	2.6	<0.2
Acenaphthylenes	1.6	<0.2
Tricyclic Aromatics	0.6	<0.2
Total	100.0	100.0

REFERENCES

1) Kuprowicz, N., Zabarnick, S., West, Z. J., and Ervin, J. "Use of Measured Species Class Concentrations with Chemical Kinetic Modeling for the Prediction of Autoxidation and Deposition of Jet Fuels," Energy & Fuels. Vol. 21, pp. 530-544, 2007.

2) Edwards, T., DeWitt, M, Shafer, L., Brooks, D., Huang, H., Bagley, S, Oña, J., and Wornat, M. J., "Fuel Composition Influence on Deposition in Endothermic Fuels, AIAA Paper 2006-7973, November 2006.

3) Shafer, L, Striebich, R., Gomach, J., Edwards, T., "Chemical Class Composition of Commercial Jet Fuels and Other Specialty Kerosene Fuels," AIAA Paper 2006-7972, November 2006.

4) Colket, M. B., et al, "Development of an Experimental Database and Kinetic Models for Surrogate Jet Fuels," AIAA Paper 2007-770, January 2007.

EXPERIMENTS AND REACTION MODELS OF FUNDAMENTAL COMBUSTION PROPERTIES

(AFOSR Grant No. FA9550-07-1-0168)

Principal Investigators: Fokion N. Egolfopoulos and Hai Wang

Department of Aerospace & Mechanical Engineering
University of Southern California
Los Angeles, California 90089-1453

SUMMARY/OVERVIEW

The main goal of this research is to provide insight into the physico-chemical processes that control the burning behavior of practical fuels that are of relevance to high-speed air-breathing propulsion. This is achieved through combined experimental, theoretical, and detailed numerical studies of a number of fundamental combustion properties. Experimentally, the phenomena of flame ignition, propagation, and extinction as well as flame structures of systematically chosen fuel/oxidizer mixtures are considered and characterized in well-controlled configurations. The studies involve both small (gaseous) and large (liquid) hydrocarbon molecules in view of their importance towards the accurate description of the combustion behavior of practical fuels. Theoretically, the detailed modeling of the experimental data, along with existing ones, is performed by using well-established numerical codes and reaction and transport models that have been developed based on a novel approach. More specifically, deriving reliable kinetics models is based on the following four specific objectives: (a) to develop and test a suitable array of mathematical and computational tools that can be used to quantify the joint rate-parameter uncertainty space and in doing so, to facilitate the rational design of reaction models suitable for any given target fuel or a mixture of these fuels; (b) to examine the applicability of the $H_2/CO/C_{1-4}$ reaction model, developed under prior AFOSR support, to predict the phenomena of flame ignition, propagation, and extinction along with flame structures; (c) to examine the effect of inelastic collision on binary diffusion coefficients; and (d) to test the hypothesis that there exists a critical reaction model for use as the quantitative kinetic foundation for modeling higher hydrocarbon combustion. During the reporting period, studies were conducted in several areas directly related to the overall objective of the research objectives: (1) flame ignition of mixtures of H_2 and CO with CO_2, H_2O, O_2, and N_2, (2) extinction of benzene/air and toluene/air premixed flames, (3) an *ab initio* quantum chemistry and reaction rate theory analysis for the reaction between CO and HO_2, (4) the development of a straight-chain alkane kinetic model, and (5) the development of methodology for combined kinetic model optimization and uncertainty propagation.

TECHNICAL DISCUSSION

1. Flame Ignition of Mixtures of H_2 and CO with CO_2, H_2O, O_2, and N_2

The effects of the addition of H_2O and CO_2 on the ignition of flames of mixtures of H_2 and CO (synthesis gas or syngas) with air were investigated both experimentally and numerically; more details can be found in Ref. 1. The experiments were conducted in the counterflow configuration, utilizing hot vitiated air as the ignition source. The diluents were added to both the syngas/air and

the hot vitiated air jets. As expected, it was determined that adding H_2O and CO_2 increases the ignition temperature, T_{ign}. This effect was found to be more prominent when the diluent is added to the hot vitiated air jet, in comparison to adding it to the synthesis gas/air jet, as shown in Fig. 1 for the CO_2 addition. The numerical predictions under-predicted the experimental data, but did reproduce the measured response to the addition of CO_2 and H_2O. Additional numerical simulations were also conducted, and results show that for both premixed and non-premixed configurations the effect of H_2O and CO_2 on ignition is greater when they are added to the heated jet. This is physically reasonable, due to the fact that the ignition kernel resides close to the hot boundary of the domain and the diluent is readily transported into it. In all cases, it was shown that H_2O has a stronger effect on ignition compared to CO_2, and this is attributed to the enhanced chaperon collision efficiency of H_2O.

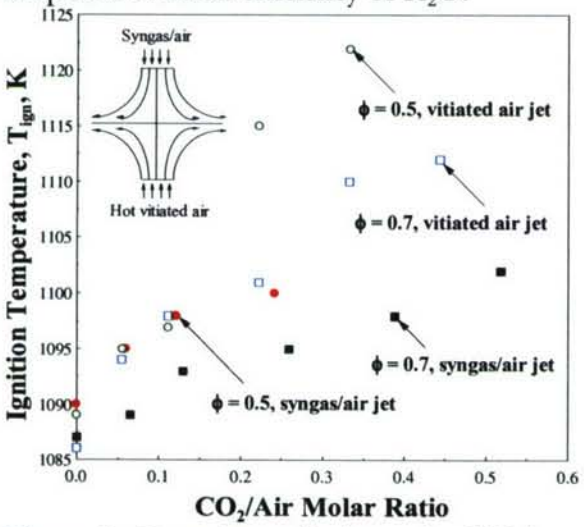

Figure 1. Experimentally determined T_{ign}'s as function of CO_2/air molar ratio. CO_2 is added to either the syngas/air or vitiated air jet.

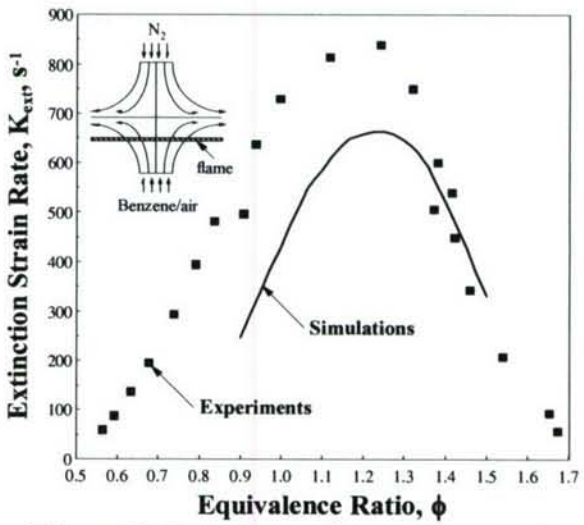

Figure 2. Experimentally and numerically determined K_{ext}'s of premixed benzene/air flames as functions of ϕ.

2. Extinction of Benzene/Air and Toluene/Air Premixed Flames

The extinction strain rates, K_{ext}, of premixed benzene/air and toluene/air flames were experimentally determined over a wide range of equivalence ratios at ambient temperature and pressure and details can be found in Ref. 2. The experiments were conducted in the counterflow configuration and utilized DPIV to accurately determine the flow field. The experimental data were simulated using a detailed kinetic mechanism [3], and compared with the experimental results. It was found that the mechanism tends to under predict the experimental results for fuel-lean conditions, as shown in Fig. 2 for benzene/air flames. The experimental data were compared with literature K_{ext} data taken at the exact same experimental configuration and conditions for *n*-heptane/air and *iso*-octane/air flames. It was found that benzene/air flames are the most resistant to extinction, followed by toluene/air and *n*-heptane/air flames, and finally *iso*-octane/air flames are the least resistant to extinction. These studies are important towards the development of jet fuel surrogates, given that aromatics are part of the candidate compound palette.

3. Reaction Kinetics of $CO + HO_2 \rightarrow CO_2 + OH$

The reaction $CO+HO_2\bullet \rightarrow CO_2 + \bullet OH$ exhibits a notable influence on hydrogen ignition at high-pressures [4]. The kinetic accuracy of this reaction has a direct impact on the accuracy of the hydrogen combustion model, which in term, impacts the accuracy of liquid hydrocarbon combustion model. Most of the measurements reported for the rate parameters of this reaction were made indirectly and at temperatures below ~800 K. For these reasons, the reaction

parameters remain highly uncertain. Here, the reaction kinetics of $CO+HO_2\bullet \rightarrow CO_2 + \bullet OH$ was studied using a combination of *ab initio* electronic structure theory, transition state theory, and master equation modeling. The potential energy surface was examined with the Coupled Cluster with the Single and Double Excitation (CCSD(T)) and Complete Active Space CASPT2 methods. The classical energy barriers were found to be about 18 and 19 kcal/mol for $CO + HO_2\bullet$ addition following the *trans* and *cis* paths, respectively. For the *cis* path, rate constant calculations were carried out with canonical transition state theory. For the *trans* path, master equation modeling was also employed in order to examine the pressure dependence. Special attention was paid to the hindered internal rotations of the HOOC•O adduct and transition states. The theoretical analysis shows that the overall rate coefficient is independent of pressure up to 500 atm for temperature ranging from 300 K to 2500 K. Based on this analysis, the following rate expression was recommended for the reaction $k\left(cm^3/mol\cdot s\right)=1.57\times10^5 T^{2.18} e^{-9030/T}$ for $300 \le T \le 2500$ K with the uncertainty factor equal to 8, 2 and 1.7 at temperatures of 300, 1000, and 2000 K, respectively.

This work was reported in Ref. 5.

4. Kinetic Model of Straight-Chain Alkane Combustion

The $H_2/CO/C_{1-4}$ combustion model was extended to include higher, straight-chain alkane combustion. The current reaction model consists of 157 species and 1204 elementary reactions. Preliminary validation tests show that the reaction model predicts a wide range of C_{5-10} combustion data satisfactorily, in addition to its ability to predict all C_{1-4} hydrocarbon combustion accurately. As examples, Table 1 shows the comparison of experimental and predicted flame speeds for selected fuel-air mixtures at a pressure of 1 atm; and Fig. 3 presents a comparison of experimental and computed ignition delay times for *n*-decane oxidation in air behind reflected shock waves.

Table 1. Experimental and computed flame speeds (cm/s) of selected straight-chain alkanes

Reactants	ϕ	Experimental	Computed
n-Pentane	1	38.6[a], 36.7[b]	37.8
n-Hexane	1	38.6[a], 36.8[b]	38.2
n-Heptane	1	39.0[a], 37.2[b]	38.1
n-Decane	1.05	40.5[c]	40.6

[a] Ref. 6, linear extrapolation. [b] Ref. 6, nonlinear extrapolation.
[c] Ref. 7, scaled from measurements at a higher unburned gas temperature.

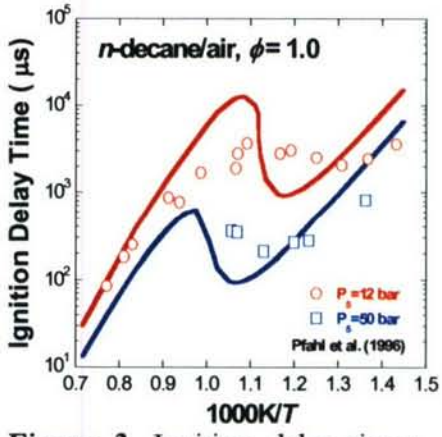

Figure 3. Ignition delay times of *n*-decane ignition behind reflected shock waves. Symbols: experimental data [8], lines model predictions.

5. Method of Coupled Model Optimization and Uncertainty Propagation

The development of a detailed reaction model is inherently an ill-defined mathematical problem, arising from an inability to attain complete kinetic isolation of each rate parameter in experimental observation, as well as kinetic coupling in reaction models obtained through an inverse-problem approach. In general, accuracy of the model is ensured by an optimization procedure such as that used in the development of the GRI-Mech. In that approach, a trial model is compiled, and the uncertainty of each parameter identified, on the basis of current kinetic knowledge. A set of fundamental combustion targets is then chosen to define the applicability of the model. Model predictions of these targets are cast into response surfaces with respect to the kinetic parameters, followed by a multi-parameter optimization within the prescribed uncertainty space. Because of kinetic parameter coupling and inherent uncertainties in the targets, the resulting optimized model, with its inherent uncertainty, is represented by a finite kinetic uncertainty space. In this work, the spectral expansion method was explored to numerically project this uncertainty in

into an application space, using as an example a recently-optimized H_2/CO reaction model to predict the oxidation rates in a perfectly-stirred reactor. In this method, uncertain parameters are expressed in the form of random variables as a polynomial chaos expansion of a set of basis random variables $\boldsymbol{\xi}$ [9], and the normalized rate parameters $\mathbf{x}$ are expressed as

$$\mathbf{x} = \mathbf{x}_0 + \sum_{i=1}^{M} \boldsymbol{\alpha}_i \xi_i + \sum_{i=1}^{M} \sum_{j=i}^{M} \boldsymbol{\beta}_{ij} \xi_i \xi_j + \ldots .,$$

where α and β are expansion coefficients, and $\mathbf{x}_0$ is the vector of mean value of the normalized rate parameters. The above equation may be used directly in the objective function of model optimization. Figure 4 shows the predicted water concentration for hydrogen oxidation in air in an adiabatic PSR (ϕ = 1, inlet temperature T_{in} = 300 K, residence time τ = 70 μs), comparing a trial (unoptimized) model with an optimized model. In this test case, the optimization used 3 ignition delay times and 3 flame speeds; the uncertainties of the rate parameters are assumed to be normally distributed; and the rate parameters were not allowed to assume values outside their respective uncertainty bounds. As seen, the method just discussed allows us to present the prediction on the basis of probability density function, which quantifies the uncertainties of the rate parameters propagated into the PSR parameter space. In addition, it was demonstrated that computational cases in which predictive accuracy in the application space may be approached retroactively by defining the needed uncertainty in fundamental combustion data.

This work was reported in Ref. 10.

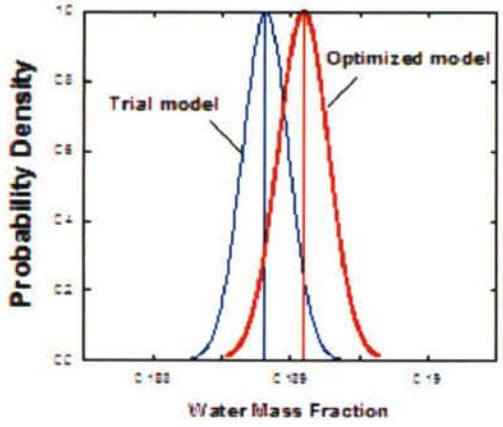

Figure 4. Probability density function predicted for water mass fraction from hydrogen oxidation in a PSR (ϕ = 1, inlet temperature T_{in} = 300 K, residence time τ = 70 *ms*).

REFERENCES

1. Ji, C., Schwab, G.F., Veloo, P., Andac, M.G., Holley, A.T., Egolfopoulos, F.N. "Flame Ignition of Mixtures of Dry and Wet Synthesis Gas with Oxygen and Nitrogen," 5th US Combustion Meeting, paper A32, San Diego, California, March 26-28, 2007.
2. Wang, Y.L., Holley, A.T., Sifounakis, A., Andac, M.G., Egolfopoulos, F.N. "Extinction of Benzene/Air and Toluene/Air Premixed Flames: Experiments and Simulations," 5th US Combustion Meeting, paper A11, San Diego, California, March 26-28, 2007.
3. Sivaramakrishnan, R., Tranter, R.S., Brezinsky, K., *Combust. Flame* **2004**, *139*, 340-350.
4. Mittal, G., Sung, C. J., Fairweather, M., Tomlin, A. S., Griffiths, J. F., Gughes, K. J. *Proc. Combust. Inst.* **2007**, *31*, 419.
5. You, X., Wang, H., Goos, E., Sung, C. J., Klippenstein, S. J. "Reaction Kinetics of CO+HO_2 → products: ab initio transition state theory study with master equation modeling," *Journal of Physical Chemistry A*, in press, 2007.
6. Davis, S. G. and Law, C. K. *Comb. Sci. Tech.* **1998**, *140*, 427.
7. Wagner, P. and Dugger, G. L. *J. Am. Chem. Soc.* **1955**, *77*, 227.
8. Pfahl, U., Fieweger, K., Adomeit, G. *Proc. Combust. Inst.* **1996**, *26*, 781.
9. Celani, P., Werner, H.-J. *J. Chem. Phys.* **2000,** *112*, 5546.
10. Sheen, D., Wang, H. "Expansion analysis of kinetic model uncertainty beyond parameter optimization," 5th US Combustion Meeting, paper 07-P24, San Diego, California, March 26-28, 2007.

LASER DIAGNOSTICS FOR REACTING FLOWS

AFOSR Grant FA9550-07-1-0020
Principal Investigator: Ronald K. Hanson

Mechanical Engineering Department
Stanford University, Stanford, California 94305-3032

SUMMARY/OVERVIEW:

Recent advances in this program's research on non-intrusive diagnostics for air-breathing combustion applications are reported. Progress is highlighted on two combustion diagnostics and sensing strategies: (1) *quantitative laser-induced fluorescence (LIF) imaging*, including the first infrared PLIF of pressure and temperature in a supersonic jet, tracer-based (3-pentanone) imaging of temperature, and 1-D LIF for detection of trace amounts of NO in high-pressure flames; and (2) *laser-absorption spectroscopy*, including the use of a new generation of longer-wavelength diode lasers for sensitive measurements of CO_2 and H_2O, development of a normalized wavelength-modulation strategy for high-speed absorption sensing of temperature behind shock waves, and development of a novel time-multiplexed two-color tunable mid-IR laser for measurements of hydrocarbon fuels. In addition, practical implementation of laser absorption sensing was demonstrated for time-resolved temperature and water vapor measurements in a model scramjet at AFRL's Propulsion Directorate at WPAFB.

TECHNICAL DISCUSSION:

1. Quantitative Laser-Induced Fluorescence Imaging

1.1 Infrared-PLIF imaging diagnostics: Earlier work to image species concentrations of infrared-active molecules using infrared planar laser-induced fluorescence (IRPLIF) has been extended. We have made the first IRPLIF measurements of temperature and pressure in supersonic flowfields by ratioing images of CO_2 fluorescence produced by narrow-line excitation of different CO_2 lines or different positions in a single CO_2 line, respectively. Demonstration measurements were made in a Mach 1.4 underexpanded jet of 30% CO_2, 70% N_2. Fig. 1 is a typical single-shot image used in the pressure measurement; in this case the excitation wavelength is 0.0013 nm from the center of the transition, which sensitizes the image to pressure variations. Improved signal-to-noise has been achieved by upgrading our injection-seeded optical parametric amplifier (funded through an AFOSR DURIP).

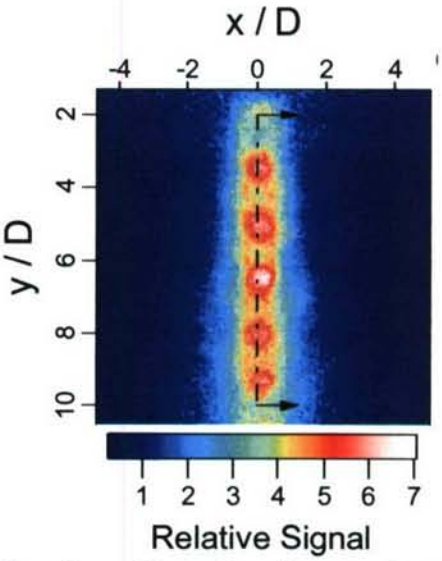

Fig. 1. Single-shot image of an underexpanded jet using excitation of the CO_2 R(22) line of the $00^00_I\text{-}20^01_{II}$ band offset by 0.0013 nm from line center; fluorescence from transitions with $\Delta v_3=1$ is collected near 4.3 μm.

1.2 Tracer-based PLIF imaging of temperature:
Recent advances in the photophysical model of 3-pentanone fluorescence have enabled the development of an improved single-shot temperature imaging strategy based on the ratio of

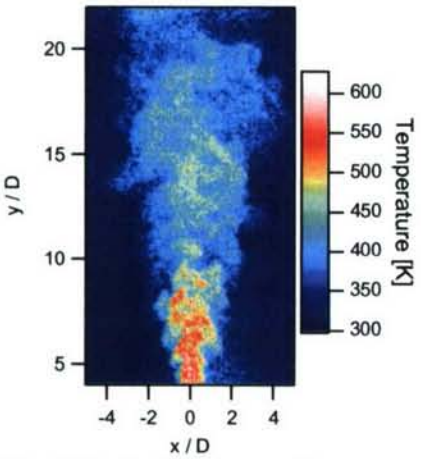

Fig. 2. Single-shot image of temperature inferred from the ratio of PLIF images (on one camera) of 3-pentanone excited at 277 and 308 nm.

fluorescence intensities from two rapidly-sequenced (1-5 μs) laser pulses of differing wavelength. For the temperature range 300-1000 K, near optimum temperature sensitivity and accuracy are attained using the 308 nm light from a XeCl excimer laser and the 277 nm light from the Raman shift in hydrogen of a KrF excimer. Fig. 2 illustrates a measured single-shot temperature field in a 14 m/s heated jet. Continued refinement of the model of 3-pentanone fluorescence has the potential to provide further improvements in the diagnostic's capabilities, particularly at high pressures and temperatures.

1.3 1-D Imaging for sensitive detection of NO LIF in high-pressure combustion gases: LIF detection of minute levels of NO within high-pressure flames is complicated by reduced signals, increased noise, and interference from O_2 and CO_2. During the past year we have investigated a 1-D LIF (line-imaging) single-shot strategy. Use of wavelength-resolved fluorescence enables small NO LIF signals to be separated from the O_2 and CO_2 interference signals. Fig. 3 illustrates the minimum detectable NO concentration in slightly lean (ϕ=0.9) flames over the investigated range of pressure (10 - 60 bar) measured with 0.8 mJ/pulse. On-chip averaging enables extrapolation of the detection limit to laser sources with higher pulse energy; the figure illustrates the effective detection limits for 4 and 16 mJ/pulse.

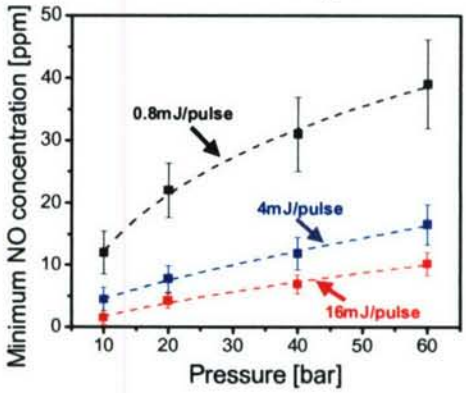

Fig 3. Minimum detectable NO concentration for 0.8mJ/pulse (single-shot, 7 ns pulse, 0.4 cm^{-1} bandwidth, and 1 mm diameter laser beam), 4 mJ/pulse (projected based on 5-shot average), and 16 mJ/pulse (projected based on 20-shot average) for CH_4+Ar/O_2, ϕ=0.9, flame at 10, 20, 40, and 60 bar.

2. Advanced Absorption Spectroscopy

2.1 TDL measurements of CO_2 and H_2O near 2.7 μm: The range of available room temperature diode lasers recently has been extended to 2.7 μm, allowing access to stronger vibrational bands of CO_2 and H_2O. Candidate CO_2 and H_2O absorption transitions were selected from spectral simulation calculations and measurements initiated to develop a spectroscopic database for linestrength and collisional broadening. A prototype temperature sensor using CO_2 was validated for 500<T<1200 K in a heated static cell, and measurements initiated for CO_2 and H_2O concentration, as well as gas temperature, in laboratory flames and shock tubes. The increased absorption strength of transitions in this new wavelength range provides greatly enhanced sensitivity and the potential for accurate and sensitive measurements in combustion gases with much shorter optical path lengths.

2.2 Normalized WMS-2f/1f for rapid (100kHz) temperature sensing behind shock waves: We have extended the capabilities of tunable diode laser (TDL) absorption sensors through a modified form of wavelength-modulation spectroscopy with detection at the twice the modulation frequency (WMS-2f). Traditionally, WMS-2f is used to improve the signal-to-noise ratio by shifting the detection frequency to values well above those of low-frequency noise sources. Recently we have realized that simultaneous detection of the intensity modulation from injection-current-tuned TDLs (i.e., the 1f signal) offers the potential for real-time normalization that can account for transmission loses from scattering, beam steering, and window fouling. Furthermore, by incorporating a measurement of the tuning characteristics of the specific diode

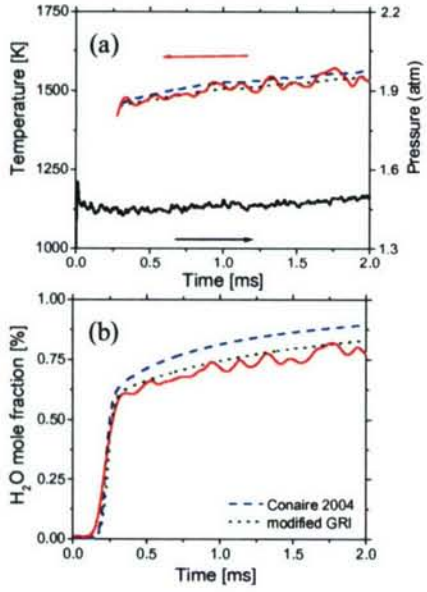

Fig. 4. Shock-heated stoichiometric H_2/O_2 dilute in argon: (a) measured temperature rise after ignition; (b) measured H_2O time history using known temperature can distinguish model predictions from different reaction mechanisms.

laser, we can achieve a calibration-free form of WMS we term normalized WMS-2f/1f. Using this strategy we have developed a new fast-response (100 kHz) sensor to measure temperature and H_2O concentration behind shock waves using absorption transitions near 1.4 μm. This sensor provides a unique and valuable new diagnostic for studying combustion mechanisms of hydrocarbon fuels in shock tubes, particularly in cases where the heat release of the post-shock chemistry alters the local temperature. The sensor accuracy was validated in a heated static cell and shock-heated H_2O-Ar mixtures, and then used in a first study of reactive chemistry with heat release, as shown in Fig. 4 for ignition of hydrogen in oxygen.

2.3 Time-multiplexed two-color tunable mid-IR sensing of hydrocarbon fuels: Monitoring and control of fuel concentration in propulsion systems is critical for maximizing performance and efficiency while minimizing pollutant emissions. Mid-infrared absorption diagnostics using the C-H stretching transitions of hydrocarbons can provide sensitive, time-resolved measurements of fuel concentration in these environments. Previously the availability of laser sources has been constrained in practice to 3.39 μm (HeNe). However, the utility of single-fixed-wavelength absorption is limited by optical interferences common in practical engine environments, including droplet scattering, window fouling, and absorption from other gas constituents. Recently, using AFOSR DURIP funds, we have acquired a laser based on difference-frequency-generation from two near-IR diode lasers, which provides tunable, cw, narrow-linewidth mid-IR light. We modified this laser to provide two rapidly (~100kHz) alternating output wavelengths, thereby enabling either two channels of single-wavelength absorption or a direct measurement of differential absorption at the two wavelengths, with 10μs time resolution. Differential absorption uses the time-multiplexed two-wavelength light and extracts the species concentration from the difference in absorption at these two wavelengths. The use of this method for n-heptane concentration measurements in shock-heated flows is illustrated in Fig. 5. The thermal decomposition of n-heptane is monitored following shock heating and compared to model calculations using the simultaneously measured gas temperature.

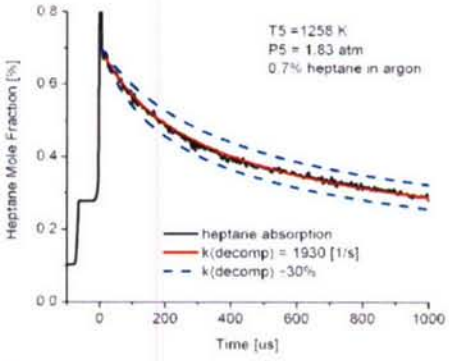

Fig. 5. Dual-wavelength differential absorption of n-heptane following shock-heating compared to model calculations of the thermal decomposition to determine the rate coefficient.

3. Time-Resolved Temperature and Water Vapor Concentration Sensing in a Model Scramjet at AFRL/PRAS WPAFB

A wavelength-multiplexed tunable diode laser (TDL) sensor tuned to water vapor absorption was used to make time-resolved temperature measurements at a 4 kHz rate in the model scramjet

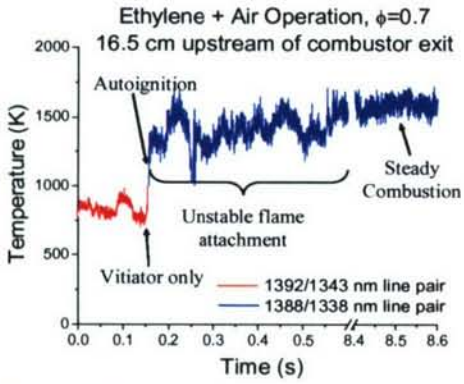

Fig. 6. TDL temperature measurements during the startup transient in the scramjet combustor at WPAFB.

combustor in Research Cell 22 (Drs. M. Gruber and C. Carter) of the Propulsion Directorate at AFRL at WPAFB. Normalized WMS-2f/1f was employed to provide quantitative measurements even when dirty combustor windows attenuated 80% of the laser light. We implemented a hybrid electro-optical scheme that allowed demultiplexing the suite of five lasers with a combination of wavelength dispersion and frequency-demultiplexing, thereby increasing the number of laser channels with a smaller number of detectors. Sensor software enhancements allowed measurement times of more than 300 seconds, thereby allowing capture of the inlet flow temperature before ignition, the fluctuating temperature as the flame stabilizes, and finally the full duration of steady combustion temperature (see Fig. 6). Time-resolved temperature measurements provide a direct measure of combustion stability, while the measurements of water vapor mole fraction are useful in evaluating combustion efficiency. The use of multiple laser colors (i.e. absorption transitions) increases the sensitivity of the sensor over a wide range of temperature and provides information about the relative non-uniformity of temperature along the laser beam path.

AFOSR-SPONSORED PUBLICATIONS (2006-2007):

Twelve AFOSR-sponsored papers appeared in archival journals, in addition one JANNAF and five AIAA conference papers were published, and seven meeting presentations were made. AFOSR-sponsored journal papers appearing in 2006-7:

1. Ben-Yakar, M.G. Mungal, and R.K. Hanson, "Time evolution and mixing characteristics of hydrogen and ethylene jets in supersonic crossflows," *Physics of Fluids* **18**, 026101/1-026101/16 1-16 (2006).
2. J.T.C. Liu, G.B. Rieker, J.B. Jeffries, R.K. Hanson, M.R. Gruber, C.D. Carter, and T. Mathur, "Near-infrared diode laser absorption diagnostic for temperature and water vapor in a scramjet combustor," *Applied Optics* **44**, 6701-6711 (2006).
3. X. Liu, X. Zhou, J.B. Jeffries, and R.K. Hanson, "Experimental study of H_2O spectroscopic parameters in the near-IR (6940 - 7440 cm^{-1}) for gas sensing applications at elevated temperatures," *Journal Quantitative Spectroscopy and Radiative Transfer* **103**, 565-577 (2006).
4. H. Li, G.B. Rieker, X. Liu, J.B. Jeffries, R.K. Hanson, "Extension of wavelength-modulation spectroscopy to large modulation depth for diode laser absorption measurements in high-pressure gases," *Applied Optics* **45**, 1052-1061 (2006).
5. A.E. Klingbeil, J.B. Jeffries, and R.K. Hanson, "Temperature- and pressure-dependent absorption cross-sections of gaseous hydrocarbons at 3.39μm," *Measurement Science and Technology* **17**, 1950-1957 (2006).
6. T. Lee, J.B. Jeffries, and R.K. Hanson, "Experimental Evaluation Strategies for Quantitative Laser-Induced Fluorescence Imaging of Nitric Oxide in High-Pressure Flames," *Proceedings Combustion Institute* **31,** 757-764 (2007).
7. A.E. Klingbeil, J.B. Jeffries, and R.K. Hanson, "Tunable Mid-IR Laser Absorption Sensor for Time-Resolved Hydrocarbon Measurements," *Proceedings Combustion Institute* **31,** 807-815 (2007).
8. H. Li, X. Zhou, J.B. Jeffries, R.K. Hanson, "Active control of lean blowout in a swirl-stabilized combustor using a tunable diode laser," *Proceedings Combustion Institute* **31**, 3215-3223 (2007).
9. H. Li, X. Zhou, J.B. Jeffries, R.K. Hanson, "Sensing and control of combustion instabilities in swirl-stabilized combustors using diode-laser absorption," *AIAA Journal* **45**, 390-398 (2007).
10. X. Liu, J.B. Jeffries, R.K. Hanson, "Measurements of nonuniform temperature distributions using line-of-sight absorption spectroscopy, *AIAA Journal* **45**, 411-419 (2007).
11. A.E. Klingbeil, J.B. Jeffries, and R.K. Hanson, "Design of a fiber-coupled mid-IR fuel sensor for pulse detonation engines," *AIAA Journal* 45, 772-778 (2007).
12. G.B. Rieker, X. Liu, H. Li, J.B. Jeffries, R.K. Hanson, "Measurements of near-IR water vapor absorption at high pressure and temperature," *Applied Physics B* **87**, 169-178 (2007).

DETAILED AND SIMPLIFIED CHEMICAL KINETICS OF AVIATION FUELS AND SURROGATES

Grant Number FA8655-06-1-3052

R.P. Lindstedt and V. Markaki

Department of Mechanical Engineering, Imperial College London,
Exhibition Road, London SW7 2 AZ, UK.

SUMMARY/OVERVIEW

The chemistries of aviation fuels are invariably complex due to large molecules and mixtures thereof. There are also large variations for a given fuel type such as Jet-A. Flow timescales encountered in high performance propulsion devices increasingly lead to difficulties associated with kinetically controlled or influenced phenomena such as flame stability, extinction and re-light. Current indications also suggest that fuel sources will become significantly more diverse in the future and may, for example, encompass Fischer-Tropsch and/or bio-derived components. The current work outlines a route towards surrogate fuel mechanisms of sufficient accuracy and generality to support the development of practical devices. The approach features the use of a reaction class based concept for the generation of chemical mechanisms for surrogate fuels. Such reaction classes are currently in the process of being refined and will form the basis of an automatic JAVA based mechanism generation tool with the produced mechanisms subsequently simplified to meet applicability constraints. A reaction class based route to the derivation of detailed chemical kinetic mechanisms for alkyl-substituted aromatics is outlined and the example given considers the toluene/1-methyl naphthalene system. Critical reaction steps in the oxidation process have been identified and are currently the subject of detailed investigations via quantum mechanical methods using Gaussian-03. The latter was also used at the G3B3 level in combination with DFT analysis for internal rotations to provide improved thermodynamic data for a wide range of the intermediate species. The current work examines general trends for a variety of species of interest and it is shown that critical reaction paths include the $C_9H_7 + O_2$ channels and the linkage of C_5 and C_6 rings as part of the oxidation process. The current work also has implications for model fuel compounds used in Diesel combustion.

TECHNICAL DISCUSSION

One of the targets of the current work is the derivation of detailed reaction mechanisms for alkyl-substituted aromatics such as toluene, m-xylene, 1-methyl naphthalene and n-propyl benzene. The work has started by considering methyl-substituted aromatics. This class of compound is abundant in aviation fuels and presents a number of challenges. Furthermore, recent work reported by Colket et al. [1] indicates that methyl-substituted aromatics are potentially important in the context of the overall reactivity of fuel mixtures through the thermodynamic stability of benzyl-like structures. Specifically, it was shown [1] that multiply methyl-substituted aromatics may serve to bring the reactivity and ignition characteristics of

comparatively simple (e.g. 2 component) surrogate fuels close to that of JP-8. A possible explanation for the behaviour can be found in the stability of benzyl type structures and their potential ability to act as radical scavengers. The stability of the benzyl radicals also provides a possible route to PAH and soot formation.

The starting point for the current work was the toluene sub-mechanism of Lindstedt and Maurice [2] with subsequent developments by Potter [3]. The mechanism consisted of 88 reactions and 13 species and considers oxidation and pyrolysis of the CH_3 group as well as radical attack on the ring. The 1-methyl naphthalene mechanism was derived directly from the equivalent toluene reactions following appropriate adjustments to account for molecular size and thermochemical differences. A wide range of conditions has been used to validate the toluene and 1-methyl naphthalene sub-mechanisms including data obtained in a Jet Stirred Reactor (JSR). In light of the work by Colket et al. [1], the cases presented here include a comparison of the temporal evolution of the ignition process for toluene. The reaction mechanism has been updated using the latest available data for key reactions (e.g. [4]). The derived mechanisms for the oxidation of naphthalene and 1-methyl naphthalene are based on reaction classes derived from the oxidation of toluene, benzene and cyclo-pentadiene. The current work contains differences from earlier efforts. For example, reaction sequences (1-4) have replaced more global steps present in earlier studies.

$$C_7H_7 + O_2 = C_7H_7O + O \quad (1)$$
$$C_7H_7 + HO_2 = C_7H_7O + OH \quad (2)$$
$$C_7H_7O = C_7H_6O + H \quad (3)$$
$$C_7H_7O = C_6H_6 + CHO \quad (4)$$

The C_7H_7O radical produced from reactions (1) and (2) thermally decomposes via (3) C - H (60%) and (4) C - C cleavage (40%). Benzaldehyde is further consumed by thermal decomposition via C - H cleavage (15%) as well as OH (10%), H (25%), CH_3 (10%) and O (25%) radical attack. The fate of the OC_7H_7 radical, formed via attack on the ring, is interesting as it predominantly decomposes (80%) via reaction (5).

$$OC_7H_7 = C_5H_4CH_3 + CO \quad (5)$$
$$C_5H_4CH_3 = C_6H_6(F) + H \quad (6)$$

Lindstedt and Rizos [5] suggest that $C_5H_4CH_3$ eventually leads to C_6H_6 via $C_6H_6(F)$ (fulvene), supporting the proposal by Moskaleva *et al.* [6] who explored the possibility of C_6H_6 formation from $C_5H_4CH_3$ radicals. The current toluene mechanism does reproduce, with reasonable accuracy, the H radical concentrations formed during toluene pyrolysis, as measured by Braun-Unkoff et al. [7], and ignition delay times as measured by different groups. It is perhaps particularly pleasing that the recent time resolved OH radical data obtained by Vasudevan et al. [8] is well reproduced as shown in Fig. 1.

The ability of the corresponding 1-methyl naphthalene mechanism to reproduce JSR data was explored and the cases presented here feature a temperature range $1090 < T\ (K) < 1440$, a mean residence time of 100 ms and a pressure of 1 atm. Selected results are shown in Fig. 1b and major intermediates in Fig. 2a,b. The fuel consumption and oxygen consumption along with CO and CO_2 are shown in Fig. 1b for a fuel lean case with a stoichiometry of 0.5. The agreement is encouraging and is maintained also for fuel rich mixtures. A more demanding test concerns the formation of major single ring aromatics as part of the oxidation process.

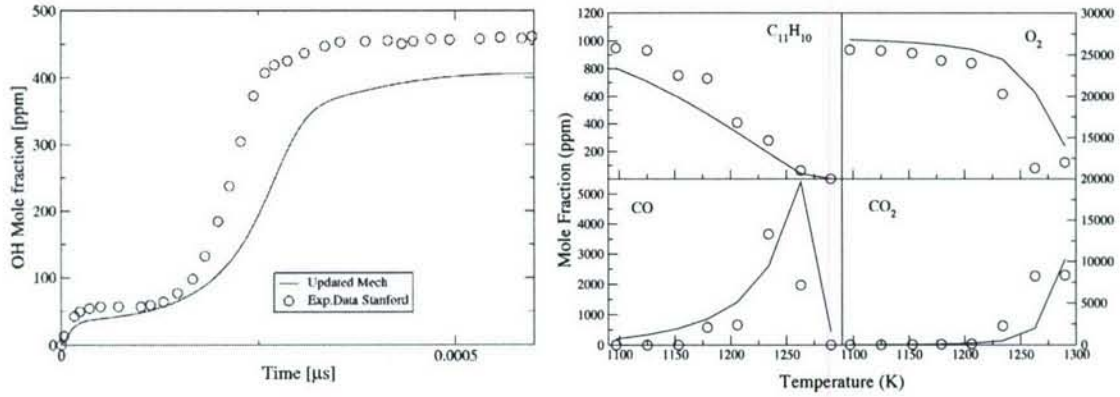

Fig. 1. Left: Ignition delay times for stoichiometric toluene mixtures in Ar, T = 1689 K and P = 1.79 atm Experimental data from Vasudevan et al. [8]. Right: Consumption of $C_{11}H_{10}$ and O_2 along with primary products CO and CO_2 formed during the oxidation of 1-methyl naphthalene in a JSR at atmospheric pressure with a mean residence time of 100 ms and a stoichiometry of 0.5 [9].

The latter are strongly dependent upon the pathways via indene formation and oxidation. The application of analogous reaction sequences of the above type to the modeling of 1-methyl naphthalene oxidation suggest that reaction (7),

$$C_{11}H_{10} + OH = C_{11}H_9 + H_2O \qquad (7)$$

is the dominant fuel consumption reaction at 1170 K. The distribution of principal single ring aromatics is shown in Fig. 2a. The corresponding primary two-ringed products are shown in Fig. 2b. By analogy with the above discussion, it is interesting to note that reaction (8) is a primary source (~35%) of naphthalene.

$$C_9H_6CH_2 + H = C_{10}H_8 + H \qquad (8)$$

It can be seen that the quantitative agreement is good with concentration levels from around 10 ppm ($C_{11}H_8O$) to 250 ppm ($C_{10}H_8$) reproduced. Similar agreement is obtained for fuel-lean mixtures.

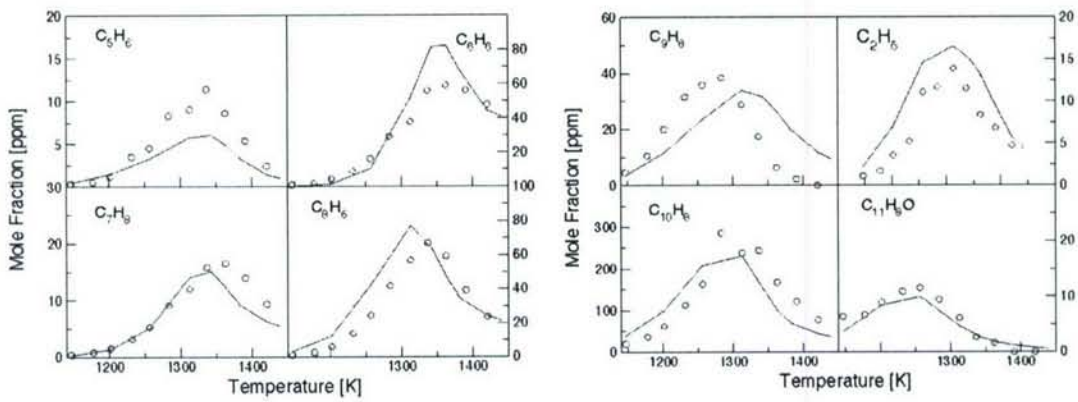

Fig. 2. Left: (a) Formation of single ring aromatics C_5H_6, C_6H_6, C_7H_8 and C_8H_6 during the oxidation of 1-methyl naphthalene in a JSR at atmospheric pressure with a mean residence time of 100 ms and a stoichiometry of 1.5 [9]. Right: (b) Formation of C_9H_8, $C_{10}H_8$ and $C_{11}H_8O$. Ethane concentrations are also shown due to their sensitivity to methyl radical production.

The formation of naphthalene and the naphthyl radical thus follow paths directly analogous with benzene formation from toluene. For example, the extraction of CO from the C_6 ring, eventually leading to indene, follows from the work by Lindstedt and Rizos [5]. It does appear that the current approach can lead to encouraging agreement with respect to the modeling of oxidation of complex molecules. The work also forms a natural extension to studies of formation paths of two-ringed structures performed in earlier work [10].

CONCLUSIONS

The current paper has sought to illustrate the use of a reaction class based approach for the oxidation of substituted aromatics. An analogy with toluene was used to develop a comprehensive detailed chemical kinetic mechanism for 1-methyl naphthalene with encouraging results. Past problems with predictions of principal aldehydes (C_7H_6O and $C_{11}H_8O$) have been resolved and concentration profiles of single-ring aromatics have been reproduced with encouraging accuracy. The $C_9H_7 + O_2 =$ *products* channel has been found to be of key importance and to require further clarification. The reaction is currently the subject of detailed investigations via quantum mechanical methods using Gaussian-03. A major challenge is to reduce the detailed reaction sequences in a manner that permits the inclusion into modeling techniques for turbulent flames. Lindstedt and Louloudi [11] showed that a systematic reduction of the corresponding naphthalene oxidation sequence is possible. Overall, the analogies used for the development of a comprehensive detailed chemical kinetic mechanism for two-ringed aromatics have been found to work well. Generally, comparisons with earlier efforts show that the replacement of global reaction steps with elementary sequences improves agreement with experimental data.

ACKNOLWLEDGEMENT

The authors wish to gratefully acknowledge the support of the EOARD for the current work.

REFERENCES

[1] Colket, M., Edwards, T., William, S., Cernansky, N., Miller, D., Egolfopoulos, F., Lindstedt, P., Seshadri, K., Dryer, F., Law, C.K., Friend. D., Lenhert, D.B., Pitsch, H., Sarofim, A., Smooke, M. and Tsang, W., Paper AIAA-2007-770, Presented at 45th AIAA Aerospace Sciences Meeting, Reno, January 2007.

[2] Lindstedt, R.P. and Maurice, L.Q., Combust. Sci. and Technol., 120:119-167 (1996).

[3] Potter, M. L. Detailed Chemical Kinetic Modelling of Propulsion Fuels, PhD Thesis, Imperial College London, 2003.

[4] Oehlschlaeger, M.A., Davidson, D.F. and Hanson, R.K., Proc. Combust Inst. 31 (2007).

[5] Lindstedt, R.P. and Rizos, K.-A., Proc. Comb. Inst. 29:2291-2298 (2002).

[6] L.V. Moskaleva, A.M. Mebel and M.C. Lin, Proc. Combust. Inst., 26 (521 (1996).

[7] Braun-Unkhoff, M., Frank, P. and Just, Th., Proc. Combust. Inst. 22:1053 (1988).

[8] Vasudevan, V., Davidson, D.F. and Hanson, R.K. Proc. Combust. Inst 30:1155 (2005).

[9] K. Mati, A. Ristori, G. Pengloan and P.Dagaut Combust. Sci. Technol.} In Press.

[10] Lindstedt, R.P., Maurice, L.Q. and Meyer, M. The Royal Society of Chemistry, Faraday Discussion 119:409-432 (2001).

[11] R.P. Lindstedt and S.A. Louloudi, Proc. Combust. Inst. 30:775 (2005).

COMPUTATIONAL AND EXPERIMENTAL STUDY OF JET FUEL COMBUSTION

Grant #FA9550-06-1-0018
Principal Investigators: M. D. Smooke and A. Gomez

Department of Mechanical Engineering
Yale University
New Haven, CT 06520-8284

SUMMARY/OVERVIEW

Since jet fuel will continue to play a central role in US Air Force operations for the foreseeable future from both a logistical and an economic viewpoint, a coordinated experimental and computational program is needed to develop chemical models of jet fuel that can be used within a larger research and development program. In this project we have initiated a joint experimental and computational program designed to test how well surrogate formulations of JP-8 match overall properties of the complex fuel and more detailed aspects of its combustion, such as flame structures. The work is being leveraged on complementary research at the University of Utah and the University of Milan (Italy). The work will help establish a research infrastructure to provide a better understanding of the combustion of jet fuel, to the benefit of both commercial and military users.

TECHNICAL DISCUSSION

We initiated a joint experimental and computational program designed to test how well surrogate formulations of JP-8 match overall properties of the complex fuel and more detailed aspects of its combustion, such as flame structures. Specifically, a comprehensive campaign of measurements and computations in prototypical flame environments, such as premixed flames and diffusion flames, is being undertaken which includes measuring and computing global properties such as laminar flame speeds, S_L, extinction strain rates, a_{ext}, and ignition strain rates, a_{ign}. We also plan on comparing flame structure including the temperature and gaseous hydrocarbons up to C_{12}.

Computational Methodology

Of inherent importance to both the premixed and nonpremixed studies is the ability to vary one or more quantities as the remaining system parameters are held fixed. For example, in the premixed problems we are interested in allowing the equivalence ratio to change as the pressure and inlet temperature are held fixed or we may want to vary the inlet temperature as the pressure and equivalence ratio are fixed. For the diffusion flames, the strain rate, inlet mass flow rates and temperatures are parameters of interest. While we could compute a single flame with specified values of these parameters and then use

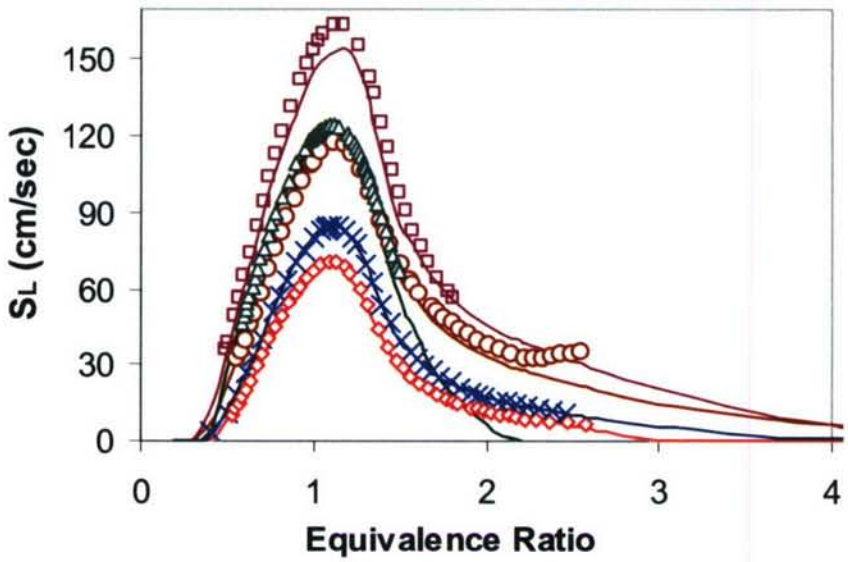

Figure 1: Comparison of JP-8 (six-component surrogate) flame speeds as a function of equivalence ratio. O 800K/35 atm, Δ 572K/1 atm, X 600K/10 atm, ◊500K/5 atm. Solid lines are correlations.

this computed solution as a starting estimate for a new problem with different parameter values, this approach is extremely inefficient. Instead, we are applying a continuation method such that the grid and the solution smoothly change as the parameter is varied. We have implemented both a freely propagating and a counterflow diffusion flame continuation program designed to follow changes in the equivalence ratio, pressure and inlet temperature in the freely propagating flames (e.g., see Fig. 1) as well as the strain rate and the inlet mass fractions in the counterflow flames. This has led to flame speed profiles for the premixed systems and flame structure results for the nonpremixed counterflow flames. In addition, a preliminary mechanism reduction has been implemented with our initial efforts directed at the generation of a skeletal mechanism. Specifically, sensitivity analysis has been applied to a six-species counterflow JP-8 surrogate flame to identify reactions and species that can be removed. Peak first-order sensitivity coefficients (F.O.S.C.) of temperature with respect to reaction rate are used to gauge the importance of each reaction. Four candidate skeletal mechanisms (Table 1) are generated after eliminating those reactions with peak temperature F.O.S.C. less than some limiting value.

Table 1

Mechanism	Minimum Temperature F.O.S.C	Number of Species	Number of Reactions
A	1×10^{-7}	179	1159
B	5×10^{-7}	168	867
C	1×10^{-6}	157	740
D	5×10^{-6}	131	505

Experimental Approach

The bulk of the experimental activity in the past year was focused on optimizing the counterflow JP-8 burner for gas analysis using a semi-automated GC/MS system. To develop a flame structure database of various surrogates and of individual components requires a measurement system that is robust and with the necessary pre-requisite of data reproducibility. Our approach entails gas sampling by fine quartz microprobes and detailed analysis by GC/MS. It should yield a wealth of data that will be used to validate surrogate model formulations and is clearly preferable in terms of specificity of measured species and sensitivity of the chemical kinetic models of large hydrocarbons to alternatives, such as laser diagnostic techniques, that are typically limited to the measurement of a handful of light species. The main drawback of GC/MS analysis is that it takes a very long time to perform a flame scan. A concentration measurement at any point in the flame typically requires: five minutes to load the sample loop, two minutes for the analysis of O_2 and N_2 by a Thermal Conductivity Detector (TCD), 25 minutes for the analysis of light (C_1 and C_2) species by a Flame Ionization Detector (FID) and as long as two hours for the analysis of large molecular-weight compounds by a quadrupole Mass-spectrometer (MS). Clearly, a full scan of a flame with a minimum of 10-12 points would entail a tedious procedure lasting in excess of 30 hours. Maintaining a concentrated effort over such a prolonged time is problematic even for the most committed graduate student. Preserving a steady-state flame over such a time would be challenging, especially in the case of JP-8 that requires fuel vaporization and precise metering of small liquid flow rates. Using a syringe pump, as is typically done at the flow rates of interest, would entail repeated flame shut-offs with reloading of syringes. If one factors in thermal transients of the burner and other uncontrolled variables, such as, for example, sampling probe distortions through flame start up and shut down over a thirty hour time period, it should come as no surprise that initial measurements were plagued by reproducibility problems, as reflected by data profiles that lacked the required "smoothness".

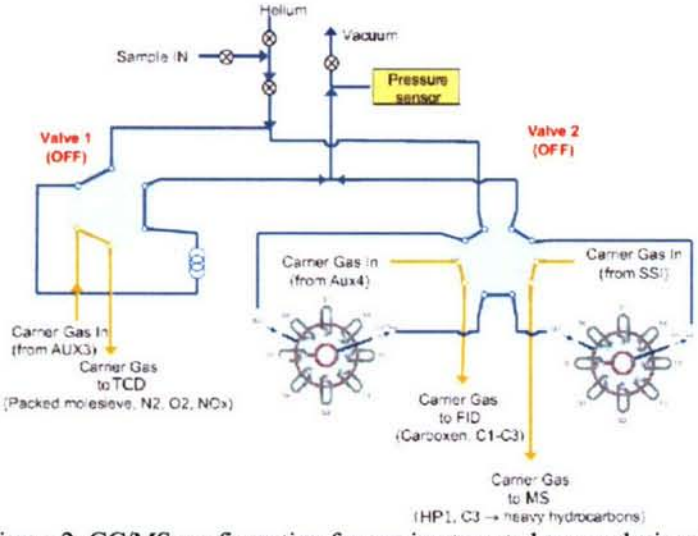

Figure 2: GC/MS configuration for semi-automated gas analysis using three detectors (TCD, FID and a quadrupole Mass Spectrometer).

To address this difficulty, we developed an automated sampling system that would allow for sampling/storing using two multi-position valves, two pneumatic-actuated injection valves and a battery of sampling loops, as shown in Fig. 2. One of the pneumatic valves is responsible for the TCD analysis (left in the figure) that is executed in real time

since it requires only two minutes per data point. The valve on the right, on the other hand, controls the FID and the MS. Since these two instruments require a much longer time to complete a measurement, the samples are stored in 16 sample loops using two multi-position valves and analyzed overnight by a computer automated sequence. Thanks to this improvement, a full flame scan requires at most five-six hours of operator work during which the flames has to run continuously, i.e., a fraction of the time it took in the first semi-automated configuration we tested. This dramatic gain in the implementation of the experiment opens up the doors to more stringent tests of reproducibility and to the systematic test of several flames with relative ease.

The burner was described in the 2006 abstract. The only modification with respect to that configuration was the replacement of the ultrasonic nebulizer, that lacked the necessary flow rate flexibility, with an electrospray atomizer to disperse the liquid fuel and ensure its complete evaporation by the time the gaseous mixture reaches the burner mouth. We have considerable experience with this type of atomizer.

Preliminary tests were conducted on an overall lean flame of JP-8 that was stabilized with the following flow conditions: on the fuel side, the liquid flow rate and the N_2 flow rate were measured at was 30 cc/min and 2 l/min, respectively; on the oxidizer side, the inert and oxygen flow rates were 0.61 l/min and 2.02 l/min, respectively, which resulted in a blue flame at moderate strain rate. To enhance the flame stability and prevent soot formation at the interface of the flame with the room air, a shroud flow of N_2 was provided. The fuel side was preheated and maintained at a temperature above the dew point of the nitrogen-diluted fuel mixture. Preliminary calibrations of the GC/MS using calibrated gaseous mixtures and direct injection of less volatile hydrocarbons into the GC/MS showed linearity of each of the three detectors. As a sample of the instrument capabilities, Figure 3 illustrates profiles of some light and heavy species obtained in the JP-8 flame scan, including: acetylene, ethylene, ethane, benzene, toluene, m-xylene and octane. Some difficulties were encountered with dodecane that exhibited a non-monotonic behavior for which probe condensation effects may be responsible. Additional tests are under way to ascertain this point. All in all, the measurement system is performing well and systematic scans under different flame conditions are under way to create a database, test various surrogates and select an optimal surrogate kinetic model.

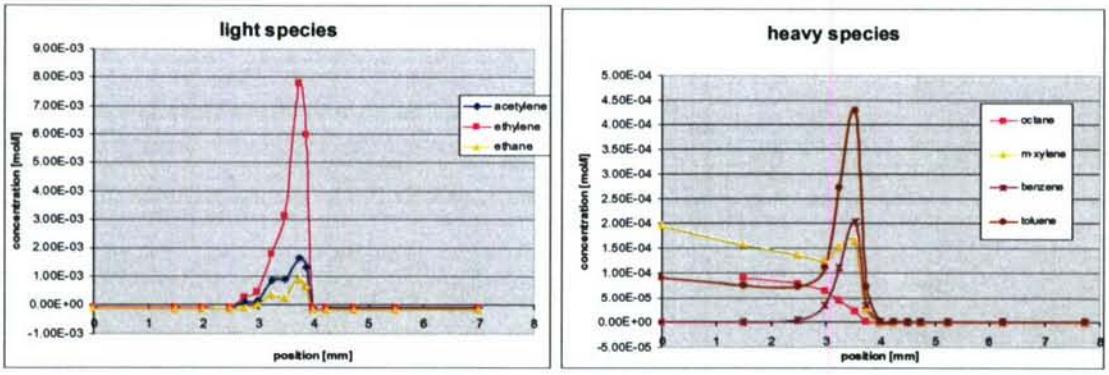

Figure 3: Profiles of C1 and C2 hydrocarbons (left), as measured by FID, and of heavier hydrocarbons (right), as measured by the mass spectrometer

The Decomposition of Surrogate Fuel Molecules During Combustion

F1AT06004G003
Wing Tsang and Jeffrey A. Manion

National Institute of Standards and Technology
Gaithersburg, MD 20899

SUMMARY AND OVERVIEW: Continual improvements in the capability of Computational Fluid Dynamics codes have made it possible to consider the computer simulation of real fuel in real devices[1]. Recent workshops have led to the selection of a limited number of compounds that can serve as surrogates for gasoline, diesel and aviation fuels[2]. This project is aimed at developing the chemical kinetic databases necessary to support this effort. The elements of this database consist of the rate constants of fundamental single step reactions that describe the pyrolytic decomposition of surrogate fuels molecules. These reactions represent an integral part of any complete combustion kinetics database. They can be competitive with oxidation processes and hence extend the range of current combustion models to richer mixtures. Particular focus is placed on the decomposition of radicals formed by the abstraction of hydrogen from a fuel compounds. The specific radicals that have now been studied are the 1-hexenyl radicals, the cyclohexyl radicals and the radicals that are formed as a result of isomerization. The latter is in fact the key new element in the reactions involving real fuels. The increase in the size of the fuel molecule leads to the possibility of contributions from isomerization channels that are not present for smaller fuel molecules. The present work has led to rate expressions for the cyclization of olefinyl radicals to form 5 and 6 carbon cyclic radicals and the reverse as well as the effect of ring structure on 1,4-H-transfer isomerization. Due to the variety of possible structures this is an area where future work will be focused.

TECHNICAL DISCUSSION: This mechanism for the destruction of fuel molecules during combustion can be found in Figure 1. The vertical set of reactions represent the oxidation processes. Practically all the existing databases have dealt with these processes. They are thus applicable to near stoichiometric processes. The horizontal set of reactions are pyrolytic processes. They are competitive with the oxidation reactions and thus extend the range covered by combustion models. The set of reactions are particularly important in the context of PAH/Soot formation processes, since the unsaturated compounds are generally the starting point of such models. Of course unsaturated compounds are generally present in very small amounts in hydrocarbon fuels. Therefore there is the need for information on the cracking patterns subsequent to PAH/Soot formation.

The experimental procedure involves generating the appropriate radical in the high temperature environment of a single pulse shock tube[3]. Reaction conditions are set so that only unimolecular decompositions and isomerizations can occur in this environment. This is achieved by taking advantage of the short reaction time of the shock tube, through the use of highly dilute mixtures and the addition of a chemical scavenger in large excess so as to remove the most reactive radicals. A special feature of the radicals being studied is their short lifetimes under shock tube conditions. For the present studies they are of the order of 1 micrsec or

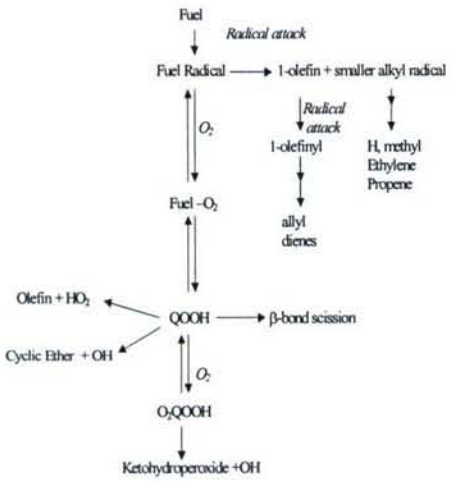

Figure 1: Mechanism for fuel degradation

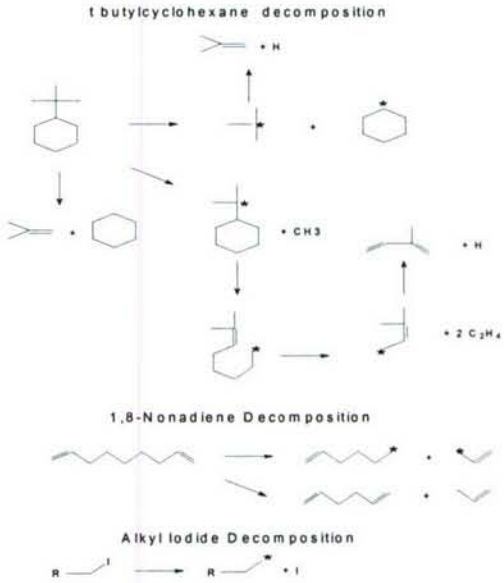

Figure 2: The generation of cyclohexyl, 1-hexenyl-6 and alkyl radicals

less. Figure 2 summarizes the various starting materials for generating the radicals of interest. Note that in all cases there are in fact side reactions. They do not interfere with the analysis of the data. Figure 3 contains the results of shocking tertbutylhexane. It can be seen that there is a large number of products. These can however be identified with particular reaction channels. The isobutene is formed as a consequence of the breaking of the most highly substituted C-C bond. The cyclohexane is the result of a molecular channel for the decomposition of tert-butylcyclohexane. Isoprene is the consequence of the cleavage of a C-methyl bond followed

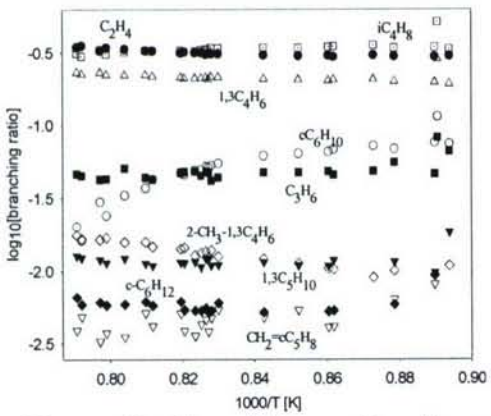

Figure 3: Branching ratios for olefins formed during tert-butyl cyclohexane decomposition at 4 bar pressure

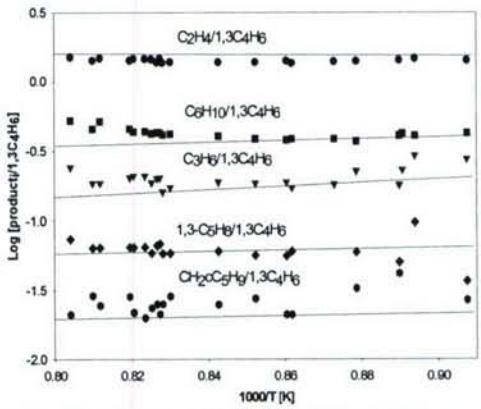

Figure 4: Product versus 1,3-butadiene formed during the decomposition of cyclohexyl radicals at 4 bar pressure

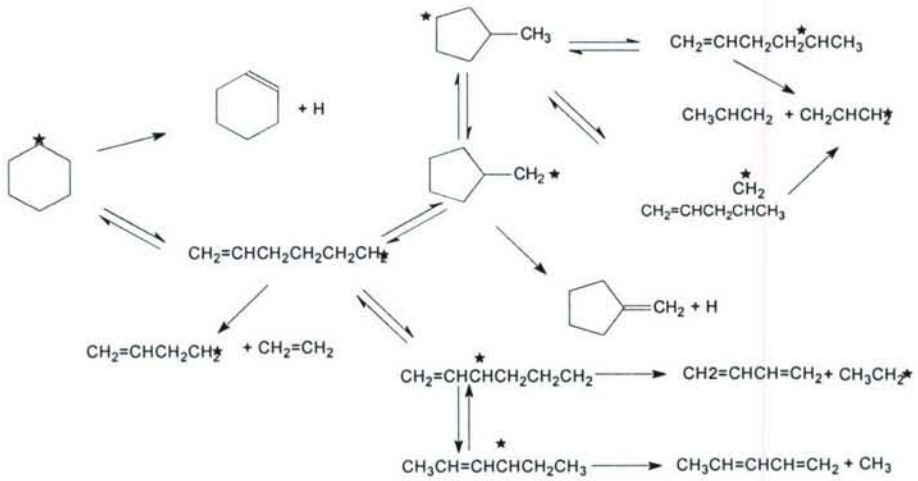

Figure 5: Mechanism for the decomposition of cyclohexyl and 1-hexenyl-6 radicals.

By successive beta C-C bond cleavages.The yields of cyclohexene decreases drastically as the temperatiure is increased. This is a consequence of the reverse Diels-Alder reaction to form ethylene and butadiene. This can be corrected since the rate constant for this process is well known.

All of the other products are the direct consequence of the decomposition of cyclohexyl radical. The general mechanism is outlined in Figure 5. From Figure 4 it can be seen that butadiene is one of the main products. Yields are close to that of ethylene. Unlike the situation for linear alkane fuels yields of propene are relatively small. It is interesting propene can only be formed from cyclopentyl radicals. More direct evidence for the presence of five carbon cyclic compounds is the detection of methylene cyclopentane. Thus 1-hexenyl radical can cyclize via terminal and non-terminal addition. Rate constants for the cyclization processes are fairly close to each other. Near room temperature the preference is for the former. Under shock tube conditions the latter is preferred. The addition of this isomerization channel to the possible pathways represents an added complication. Thus the relative importance of the terminal to non-terminal cyclization channels could not be uniquely determined without the experimental results from the chemical activation studies summarized in Figure 6. Figure 7 contains data pertaining to the cracking pattern for the decomposition of 1-hexenyl-6 radical. This was generated from the decomposition of 1-8-nonadiene. A major product from the decomposition of 1,8-nonadiene is propene. Large yields of allyl radicals are also formed. Thus it is impossible to assess from these results the contribution of propene to the cracking pattern from 1-hexenyl-6 radicals. However for all except the cyclohexene the ratio of yields to 1,3-butadiene are the same as those derived from cyclohexyl radicals. This is a very satisfactory demonstration of the postulated mechanism. The relative yields of cyclohexene is about a factor of two higher in favor of the case where cyclohexyl radical is the starting reactant. This is indicative of these studies being in

stem in Figure 5 involve 8 isomers that undergo 7 beta
le isome
-5 radica
small (

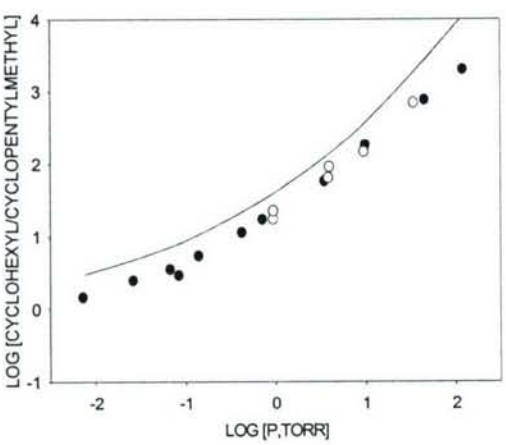

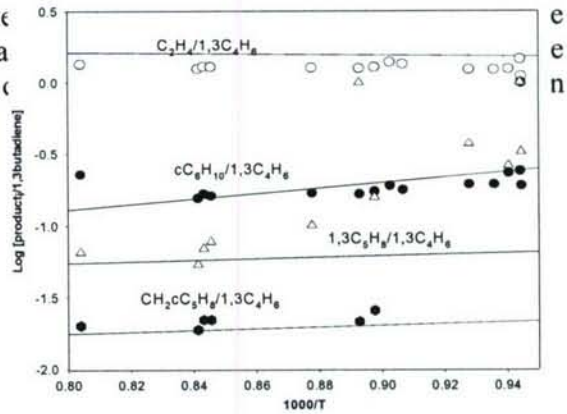

Figure 6: Ratio of cyclohexyl and cyclopentyl radicals formed during the chemically activated decomposition of cyclohexyl formed Symbols are experimental results. Lines are from rate constants derived from fit to Figure 4

Figure 7: Product to 1,3-butadiene formed during the decomposition 1-hexenyl-6 radicals at 4 bar pressure. are experimental values. Symbols are experimental values. Lines are calculated values from rate constants derived from data in Figure 4

Another interesting consequence of the nature of the cracking pattern in Figures 4 and 6 are rate expressions for 1,4- H-atom transfer isomerization involving a five carbon ring structure and across a double bond. These are uniformly smaller than those for the case for a linear system. This is not surprising since the bond angles are larger and the molecules are much less flexible. This opens up the issue of the rate expressions for H-transfer isomerization for reactions involving ring structures. From these results we derive high pressure rate expressions in order to account for energy transfer contributions to our rate expressions. The former can now be used to project results over all combustion conditions.

The unsubstituted cyclohexyl radical treated here is probably the simplest of this type of compound. With substitution the number of possible channels increase drastically. The overall situation is rendered more complex. Using custom synthesized alkyl iodide we are completing work on the effect of methyl substitution on 1-4 and 1-5 hydrogen atom isomerization. These results have direct bearing on Fischer-Tropsch fuels. Thus except for the cyclic compounds we are well on the way towards a complete understanding of the cracking of hydrocarbon fuels.

References:

1. Kee, R. J., Coltrin, M. E. and Glarborg, P., "Chemically Reacting Flow" Theory and Practice, Wiley, Interscience, New York, 2003
2. Colket M., Edward, C. T., Williams, S., Cernansky, N. P., Miller, D. L., Egolfopoulos, F., Lindstedt, P., Seshadri, K., Dryer F. L., Law, C. K., Friend, D., Lenhart, D. B., Pitsc, H., Sarofim, A, Smooke, M., Tsang, W., "Development of an Experimental Database and Kinetic Models for Surrogate Fuels", 45th AIAA Aerospace Sciences Meeting and Exhibit, Reno, Nevada, January 9, 2007
3. Stein, S.E and Rabinovitch, B. S. J. Phys. Chem.,1975, 79, 191
4. Tsang, W. and Lifshitz, A., Shock Tube Methods in Chemical Kinetics" Annual Reviews of Physical Chemistry, 1990, 41, 559.

AN AUTOMATED PROCESS FOR GENERATION OF NEW FUEL BREAKDOWN MECHANISMS

Grant/Contract Number: FA9550-06-1-0376

Principal Investigator:

Angela Violi

Assistant Professor
Department of Mechanical Engineering, Chemical Engineering and Biomedical Engineering
University of Michigan
2150 G.G. Brown
2350 Hayward Rd.
Ann Arbor, MI 48109

SUMMARY/OVERVIEW:

This work revolves around an innovative, comprehensive, and integrated approach for predicting new fuel reaction mechanisms. It combines advanced computational techniques in a synergistic study of the critical processes in fuel decomposition at a level of detail that can help distinguish, correct, and quantify mechanisms for these processes. The innovative aspect of the modeling effort is to integrate computational tools that can be used to build reaction pathways for new fuel mechanisms, starting from the structure of the proposed fuel components and ending with a list of reactions pathways, rate constants, thermodynamic, and transport data that can be feed into existing combustion mechanisms. Studies were conducted on the breakdown kinetic mechanisms of decalin, one of the main constituents of jet fuel surrogates. Density Functional Theory calculations (B3LYP and BH&HLYP functionals) together with the Rice-Ramsperger-Kassel-Marcus and transition state theory methods were used to compute the pressure dependent thermal rate constants for the new reaction pathways. The new pathways connect decalin to five primary mono-aromatic species; benzene, toluene, styrene, ethylbenzene and xylene. The reactions used

for the new routes are carbon-carbon bond cleavage reaction, dissociation reaction and hydrogen abstraction and addition reactions. A kinetic analysis was performed for pyrolytic conditions and benzene, toluene and xylene were identified as major products.

Preliminary results on transport properties using Molecular Dynamics simulations are reported for small hydrocarbons.

2. TECHNICAL DISCUSSION

In combustion conditions, the propagation rate of a laminar flame is determined by the rates of chemical reaction and heat release, which are strongly coupled with heat conduction and molecular diffusion. An accurate description of diffusion rates is perhaps as critical to flame simulation as a quantitative knowledge of elementary reaction kinetics [1–5]. Little to no progress has been made in improving the accuracy of transport coefficients. Most of the measurements for the diffusion coefficient have been carried out at or near room temperature. In flame simulation, extrapolation to high temperatures is made by the Chapman-Enskog equation using the Lennard-Jones (L-J) 12–6 potential energy function.

In this work we present results related to the thermochemistry of key compounds for real fuel surrogates, such as decalin and preliminary results for the computation of transport properties of simple hydrocarbons.

2.1 COMPUTATIONAL METHODOLOGY

All electronic structure calculations were previously carried out at DFT methods, particularly B3LYP and BHandHLYP levels of theory, using the Gaussian 03 program package.[1] The electronic results, namely optimized structures, frequencies and energies of reactants, transition state and products, were given in the supporting material of the previous publication.[2]

In this study we use the previously-calculated electronic results to extend rate constant calculations to the atmospheric pressure condition for unimolecular reactions in order to compare to available experimental data of the pyrolysis of decalin. It is noted that previously the high-pressure limit rate constants were previously calculated using TST and RRKM methods for bimolecular and unimolecular reactions, respectively. In this study pressure-dependent rate constants for the unimolecular reactions were carried out using the Master Equation approach,[3] employing the kinetic module of the web-based Computational Science and Engineering Online (CSE-Online) environment.[4]

Pressure-Dependent Rate Constants

The master equation can be formulated in the discrete form for a uni-molecular reaction as follows,[3]

$$\frac{\mathrm{d}P(E_i)}{\mathrm{d}t} = \omega\sum_j \Big(R(E_i;E_j)P(E_j) - R(E_j;E_i)P(E_i)\Big) - k(E_i)P(E_i) \qquad (1)$$

where ω is the collision frequency of the reactant molecules with bath gas; $P(E_i)$ is the population of the activated reactant with an energy between E_i and $E_i + dE$; $R(E_i;E_j)$ is the collision induced transition rate of reactant with an energy between E_j and $E_j + dE$ to a state with an energy between E_i and $E_i + dE$; $k(E_i)$ is the micro-canonical rate constants of reactant with an energy between E_i and $E_i + dE$. In this study the first term on the right-hand side of eq (1) describes the increase in the population of the reactant between E_i and $E_i + dE$, while the remaining two terms describes the decrease in its population via collision with bath molecules and via a chemical reaction, respectively.

Collision frequency ω can be calculated using Lennard-Jones potential parameters as:

$$\omega = \omega_{hard-sphere}\Omega \qquad (2)$$

where $\omega_{hard-sphere}$ is the hard-sphere collision rate derived from the elementary gas-phase kinetic theory and Ω is a dimensionless collision integral which was calculated by the expression proposed by Reid *et al.*[5] It is noted that the value of ω is pressure dependent.

The function $R(E_i;E_j)$ is the probability that a reactant with an energy between E_j and $E_j + dE_j$ will be transferred by a collision to a state with an energy between E_i and $E_i + dE$. It can be approximated by a single-exponential down function:

$$R(E_i;E_j) = \frac{1}{C_N(E_j)}\exp\left(-\frac{E_j - E_i}{\langle\Delta E_d\rangle}\right),\ E_j > E_i \qquad (3)$$

where $C_N(E_j)$ is the normalization constant; $\langle\Delta E_d\rangle$ is the averaged energy transferred in a deactivating collision, which depends on the nature of the colliding gas as a function of temperature, or in some cases, of temperature and energy. $R(E_j;E_i)$ can be calculated through $R(E_i;E_j)$ using the detailed-balance condition.

A summary of the thermochemical results are reported below. More details can be found in ref. 2.

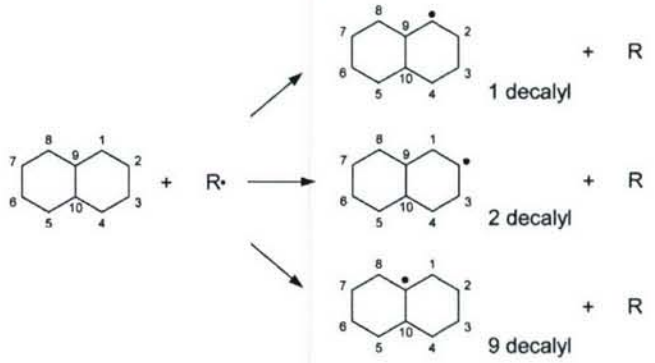

Carbon-hydrogen bond breaking

From 1-decalyl (***'1b'***) we identified nine pathways leading to the formation of various aromatics including benzene, styrene and xylene. Paths 1 – 6 begins with the $C_8 - C_9$ bond cleavage and Paths 7 – 9 with the C_2 - C_3 bond scission.

The figure below reports Paths 1 and 2 to form toluene (C_7H_8) and propyl (C_3H_7). The energy barrier for the formation of radical ***'1c'*** is 34.62 *kcal/mol* and the following *h*ydrogen migration to produce ***'1d'*** has transition energy of 11.32 *kcal/mol.*

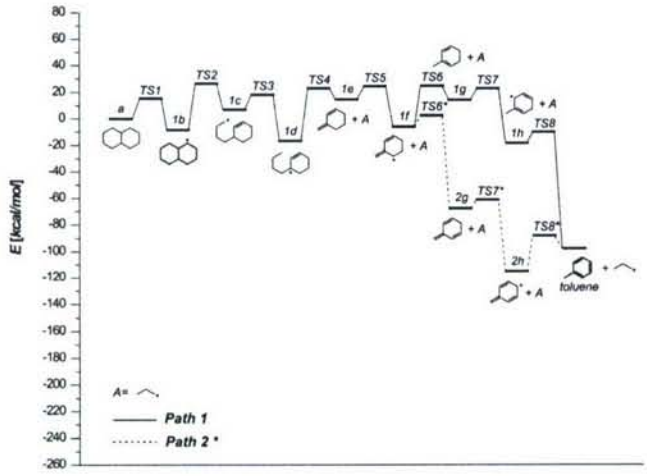

Subsequently, '***1d***' decomposes to form ***'1e'*** and propyl radical (***'1d → 1e'*** reaction). Hydrogen abstraction from intermediate ***'1e'*** produces radical ***'1f'*** with transition energy of *10.10 kcal/mol.* From ***'1f'*** two different pathways have been identified that lead to the formation of toluene. The ***'1f → 1g'***, ***'1g → 1h'*** and ***'1h → toluene'*** route (Path 1) involves hydrogen addition, abstraction and further addition to produce toluene. From intermediate ***'1f'*** the most significant barrier is represented by ***'1f → 1g'***, being *31.21 kcal/mol.*

In Path 2, ***'1f'*** undergoes two hydrogen abstraction reactions (***'1f → 2g'*** and ***'2g → 2h'***) and hydrogen addition (***'2h → toluene'***) to produce toluene. The energy barriers involved in this route are lower than the ones in Path 1 and the intermediates formed are very stable.

REFERENCES

(1) Frisch, M. J.; Trucks, G. W.; Schlegel, H. B. et al. *Gaussian 03, Revision A.1, Gaussian, Inc., Pittsburgh PA,* **2003**.
(2) Chae, K.; Violi, A. *J. Org. Chem.* **2007**, *72*, 3179.
(3) Gilbert, R. G.; Smith, S. C. *Theory of Unimolecular and Recombination Reactions*; Blackwell: Oxford, 1990.
(4) Truong, T. N.; Nayak, M.; Huynh, H. H. et al. *J. Chem. Inf. Model.* **2006**, *46*, 971.
(5) Reid, R. C.; Prausnitz, J. M.; Sherwood, T. K. *The Properties of Gases and Liquids*, 3rd ed.; McGraw-Hill: New York, 1977.

SUPERCRITICAL FUEL PYROLYSIS

AFOSR Grant No. FA9550-07-1-0033

Principal Investigator: Mary Julia (Judy) Wornat

Louisiana State University
Department of Chemical Engineering
Baton Rouge, Louisiana 70803

SUMMARY/OVERVIEW:

The fuels used in the next generation of hypersonic aircraft will have to operate under very high pressures (beyond the critical pressures of most hydrocarbons) and will have to sustain very high heat loads in order to meet aircraft cooling requirements [1-3]. Critical to the development of the fuel systems in these aircraft is an understanding of the fuel pyrolysis reaction mechanisms under the conditions that the fuels will be operating. Of particular interest are the reactions leading to polycyclic aromatic hydrocarbons (PAH), which can serve as precursors to fuel-line deposits [3,4], a problem of critical importance to avoid, for safe aircraft operation. In order to better elucidate the mechanisms and kinetics of the reactions of fuel pyrolysis and PAH formation under supercritical conditions, pyrolysis experiments are being conducted, under the present research program, with model fuels at temperatures of 400-700 °C, pressures of 20-100 atm, and residence times of 30-1000 sec. The model fuels include alkane and aromatic components of jet fuels as well as combinations of these components. The supercritical pyrolysis experiments are conducted in an isothermal silica-lined stainless-steel coil reactor specially designed for such experiments, and PAH reaction products are analyzed by high-pressure liquid chromatography with diode-array ultraviolet-visible absorbance and mass spectrometric detection (HPLC/UV/MS), an isomer-specific technique ideally suited for the analysis of PAH [5,6]. It is anticipated that the results from this research will provide information of critical importance to the design and development of fuel systems for high-speed aircraft.

TECHNICAL DISCUSSION

Supercritical pyrolysis experiments have been conducted with the model fuel *n*-decane (critical temperature, 345 °C; critical pressure, 20.8 atm), an alkane component of jet fuels such as Jet A-1 and JP-8, as well as the Fischer-Tropsch synthetic jet fuel S-8. The experiments have been performed in the new high-temperature reactor at temperatures of 600 to 700 °C, pressures up to 50 atm, and a residence time of 140 sec. The PAH products have been analyzed by reversed-phase and normal phase HPLC/UV/MS.

Figure 1 presents the reversed-phase HPLC chromatogram of the products of *n*-decane pyrolysis at 600 °C, 50 atm, and 140 sec. Fifty-five of the product components, ranging in size from two to seven aromatic rings, are well-enough resolved in Figure 1 to permit identification by their UV spectra, and the peaks of these components in Figure 1 have been labelled with the corresponding PAH product structures. Because of the aliphatic nature of the *n*-decane fuel (and the relative ease of breaking alkane C-C bonds), a huge number of alkylated PAH are formed from *n*-decane pyrolysis, as Figure 1 reveals. As a consequence of the abundance of alkylated

PAH in the product mixture (alkyl groups of varying carbon number, in multiple positions and combinations.), however, not all of the products of *n*-decane pyrolysis at 600 °C are well-enough resolved to permit identification or quantification from the reversed-phase HPLC analysis alone.

Because elucidation of the structures of the PAH products is critical to discerning PAH formation mechanisms, we have developed a normal-phase HPLC fractionation technique to use in conjunction with our reversed-phase HPLC analysis. The normal-phase HPLC column is fairly insensitive to alkyl group functionality and is employed to fractionate the *n*-decane product components into groups by ring number. The collected fractions are then subjected to reversed-phase HPLC analyses. The reversed-phase HPLC chromatograms of the four normal-phase HPLC fractions of the 600-°C *n*-decane pyrolysis products of Figure 1 appear in Figure 2. As Figure 2 reveals, the coupling of the normal-phase HPLC fractionation and reversed-phase HPLC analyses yields a tremendous improvement in product component resolution, permitting the identification of 93 individual PAH product species (compared to the 55 of Figure 1). In addition, the more clearly defined product component peaks in Figure 2 lend themselves to accurate product quantification. The combined normal-phase/reversed-phase HPLC analysis method, illustrated here for the *n*-decane pyrolysis products, is also applicable to the analyses of other product samples in which the PAH are highly alkylated. We have recently employed this method in the analyses [7] of stressed Jet A-1 fuel samples produced at AFRL.

Supercritical *n*-decane pyrolysis has also been investigated at higher temperatures, and the reversed-phase HPLC chromatogram of the PAH produced at 700 °C, 30 atm, and 140 sec appears in Figure 3. (An attempt to pyrolyze *n*-decane at 700 °C and 50 atm, the same pressure as in Figure 1, failed due to the large production of solid deposits, which clogged the reactor.) Readily apparent from Figure 3 are the presence of larger-ring-number PAH and the improved resolution of individual product components in the 700-°C product sample, compared to the 600-°C product sample of Figure 1. These effects of temperature on the *n*-decane PAH product distribution are fully consistent with our findings [8] from other fuels: higher pyrolysis temperatures (1) facilitate PAH growth reactions, leading to PAH of higher ring number, and (2) reduce the degree of PAH product alkylation, since aryl-alkyl C-C bonds are easily broken at higher temperatures. Fewer alkylated species in the 700-°C product mixture thus lead to the "cleaner" chromatogram of Figure 3. Nevertheless, application of the normal-phase HPLC fractionation method to the 700-°C product sample, followed by concentration of the highest-ring-number fraction, greatly enhances our ability to detect and identify large PAH in these products as well, as revealed in the inset of Figure 3. As this inset shows, several 7-, 8-, and 9-ring PAH are produced by *n*-decane pyrolysis at 700 °C and 30 atm—none of which have ever before been reported as products of *n*-decane pyrolysis or combustion.

Of particular interest are the five $C_{28}H_{14}$ benzenoid 8-ring products eluting between 120 and 135 min in the inset of Figure 3. All five of these 8-ring PAH we have also observed [5,9] in the supercritical pyrolysis products of toluene and of the Fischer-Tropsch fuel S-8. The relative amounts of these isomers differ, however, according to the fuel type. In the case of toluene—where the formation of the 8-ring PAH is constrained by a mechanism [9] involving the benzyl, methyl, and phenyl building blocks of the supercritical toluene pyrolysis environment—the dominant $C_{28}H_{14}$ isomer is benzo[*ghi*]naphtho[8,1,2-*bcd*]perylene. In the supercritical *n*-decane pyrolysis environment, however, where C_{10} alkane chains dominate, a different mechanism appears to prevail, and the dominant $C_{28}H_{14}$ product is benzo[*pqr*]naphtho[8,1,2-*bcd*]perylene. Its dominance is echoed by the five alkylated derivatives of this $C_{28}H_{14}$ PAH, eluting between 140 and 190 min in the inset of Figure 3. In order to better elucidate the mechanisms responsible for large PAH formation from alkane fuels, we plan experiments with *n*-tetradecane (which should produce a dominant 10-ring analogue to benzo[*pqr*]naphtho[8,1,2-*bcd*]perylene). We anticipate

that an uncovering of the mechanisms leading to large PAH formation from these alkane fuels will provide insight into why these particular fuels are prone to high solid deposit formation.

REFERENCES

1. Heneghan, S.P., Zabarnick, S., Ballal, D.R., Harrison W.E. III. "JP-8+100: The Development of High-Thermal Stability Jet Fuel," *Journal of Energy Resources Technology 118*: 170-179 (1996).
2. Doungthip, T., Ervin, J.S., Williams, T.F., and Bento, J. "Studies of Injection of Jet Fuel at Supercritical Conditions," *Industrial and Engineering Chemistry Research 41:* 5856-5866 (2002).
3. Edwards, T., Zabarnick, S. "Supercritical Fuel Deposition Mechanisms," *Industrial and Engineering Chemistry Research 32:* 3117-3122 (1993).
4. Stewart, J. F. "Supercritical Pyrolysis of Endothermic Fuels," Ph.D. Thesis, Department of Mechanical and Aerospace Engineering, Princeton University, 1999.
5. McClaine, J. W., Zhang, X., and Wornat, M. J., "First Identification of Benzo[*ghi*]naphtho-[8,1,2-*bcd*]perylene as a Product of Fuel Pyrolysis," *Journal of Chromatography A 1127:* 137-146 (2006).
6. Somers, M. L., McClaine, J. W., and Wornat, M. J., "The Formation of Polycyclic Aromatic Hydrocarbons from the Supercritical Pyrolysis of 1-Methylnaphthalene," *Proceedings of the Combustion Institute 31:* 501-509 (2007).
7. Wornat, M. J., personal communication to M. J. DeWitt and T. Edwards, December 12, 2006.
8. Wornat, M. J., Sarofim, A. F., and Longwell, J. P., "Pyrolysis-Induced Changes in the Ring Number Composition of Polycyclic Aromatic Compounds from a High Volatile Bituminous Coal," *Proceedings of the Combustion Institute 22:* 135-143 (1988).
9. McClaine, J. W., and Wornat, M. J., "Reaction Mechanisms Governing the Formation of Polycyclic Aromatic Hydrocarbons in the Supercritical Pyrolysis of Toluene: $C_{28}H_{14}$ Isomers," *Journal of Physical Chemistry C 111*: 86-95 (2007).

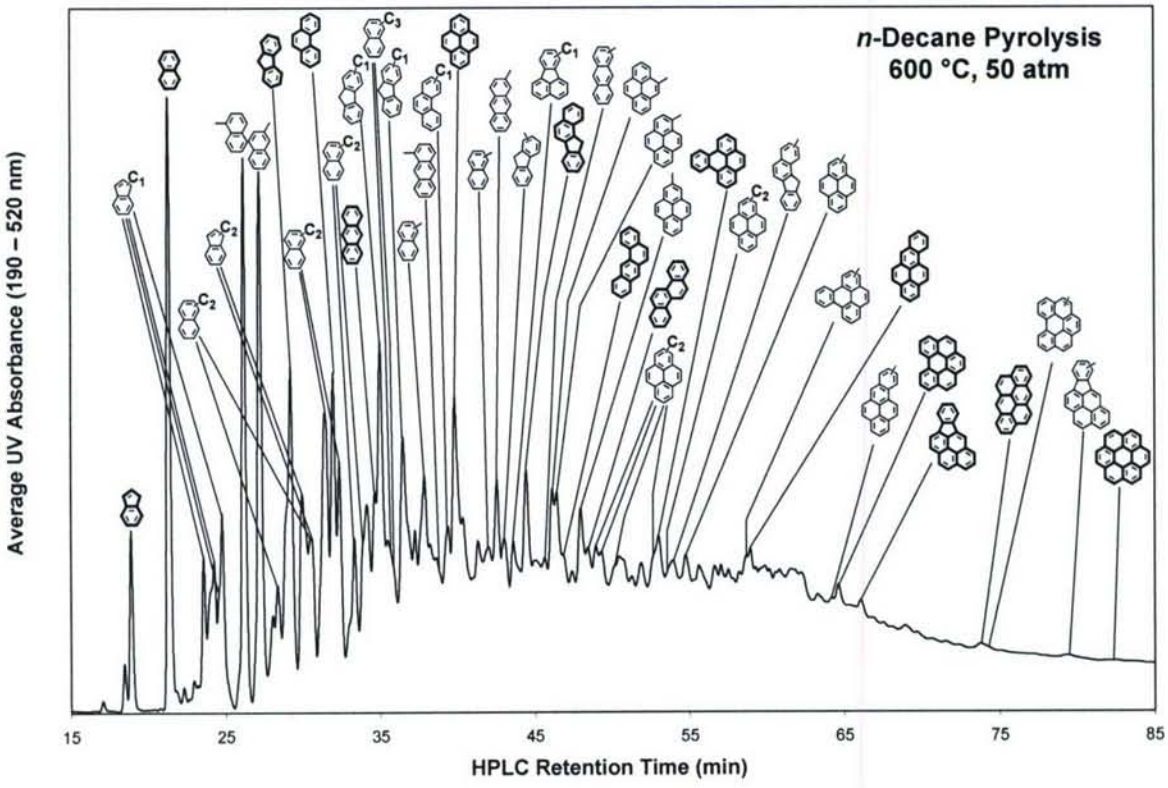

Figure 1. Reversed-phase HPLC chromatogram of the products of *n*-decane pyrolysis at 600 °C, 50 atm, and 140 sec. Bold structures are unsubstituted PAH; others are alkylated PAH.

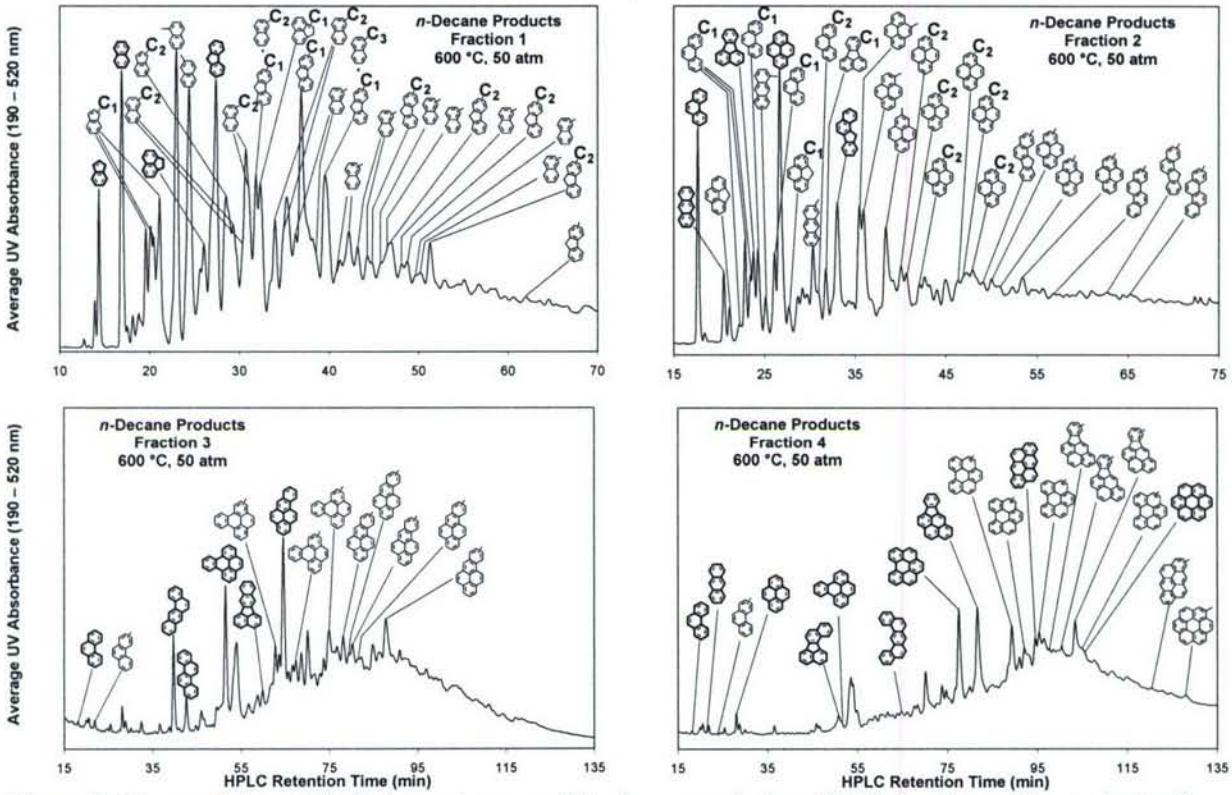

Figure 2. Reversed-phase HPLC chromatograms of the four normal-phase HPLC fractions of the products of *n*-decane pyrolysis at 600 °C, 50 atm, and 140 sec. Bold structures are unsubstituted PAH; others are alkylated PAH.

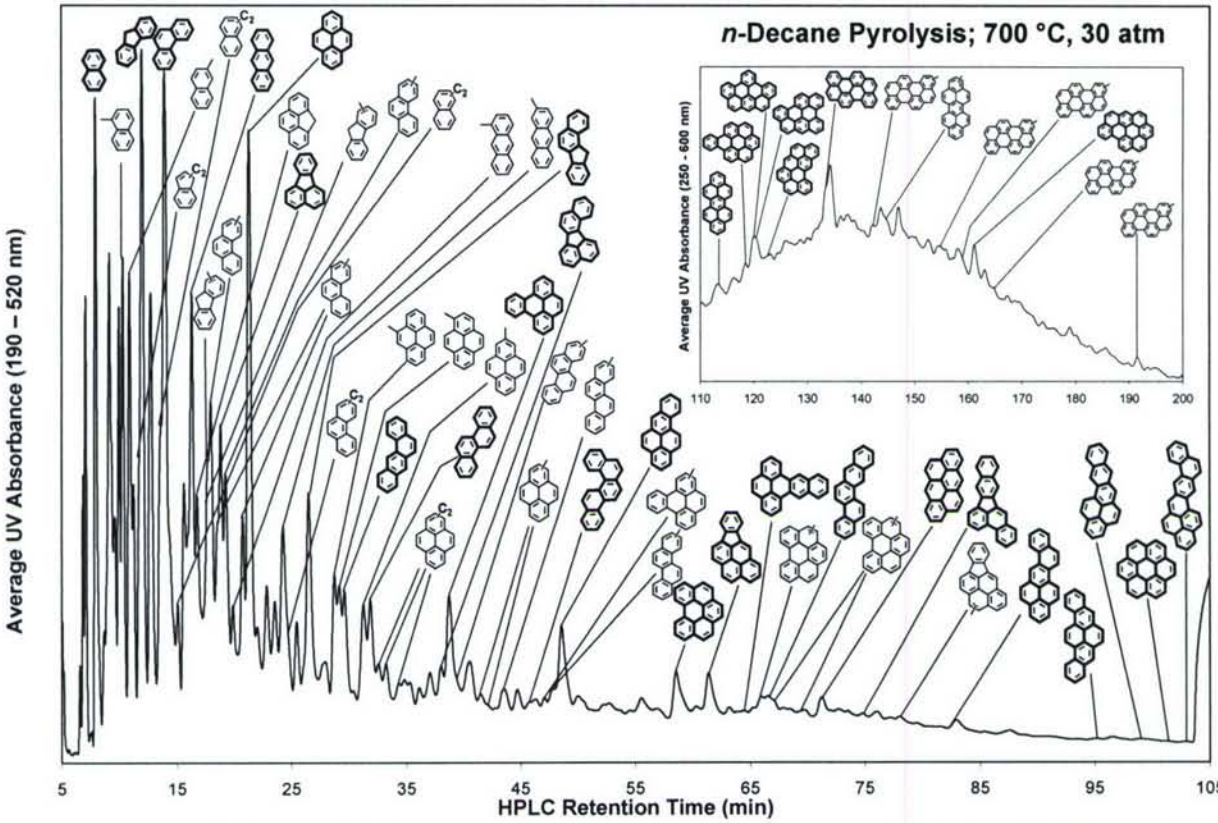

Figure 3. Reversed-phase HPLC chromatograms of the products of *n*-decane pyrolysis at 700 °C, 30 atm, and 140 sec. **Inset:** large-ring-number PAH fraction. Bold structures are unsubstituted PAH; others are alkylated PAH.

INVITEES

Dr. Waldo Acosta
Vehicle Technology Directorate, Army Research Lab.
NASA Glenn Res. Ctr.
21000 Brookpark Road
Cleveland OH 44135-3191
(216) 433-3393
waldo.acosta@us.army.mil

Dr. Ajay Agrawal
Aerospace and Mechanical Engineering
University of Oklahoma
865 Asp Avenue, Room 212
Norman OK 73019
(405) 325-1754
aagrawal@ou.edu

Dr. M. S. Anand
Rolls-Royce Corporation,
P.O. Box 420
Speed Code T14
Indianapolis IN 46206-0420
(317)230-2828
m.s.anand@rolls-royce.com

Dr. William Anderson
AMSRL-WT-PC
US Army Research Laboratory
Aberdeen Proving Ground MD 21005-5066
(410)306-0731
willie@arl.army.mil

Dr Kurt Annen
Aerodyne Research, Inc.
45 Manning Road
Manning Park Research Center
Billerica MA 01821-3976
(978)663-9500
kannen@aerodyne.com

Dr. Ralph Anthenien
Propulsion and Energetics
U.S. Army Research office
P.O. Box 12211
Research Triangle Park NC 27709-2211
(919)549-4317
Ralph.anthenien1@us.army.mil

Dr Chris Atkinson
Dept of Mech. & Aerospace Eng.
West Virginia University
PO Box 6106
Morgantown WV 26506-6106
(304)293-4111

Mr. Steve Beckel
Pratt and Whitney
M/S 715-83
P.O. Box 109600
West Palm Beach FL 33410-9600

Dr Josette Bellan
Jet Propulsion Laboratory
MS 125-109
4800 Oak Grove Drive
Pasadena CA 91109
(818)354-6959
josette.bellan@jpl.nasa.gov

Dr. Michael Berman
Air Force Office of Scientific Research
ATTN: Michael Berman - NL
875 North Randolph Street
Suite 325, Room 3112
Arlington VA 22203-1768
(703)696-7781
michael.berman@afosr.af.mil

Dr Mitat Birkan
Air Force Office of Scientific Research
ATTN: Mitat Birkan - NA
875 North Randolph Street
Suite 325, Room 3112
Arlington VA 22203-1768
(703)696-7234
mitat.birkan@afosr.af.mil

Dr Kevin Bowcutt
North American Aircraft Div.
Rockwell International Corp.
P.O. Box 3644
Seal Beach CA 90740-7644

Mr. Andreja Brankovic
Flow Parametrics, LLC
15 Debra Drive
Bear DE 19701
(302)838-7368
brankov@flowparametrics.com

Dr R C Brown
Aerodyne Research, Inc.
45 Manning Road
Manning Park Research Center
Billerica MA 01821-3976
(978)663-9500

Dr. Thomas Bruno
National Institute of Standards and Technology
Physical and Chemical Properties Division
Boulder CO 80305-3328
(303)497-5158
bruno@boulder.nist.gov

Dr. Walter Bryzik
Propulsion Systems Division
ATTN: AMSTA-TR-R, MS 121
USA Tank-Automotive Command
Warren MI 48397-5000
(810)574-6461
bryzikw@tacom.army.mil

Dr T D Butler
MS B-210 T-DO: THEORETICAL DIVISION
Los Alamos National Laboratory
Los Alamos NM 87545
(505)667-4401
tdbutler@lanl.gov

Dr George Caledonia
Physical Sciences, Inc
20 New England Business Center
Andover MA 01810
(508)689-0003

Dr. Campbell Carter
AFRL/PRA
1950 Fifth Street
Building 18, Room D224
Wright-Patterson AFB OH 45433-7251
(937)255-7203
Campbell.Carter@wpafb.af.mil

Dr. Len Caveny
13715 Piscataway Drive
Ft Washington MD 20744
(301)292-5319
lhcaveny@cs.com

Dr. Nicholas Cernansky
Mechanical Engineering Dept.
Drexel University
32nd and Chestnut Streets
Philadelphia PA 19104-2884

Dr. Harsha Chelliah
Department of Mechanical, Aero
and Nuclear Engineering
University of Virginia
Charlottesville VA 22903-2442
(804)924-6037
harsha@virginia.edu

Dr. Jacqueline Chen
MS 9051
Sandia National Laboratories
P.O. Box 969
Livermore CA 94551-0969
(510)294-2586
jhchen@sandia.gov

Dr S Y Cho
Department of Mechanical and
Aerospace Engineering
Princeton University
Princeton NJ 08544-5263

Dr M B Colket
United Technologies Research
Center
411 Silver Lane, MS 129-29
East Hartford CT 06108
(860)610-7481
colketmb@utrc.utc.com

Dr S M Correa
GE Corp. Research & Development
PO Box 8, K1ES112
Schenectady NY 12301
(518)387-5853
correa@crd.ge.com

Dr Werner Dahm
Department of Aerospace Engineering
3056 FXB 2140
The University of Michigan
Ann Arbor MI 48109-2140
(734)764-4318
wdahm@umich.edu

Mr. Eugene Danielson
US Army Tank-Automotive
and Armaments Command
ATTN: AMSTA-TR-R - MS 121
Warren MI 48397-5000

Dr Ron Davis
Chemical Science and Techn Lab
Building 221, Room B312
National Inst of Stds & Tech
Gaithersburg MD 20899

Dr. Peter A. DeBarber
MetroLaser
2572 White Road
Irvine CA 92614
(949)553-0688
debarber@deltanet.com

Dr. John DeLaat
Active Combustion Control Technology
Controls and Dynamics Branch
NASA Glenn Res. Ctr.
21000 Brookpark Road
Cleveland OH 44135
(216)433-3744
jdelaat@nasa.gov

Dr Paul Dimotakis
California Institute of Tech
1201 East California Blvd.
MC 301-46
Pasadena CA 91125
(626)395-4456
dimotakis@caltech.edu

Dr Gregory Dobbs
United Technologies Research
Center - Mail Stop 90
Silver Lane
East Hartford CT 06108
(860)610-7145

Dr. James F. Driscoll
Department of Aerospace Engrg
3004 FXB Building
University of Michigan
Ann Arbor MI 49109-2118
(734)936-0101
jamesfd@umich.edu

Dr. J. Philip Drummond
NASA Langley Research Center
Mail Stop 197
Hampton VA 23681-0001
(757)864-2298
j.p.drummond@larc.nasa.gov

Dr C Dutton
Department of Mechanical and
Industrial Engineering
University of Illinois
Urbana IL 61801

Dr. Tarek Echekki
Department of Mechanical & Aerospace Engrg
North Carolina State University
2601 Stinson Drive - Campus Box 7910
Raleigh NC 27695-7910
(919)515-5238
techekk@eos.ncsu.edu

Dr. Wayne Eckerle
Cummins Engine Company
PO Box 3005
Columbus IN 47202-3005
wayne.a.eckerle@cummins.com

Dr J T Edwards
AFRL/PRTG
Building 490, Room 111
1790 Loop Road, N
Wright-Patterson AFB OH 45433-7251
(937)255-3524
james.edwards@wpafb.af.mil

Dr. Fokion N. Egolfopoulos
Department of Mechanical Engrg
University of Southern Calif
Olin Hall 400B
Los Angeles CA 90089-1453
(213)740-0480
egolfopo@almaak.usc.edu

Dr. Parviz Famouri
Department of Computer Science and Electrical
Engineering
West Virginia University
PO Box 6109
Morgantown WV 26506
(304) 293-0405 x 2530
pfamouri@wvu.edu

Dr Gregory W Faris
Molecular Physics Laboratory
SRI International
333 Ravenswood Avenue
Menlo Park CA 94025-3493
(650)859-4131
gregory.faris@sri.com

Dr. Partick Farrell
Engine Research Center
1500 Engineering Drive
University of Wisconsin
Madison WI 53706
(608)263-1686
farrell@engr.wisc.edu

Dr. David E. Foster
Engine Research Center
1500 Engineering Drive
University of Wisconsin
Madison WI 53706
(608)263-1617
foster@engr.wisc.edu

Dr Bish Ganguly
AFRL/PRPE
2645 Fifth Street, Suite 13
Wright-Patterson AFB OH 45433-7919
(937)255-2923
biswa.ganguly@pr.wpafb.af.mil

Dr Alan Garscadden
AFRL/PR
1950 Fifth Street, Building 18A
Wright-Patterson AFB OH 45433-7251
(937)255-2246
alan.garscadden@pr.wpafb.af.mil

Dr. Kresimir Gebert
BKM, Inc.
5141 Santa Fe Street
San Diego CA 92109
(858)270-6760
bkm-inc@worldnet.att.net

Mr R Giffen
General Electric Company
Aircraft Engine Group
Neumann Way
Cincinnati OH 45215

Dr. Sharath Girimaji
Department of Aerospace Engineering
Texas A&M University
College Station TX 77843-3141
(979)845-1674
girimaji@aero.tamu.edu

Dr Peyman Givi
Department of Mechanical Engineering
University of Pittsburgh
644 Benedum Hall
Pittsburgh PA 15261
(412)624-9605
givi@engr.pitt.edu

Dr Irvin Glassman
Department of Mechanical and
Aerospace Engineering
Princeton University
Princeton NJ 08544-5263
(609)258-5199
glassman@princeton.edu

Dr. Brendan Godfrey
Air Force Office of Scientific Research
ATTN: Brenddan Godfrey - CC
875 North Randolph Street
Suite 325, Room 3112
Arlington VA 22203-1768
(703)696-7553
brendan.godfrey@afosr.af.mil

Dr. George Gogos
Department of Mechanical Engineering
University of Nebraska-Lincoln
Lincoln NE 68588-0656
(402)472-3006
ggogos1@unl.edu

Dr Judah Goldwasser
Office of Naval Research
Mechanics Division, Code 333
800 North Quincy Street
Arlington VA 22217-5660
(703)696-2164
goldwaj@onr.navy.mil

Dr. James Gord
AFRL/PRTS
Building 5, Room 5P23
1790 Loop Road N
Wright-Patterson AFB OH 45433-7251
(937)255-7431
james.gord@pr.wpafb.af.mil

Dr. Jay P. Gore
School of Mechanical Engrg
Purdue University
1003 Chaffee Hall
West Lafayette IN 47907-1003
(317)494-1500

Dr Larry Goss
Research Applications Division
Systems Research Labs, Inc.
2800 Indian Ripple Road
Dayton OH 45440-3696
(513)252-2706

Dr Richard Gould
Department of Mechanical and Aerospace
Engineering
Box 7910
North Carolina State University
Raleigh NC 27695-7910
(919)515-5236
gould@eos.ncsu.edu

Dr Frederick Gouldin
Department of Mechanical and
Aerospace Engineering
Cornell University
Ithaca NY 14853-5692
(607)255-5280
fcg2@cornell.edu

Dr. Mark Gruber
AFRL/PRA
1790 Loop Road North
Wright-Patterson AFB OH 45433-7251
(937)255-2175
Mark.Gruber@afrl.af.mil

Dr. Brian K. Gullett
U.S. Environmental Protection Agency
National Risk Management Research Laboratory
Air Pollution Technology Branch (MD-65)
Research Triangle Park NC 27711
(919)541-1534
gullett.brian@epa.gov

Dr. Rajendra Gupta
Department of Physics
226 Physics Building
University of Arkansas
Fayetteville AK 72701
(501)575-5933
rgupta@comp.uark.edu

Dr. Mark A. Hagenmaier
AFRL/PRA
Building 18
1950 Fifth Street, Suite 10
Wright-Patterson AFB OH 45433-7251
(937)255-5210
hagenma@possum.appl.wpafb.af.mil

Dr. Nabil S. Hakim
Director, Advanced Engineering
Detroit Diesel Corporation
13400 W. Outer Drive, R03-B
Detroit MI 48239-4001
(313)592-7455

Dr Robert D. Hancock
AFRL/PRTS
Building 490
1790 Loop Road, N
Wright-Patterson AFB OH 45433-7103
(937)255-6814
hancockr@ward.appl.wpafb.af.mil

Dr Ronald Hanson
Mechanical Engineering Department
Stanford University
Building 530, Room 112
Stanford CA 94305-3030
(650)723-6850
hanson@me.stanford.edu

Dr. Naeim Henein
Department of Mechanical Engrg
Wayne State University
2121 Engineering Building
Detroit MI 48201
(313)577-3887
henein@me1.eng.wayne.edu

Dr Cecil F. Hess
MetroLaser
2572 White Road
Irvine CA 92614
(949)553-0688
chess@metrolaserinc.com

Mr Robert Holland
United Technologies Chemical
Systems Division
P O Box 49028
San Jose CA 95161-9028
(408)224-7656

Laura Hoogterp
Propulsion Systems Division
ATTN: AMSTA-TR-R, MS 121
USA Tank Automotive Command
Warren MI 48397-5000
586-574-6696
laura.hoogterp@us.army.mil

Dr. Tian-Sen Huang
Prairie View A&M University
PO Box 307
Prairie View TX 77446-0307
(936) 857-2859
ts_huang@pvamu.edu

Dr Lawrence Hunter
Applied Physics Laboratory
Johns Hopkins University
Johns Hopkins Road
Laurel MD 20707-6099
(301)953-5000

Dr. Frank Hurley
US Army Research Office
PO Box 12211
Research Triangle Park NC 27709-2211
(919)549-4432
hurley@aro-emh1.army.mil

Dr. Thomas Hussey
Air Force Office of Scientific Research
ATTN: Thomas Hussey - CS
875 North Randolph Street
Suite 325, Room 3112
Arlington VA 22203-1768
(703)696-7556
thomas.hussey@afosr.af.mil

Dr. Farhad Jaberi
Department of Mechanical and
Nuclear Engineering
Kansas State University
Manhattan KS 66506
(785)532-5619
jaberi@mne.ksu.edu

Dr. Thomas Jackson
AFRL/PRSC
Building 18
1950 Fifth Street
Wright-Patterson AFB OH 45433-7251
(937)255-2175
thomas.jackson@afrl.af.mil

Dr. Jeff Jagoda
School of Aerospace Engineering
Georgia Institute of Technology
Atlanta GA 30332-0150
(404)894-3060
jeff.jagoda@aerospace.gatech.edu

Dr Jay Jeffries
Mechanical Engineering Department
Thermophysics Division, Building 520
Stanford University
Stanford CA 94305-3032
(650)736-0007
Jeffries@Navier.Stanford.edu

Mr Gordon Jensen
United Technologies Chemical
Systems Division
P O Box 49028
San Jose CA 95161-9028
(408)365-5552

Mr. Jeff Jensen
Kaiser-Marquardt
16555 Staycoy Street
Van Nuys CA 91406

Mr. Craig Johnston
Lockheed Advanced Dev. Company
Lockheed-Martin Corporation
1011 Lockheed Way
Palmdale CA 93599-7212

Dr John Kelly
Altex Technologies Corporation
650 Nuttman Road
Suite 114
Santa Clara CA 95054
(408)980-8610

Dr. Barry Kiel
AFRL/PRTC
Building 490, Room 109
1950 Fifth Street
Wright-Patterson AFB OH 45433-7251
(937)255-7272
Barry.Kiel@wpafb.af.mil

Dr G B King
Department of Mechanical
Engineering
Purdue University
West Lafayette IN 47907-1288
(765)494-6518
kinggb@ecn.purdue.edu

Dr. David E. Klett
Mechanical Engineering Dept
North Carolina Agricultural
and Technical State Univ
Greensboro NC 27401-3209

Dr Charles Kolb
Aerodyne Research, Inc.
45 Manning Road
Manning Park Research Center
Billerica MA 01821-3976
(978)663-9500

Mr. John Koshoffer
General Electric Aircraft Engines
1 Neuman Way
M.D. G52
Cincinnati OH 45215
(513)243-2995
john.koshoffer@ae.ge.com

Dr Kenneth Kuo
Department of Mechanical
Engineering
Pennsylvania State University
University Park PA 16802
(814)865-6741

Dr. Ming-Chia Lai
Department of Mechanical Engrg
Wayne State University
Detroit MI 48202

Dr John Larue
Department of Mechanical
Engineering
University of California
Irvine CA 92717

Dr Allan Laufer
Office of Energy Research
U. S. Department of Energy
19901 Germantown Road
Germantown MD 20874
(202)903-5820
Allan.Laufer@oer.doe.gov

Dr Normand Laurendeau
School of Mechanical
Engineering
Purdue University
West Lafayette IN 47907-1288
(765)494-2713
Laurende@ecn.purdue.edu

Dr C K Law
Department of Mechanical and
Aerospace Engineering
Princeton University
Princeton NJ 08544-5263
(609)258-5271
cklaw@princeton.edu

Dr. Calvin Lee
Applied Research Division
Natick Research, Development & Engr. Ctr.
Kansas Street
Natick MA 01760-5017
(508)233-4267
calvin.k.lee@us.army.mil

Dr C C Lee
Environmental Protection
Agency
Cincinnati OH 45268
(513)569-7520

Dr Anthony Leonard
Graduate Aeronautical Labs
California Institute of
Technology
Pasadena CA 91125
(626)395-4465

Dr. Arthur Lewis
University of Dayton Research Inst.
Aerospace Mechanics Division
300 College Park
Dayton OH 45469-0110
(937)229-4235

Dr. Mark Lewis
AF/ST
1075 Air Force Pentagon
Washington DC 20330-1075
(703)697-7842
mark.lewis@pentagon.af.mil

Mr. Randy L. Lewis
General Electric Aircraft Engines
1 Neuman Way
M.D. G52
Cincinnati OH 45215
(513)243-0517
Randy.Lewis@ae.ge.com

Dr Goang Liaw
Department of Civil Engineering
Alabama A&M University
PO Box 367
Normal AL 35762
(205)851-5565

Dr. Timothy Lieuwen
School of Aerospace Engineering
Georgia Institute of Technology
Atlanta GA 30332-0150
(404)894-3041
tim.lieuwen@aerospace.gatech.edu

Dr. Peter Lindstedt
Department of Mechanical Engineering
Imperial College of Science, Technology, and
Medicine
Exhibition Road
London SW7 2 BX England UK
p.lindstedt@imperial.ac.uk

Dr. Mark A. Linne
Department of Combustion Physics
Lund Institute of Technology
PO Box 118
S-221 00 Lund, Sweden
+46 (0) 46-2224756
mark.linne@forbrf.lth.se

Dr. Charles L. Liotta
Department of Chemical Engrg
Georgia Institute of
Technology
Atlanta GA 30332-0100
(404)853-9344

Dr. Thomas A. Litzinger
Department of Mechanical Engineering
Pennsylvania State University
0201 Hammond Building
University Park PA 16802
(814) 865-4015
tal2@psu.edu

Dr Lyle N Long
Department of Aerospace Engrg
233 Hammond Building
Pennsylvania State University
University Park PA 16802
(814)865-1172
lnl@psu.edu

Dr. Jeffery Lovett
Pratt and Whitney
400 Main Street
MS 163-03
East Hartford CT 06108
(860)557-0559
jeffery.lovett@pw.utc.com

Dr Kevin Lyons
Department of Mechanical and Aerospace
Engineering
North Carolina State University
PO Box 7910
Raleigh NC 27695
(919)515-5293
lyons@eos.ncsu.edu

Dr Bruce MacDonald
Research Applications Division
Systems Research Labs, Inc.
2800 Indian Ripple Road
Dayton OH 45440-3696
(513)252-2706

Mr Nick Makris
SA-ALC/SFT
Kelly AFB TX 78241-5000
AV945-8212

Dr David Mann
U. S. Army Research Office
P. O. Box 12211
4300 South Miami Boulevard
Research Triangle Pk NC 27709-2211
(919)549-4249
david.mann1@us.army.mil

Dr Nagi Mansour
Computational Fluid Mechanics
Branch, RFT 202A-1
NASA Ames Research Center
Moffett Field CA 94035
(415)604-6420

Dr John Marek
NASA Glenn Research Center
Mail Stop 5-11
21000 Brookpark Road
Cleveland OH 44135-3127
(216)433-3584
cecil.j.marek@lerc.nasa.gov

Dr. Jochen Marschall
SRI International
333 Ravenswood Avenue
Menlo Park CA 94025-3493
(650)859-2667
jochen.marschall@sri.com

Dr. Jay Martin
University of Wisconsin-Madison
Engine Research Center
1500 Engineering Drive
Madison WI 53706
(608)263-9460
martin@engr.wisc.edu

Dr James McDonald
Code 6110
Naval Research Laboratory
Chemistry Division
Washington DC 20375-5342
(202)767-3340

Dr. Kevin McNesby
Army Research Laboratory
Army Research Office
P.O. Box 12211
Research Triangle Park NC 27709-2211
(410)306-0715
mcnesby@arl.army.mil

Dr A M Mellor
Mech & Matls Engrg Dept
512 Kirkland Hall
Vanderbilt University
Nashville TN 37240
(615)343-6214

Dr Lynn Melton
Programs in Chemistry
University of Texas, Dallas
P. O. Box 830688
Richardson TX 75083-0688
(972)883-2913
melton@utdallas.edu

Dr. Suresh Menon
School of Aerospace Engineering
Georgia Institute of Technology
270 Ferst Drive
Atlanta GA 30332-0150
(404)894-9126
suresh.menon@aerospace.gatech.edu

Dr Hameed Metghalchi
Mechanical, Industrial and Manufacturing Dept.
334SN
Northeastern University
360 Huntington Avenue
Boston MA 2115
(617)-373-2973
metghal@coe.neu.edu

Dr Michael M Micci
Department of Aerospace Engrg
233 Hammond Building
Pennsylvania State University
University Park PA 16802
(814)863-0043
micci@henry2.aero.psu.edu

Dr Andrzej Miziolek
AMSRL-WT-PC
Army Research Laboratory
Aberdeen Proving Gnd MD 21005-5066
(410)278-6157
miziolek@arl.army.mil

Dr. H. C. Mongia
Manager, Combustion Technology
GE Aircraft Engines
One Neumann Way, M/D A404
Cincinnati OH 45215-6301
(513)243-2552
Hukam.Mongia@ae.ge.com

Dr Arje Nachman
Air Force Office of Scientific Research
ATTN: Arje Nachman - NM
875 North Randolph Street
Suite 325, Room 3112
Arlington VA 22203-1768
(703)696-8427
arje.nachman@afosr.af.mil

Dr Herbert Nelson
Code 6110, Chemistry Division
Naval Research Laboratory
4555 Overlook Avenue, SW
Washington DC 20375-5342
(202)767-3686

Dr. Matthew Oehlschlaeger
Department of Mechanical, Aerospace, and
Nuclear Engineering
Rensselaer Polytechnic Institute
JEC 2049
110 8th Street
Troy NY 12180-3590
(518)276-8115
oehlsm@rpi.edu

Dr Elaine Oran
LCP&FD, Code 6404
US Naval Research Laboratory
4555 Overlook Avenue, SW
Washington DC 20375-5344
(202)767-2960
ORAN@lcp.nrl.navy.mil

Dr. Michelle Pantoya
Department of Mechanical Engineering, MS
1021
Texas Tech University
Lubbock TX 79409
(806) 742-3563
michelle.pantoya@coe.ttu.edu

Dr T E Parker
Engineering Division
Colorado School of Mines
Golden CO 80401-1887
(303)273-3657
tparker@mines.colorado.edu

Dr. Phillip H. Paul
MS 9051
Sandia National Laboratories
P. O. Box 969
Livermore CA 94551-9051
(510)294-1465
phpaul@sandia.gov

Dr Lisa Pfefferle
Department of Chemical
Engineering
Yale University
New Haven CT 06520-8286
(203)432-2222
pfefferle@htcre.eng.yale.edu

Dr Emil Pfender
Department of Mechanical Engrg
125 Mechanical Engineering
The University of Minnesota
Minneapolis MN 55455

Dr. Heinz G Pitsch
Department of Mechanical Engineering
Building 500, Room 500M
Stanford University
Stanford CA 94305-3035
(650)725-6635
h.pitsch@stanford.edu

Dr Robert Pitz
Department of Mechanical and
Materials Engineering
Vanderbilt University
Nashville TN 37235
(615)322-0209
pitzrw@ctrvan.vanderbilt.edu

Dr S B Pope
Department of Mechanical and
Aerospace Engineering
Cornell University
Ithaca NY 14853-7501
(607)255-4314
pope@mae.cornell.edu

Dr. David Pratt
AFRL/VAS
Building 45 Annex
2130 Eighth Street, Suite 1
Wright-Patterson AFB OH 45433-7542
(937)255-5042
David.Pratt@va.afrl.af.mil

Dr. Ala Qubbaj
Department of Mechanical Engineering, ENB
3230
University of Texas-Pan American
1201 West University Drive
Edinburg TX 78539-2999
(956) 318-5220
qubbaj@panam.edu

Dr. Larry Rahn
Sandia National Laboratories
7011 East Avenue
Mail Stop 9056
Livermore CA 94551-0969
(510)294-2091
rahn@sandia.gov

Dr. Mohan K. Razdan
Rolls-Royce Company
P.O. Box 420
Speed Code T10B
Indianapolis IN 46206-0420
(317)230-6404
mohan.razdan@rolls-royce.com

Mr. Robert Reed
Sverdrup Technology, Inc.
AEDC
1099 Avenue C
Arnold AFB TN 37389-9013
(615)454-4648

Dr Rolf D Reitz
Mechanical Engineering Dept
University of Wisconsin
1500 Johnson Drive
Madison WI 53706
(608)262-0145

Dr. Kyung T. Rhee
Department of Mechanical and
Aerospace Engineering
Rutgers, The State Univ of NJ
Piscataway NJ 08854-0909
(732)445-3651
KTRhee@jove.rutgers.edu

Dr James Riley
Mechanical Engineering Dept
University of Washington
Seattle WA 98195
(206)543-5347
73671.737@Compuserve.com

Dr William Roberts
Department of Mechanical and Aerospace Engineering
Box 7910
North Carolina State University
Raleigh NC 27695-7910
(919)515-5294
wlrobert@eos.ncsu.edu

Mr. Gerald A. Roffe
GASL
77 Raynor Avenue
Ronkonkoma NY 11779

Dr W M Roquemore
AFRL/PRTS
Building 5
Wright-Patterson AFB OH 45433-7251
(937)255-6813
melvyn.roquemore@wpafb.af.mil

Dr Daniel Rosner
Department of Chemical Engineering
Yale University
New Haven CT 06520-8286
(203)432-4391
daniel.rosner@yale.edu

Dr John Ross
Department of Chemistry
Stanford University
Stanford CA 94305-3032
(650)723-9203

Dr Gabriel Roy
Office of Naval Research
Mechanics Division, Code 1132
800 North Quincy Street
Arlington VA 22217-5660
(703)696-4406
roy@ocnr-hq.navy.mil

Dr Thomas Russell
Air Force Office of Scientific Research
ATTN: Thomas Russell - NA
875 North Randolph Street
Suite 325, Room 3112
Arlington VA 22203-1768
(703)696-8457
thomas.russell@afosr.af.mil

Dr. Robert C. Ryder
Flow Parametrics, LLC
15 Debra Drive
Bear DE 19701
(302)838-7368
rryder@flowparametrics.com

Mr Kurt Sacksteder
NASA Glenn Research Center
MS 500-217
21000 Brookpark Road
Cleveland OH 44135
(216)433-2857

Dr Mohammad Samimy
Ohio State University
Mechanical Engineering Dept
206 West 18th Street
Columbus OH 43210-1107
(614)422-6988
msamimy@magnus.acs.ohio-state.edu

Dr G S Samuelsen
Department of Mechanical and Aerospace Engineering
University of California
Irvine CA 92697-3975
(949)824-5468

Dr Lakshmi Sankar
School of Aerospace Engrg
Georgia Institute of Technology
Atlanta GA 30332
(404)894-3014

Dr Domenic Santavicca
Propulsion Engineering Research Center
Pennsylvania State University
106 Research Building East - Bigler Road
University Park PA 16802-2320
(814)863-1863

Dr R J Santoro
Department of Mechanical Engineering
Pennsylvania State University
University Park PA 16802-2320
(814)863-1285
rjs2@email.psu.edu

Dr Sutanu Sarkar
Department of Applied Mech
and Engr Science, MC 0411
University of California
La Jolla CA 92093-0411
(858)534-8243
ssarkar@ucsd.edu

Dr John Schaefer
Energy and Environmental Div.
Acurex Corporation
555 Clyde Ave., P. O. Box 7555
Mountain View CA 94039

Dr. Frederick Schauer
AFRL/PRTS
Building 490, Room 112
1790 Loop Road, N
Wright-Patterson AFB OH 45433-7251
(937)255-6462
frederick.schauer@wpafb.af.mil

Dr. Peter Schihl
Propulsion Systems Division
ATTN: AMSTA-TR-R, MS 121
USA Tank Automotive Command
Warren MI 48397-5000
schihlp@tacom.army.mil

Dr. John Schmisseur
Air Force Office of Scientific Research
ATTN: John Schmisseur - NA
875 North Randolph Street
Suite 325, Room 3112
Arlington VA 22203-1768
(703)696-6962
john.schmisseur@afosr.af.mil

Dr. Ernest Schwarz
Propulsion Systems Division
ATTN: DRSTA-RGD
USA Tank-Automotive Command
Warren MI 48397-5000
(810)574-5656
schwarze@cc.tacom.army.mil

Mr. Lee Scuderi
McDonnell Douglas Aerospace
P.O. Box 516
St. Louis MO 63166-0516

Dr Jerry Seitzman
School of Aerospace Engineering
Georgia Institute of Technology
Atlanta GA 30332-0150
(404)894-0013
jerry.seitzman@ae.gatech.edu

Dr Kalyanasundaram Seshadri
Center for Energy and
Combustion Research, 0407
University of California
La Jolla CA 92093-0407
(619)534-4876
seshadri@ames.ucsd.edu

Dr Robert Shaw
Division of Chemical and
Biological Sciences
U S Army Research Office
Research Triangle Park NC 27709-2211
(919)549-0641

Dr. Adam Siebenhaar
Aerojet Propulsion Division
P.O. Box 13222
Sacramento CA 95813-6000

Dr. Gupreet Singh
U.S. Department of Energy
1000 Independence Avenue, S.W.
Washington DC 20585
(202)586-2333
GUPREET.SINGH@hq.doe.gov

Dr William Sirignano
Department of Mechanical and
Aerospace Engineering
University of California
Irvine CA 92697-3975
(949)824-3700
sirignan@uci.edu

Mr. Davey Smith
Northrop Grumman Corporation
B-2 Division Dayton Office
2850 Presidential Dr., Ste 100
Fairborn OH 45324

Dr Gregory Smith
Department of Chem Kinetics
SRI International
333 Ravenswood Avenue
Menlo Park CA 94025-3493
(415)859-3496

Dr. Kenneth A. Smith
Department of Chemical Engrg.
Room 66-540
Massachusetts Inst. Of Technology
Cambridge MA 02139
(617)253-1973
kas@mit.edu

Dr. James Smith
Department of Chemical Engineering
University of Alabama in Huntsville
Huntsville AL 35899
(256) 824-3594
smithje1@uah.edu

Dr. Mitchell Smooke
Department of Mechanical Engineering
205 Becton Center
15 Prospect Street
Yale University
New Haven CT 6520
(203)432-4344
mitchell.smooke@yale.edu

Dr. Judi Steciak
University of Idaho-Boise
800 Park Boulevard
Boise ID 83712-7742
(208)364-4080
jsteciak@uidaho.edu

Dr David Stewart
Department of Theoretical and
Applied Mechanics
University of Illinois
Urbana IL 61801

Dr Geoffrey J Sturgess
Dayton
gsturgess@aol.com

Dr B Sturtevant
Engrg and Appl Sci Dept
California Institute of
Technology
Pasadena CA 91125

Dr G Sullins
Applied Physics Laboratory
Johns Hopkins University
Johns Hopkins Road
Laurel MD 20707-6099
(301)953-5000

Dr Chih-Jen (Jackie) Sung
Dept. of Mechanical and Aerospace Engineering
Case Western Reserve University
10900 Euclid Avenue
Cleveland OH 44106-7222
216-368-2942
cjs15@case.edu

Dr. Rodney Tabacyznski
Director, Power Train Research Lab
Ford Motor Research Laboratory
3623 Scientific Research Lab, PO Box 2053
Dearborn MI 48121-2053
(313)322-8930

Dr. Douglas Talley
AFRL/PRSA
10 East Saturn Boulevard
Edwards AFB CA 93524-7660
(661)275-6174
Douglas.Talley@ple.af.mil

Dr. Dinu Taraza
Dept of Mechanical Engineering
2100 Engineering Building
Wayne State University
5050 Anthony Wayne Drive
Detroit MI 48202-3902
313-577-3701
taraza@eng.wayne.edu

Dr. Jefferson W. Tester
M.I.T. Energy Laboratory
Room E40-455
Massachusetts Inst. Of Technology
Cambridge MA 02139
(617)253-3401
testerel@mit.edu

Dr. Don Thompson
Dept of Chemistry
University of Missouri Columbia
125 Chemistry Bldg
Columbia MO 65211
573-882-0051
thompsondon@missouri.edu

Dr. Stefan Thynell
Department of Mechanical Engineering
0309 Reber Building
Pennsylvania State University
University Park PA 16802
(814) 863-0977
umt@psu.edu

Dr Julian Tishkoff
Air Force Office of Scientific Research
ATTN: Julian Tishkoff - NA
875 North Randolph Street
Suite 325, Room 3112
Arlington VA 22203-1768
(703)696-8478
julian.tishkoff@afosr.af.mil

Dr. Chenning Tong
Mechanical Engineering Department
Clemson University
248 Fluor Daniel EIB
Clemson SC 29634-0921
(864)656-7225
ctong@ces.clemson.edu

Dr Michael Trenary
Department of Chemistry
The University of Illinois
Chicago IL 60680

Dr James Trolinger
MetroLaser
2572 White Road
Irvine CA 92614
(949)553-0688
jtrolinger@vmsa.oac.uci.edu

Dr Timothy Troutt
Department of Mechanical
Engineering
Washington State University
Pullman WA 99164-2920

Dr. Gretar Tryggvason
Dept of Mech Engrg & Appl Mech
2350 Hayward, Room 2250
The University of Michigan
Ann Arbor MI 48109-2125
(734)763-1049
gretar@umich.edu

Dr. Wing Tsang
National Institute of Standards and Technology
Physical and Chemical Properties Division
Route 270 and Quince Orchard Road
Gaithersburg MD 20899
(301)975-2507
wing.tsang@nist.gov

Dr. Frank Tully
U.S. Department of Energy
SC-141
19901 Germantown Road
Germantown MD 20874
(301)903-5998
Frank.Tully@science.doe.gov

Dr A D Vakili
University of Tennessee
Space Institute
Tullahoma TN 37388

Dr. Mark Valco
Propulsion Directorate
Army Research Laboratory, MS 49-1
NASA Glenn Research Center
Cleveland OH 44135-3127
(216)433-3717
aamark@lims01.lerc.nasa.gov

Dr. David Van Wie
The Johns Hopkins University
Applied Physics Laboratory
11100 Johns Hopkins Road
Laurel MD 20723-6099
(240)228-5194
David.VanWie@jhuapl.edu

Dr. Angela Violi
Department of Mechanical Engineering
2150 GG Brown
The University of Michigan
Ann Arbor MI 48109-2125
(734)615-6448
avioli@umich.edu

Dr. Ian Waitz
Department of Aaeronautics and Astronautics,
Bldg. 33-207
Massachusetts Institute of Technology
77 Massachusetts Avenue
Cambridge MA 02139-4307
(617)253-0218
iaw@mit.edu

Dr Joe Wander
AFRL/MLQL
139 Barnes Drive
Suite 2
Tyndall AFB FL 32403-5323
(904)283-6240
Jwander@mlq.afrl.af.mil

Dr. Hai Wang
Department of Mechanical & Aerospace Engineering
University of Southern California
OHE 400, Mail Code 1453
Los Angeles CA 90089
(213)740-0499
haiw@usc.edu

Dr Charles Westbrook
Lawrence Livermore National Laboratories
P. O. Box 808
Livermore CA 94551
(925)422-4108
westbrook1@llnl.gov

Dr. Phillip R. Westmoreland
National Science Foundation
Chemical and Transport Systems
4201 Wilson Boulevard
Arlington VA 22230
(703)292-8371
pwestmor@nsf.gov

Dr Forman Williams
Center for Energy and Combustion Research, 0310
University of California
La Jolla CA 92093-0310
(858)534-5492
fwilliams@ucsd.edu

Dr. Skip Williams
AFRL/PRAS
1950 Fifth Street
Building 18D, Room D234
Wright-Patterson AFB OH 45433-7251
(937)255-7292
skip.williams@wpafb.af.mil

Dr Bernard T Wolfson
Wolfson Associates International
4797 Lake Valencia Blvd West
Palm Harbor FL 33563
(813)786-3007

Dr. Mary J. Wornat
Department of Chemical Engineering
South Stadium Drive
Louisiana State University
Baton Rouge LA 70803
(225)578-7509
mjwornat@lsu.edu

Dr J M Wu
University of Tennessee
Space Institute
Tullahoma TN 37388

Dr. Vigor Yang
Propulsion Engrg Rsrch Ctr
The Pennsylvania State Univ
111 Research Building East
University Park PA 16802-2320
(814)863-1502
vigor@arthur.psu.edu

Dr Richard Yetter
Department of Mechanical and Nuclear Engineering
Pennsylvania State University
State College PA 16802
(814)863-6375
rayetter@psu.edu

Dr. Joseph Zelina
AFRL/PRTC
Building 490, Room 109
1790 Loop Road, N
Wright-Patterson AFB OH 45433-7251
(937)255-7487
joseph.zelina@wpafb.af.mil

Dr Ben Zinn
School of Aerospace Engineering
Georgia Institute of Technology
Atlanta GA 30332-0150
(404)894-3033
ben.zinn@aerospace.gatech.edu

Dr. Waldo Acosta
Vehicle Technology Directorate, Army Research Lab.
NASA Glenn Res. Ctr.
21000 Brookpark Road
Cleveland OH 44135-3191
(216) 433-3393
waldo.acosta@us.army.mil

Dr. Ajay Agrawal
Aerospace and Mechanical Engineering
University of Oklahoma
865 Asp Avenue, Room 212
Norman OK 73019
(405) 325-1754
aagrawal@ou.edu

Dr. M. S. Anand
Rolls-Royce Corporation,
P.O. Box 420
Speed Code T14
Indianapolis IN 46206-0420
(317)230-2828
m.s.anand@rolls-royce.com

Dr. William Anderson
AMSRL-WT-PC
US Army Research Laboratory
Aberdeen Proving Ground MD 21005-5066
(410)306-0731
willie@arl.army.mil

Dr Kurt Annen
Aerodyne Research, Inc.
45 Manning Road
Manning Park Research Center
Billerica MA 01821-3976
(978)663-9500
kannen@aerodyne.com

Dr. Ralph Anthenien
Propulsion and Energetics
U.S. Army Research office
P.O. Box 12211
Research Triangle Park NC 27709-2211
(919)549-4317
Ralph.anthenien1@us.army.mil

Dr Chris Atkinson
Dept of Mech. & Aerospace Eng.
West Virginia University
PO Box 6106
Morgantown WV 26506-6106
(304)293-4111

Mr. Steve Beckel
Pratt and Whitney
M/S 715-83
P.O. Box 109600
West Palm Beach FL 33410-9600

Dr Josette Bellan
Jet Propulsion Laboratory
MS 125-109
4800 Oak Grove Drive
Pasadena CA 91109
(818)354-6959
josette.bellan@jpl.nasa.gov

Dr. Michael Berman
Air Force Office of Scientific Research
ATTN: Michael Berman - NL
875 North Randolph Street
Suite 325, Room 3112
Arlington VA 22203-1768
(703)696-7781
michael.berman@afosr.af.mil

Dr Mitat Birkan
Air Force Office of Scientific Research
ATTN: Mitat Birkan - NA
875 North Randolph Street
Suite 325, Room 3112
Arlington VA 22203-1768
(703)696-7234
mitat.birkan@afosr.af.mil

Dr Kevin Bowcutt
North American Aircraft Div.
Rockwell International Corp.
P.O. Box 3644
Seal Beach CA 90740-7644

Mr. Andreja Brankovic
Flow Parametrics, LLC
15 Debra Drive
Bear DE 19701
(302)838-7368
brankov@flowparametrics.com

Dr R C Brown
Aerodyne Research, Inc.
45 Manning Road
Manning Park Research Center
Billerica MA 01821-3976
(978)663-9500

Dr. Thomas Bruno
National Institute of Standards and Technology
Physical and Chemical Properties Division
Boulder CO 80305-3328
(303)497-5158
bruno@boulder.nist.gov

Dr. Walter Bryzik
Propulsion Systems Division
ATTN: AMSTA-TR-R, MS 121
USA Tank-Automotive Command
Warren MI 48397-5000
(810)574-6461
bryzikw@tacom.army.mil

Dr T D Butler
MS B-210 T-DO: THEORETICAL DIVISION
Los Alamos National Laboratory
Los Alamos NM 87545
(505)667-4401
tdbutler@lanl.gov

Dr George Caledonia
Physical Sciences, Inc
20 New England Business Center
Andover MA 01810
(508)689-0003

Dr. Campbell Carter
AFRL/PRA
1950 Fifth Street
Building 18, Room D224
Wright-Patterson AFB OH 45433-7251
(937)255-7203
Campbell.Carter@wpafb.af.mil

Dr. Len Caveny
13715 Piscataway Drive
Ft Washington MD 20744
(301)292-5319
lhcaveny@cs.com

Dr. Nicholas Cernansky
Mechanical Engineering Dept.
Drexel University
32nd and Chestnut Streets
Philadelphia PA 19104-2884

Dr. Harsha Chelliah
Department of Mechanical, Aero
and Nuclear Engineering
University of Virginia
Charlottesville VA 22903-2442
(804)924-6037
harsha@virginia.edu

Dr. Jacqueline Chen
MS 9051
Sandia National Laboratories
P.O. Box 969
Livermore CA 94551-0969
(510)294-2586
jhchen@sandia.gov

Dr S Y Cho
Department of Mechanical and
Aerospace Engineering
Princeton University
Princeton NJ 08544-5263

Dr M B Colket
United Technologies Research
Center
411 Silver Lane, MS 129-29
East Hartford CT 06108
(860)610-7481
colketmb@utrc.utc.com

Dr S M Correa
GE Corp. Research & Development
PO Box 8, K1ES112
Schenectady NY 12301
(518)387-5853
correa@crd.ge.com

Dr Werner Dahm
Department of Aerospace Engineering
3056 FXB 2140
The University of Michigan
Ann Arbor MI 48109-2140
(734)764-4318
wdahm@umich.edu

Mr. Eugene Danielson
US Army Tank-Automotive
and Armaments Command
ATTN: AMSTA-TR-R - MS 121
Warren MI 48397-5000

Dr Ron Davis
Chemical Science and Techn Lab
Building 221, Room B312
National Inst of Stds & Tech
Gaithersburg MD 20899

Dr. Peter A. DeBarber
MetroLaser
2572 White Road
Irvine CA 92614
(949)553-0688
debarber@deltanet.com

Dr. John DeLaat
Active Combustion Control Technology
Controls and Dynamics Branch
NASA Glenn Res. Ctr.
21000 Brookpark Road
Cleveland OH 44135
(216)433-3744
jdelaat@nasa.gov

Dr Paul Dimotakis
California Institute of Tech
1201 East California Blvd.
MC 301-46
Pasadena CA 91125
(626)395-4456
dimotakis@caltech.edu

Dr Gregory Dobbs
United Technologies Research
Center - Mail Stop 90
Silver Lane
East Hartford CT 06108
(860)610-7145

Dr. James F. Driscoll
Department of Aerospace Engrg
3004 FXB Building
University of Michigan
Ann Arbor MI 49109-2118
(734)936-0101
jamesfd@umich.edu

Dr. J. Philip Drummond
NASA Langley Research Center
Mail Stop 197
Hampton VA 23681-0001
(757)864-2298
j.p.drummond@larc.nasa.gov

Dr C Dutton
Department of Mechanical and
Industrial Engineering
University of Illinois
Urbana IL 61801

Dr. Tarek Echekki
Department of Mechanical & Aerospace Engrg
North Carolina State University
2601 Stinson Drive - Campus Box 7910
Raleigh NC 27695-7910
(919)515-5238
techekk@eos.ncsu.edu

Dr. Wayne Eckerle
Cummins Engine Company
PO Box 3005
Columbus IN 47202-3005
wayne.a.eckerle@cummins.com

Dr J T Edwards
AFRL/PRTG
Building 490, Room 111
1790 Loop Road, N
Wright-Patterson AFB OH 45433-7251
(937)255-3524
james.edwards@wpafb.af.mil

Dr. Fokion N. Egolfopoulos
Department of Mechanical Engrg
University of Southern Calif
Olin Hall 400B
Los Angeles CA 90089-1453
(213)740-0480
egolfopo@almaak.usc.edu

Dr. Parviz Famouri
Department of Computer Science and Electrical
Engineering
West Virginia University
PO Box 6109
Morgantown WV 26506
(304) 293-0405 x 2530
pfamouri@wvu.edu

Dr Gregory W Faris
Molecular Physics Laboratory
SRI International
333 Ravenswood Avenue
Menlo Park CA 94025-3493
(650)859-4131
gregory.faris@sri.com

Dr. Partick Farrell
Engine Research Center
1500 Engineering Drive
University of Wisconsin
Madison WI 53706
(608)263-1686
farrell@engr.wisc.edu

Dr. David E. Foster
Engine Research Center
1500 Engineering Drive
University of Wisconsin
Madison WI 53706
(608)263-1617
foster@engr.wisc.edu

Dr Bish Ganguly
AFRL/PRPE
2645 Fifth Street, Suite 13
Wright-Patterson AFB OH 45433-7919
(937)255-2923
biswa.ganguly@pr.wpafb.af.mil

Dr Alan Garscadden
AFRL/PR
1950 Fifth Street, Building 18A
Wright-Patterson AFB OH 45433-7251
(937)255-2246
alan.garscadden@pr.wpafb.af.mil

Dr. Kresimir Gebert
BKM, Inc.
5141 Santa Fe Street
San Diego CA 92109
(858)270-6760
bkm-inc@worldnet.att.net

Mr R Giffen
General Electric Company
Aircraft Engine Group
Neumann Way
Cincinnati OH 45215

Dr. Sharath Girimaji
Department of Aerospace Engineering
Texas A&M University
College Station TX 77843-3141
(979)845-1674
girimaji@aero.tamu.edu

Dr Peyman Givi
Department of Mechanical Engineering
University of Pittsburgh
644 Benedum Hall
Pittsburgh PA 15261
(412)624-9605
givi@engr.pitt.edu

Dr Irvin Glassman
Department of Mechanical and
Aerospace Engineering
Princeton University
Princeton NJ 08544-5263
(609)258-5199
glassman@princeton.edu

Dr. Brendan Godfrey
Air Force Office of Scientific Research
ATTN: Brenddan Godfrey - CC
875 North Randolph Street
Suite 325, Room 3112
Arlington VA 22203-1768
(703)696-7553
brendan.godfrey@afosr.af.mil

Dr. George Gogos
Department of Mechanical Engineering
University of Nebraska-Lincoln
Lincoln NE 68588-0656
(402)472-3006
ggogos1@unl.edu

Dr Judah Goldwasser
Office of Naval Research
Mechanics Division, Code 333
800 North Quincy Street
Arlington VA 22217-5660
(703)696-2164
goldwaj@onr.navy.mil

Dr. James Gord
AFRL/PRTS
Building 5, Room 5P23
1790 Loop Road N
Wright-Patterson AFB OH 45433-7251
(937)255-7431
james.gord@pr.wpafb.af.mil

Dr. Jay P. Gore
School of Mechanical Engrg
Purdue University
1003 Chaffee Hall
West Lafayette IN 47907-1003
(317)494-1500

Dr Larry Goss
Research Applications Division
Systems Research Labs, Inc.
2800 Indian Ripple Road
Dayton OH 45440-3696
(513)252-2706

Dr Richard Gould
Department of Mechanical and Aerospace
Engineering
Box 7910
North Carolina State University
Raleigh NC 27695-7910
(919)515-5236
gould@eos.ncsu.edu

Dr Frederick Gouldin
Department of Mechanical and
Aerospace Engineering
Cornell University
Ithaca NY 14853-5692
(607)255-5280
fcg2@cornell.edu

Dr. Mark Gruber
AFRL/PRA
1790 Loop Road North
Wright-Patterson AFB OH 45433-7251
(937)255-2175
Mark.Gruber@afrl.af.mil

Dr. Brian K. Gullett
U.S. Environmental Protection Agency
National Risk Management Research Laboratory
Air Pollution Technology Branch (MD-65)
Research Triangle Park NC 27711
(919)541-1534
gullett.brian@epa.gov

Dr. Rajendra Gupta
Department of Physics
226 Physics Building
University of Arkansas
Fayetteville AK 72701
(501)575-5933
rgupta@comp.uark.edu

Dr. Mark A. Hagenmaier
AFRL/PRA
Building 18
1950 Fifth Street, Suite 10
Wright-Patterson AFB OH 45433-7251
(937)255-5210
hagenma@possum.appl.wpafb.af.mil

Dr. Nabil S. Hakim
Director, Advanced Engineering
Detroit Diesel Corporation
13400 W. Outer Drive, R03-B
Detroit MI 48239-4001
(313)592-7455

Dr Robert D. Hancock
AFRL/PRTS
Building 490
1790 Loop Road, N
Wright-Patterson AFB OH 45433-7103
(937)255-6814
hancockr@ward.appl.wpafb.af.mil

Dr Ronald Hanson
Mechanical Engineering Department
Stanford University
Building 530, Room 112
Stanford CA 94305-3030
(650)723-6850
hanson@me.stanford.edu

Dr. Naeim Henein
Department of Mechanical Engrg
Wayne State University
2121 Engineering Building
Detroit MI 48201
(313)577-3887
henein@me1.eng.wayne.edu

Dr Cecil F. Hess
MetroLaser
2572 White Road
Irvine CA 92614
(949)553-0688
chess@metrolaserinc.com

Mr Robert Holland
United Technologies Chemical
Systems Division
P O Box 49028
San Jose CA 95161-9028
(408)224-7656

Laura Hoogterp
Propulsion Systems Division
ATTN: AMSTA-TR-R, MS 121
USA Tank Automotive Command
Warren MI 48397-5000
586-574-6696
laura.hoogterp@us.army.mil

Dr. Tian-Sen Huang
Prairie View A&M University
PO Box 307
Prairie View TX 77446-0307
(936) 857-2859
ts_huang@pvamu.edu

Dr Lawrence Hunter
Applied Physics Laboratory
Johns Hopkins University
Johns Hopkins Road
Laurel MD 20707-6099
(301)953-5000

Dr. Frank Hurley
US Army Research Office
PO Box 12211
Research Triangle Park NC 27709-2211
(919)549-4432
hurley@aro-emh1.army.mil

Dr. Thomas Hussey
Air Force Office of Scientific Research
ATTN: Thomas Hussey - CS
875 North Randolph Street
Suite 325, Room 3112
Arlington VA 22203-1768
(703)696-7556
thomas.hussey@afosr.af.mil

Dr. Farhad Jaberi
Department of Mechanical and
Nuclear Engineering
Kansas State University
Manhattan KS 66506
(785)532-5619
jaberi@mne.ksu.edu

Dr. Thomas Jackson
AFRL/PRSC
Building 18
1950 Fifth Street
Wright-Patterson AFB OH 45433-7251
(937)255-2175
thomas.jackson@afrl.af.mil

Dr. Jeff Jagoda
School of Aerospace Engineering
Georgia Institute of Technology
Atlanta GA 30332-0150
(404)894-3060
jeff.jagoda@aerospace.gatech.edu

Dr Jay Jeffries
Mechanical Engineering Department
Thermophysics Division, Building 520
Stanford University
Stanford CA 94305-3032
(650)736-0007
Jeffries@Navier.Stanford.edu

Mr Gordon Jensen
United Technologies Chemical
Systems Division
P O Box 49028
San Jose CA 95161-9028
(408)365-5552

Mr. Jeff Jensen
Kaiser-Marquardt
16555 Staycoy Street
Van Nuys CA 91406

Mr. Craig Johnston
Lockheed Advanced Dev. Company
Lockheed-Martin Corporation
1011 Lockheed Way
Palmdale CA 93599-7212

Dr John Kelly
Altex Technologies Corporation
650 Nuttman Road
Suite 114
Santa Clara CA 95054
(408)980-8610

Dr. Barry Kiel
AFRL/PRTC
Building 490, Room 109
1950 Fifth Street
Wright-Patterson AFB OH 45433-7251
(937)255-7272
Barry.Kiel@wpafb.af.mil

Dr G B King
Department of Mechanical
Engineering
Purdue University
West Lafayette IN 47907-1288
(765)494-6518
kinggb@ecn.purdue.edu

Dr. David E. Klett
Mechanical Engineering Dept
North Carolina Agricultural
and Technical State Univ
Greensboro NC 27401-3209

Dr Charles Kolb
Aerodyne Research, Inc.
45 Manning Road
Manning Park Research Center
Billerica MA 01821-3976
(978)663-9500

Mr. John Koshoffer
General Electric Aircraft Engines
1 Neuman Way
M.D. G52
Cincinnati OH 45215
(513)243-2995
john.koshoffer@ae.ge.com

Dr Kenneth Kuo
Department of Mechanical
Engineering
Pennsylvania State University
University Park PA 16802
(814)865-6741

Dr. Ming-Chia Lai
Department of Mechanical Engrg
Wayne State University
Detroit MI 48202

Dr John Larue
Department of Mechanical
Engineering
University of California
Irvine CA 92717

Dr Allan Laufer
Office of Energy Research
U. S. Department of Energy
19901 Germantown Road
Germantown MD 20874
(202)903-5820
Allan.Laufer@oer.doe.gov

Dr Normand Laurendeau
School of Mechanical
Engineering
Purdue University
West Lafayette IN 47907-1288
(765)494-2713
Laurende@ecn.purdue.edu

Dr C K Law
Department of Mechanical and
Aerospace Engineering
Princeton University
Princeton NJ 08544-5263
(609)258-5271
cklaw@princeton.edu

Dr. Calvin Lee
Applied Research Division
Natick Research, Development & Engr. Ctr.
Kansas Street
Natick MA 01760-5017
(508)233-4267
calvin.k.lee@us.army.mil

Dr C C Lee
Environmental Protection
Agency
Cincinnati OH 45268
(513)569-7520

Dr Anthony Leonard
Graduate Aeronautical Labs
California Institute of
Technology
Pasadena CA 91125
(626)395-4465

Dr. Arthur Lewis
University of Dayton Research Inst.
Aerospace Mechanics Division
300 College Park
Dayton OH 45469-0110
(937)229-4235

Dr. Mark Lewis
AF/ST
1075 Air Force Pentagon
Washington DC 20330-1075
(703)697-7842
mark.lewis@pentagon.af.mil

Mr. Randy L. Lewis
General Electric Aircraft Engines
1 Neuman Way
M.D. G52
Cincinnati OH 45215
(513)243-0517
Randy.Lewis@ae.ge.com

Dr Goang Liaw
Department of Civil Engineering
Alabama A&M University
PO Box 367
Normal AL 35762
(205)851-5565

Dr. Timothy Lieuwen
School of Aerospace Engineering
Georgia Institute of Technology
Atlanta GA 30332-0150
(404)894-3041
tim.lieuwen@aerospace.gatech.edu

Dr. Peter Lindstedt
Department of Mechanical Engineering
Imperial College of Science, Technology, and
Medicine
Exhibition Road
London SW7 2 BX England UK
p.lindstedt@imperial.ac.uk

Dr. Mark A. Linne
Department of Combustion Physics
Lund Institute of Technology
PO Box 118
S-221 00 Lund, Sweden
+46 (0) 46-2224756
mark.linne@forbrf.lth.se

Dr. Charles L. Liotta
Department of Chemical Engrg
Georgia Institute of
Technology
Atlanta GA 30332-0100
(404)853-9344

Dr. Thomas A. Litzinger
Department of Mechanical Engineering
Pennsylvania State University
0201 Hammond Building
University Park PA 16802
(814) 865-4015
tal2@psu.edu

Dr Lyle N Long
Department of Aerospace Engrg
233 Hammond Building
Pennsylvania State University
University Park PA 16802
(814)865-1172
lnl@psu.edu

Dr. Jeffery Lovett
Pratt and Whitney
400 Main Street
MS 163-03
East Hartford CT 06108
(860)557-0559
jeffery.lovett@pw.utc.com

Dr Kevin Lyons
Department of Mechanical and Aerospace
Engineering
North Carolina State University
PO Box 7910
Raleigh NC 27695
(919)515-5293
lyons@eos.ncsu.edu

Dr Bruce MacDonald
Research Applications Division
Systems Research Labs, Inc.
2800 Indian Ripple Road
Dayton OH 45440-3696
(513)252-2706

Mr Nick Makris
SA-ALC/SFT
Kelly AFB TX 78241-5000
AV945-8212

Dr David Mann
U. S. Army Research Office
P. O. Box 12211
4300 South Miami Boulevard
Research Triangle Pk NC 27709-2211
(919)549-4249
david.mann1@us.army.mil

Dr Nagi Mansour
Computational Fluid Mechanics
Branch, RFT 202A-1
NASA Ames Research Center
Moffett Field CA 94035
(415)604-6420

Dr John Marek
NASA Glenn Research Center
Mail Stop 5-11
21000 Brookpark Road
Cleveland OH 44135-3127
(216)433-3584
cecil.j.marek@lerc.nasa.gov

Dr. Jochen Marschall
SRI International
333 Ravenswood Avenue
Menlo Park CA 94025-3493
(650)859-2667
jochen.marschall@sri.com

Dr. Jay Martin
University of Wisconsin-Madison
Engine Research Center
1500 Engineering Drive
Madison WI 53706
(608)263-9460
martin@engr.wisc.edu

Dr James McDonald
Code 6110
Naval Research Laboratory
Chemistry Division
Washington DC 20375-5342
(202)767-3340

Dr. Kevin McNesby
Army Research Laboratory
Army Research Office
P.O. Box 12211
Research Triangle Park NC 27709-2211
(410)306-0715
mcnesby@arl.army.mil

Dr A M Mellor
Mech & Matls Engrg Dept
512 Kirkland Hall
Vanderbilt University
Nashville TN 37240
(615)343-6214

Dr Lynn Melton
Programs in Chemistry
University of Texas, Dallas
P. O. Box 830688
Richardson TX 75083-0688
(972)883-2913
melton@utdallas.edu

Dr. Suresh Menon
School of Aerospace Engineering
Georgia Institute of Technology
270 Ferst Drive
Atlanta GA 30332-0150
(404)894-9126
suresh.menon@aerospace.gatech.edu

Dr Hameed Metghalchi
Mechanical, Industrial and Manufacturing Dept.
334SN
Northeastern University
360 Huntington Avenue
Boston MA 2115
(617)-373-2973
metghal@coe.neu.edu

Dr Michael M Micci
Department of Aerospace Engrg
233 Hammond Building
Pennsylvania State University
University Park PA 16802
(814)863-0043
micci@henry2.aero.psu.edu

Dr Andrzej Miziolek
AMSRL-WT-PC
Army Research Laboratory
Aberdeen Proving Gnd MD 21005-5066
(410)278-6157
miziolek@arl.army.mil

Dr. H. C. Mongia
Manager, Combustion Technology
GE Aircraft Engines
One Neumann Way, M/D A404
Cincinnati OH 45215-6301
(513)243-2552
Hukam.Mongia@ae.ge.com

Dr Arje Nachman
Air Force Office of Scientific Research
ATTN: Arje Nachman - NM
875 North Randolph Street
Suite 325, Room 3112
Arlington VA 22203-1768
(703)696-8427
arje.nachman@afosr.af.mil

Dr Herbert Nelson
Code 6110, Chemistry Division
Naval Research Laboratory
4555 Overlook Avenue, SW
Washington DC 20375-5342
(202)767-3686

Dr. Matthew Oehlschlaeger
Department of Mechanical, Aerospace, and
Nuclear Engineering
Rensselaer Polytechnic Institute
JEC 2049
110 8th Street
Troy NY 12180-3590
(518)276-8115
oehlsm@rpi.edu

Dr Elaine Oran
LCP&FD, Code 6404
US Naval Research Laboratory
4555 Overlook Avenue, SW
Washington DC 20375-5344
(202)767-2960
ORAN@lcp.nrl.navy.mil

Dr. Michelle Pantoya
Department of Mechanical Engineering, MS
1021
Texas Tech University
Lubbock TX 79409
(806) 742-3563
michelle.pantoya@coe.ttu.edu

Dr T E Parker
Engineering Division
Colorado School of Mines
Golden CO 80401-1887
(303)273-3657
tparker@mines.colorado.edu

Dr. Phillip H. Paul
MS 9051
Sandia National Laboratories
P. O. Box 969
Livermore CA 94551-9051
(510)294-1465
phpaul@sandia.gov

Dr Lisa Pfefferle
Department of Chemical
Engineering
Yale University
New Haven CT 06520-8286
(203)432-2222
pfefferle@htcre.eng.yale.edu

Dr Emil Pfender
Department of Mechanical Engrg
125 Mechanical Engineering
The University of Minnesota
Minneapolis MN 55455

Dr. Heinz G Pitsch
Department of Mechanical Engineering
Building 500, Room 500M
Stanford University
Stanford CA 94305-3035
(650)725-6635
h.pitsch@stanford.edu

Dr Robert Pitz
Department of Mechanical and
Materials Engineering
Vanderbilt University
Nashville TN 37235
(615)322-0209
pitzrw@ctrvan.vanderbilt.edu

Dr S B Pope
Department of Mechanical and
Aerospace Engineering
Cornell University
Ithaca NY 14853-7501
(607)255-4314
pope@mae.cornell.edu

Dr. David Pratt
AFRL/VAS
Building 45 Annex
2130 Eighth Street, Suite 1
Wright-Patterson AFB OH 45433-7542
(937)255-5042
David.Pratt@va.afrl.af.mil

Dr. Ala Qubbaj
Department of Mechanical Engineering, ENB
3230
University of Texas-Pan American
1201 West University Drive
Edinburg TX 78539-2999
(956) 318-5220
qubbaj@panam.edu

Dr. Larry Rahn
Sandia National Laboratories
7011 East Avenue
Mail Stop 9056
Livermore CA 94551-0969
(510)294-2091
rahn@sandia.gov

Dr. Mohan K. Razdan
Rolls-Royce Company
P.O. Box 420
Speed Code T10B
Indianapolis IN 46206-0420
(317)230-6404
mohan.razdan@rolls-royce.com

Mr. Robert Reed
Sverdrup Technology, Inc.
AEDC
1099 Avenue C
Arnold AFB TN 37389-9013
(615)454-4648

Dr Rolf D Reitz
Mechanical Engineering Dept
University of Wisconsin
1500 Johnson Drive
Madison WI 53706
(608)262-0145

Dr. Kyung T. Rhee
Department of Mechanical and
Aerospace Engineering
Rutgers, The State Univ of NJ
Piscataway NJ 08854-0909
(732)445-3651
KTRhee@jove.rutgers.edu

Dr James Riley
Mechanical Engineering Dept
University of Washington
Seattle WA 98195
(206)543-5347
73671.737@Compuserve.com

Dr William Roberts
Department of Mechanical and Aerospace Engineering
Box 7910
North Carolina State University
Raleigh NC 27695-7910
(919)515-5294
wlrobert@eos.ncsu.edu

Mr. Gerald A. Roffe
GASL
77 Raynor Avenue
Ronkonkoma NY 11779

Dr W M Roquemore
AFRL/PRTS
Building 5
Wright-Patterson AFB OH 45433-7251
(937)255-6813
melvyn.roquemore@wpafb.af.mil

Dr Daniel Rosner
Department of Chemical Engineering
Yale University
New Haven CT 06520-8286
(203)432-4391
daniel.rosner@yale.edu

Dr John Ross
Department of Chemistry
Stanford University
Stanford CA 94305-3032
(650)723-9203

Dr Gabriel Roy
Office of Naval Research
Mechanics Division, Code 1132
800 North Quincy Street
Arlington VA 22217-5660
(703)696-4406
roy@ocnr-hq.navy.mil

Dr Thomas Russell
Air Force Office of Scientific Research
ATTN: Thomas Russell - NA
875 North Randolph Street
Suite 325, Room 3112
Arlington VA 22203-1768
(703)696-8457
thomas.russell@afosr.af.mil

Dr. Robert C. Ryder
Flow Parametrics, LLC
15 Debra Drive
Bear DE 19701
(302)838-7368
rryder@flowparametrics.com

Mr Kurt Sacksteder
NASA Glenn Research Center
MS 500-217
21000 Brookpark Road
Cleveland OH 44135
(216)433-2857

Dr Mohammad Samimy
Ohio State University
Mechanical Engineering Dept
206 West 18th Street
Columbus OH 43210-1107
(614)422-6988
msamimy@magnus.acs.ohio-state.edu

Dr G S Samuelsen
Department of Mechanical and Aerospace Engineering
University of California
Irvine CA 92697-3975
(949)824-5468

Dr Lakshmi Sankar
School of Aerospace Engrg
Georgia Institute of Technology
Atlanta GA 30332
(404)894-3014

Dr Domenic Santavicca
Propulsion Engineering Research Center
Pennsylvania State University
106 Research Building East - Bigler Road
University Park PA 16802-2320
(814)863-1863

Dr R J Santoro
Department of Mechanical Engineering
Pennsylvania State University
University Park PA 16802-2320
(814)863-1285
rjs2@email.psu.edu

Dr Sutanu Sarkar
Department of Applied Mech
and Engr Science, MC 0411
University of California
La Jolla CA 92093-0411
(858)534-8243
ssarkar@ucsd.edu

Dr John Schaefer
Energy and Environmental Div.
Acurex Corporation
555 Clyde Ave., P. O. Box 7555
Mountain View CA 94039

Dr. Frederick Schauer
AFRL/PRTS
Building 490, Room 112
1790 Loop Road, N
Wright-Patterson AFB OH 45433-7251
(937)255-6462
frederick.schauer@wpafb.af.mil

Dr. Peter Schihl
Propulsion Systems Division
ATTN: AMSTA-TR-R, MS 121
USA Tank Automotive Command
Warren MI 48397-5000
schihlp@tacom.army.mil

Dr. John Schmisseur
Air Force Office of Scientific Research
ATTN: John Schmisseur - NA
875 North Randolph Street
Suite 325, Room 3112
Arlington VA 22203-1768
(703)696-6962
john.schmisseur@afosr.af.mil

Dr. Ernest Schwarz
Propulsion Systems Division
ATTN: DRSTA-RGD
USA Tank-Automotive Command
Warren MI 48397-5000
(810)574-5656
schwarze@cc.tacom.army.mil

Mr. Lee Scuderi
McDonnell Douglas Aerospace
P.O. Box 516
St. Louis MO 63166-0516

Dr Jerry Seitzman
School of Aerospace Engineering
Georgia Institute of Technology
Atlanta GA 30332-0150
(404)894-0013
jerry.seitzman@ae.gatech.edu

Dr Kalyanasundaram Seshadri
Center for Energy and
Combustion Research, 0407
University of California
La Jolla CA 92093-0407
(619)534-4876
seshadri@ames.ucsd.edu

Dr Robert Shaw
Division of Chemical and
Biological Sciences
U S Army Research Office
Research Triangle Park NC 27709-2211
(919)549-0641

Dr. Adam Siebenhaar
Aerojet Propulsion Division
P.O. Box 13222
Sacramento CA 95813-6000

Dr. Gupreet Singh
U.S. Department of Energy
1000 Independence Avenue, S.W.
Washington DC 20585
(202)586-2333
GUPREET.SINGH@hq.doe.gov

Dr William Sirignano
Department of Mechanical and
Aerospace Engineering
University of California
Irvine CA 92697-3975
(949)824-3700
sirignan@uci.edu

Mr. Davey Smith
Northrop Grumman Corporation
B-2 Division Dayton Office
2850 Presidential Dr., Ste 100
Fairborn OH 45324

Dr Gregory Smith
Department of Chem Kinetics
SRI International
333 Ravenswood Avenue
Menlo Park CA 94025-3493
(415)859-3496

Dr. Kenneth A. Smith
Department of Chemical Engrg.
Room 66-540
Massachusetts Inst. Of Technology
Cambridge MA 02139
(617)253-1973
kas@mit.edu

Dr. James Smith
Department of Chemical Engineering
University of Alabama in Huntsville
Huntsville AL 35899
(256) 824-3594
smithje1@uah.edu

Dr. Mitchell Smooke
Department of Mechanical Engineering
205 Becton Center
15 Prospect Street
Yale University
New Haven CT 6520
(203)432-4344
mitchell.smooke@yale.edu

Dr. Judi Steciak
University of Idaho-Boise
800 Park Boulevard
Boise ID 83712-7742
(208)364-4080
jsteciak@uidaho.edu

Dr David Stewart
Department of Theoretical and
Applied Mechanics
University of Illinois
Urbana IL 61801

Dr Geoffrey J Sturgess
Dayton
gsturgess@aol.com

Dr B Sturtevant
Engrg and Appl Sci Dept
California Institute of
Technology
Pasadena CA 91125

Dr G Sullins
Applied Physics Laboratory
Johns Hopkins University
Johns Hopkins Road
Laurel MD 20707-6099
(301)953-5000

Dr Chih-Jen (Jackie) Sung
Dept. of Mechanical and Aerospace Engineering
Case Western Reserve University
10900 Euclid Avenue
Cleveland OH 44106-7222
216-368-2942
cjs15@case.edu

Dr. Rodney Tabacyznski
Director, Power Train Research Lab
Ford Motor Research Laboratory
3623 Scientific Research Lab, PO Box 2053
Dearborn MI 48121-2053
(313)322-8930

Dr. Douglas Talley
AFRL/PRSA
10 East Saturn Boulevard
Edwards AFB CA 93524-7660
(661)275-6174
Douglas.Talley@ple.af.mil

Dr. Dinu Taraza
Dept of Mechanical Engineering
2100 Engineering Building
Wayne State University
5050 Anthony Wayne Drive
Detroit MI 48202-3902
313-577-3701
taraza@eng.wayne.edu

Dr. Jefferson W. Tester
M.I.T. Energy Laboratory
Room E40-455
Massachusetts Inst. Of Technology
Cambridge MA 02139
(617)253-3401
testerel@mit.edu

Dr. Don Thompson
Dept of Chemistry
University of Missouri Columbia
125 Chemistry Bldg
Columbia MO 65211
573-882-0051
thompsondon@missouri.edu

Dr. Stefan Thynell
Department of Mechanical Engineering
0309 Reber Building
Pennsylvania State University
University Park PA 16802
(814) 863-0977
umt@psu.edu

Dr Julian Tishkoff
Air Force Office of Scientific Research
ATTN: Julian Tishkoff - NA
875 North Randolph Street
Suite 325, Room 3112
Arlington VA 22203-1768
(703)696-8478
julian.tishkoff@afosr.af.mil

Dr. Chenning Tong
Mechanical Engineering Department
Clemson University
248 Fluor Daniel EIB
Clemson SC 29634-0921
(864)656-7225
ctong@ces.clemson.edu

Dr Michael Trenary
Department of Chemistry
The University of Illinois
Chicago IL 60680

Dr James Trolinger
MetroLaser
2572 White Road
Irvine CA 92614
(949)553-0688
jtrolinger@vmsa.oac.uci.edu

Dr Timothy Troutt
Department of Mechanical
Engineering
Washington State University
Pullman WA 99164-2920

Dr. Gretar Tryggvason
Dept of Mech Engrg & Appl Mech
2350 Hayward, Room 2250
The University of Michigan
Ann Arbor MI 48109-2125
(734)763-1049
gretar@umich.edu

Dr. Wing Tsang
National Institute of Standards and Technology
Physical and Chemical Properties Division
Route 270 and Quince Orchard Road
Gaithersburg MD 20899
(301)975-2507
wing.tsang@nist.gov

Dr. Frank Tully
U.S. Department of Energy
SC-141
19901 Germantown Road
Germantown MD 20874
(301)903-5998
Frank.Tully@science.doe.gov

Dr A D Vakili
University of Tennessee
Space Institute
Tullahoma TN 37388

Dr. Mark Valco
Propulsion Directorate
Army Research Laboratory, MS 49-1
NASA Glenn Research Center
Cleveland OH 44135-3127
(216)433-3717
aamark@lims01.lerc.nasa.gov

Dr. David Van Wie
The Johns Hopkins University
Applied Physics Laboratory
11100 Johns Hopkins Road
Laurel MD 20723-6099
(240)228-5194
David.VanWie@jhuapl.edu

Dr. Angela Violi
Department of Mechanical Engineering
2150 GG Brown
The University of Michigan
Ann Arbor MI 48109-2125
(734)615-6448
avioli@umich.edu

Dr. Ian Waitz
Department of Aaeronautics and Astronautics,
Bldg. 33-207
Massachusetts Institute of Technology
77 Massachusetts Avenue
Cambridge MA 02139-4307
(617)253-0218
iaw@mit.edu

Dr Joe Wander
AFRL/MLQL
139 Barnes Drive
Suite 2
Tyndall AFB FL 32403-5323
(904)283-6240
Jwander@mlq.afrl.af.mil

Dr. Hai Wang
Department of Mechanical & Aerospace Engineering
University of Southern California
OHE 400, Mail Code 1453
Los Angeles CA 90089
(213)740-0499
haiw@usc.edu

Dr Charles Westbrook
Lawrence Livermore National Laboratories
P. O. Box 808
Livermore CA 94551
(925)422-4108
westbrook1@llnl.gov

Dr. Phillip R. Westmoreland
National Science Foundation
Chemical and Transport Systems
4201 Wilson Boulevard
Arlington VA 22230
(703)292-8371
pwestmor@nsf.gov

Dr Forman Williams
Center for Energy and Combustion Research, 0310
University of California
La Jolla CA 92093-0310
(858)534-5492
fwilliams@ucsd.edu

Dr. Skip Williams
AFRL/PRAS
1950 Fifth Street
Building 18D, Room D234
Wright-Patterson AFB OH 45433-7251
(937)255-7292
skip.williams@wpafb.af.mil

Dr Bernard T Wolfson
Wolfson Associates International
4797 Lake Valencia Blvd West
Palm Harbor FL 33563
(813)786-3007

Dr. Mary J. Wornat
Department of Chemical Engineering
South Stadium Drive
Louisiana State University
Baton Rouge LA 70803
(225)578-7509
mjwornat@lsu.edu

Dr J M Wu
University of Tennessee
Space Institute
Tullahoma TN 37388

Dr. Vigor Yang
Propulsion Engrg Rsrch Ctr
The Pennsylvania State Univ
111 Research Building East
University Park PA 16802-2320
(814)863-1502
vigor@arthur.psu.edu

Dr Richard Yetter
Department of Mechanical and Nuclear Engineering
Pennsylvania State University
State College PA 16802
(814)863-6375
rayetter@psu.edu

Dr. Joseph Zelina
AFRL/PRTC
Building 490, Room 109
1790 Loop Road, N
Wright-Patterson AFB OH 45433-7251
(937)255-7487
joseph.zelina@wpafb.af.mil

Dr Ben Zinn
School of Aerospace Engineering
Georgia Institute of Technology
Atlanta GA 30332-0150
(404)894-3033
ben.zinn@aerospace.gatech.edu